

School of Civil and Mechanical Engineering

Nature-inspired Protective Structures against Impulsive Loading

Lalin Lam

0000-0002-4050-1251

**This thesis is presented for the Degree of
Doctor of Philosophy
of
Curtin University**

March 2024

Declaration

To the best of my knowledge and belief this thesis contains no material previously published by any other person except where due acknowledgement has been made.

This thesis contains no material which has been accepted for the award of any other degree or diploma in any university.

Signature:

Date: 17 March 2024

Abstract

This thesis aims to mimic the structural features and mechanisms found in nature to develop novel energy-absorbing structures with unique energy absorption mechanisms and high crushing efficiency. Four innovative nature-inspired designs are proposed. The first one is inspired by the unconventional shapes of plant stems, which provide additional resistance against wind loads and additional weight, i.e., leaves, flowers, and fruits, as compared to conventional shapes. The mint plant stem with a corrugated tapered/tilted shape is mimicked and implemented into the square honeycomb core to develop a corrugated tilted honeycomb (CTH) core. The dynamic crushing and energy absorption performances of the proposed CTH core are numerically investigated using finite element software LS-DYNA. The CTH core demonstrates excellent crushing performance, with higher crushing resistance without a high initial peak force under various crushing speeds, compared to the conventional square honeycomb core and aluminium foam of the same mass. In addition, the impact mitigation performance of the CTH structure as the internal core of the protective sacrificial cladding is experimentally investigated using a pendulum impact testing facility. The CTH cladding exhibits excellent impact mitigation performance as a sacrificial cladding against impact loads, showing a more stable crushing force without obviously high peaks, lower transmitted force, and larger deformation compared to sacrificial cladding with conventional square honeycomb core.

The other three nature-inspired designs are all related to the viscoelastic material found inside the protective structures of animals, such as the forewing of the beetle and the horn sheath of the bighorn sheep. These animals can protect themselves and minimise the impact force from various impact and loading conditions using their protective mechanisms. For the second nature-inspired design, the viscoelastic material and the arch shape of hollow cavity structures found inside the forewing structure of the beetle are imitated by utilising the shear thickening fluid (STF) and semi-arch cores, respectively. The proposed sandwich structure inspired by the beetle forewing (SSBF) exhibits high crushing resistance and high energy-absorbing capacity. As compared with an empty specimen with a thick core having a comparable mass, the initial peak crushing resistance of the empty specimen substantially increases with the increase in crushing speed, but its overall crushing resistance remains almost unchanged. In

contrast, the crushing resistance of SSBF enhances with the increase in crushing speed and remains stable throughout the crushing process without a noticeable initial peak, showing its ideal behaviour for energy absorption and ability to adapt to various impact scenarios.

The third innovative nature-inspired design is proposed by incorporating the STF into the origami metastructure, thus mimicking the existence of the viscoelastic material found inside the tubule of the horn sheath. The proposed nature-inspired STF-filled origami metastructure (STF-OM) can generate a higher and more stable crushing resistance without inducing significantly high initial peaks, resulting in a higher crushing resistance efficiency compared to the non-filled one. Its crushing resistance increases with the increase in crushing velocity, demonstrating its adaptive crushing performance for various impact scenarios. Partial incorporation of the STF provides support and prevents the localised deformation of the OM structure under dynamic crushing, thereby enhancing the crushing performance of the structure. Moreover, the crushing performance of STF-OM can be efficiently improved by using STF with higher shear thickening behaviour.

The fourth innovative nature-inspired mechanism is the wavy suture and the viscoelastic material between the suture interface found in the cranial bones of headbutting animals and the beaks of woodpeckers. During violent clashes of the headbutting animals, no noticeable damage or brain injury is observed for these animals. Woodpecker beaks can also withstand high impact without damage to the brain despite the multiple strikes onto the tree trunk. Therefore, the viscoelastic material and the suture interfaces of these animals are mimicked to propose a novel recoverable energy-absorbing device. The viscoelastic material and tooth of the suture are mimicked by STF and a rectangular tube, respectively. The proposed bio-inspired energy-absorbing device (BIEAD) shows good energy-absorbing capacity and can slowly recover after the impact due to the shear thickening behaviour, sticky characteristics of the STF, and the elastic springs in the prototype design, demonstrating its ability to absorb the energy and recover after impact.

Acknowledgements

First and foremost, I would like to express my deep appreciation and sincere gratitude to my supervisors, Prof. Hong Hao and Assoc. Prof. Wensu Chen, for their valuable guidance, expertise, sensible advice, and unwavering support throughout my PhD journey. Their enlightening guidance and wisdom have shaped both my academic research and life.

I would like to extend my sincere thanks to Assoc. Prof. Zhejian Li, Assoc. Prof. Thong Pham, and Dr. Ngoc San Ha for their valuable comments and contributions to this thesis as co-authors of related publications.

I would like to thank and acknowledge the group members of the Centre for Infrastructural Monitoring and Protection (CIMP) at Curtin University, including Dr. Zhijie Huang and Mr. Paing Min Htet, for their assistance during specimen preparation and impact testing. I am indebted to the staff and resources of the Civil and Mechanical Engineering Laboratory at Curtin University's Bentley campus for providing the necessary facilities and research tools essential for the impact tests during my study. I would also like to thank Mr. Ameen Topa for sharing his knowledge of numerical simulation using LS-DYNA.

I am very grateful to acknowledge the support received through the Australian Government Research Training Program Scholarship.

Last but not least, I would like to express my profound gratitude and warmest thanks to my parents, my sisters, and my grandmother for their encouragement and support. Finally, I would like to express my heartfelt thanks to my wife, Noppharat, for her unwavering love, encouragement, and understanding throughout this academic journey. Without their support, I could not have done it.

List of Published work and work prepared for publication

This thesis is assembled from a series of published journal articles. These articles form the individual chapters as indicated below.

Chapter 3

Lam L, Chen W, Hao H, Li Z. Crushing behaviour of corrugated tilted honeycomb core inspired by plant stem. *Thin-Walled Structures* 2023;188:110852.

<https://doi.org/10.1016/j.tws.2023.110852>

Chapter 4

Lam L, Chen W, Hao H, Huang Z, Li Z. Impact performance of sandwich cladding with corrugated tilted honeycomb core. *Structures* 2024;61:106072.

<https://doi.org/10.1016/j.istruc.2024.106072>

Chapter 5

Lam L, Chen W, Hao H, Li Z, Ha NS. Dynamic crushing performance of bio-inspired sandwich structures with beetle forewing cores. *International Journal of Impact Engineering* 2023;173:104456.

<https://doi.org/10.1016/j.ijimpeng.2022.104456>

Chapter 6

Lam L, Chen W, Hao H, Li Z. Dynamic crushing and energy absorption of bio-inspired shear thickening fluid-filled origami metastructure. *Engineering Structures* 2024;299:117122.

<https://doi.org/10.1016/j.engstruct.2023.117122>

Chapter 7

Lam L, Chen W, Hao H, Li Z, Ha NS, Pham TM. Numerical study of bio-inspired energy-absorbing device using shear thickening fluid (STF). *International Journal of Impact Engineering* 2022;162:104158.

<https://doi.org/10.1016/j.ijimpeng.2022.104158>

List of Relevant Additional works

Lam L, Chen W, Hao H, Li Z, Ha NS. Dynamic crushing behaviours of sandwich structures inspired by beetle forewing core (SSBF). 6th International Conference on Protective Structures; 2023, Auburn, USA.

Statement of Contribution of Others

The work presented in this thesis was primarily designed, numerically simulated, experimentally executed, analysed, and written by the first author (Lalin Lam) of the individual manuscripts. Contributions by others are described as follows. The signed contribution forms are attached in the appendix.

Chapter 3 and Chapter 6

Prof. Hong Hao, Assoc. Prof. Wensu Chen, and Assoc. Prof. Zhejian Li revised and edited the manuscripts, and provided intellectual input towards the conceptual design, data processing, analysis, and discussion of the results.

Chapter 4

Prof. Hong Hao, Assoc. Prof. Wensu Chen, and Assoc. Prof. Zhejian Li revised and edited the manuscript, and provided intellectual input towards the planning of the impact tests, data processing, analysis, and discussion of the results. Dr. Zhijie Huang assisted with the impact testing set-up, data recording, and control settings. Mr. Paing Min Htet assisted with the specimen preparation. Civil and Mechanical Engineering Laboratory at Curtin University's Bentley campus helped with the testing of specimens.

Chapter 5

Prof. Hong Hao, Assoc. Prof. Wensu Chen, Assoc. Prof. Zhejian Li, and Dr. Ngoc San Ha revised and edited the manuscript, and provided intellectual input towards the conceptual design, data processing, analysis, and discussion of the results.

Chapter 7

Prof. Hong Hao, Assoc. Prof. Wensu Chen, Assoc. Prof. Zhejian Li, Dr. Ngoc San Ha, and Assoc. Prof. Thong M. Pham revised and edited the manuscript, and provided intellectual input towards the conceptual design, data processing, analysis, and discussion of the results.

Table of Contents

Declaration	i
Abstract	ii
Acknowledgements	iv
List of Published work and work prepared for publication.....	v
List of Relevant Additional works	vii
Statement of Contribution of Others	viii
Table of Contents	ix
Chapter 1. Introduction	1
1.1 Background	1
1.2 Objectives.....	1
1.3 Research outline	2
Chapter 2. Literature review	6
2.1 Overview of protective structures	6
2.2 Ideal characteristics of energy absorber for protective structures.....	7
2.3 Crushing performance investigation of structures	8
2.3.1 Experimental investigations	9
2.3.2 Numerical investigations.....	12
2.4 Conventional energy-absorbing structures.....	13
2.5 Folded structures	15
2.6 Metastructures	18
2.7 Existing nature-inspired structures.....	19
2.8 Interesting feature and protective mechanism in nature	22
2.8.1 Structural feature of the cross-section of mint plant stem	22
2.8.2 Viscoelastic material inside the protective structures of animals	23
2.8.3 Viscoelastic material inside the wavy suture interfaces.....	24
2.8.4 Shear thickening fluid (STF)-viscoelastic material	25
2.9 Summary	28
Chapter 3. Corrugated tilted honeycomb (CTH) core inspired by plant stem	30
3.1 Introduction.....	30
3.2 Numerical model calibration.....	31
3.2.1 Numerical model.....	31
3.2.2 Model calibration	32

3.3	Corrugated tilted honeycomb (CTH) core inspired by plant stem	33
3.3.1	Geometries and loading conditions	33
3.3.2	Mesh convergence test	38
3.4	Results and discussions	38
3.4.1	Crushing responses of CTH cores under various crushing speeds	39
3.4.2	Effect of tilted angle on the CTH core	47
3.4.3	Effect of relative density on the CTH core.....	48
3.5	Comparison of crushing performances of similar cellular structures	51
3.6	Summary	55
Chapter 4. Impact performance of sandwich cladding with CTH core.....		57
4.1	Introduction	57
4.2	Specimen configurations and preparation	57
4.2.1	Core configurations	57
4.2.2	Cladding preparation and material property.....	58
4.3	Experimental program.....	60
4.3.1	Impact test setup and instrumentation.....	60
4.3.2	Impact scenarios	63
4.4	Results and discussions	64
4.4.1	Impact performances of claddings with different cores	64
4.4.2	Effect of impact velocity	69
4.4.3	Effect of combination of various impact masses and velocities	75
4.5	Summary	80
Chapter 5. Sandwich structures inspired by beetle forewing (SSBF).....		82
5.1	Introduction	82
5.2	Numerical model calibration.....	83
5.2.1	Boundary conditions and contact	84
5.2.2	Element types and material models.....	85
5.2.3	Model calibration	86
5.3	Sandwich structure inspired by beetle forewing (SSBF)	87
5.3.1	Geometries and loading conditions	87
5.3.2	Material models.....	89
5.3.3	Mesh convergence test	92
5.4	Results and discussions	93

5.4.1	Force-displacement and energy absorption of SSBF under various crushing speeds	93
5.4.2	Deformation mode of SSBF.....	100
5.4.3	Comparison between SSBF and conventional specimen with comparable mass.....	102
5.5	Summary	103
Chapter 6. Bio-inspired shear thickening fluid-filled origami metastructure (STF-OM).....		105
6.1	Introduction.....	105
6.2	Numerical model calibration.....	106
6.2.1	Numerical model.....	108
6.2.2	Model calibration	108
6.3	Shear thickening fluid-filled origami metastructure (STF-OM).....	109
6.3.1	Geometries and loading conditions.....	109
6.3.2	Material models and FE modelling techniques.....	112
6.4	Results and discussions	113
6.4.1	Dynamic crushing of STF-OM under different velocities.....	113
6.4.2	Comparison of the crushing performances under various crushing velocities	119
6.5	Parametric studies of STF-OM	122
6.5.1	Effect of the filled height of STF	122
6.5.2	Effect of viscosity of STF	123
6.5.3	Effect of origami folding angle.....	124
6.6	Summary	126
Chapter 7. Recoverable bio-inspired energy-absorbing device (BIEAD).....		128
7.1	Introduction.....	128
7.2	Numerical model calibration.....	129
7.2.1	Element, mesh, and boundary condition of the tested beam model.....	130
7.2.2	Material models.....	131
7.2.3	Fluid-Structure-Interaction (FSI) approach	132
7.2.4	Model calibration	132
7.3	Bio-inspired energy-absorbing device (BIEAD).....	133
7.3.1	Geometries and loading conditions.....	133
7.3.2	Material model of STF	135

7.4	Results and discussions	136
7.4.1	Deformation mode of BIEAD	136
7.4.2	Force-displacement and energy absorption of BIEAD under various loading rates	138
7.4.3	Recoverability of BIEAD.....	142
7.4.4	Comparison of energy absorption capacities of BIEAD, aluminium foam and honeycomb	143
7.5	Parametric studies of BIEAD	145
7.5.1	Effect of viscosity.....	145
7.5.2	Effect of shear gap.....	147
7.5.3	Effect of contact area.....	149
7.6	Summary	151
Chapter 8. Conclusion and recommendations.....		153
8.1	Main findings	153
8.2	Recommendations for future work.....	155
References		157
Appendix A Statement of contribution of co-authors.....		179
Appendix B Copyright clearance		183

Chapter 1. Introduction

1.1 Background

In recent decades, there has been an increasing demand for the development of effective protective structures to safeguard existing and new critical structures from impulsive loads, such as blasts or impacts [1–3]. Sandwich structures, consisting of external plates and an internal core, have been extensively studied and utilised as energy-absorbing and protective structures [4]. Cellular structures of various structural forms have been extensively proposed and investigated as the internal core, which absorbs impact or blast energy through the plastic deformation of their crushable cores [4,5]. However, existing sacrificial cores have their drawbacks, such as generating a high initial peak force followed by low and fluctuating plastic crushing resistances, leading to non-ideal characteristics for energy absorption applications and compromising the protective effectiveness of the structure [4]. Furthermore, the high initial peak crushing resistance of conventional cores significantly increases with the increase in loading rate. This can lead to a high transmitted force and severe damage to the protected structures under dynamic loads [6–8]. In addition to the increase in the peak crushing resistance, the overall crushing resistance, which contributes to the energy absorption capacity of the structure, may only slightly increase with the increase in crushing speeds. Therefore, the protective sandwich structure with a specific core is constrained to a fixed energy absorption capacity, but it may become either too soft or too stiff under different impact energies or impact speeds [6,9]. Another drawback of conventional cores is their energy absorption mechanism, which absorbs the blast or impact energy through plastic deformation. Therefore, the conventional protective structures with these cores are unlikely to recover and need to be replaced after each impact or blast event, compromising the protective effectiveness of these structures against multiple-loading events.

1.2 Objectives

The objective of this study is to develop novel energy-absorbing structures with unique energy absorption mechanisms and high crushing efficiency, inspired by structural features and mechanisms found in nature. To achieve ideal energy absorption

performance, the new form of energy-absorbing structure should exhibit high crushing resistance without a significantly high initial peak. This initial peak should also be insensitive to loading rates, as it contributes only a small portion to the energy absorption but can result in unnecessarily high transmitted forces to the protected structures at the back. The first objective is to develop an ideal and easy-to-fabricate energy-absorbing structure for sacrificial cladding applications. For the development of this novel energy-absorbing structure, a numerical study of the proposed structure is first conducted, and its crushing performance is investigated and evaluated by comparing it with the existing similar structural forms found in the literature. The experimental impact test of this novel structural form as the internal core of the sacrificial protective cladding is then performed to further investigate its impact mitigation performance.

The second objective is to develop innovative structures with ideal crushing efficiency and adaptive energy-absorbing capabilities to accommodate the uncertainties of impact scenarios. These adaptive energy-absorbing structures with ideal crushing efficiency are developed by mimicking the protective mechanisms of animals that can protect themselves from various impact and loading conditions. Their dynamic crushing responses, crushing efficiency, energy absorption performances, and adaptability are numerically investigated and compared with the conventional energy-absorbing structures.

Lastly, to propose a recoverable energy-absorbing device by mimicking the mechanisms of animals that can resist multiple strikes or impacts, such as woodpeckers and headbutting animals, thereby allowing the proposed structure to recover and resist multiple impact and loading events. Its energy absorption performance and recoverability are numerically investigated. A parametric study is also carried out to investigate the influence factors on the energy absorption performance of the newly proposed device.

1.3 Research outline

This thesis comprises eight chapters. Figure 1-1 summarises the features and protective mechanisms in nature, along with the main outcomes of the corresponding nature-inspired designs in each of the main chapters, i.e., Ch 3 to Ch 7.

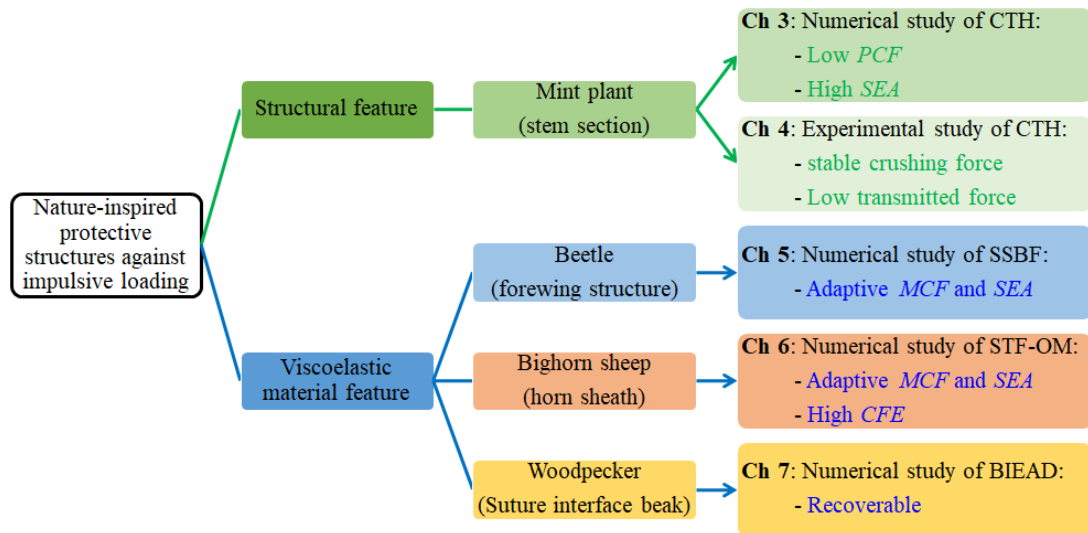


Figure 1-1. Summary of the four proposed nature-inspired designs and their main outcomes.

The contents of the six chapters following the introduction and literature review are described as follows:

Chapter 3 presents a numerical analysis of the proposed corrugated tilted honeycomb (CTH) core inspired by a mint plant stem. This study aims to investigate the dynamic crushing responses, energy absorption capacity, and crushing efficiency of the proposed CTH core. The implementation of the corrugated tilted design facilitates bending response and enhances the crushing resistance during the crushing process, thereby increasing the crushing efficiency of the proposed structure. The proposed CTH core can also be fabricated using simple slotting and pressing techniques. The calibrated numerical model is used to construct the proposed CTH cores with different numbers and dimensions of corrugations. The effects of crushing speed, tilted angle, and relative density on the crushing behaviour of the proposed CTH core are also investigated. The crushing and energy absorption efficiencies of the proposed CTH cores are evaluated by comparing them with those of commercially available cores, such as square honeycomb cores and aluminium foam of the same mass, as well as other cores of similar material and structural forms found in the literature.

Chapter 4 presents the experimental study of the previously proposed CTH core as the sacrificial core for protective cladding against impact loads. The impact tests are conducted using a pendulum impact testing facility. The impact mitigation performances of CTH cladding are compared with those of conventional square

honeycomb and corrugated square honeycomb claddings of the same mass. Four types of cladding with different cores, including square honeycomb (SH), corrugated square honeycomb (CSH), and two types of corrugated tilted honeycomb (CTH), are tested under various impact scenarios with different impact masses and velocities. The impact mitigation performances are evaluated by comparing the impact force and the transmitted forces recorded at various locations, as well as the deformation mode among each cladding.

Chapter 5 presents a numerical study of a novel sandwich structure with adaptive energy-absorbing capability for various impact scenarios, inspired by the protective mechanism of the beetle. The internal structure of the beetle forewing with the existence of viscoelastic material is mimicked to develop the proposed sandwich structure inspired by the beetle forewing (SSBF). Shear thickening fluid (STF) is used to mimic the viscoelastic material inside the beetle forewing. A dynamic compressive test of the STF specimen is used for model calibration. The proposed SSBF is crushed under various crushing speeds to investigate its dynamic crushing response and adaptive energy-absorbing capability. Its dynamic crushing performance is also compared with that of conventional energy-absorbing structures, i.e., non-filled or PU foam-filled structures.

Chapter 6 presents an adaptive crushing resistance structure with a further enhanced crushing efficiency. The viscoelastic material found inside the protective mechanism in nature, i.e., inside the tubules of the horn sheath of bighorn sheep, is mimicked by incorporating the STF into the cells of origami metastructure (OM). The crushing performance and crushing efficiency of the proposed bio-inspired STF-filled origami metastructure (STF-OM) are investigated and compared with the non-filled and viscous fluid-filled counterparts under various crushing speeds. Furthermore, the effects of the filled height of STF, the viscosity of STF, and the origami folding angle on the crushing performance of STF-OM are also examined.

Chapter 7 introduces a novel recoverable bio-inspired energy-absorbing device (BIEAD) inspired by the suture interface found inside the beaks of woodpeckers. The viscoelastic material and tooth of the suture are mimicked using STF and a rectangular tube, respectively. The thickening behaviour of the STF serves as the primary energy absorption mechanism for the proposed device, while the spring is used to restore the

device to its original shape. The recoverability of the proposed BIEAD (STF-filled specimen) is compared with that of the water-filled specimen. The effects of loading rates, the viscosity of STF, shear gap, and contact area on the crushing resistance and energy absorption capacity of the proposed BIEAD are also investigated.

Chapter 8 summarises the main findings of this thesis, draws conclusions, and provides recommendations for future work.

It should be noted that this thesis is a compilation of technical papers prepared by the candidate during his PhD study. Each technical paper serves as a chapter, spanning from Chapter 3 to Chapter 7. The published technical papers in each chapter have been formatted by the candidate in accordance with the requirements of Curtin University. Some definitions, material properties, and modelling techniques have been compiled for the convenience of readers and to maintain a logical flow throughout the chapters.

Chapter 2. Literature review

2.1 Overview of protective structures

Sandwich structures have been extensively investigated and used as energy-absorbing and protective structures against impulsive loads [4]. Various internal sacrificial cores are attached to the external plates to form these sandwich protective structures [10,11], as shown in Figure 2-1. Honeycomb [12,13], corrugation [14–17], auxetic [18], truss [19,20], and stochastic foams [21,22] are commonly explored and used as the sacrificial cores to absorb blast or impact energy through plastic deformation and crushing of their structures and materials [4,5].

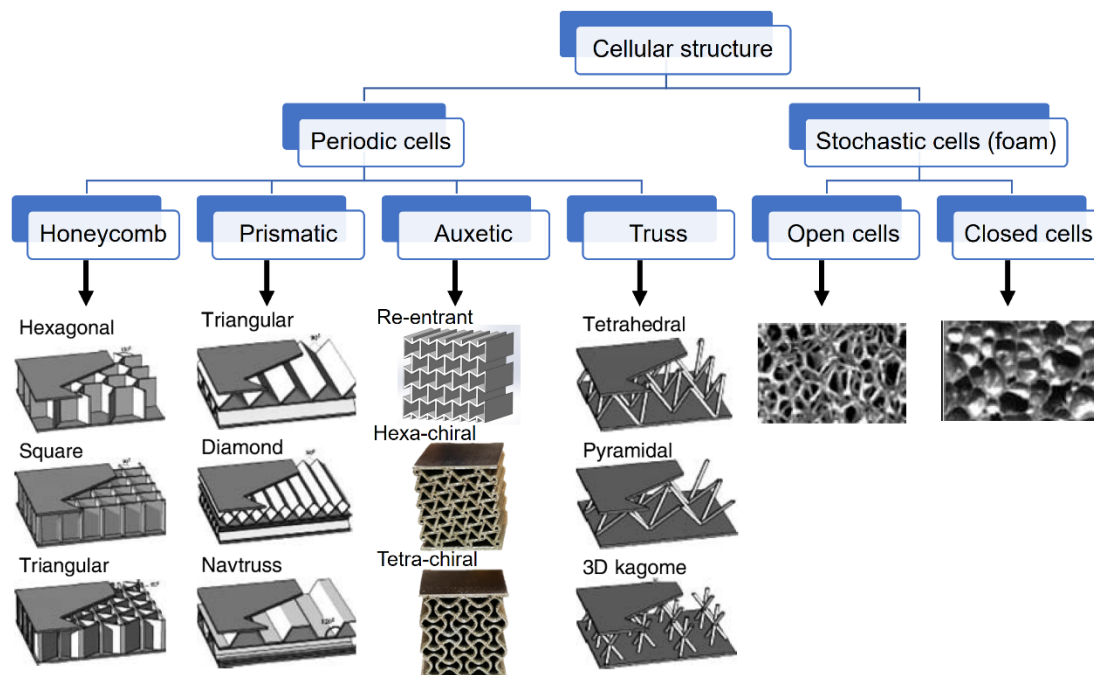


Figure 2-1. Illustration of some cellular structures used as the internal core of sandwich protective structures [23–27].

Sandwich structures have been investigated and used as energy absorbers and protective panels [9,28,29]. The energy absorbers are used as additional layers or sacrificial claddings, directly attached to the protected structures [5,30,31], while sandwich protective panels are used as stand-alone structures with supports such as blast-resistant walls or doors, as shown in Figure 2-2. Sandwich structures with various forms of internal cores have been developed as energy absorbers for various applications, including sacrificial cladding [30], vehicle frontal rails [32] and bumpers

[33], pier protection [34], helmets [35], supports for blast-resistant panels [36], and guardrail pillars [37]. The criteria for assessing cladding include energy absorption capacity, transmitted force, or pressure on the protected structure at the back.

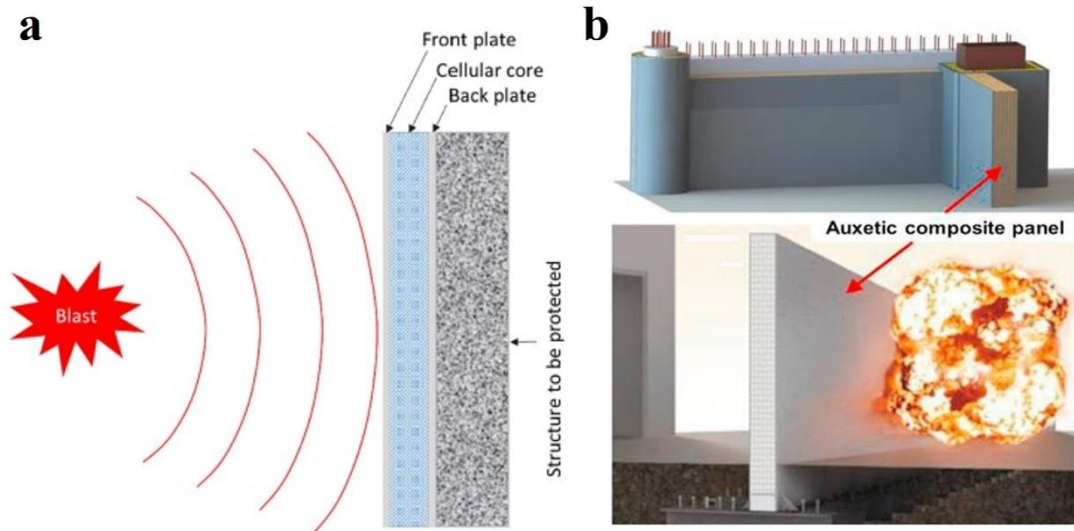


Figure 2-2. Protective structure used as (a) sacrificial cladding [38] and (b) protective panel [39].

2.2 Ideal characteristics of energy absorber for protective structures

The energy-absorbing and protective structures should be designed to suit their specific application and circumstances, while also being capable of dissipating impact or blast energy in a controlled manner [4]. Some general principles [4] are applicable to these protective structures in most applications, such as:

- Lightweight and high specific energy-absorption capacity
- Restricted and constant reactive force
- Long crushable distance/stroke
- Low cost and easy installation
- Irreversible energy conversion
- Stable and repeatable deformation mode

Ideally, the energy-absorbing structure should be lightweight, a critical factor in applications such as energy-absorbers for vehicles or aircraft, and personal protective devices. It should be capable of absorbing impact or blast energy over a large

deformation of a long deforming distance while maintaining a stable reaction force within allowable threshold values for protection. This ensures the absorption of all input energy without causing damage to the protected structure. Low cost and easy installation are also factors that need to be considered when designing an energy-absorbing structure due to budget constraints since it is a one-time-use item that cannot be recovered and needs replacement after resisting the load. Furthermore, an energy-absorbing structure should be able to efficiently absorb and dissipate impact or blast energy by converting the input energy into irreversible forms such as plastic dissipation, viscous dissipation, friction, or fracture. In other words, it should not convert the input energy into reversible forms such as elastic energy, which not only stores the energy elastically but also causes a reverse effect by converting the stored energy back into kinetic energy. This could result in subsequent damage to the protected structure and harm to individuals. Despite the uncertainty of external loading scenarios, energy-absorbing structures should be capable of absorbing external loads while maintaining a stable and repeatable deformation mode.

2.3 Crushing performance investigation of structures

The energy absorption and protective performance of the energy-absorbing material or structure can be assessed by conducting flatwise crushing tests [38]. The energy-absorbing structure is placed on a fixed supporting plate and crushed by another loading plate, as shown in Figure 2-3(a). Its energy absorption characteristics can be evaluated from the crushing force-displacement response or the crushing stress-strain response extracted from the test. The crushing stress can be obtained by dividing the crushing force by the contact surface area of the tested specimen, while the strain is calculated by dividing the crushing displacement by the overall height of the tested specimen, as shown in Figure 2-3(a). Figure 2-3(b) illustrates a typical crushing response of the energy-absorbing structure with three deformation stages: the elastic stage, followed by a long plateau stage, and the densification stage where the crushing force/stress rises significantly [40]. The peak crushing force (*PCF*) is reached during the initial elastic stage, followed by a significant drop in crushing force at the plateau stage due to the buckling and bending of the structure. Subsequently, the crushing force significantly rises due to the compaction of the structure, reaching its densification stage. The energy absorption capacity (*EA*) of the structure can be determined by

calculating the enclosed area under the force-displacement curve over the crushing distance/stroke (s), while the enclosed area under the stress-strain curve represents the energy absorption capacity per unit volume of the structure. For fair comparison, a specific energy absorption capacity (SEA), which is the energy absorption capacity per unit mass (m), is used to compare the energy-absorbing performance among different energy-absorbing materials or structures. The crushing force efficiency (CFE) is another important factor for assessing the crushing performance of the structure. It is the ratio of the mean/average crushing force (MCF) to the peak crushing force (PCF). Therefore, to achieve ideal energy-absorbing characteristics, energy-absorbing structures should possess several key factors, including a low peak crushing force, a stable and high average crushing force during plastic deformation to absorb energy, a long crushing stroke, a large energy absorption capacity, and a low loading-rate sensitivity of its peak during crushing [4,41].

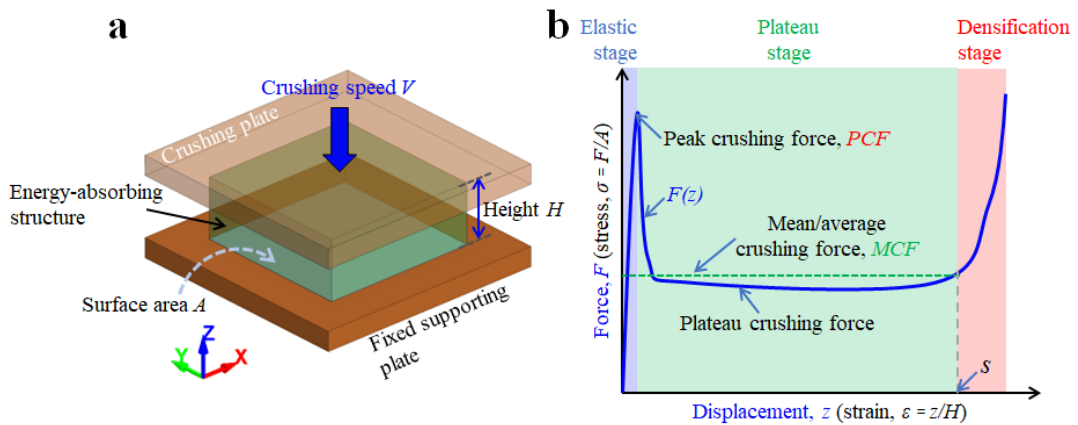


Figure 2-3. (a) Crushing setup and (b) typical crushing response of the energy-absorbing structure under compression.

2.3.1 Experimental investigations

The crushing performance of energy-absorbing structures can be investigated through quasi-static compression tests using a standard universal testing machine (UTM), allowing for easy observation of the deformation mechanism of the tested structure [4,42]. The crushing speed of the UTM can be set at a constant rate between 1 to 5 mm/min (0.02 to 0.08 mm/s), corresponding to strain rates ranging from 10^{-4} /s to 10^{-3} /s [4,42,43]. An example of the quasi-static crushing test of the auxetic structure by using the Instron 5569A UTM [44] is illustrated in Figure 2-4(a). In addition to the quasi-static responses, it is essential to understand the crushing performance of energy-

absorbing structures under dynamic loads. This can differ from their performance under quasi-static loads because the loading rate affects material properties, inertial resistance, and the inertial stabilization of the structures [12,45]. The dynamic crushing performance of the energy-absorbing structures can be investigated using various testing techniques, including high-speed testing machines [46–48], drop weight [36,49,50], pendulum [4], gas gun [51–53], and split Hopkinson pressure bar (SHPB) [54–57]. Li et al. [47] conducted dynamic crushing tests on foam-filled multi-layer folded structures using a high-speed testing machine INSTRON VHS 160/100-20, as shown in Figure 2-4(b). By utilising the controlled servo-hydraulics, a constant crushing speed can be maintained throughout the crushing process, ranging from 0.1 to 25 m/s [46]. However, in the later stages of high-speed crushing, it is necessary to gradually decrease the actual crushing speed to accommodate deceleration and avoid reaching the end position of the crushing head [46–48].

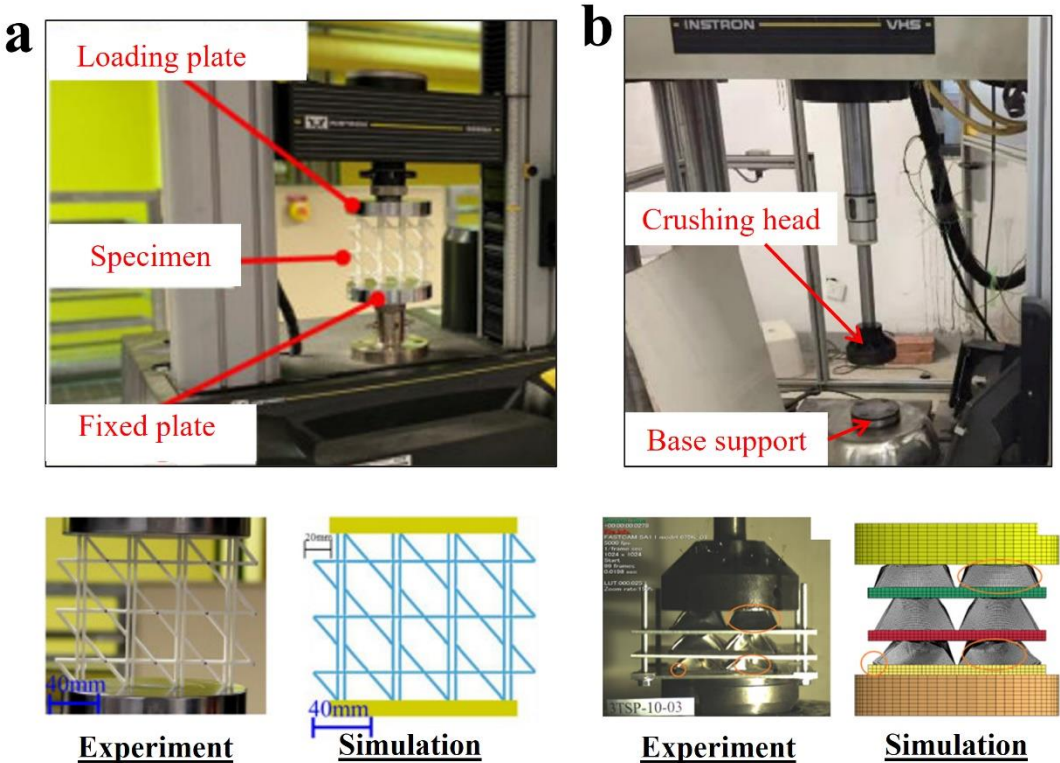


Figure 2-4. (a) Quasi-static crushing test of auxetic structure using UTM [44] and (b) dynamic crushing test of foam-filled multi-layer folded structures using high-speed testing machine [47].

The dynamic crushing response of energy-absorbing structures can also be investigated using drop-weight tests [36,49,50]. Wang et al. [36] examined the

response of an energy-absorbing connector under impact loading using the drop weight test, as shown in Figure 2-5(a). The energy-absorbing connector was placed between thick steel plate, which was impacted by a drop hammer, thereby allowing a dynamic flatwise crushing on the energy-absorbing structure [36]. Gas guns are used to propel the projectiles into the tested specimen, which is fixed on a rigid support. Harris and McShane [51] studied the dynamic compressive response of stacked origami metastructures using a gas gun, as illustrated in Figure 2-5(b). A steel projectile was propelled onto the tested specimen, which was attached to a stationary Hopkinson bar, allowing for the recording of impact force [51]. In this test, the size of the test specimen was constrained by the dimensions of the Hopkinson bar and the projectile [51]. Wu et al. [54] investigated the dynamic compressive behaviour of STF-filled lattice-core structures using a modified SHPB apparatus, as illustrated in Figure 2-5(c). A trumpet-shaped loading end was attached to the incident bar, enabling the total crushing of relatively large specimens [54].

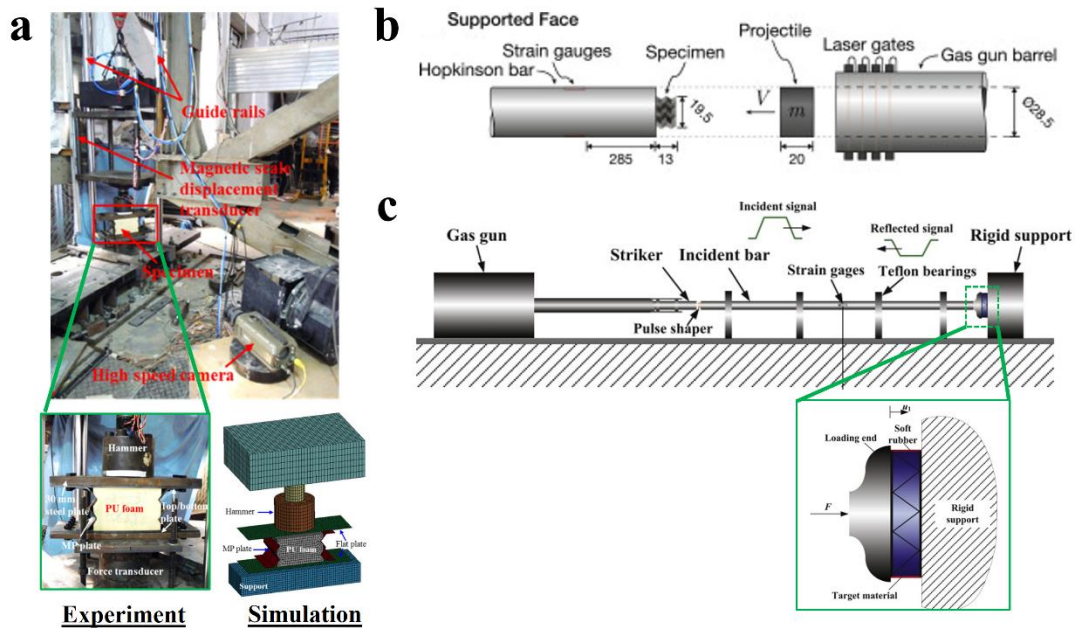


Figure 2-5. (a) Drop weight impact test of PU foam-filled multiple pleated plates [36], (b) dynamic compression test of stacked origami metastructure using gas gun [51], and (c) dynamic compression test of STF-filled lattice structure using SHPB apparatus [54].

Sandwich protective structures are used as additional layers or sacrificial cladding, directly attached to existing structures [5,30,31], thereby absorbing energy and reducing the load transmitted to the protected structure at the back [58,59]. To experimentally assess the blast or impact mitigation performance of large-scale

sandwich claddings, researchers have employed indirect methods for evaluation, such as assessing the damage and deflection of the protected structure [60,61]. Most of the experimental studies that directly recorded the transmitted force were conducted on small-scale claddings, which could be placed directly in front of the load cell [21,62,63]. Only a few experimental studies have investigated large-scale claddings and measured the transmitted forces using load cells at various locations, representing the loads transmitted to the protected structure [64].

2.3.2 Numerical investigations

Commercial finite element software packages, such as LS-DYNA and ABAQUS, have been widely used to replicate the responses of tested structures against quasi-static or dynamic loads. This enables further investigation and observation of factors such as stress-strain distribution and deformation process, which can be challenging to measure and monitor during testing. Furthermore, experimental tests, especially under impulsive loads like impact or blasts, could be dangerous, expensive, and time-consuming. Conducting numerical simulations not only eliminates these shortcomings but also allows for detailed investigation and parametric studies. This, in turn, enables the investigation and optimisation of the performance of the structure before conducting physical tests. However, it is crucial to calibrate and verify the numerical model using existing and similar structures available in the literature to ensure accuracy.

Quasi-static or dynamic crushing tests with a defined crushing speed can be simulated using `*BOUNDARY_PRESCRIBED_MOTION` keyword in LS-DYNA with an appropriate motion curve [65,66]. As shown in Figure 2-4(a), the defined motion of the moving part, i.e., the loading plate or crushing head, can be set using this keyword. For the crushing techniques involving impactors falling or moving from an initial velocity, i.e., drop hammers and projectiles shown in Figure 2-5, `*INITIAL_VELOCITY_GENERATION` keyword can be used to simulate the motion of that impactor with its exact mass. Qi et al. [61] conducted a drop weight impact test on the auxetic sandwich structure, as illustrated in Figure 2-6. The impact test can be simply simulated by omitting the falling process and imposing the initial velocity right before the impact on the drop weight using this keyword.

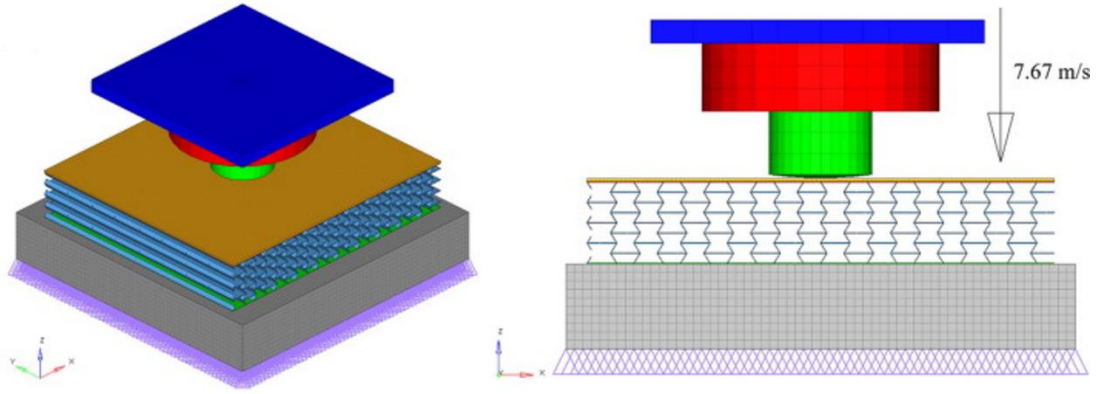


Figure 2-6. FE model of drop weight impact test of auxetic sandwich structure [61].

2.4 Conventional energy-absorbing structures

Cellular structures of various structural forms have been extensively investigated and utilised as an energy-absorbing medium in sacrificial cladding to plastically dissipate blast or impact energy [4,25,67]. Honeycomb structures have been widely studied and commercially used in various industries and applications, such as aircraft [68,69], automobiles [33], and other energy-absorbing structures [70]. This is due to their high crushing resistance, high energy absorption capacity [68,71], and ease of fabrication. Honeycomb structures exhibit high crushing resistance and energy absorption capacity when crushed in the out-of-plane direction, as compared to when crushed in their in-plane directions. However, during the initial crushing stage, their peak crushing resistance is significantly high due to the high buckling resistance of their vertical core sidewalls in the out-of-plane direction [72]. Xu et al. [73] investigated the quasi-static crushing of hexagonal and octagonal honeycomb structures in the out-of-plane direction, as shown in Figure 2-7. It was observed that the initial peak crushing resistance is significantly high, nearly four times the average crushing resistance. While this high initial peak crushing resistance contributes only a small portion to energy absorption, it can result in unnecessarily high transferred forces to the protected structures at the back, exhibiting non-ideal characteristics of honeycomb structures for energy absorption applications. Furthermore, the peak crushing force of honeycomb structures increases significantly as the crushing speed increases [13,74], leading to higher transmitted forces and severe damage to protected structures under dynamic loads [48,58].

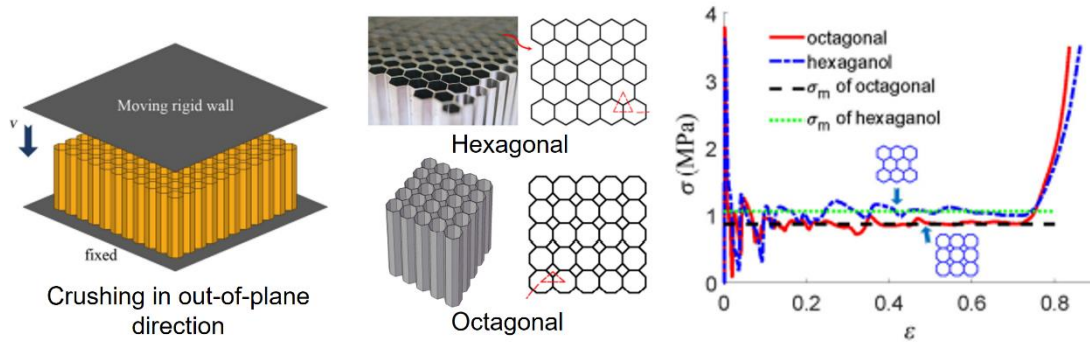


Figure 2-7. Quasi-static crushing of honeycomb structures in the out-of-plane direction [73].

Various structural forms of cellular structures have also been investigated, including corrugated structures [14–17] and lattice structures [19,20], and stochastic foams [21,22]. Rejab and Cantwell [14] examined the crushing behaviour of a corrugated sandwich structure under quasi-static loading conditions. It was found that corrugated structures exhibit non-uniform crushing resistance, with a high initial peak followed by a significant drop after the buckling of the core [14], as shown in Figure 2-8(a). In the case of multi-layer corrugations, multiple peaks fluctuate throughout the crushing process due to the individual buckling of each corrugated layer [15,16], as shown in Figure 2-8(b).

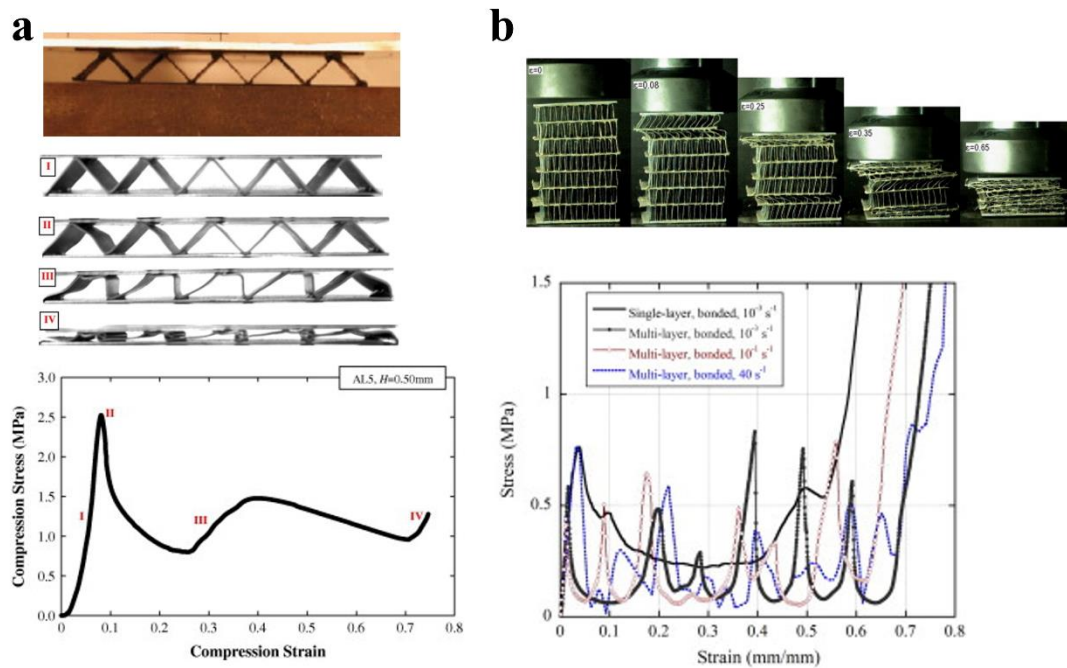


Figure 2-8. Deformation process and compressive stress-strain curve of (a) single-layered corrugated [14] and (b) multi-layered corrugated sandwich structures [17].

Regarding crushing resistance, honeycomb structures still outperform lattice and corrugated structures with the same relative or volumetric density [75–77]. In the case of stochastic foams, both metallic and polymeric foams tend to exhibit uniform crushing deformation and long plateau crushing resistance. However, the bending-dominated structure of foams leads to lower crushing resistance compared to stretching-dominated cellular structures with similar relative density [24,78].

2.5 Folded structures

Recently, foldable origami-patterned structures [79,80] have been extensively studied since origami-type structures can be manufactured by stamping or pressing a single thin sheet of material [79,81]. Low buckling resistance can be achieved by adjusting the folding pattern. Gattas and You [80] investigated the out-of-plane crushing of the standard Miura-ori foldcore and conventional honeycomb core, as shown in Figure 2-9. It was found that the crushing and energy absorption performances of the Miura-ori foldcore are inferior to those of a conventional honeycomb core with similar material and density [80,82]. In addition, a significant reduction in crushing resistance occurs after plate buckling [81,83], demonstrating undesirable behaviours for energy-absorbing applications [4,84].

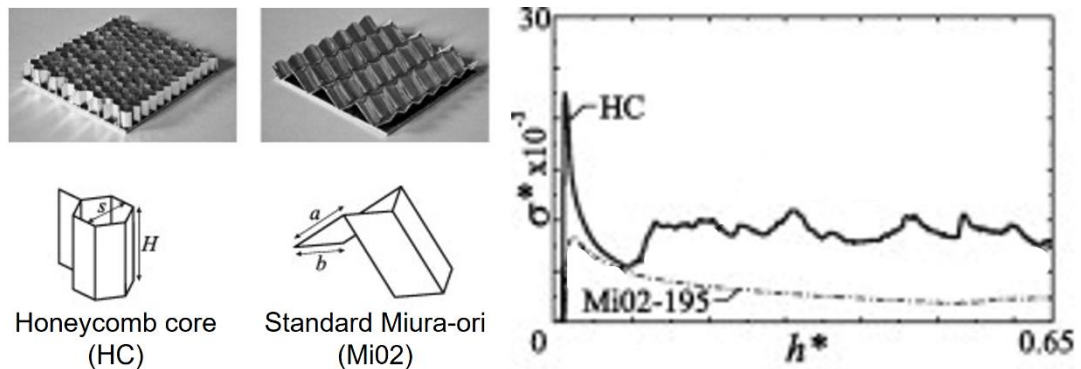


Figure 2-9. Dimensionless stress-strain responses of honeycomb core and standard Miura-ori foldcore [80].

Foldable kirigami-patterned structures [9,11,43,45,84] have also caught the attention of researchers, as complex and flexible structural forms can be fabricated by folding a thin sheet of material that is pre-cut, stamped, or punched before folding. This approach allows for the creation of more complex geometric forms and flexible designs [84–86]. Li et al. [84] investigated the flatwise crushing of truncated pyramid

kirigami foldcores with various pyramid shapes, including truncated triangular pyramid (TTP), truncated square pyramid (TSP), and truncated pentagonal pyramid (TPP), as shown in Figure 2-10. It was observed that truncated pyramid kirigami structures demonstrated superior energy absorption performance with low peak crushing force, high crushing resistance, and high energy absorption compared to cube strip or Miura-ori structures with the same relative density [45,84]. This exceptional performance is attributed to the inward bending of the top edges of the individual tapered shapes and the constraints of the triangular corrugations at the corners of the unit cell of the truncated pyramid foldcores [45]. Furthermore, the square dome kirigami foldcore exhibits similar quasi-static crushing resistance compared to aluminium foam with nearly twice its weight [5]. When used as a sacrificial cladding core under impact, the peak transmitted force at the impact location was reduced for cladding with a square dome kirigami foldcore, whereas aluminium cladding transmitted a significantly higher force due to severe localised damage. However, the square dome kirigami foldcore cladding appears to densify easily and has lower crushing resistance than aluminium cladding due to its weak constraints on the boundaries of individually folded unit cells.

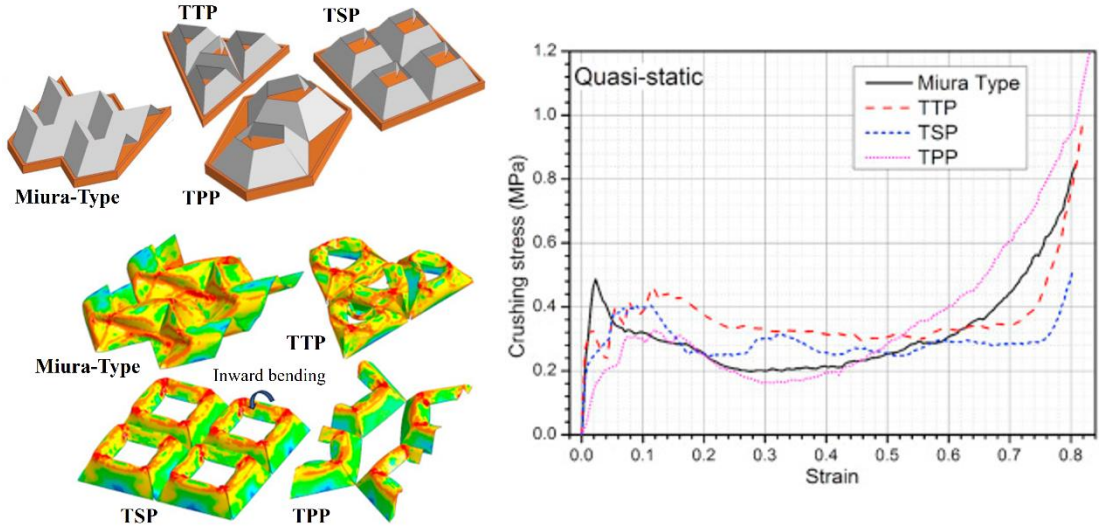


Figure 2-10. Deformation modes and quasi-static crushing responses of TTP, TSP, TTP, and Miura-type foldcores [84].

Besides the high initial peak crushing resistance, honeycomb structures seem to have high crushing resistance and specific energy absorption capacity compared to most structural cores due to their fully connected vertical sidewalls and interconnected unit

cells [87,88]. Therefore, a modification to the honeycomb structure can be proposed to eliminate its crushing peak force without compromising its overall crushing resistance. Recently, a kirigami modification technique was implemented on the sheet-reinforced honeycomb by folding both corrugations of each unit cell at the two ends [48,89], as illustrated in Figure 2-11(a). The quasi-static crushing responses of the honeycomb (HC), reinforced honeycomb (RHC), and kirigami-modified reinforced honeycomb (KHC) in the out-of-plane direction are compared in Figure 2-11(b). It was observed that the high peak crushing forces of HC and RHC are eliminated by this implementation, resulting in a high crushing force efficiency (*CFE*) of KHC [89]. However, under high crushing speeds, its *CFE* tends to decrease as the peak crushing force increases, as shown in Figure 2-11(c) and (d), due to the inertial resistance of the vertical interlayers [48]. Therefore, further enhancements of honeycomb structures are required to improve their crushing performances in both energy absorption and crushing efficiency under various dynamic crushing speeds.

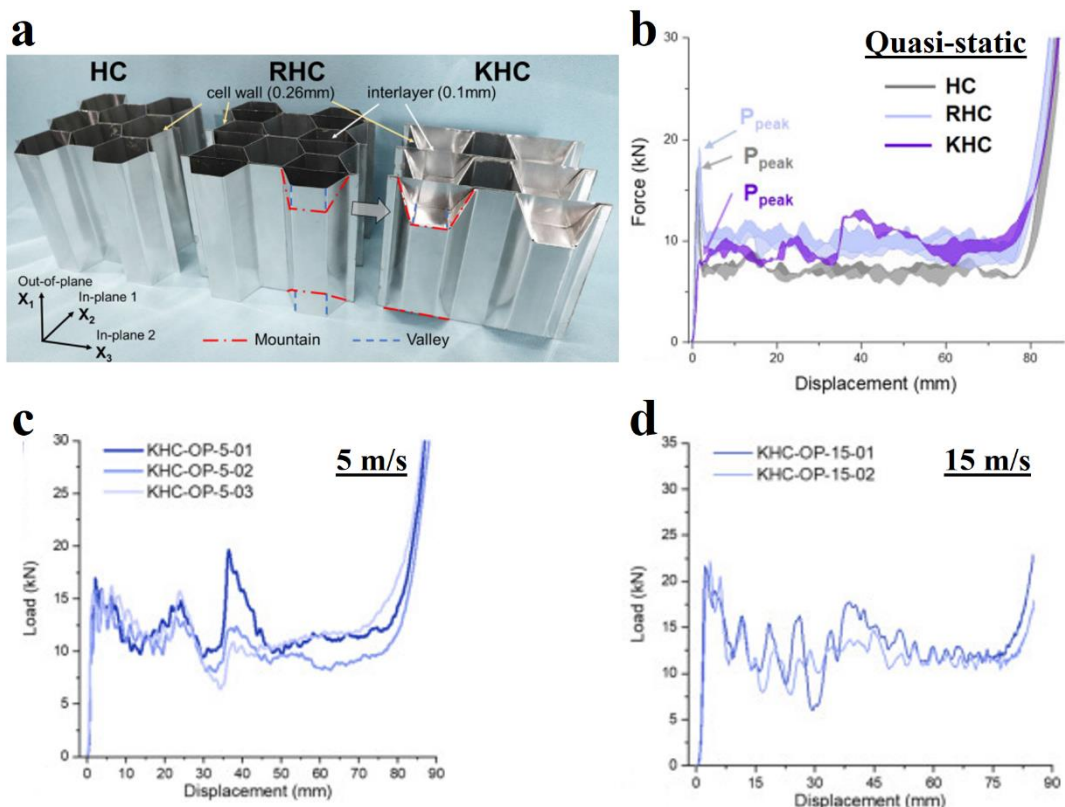


Figure 2-11. (a) HC, RHC, and KHC specimens [89], (b) quasi-static crushing responses of HC, RHC, and KHC [48,89], (c) dynamic crushing responses of KHC under 5 m/s, and (d) 15 m/s [48].

2.6 Metastructures

Recently, mechanical metastructures have been proposed by arranging their cellular structures, leading to unprecedented mechanical properties that cannot be achieved with conventional materials [90–95]. One such mechanical metastructure is the auxetic structure, which contracts perpendicularly to the compressing direction [96–98], thereby increasing the crushing resistance at the impacted area [38]. This enhancement of crushing resistance through structural contraction offers great potential for impact-resistant and energy-absorption applications [61,99,100]. 2D auxetic structures, such as double-arrowhead and re-entrant honeycombs, have been extensively investigated as protective structures against blast and impact loads [61,101,102]. Currently, 3D origami metastructures have been proposed by incorporating origami patterns into these 2D auxetic metastructures to enhance their deformation and crushing performance, as well as their auxetic behaviour [99,103,104]. The Miura-ori patterns have been integrated into each layer of the 2D metastructure along its out-of-plane direction, forming a double corrugated pattern with a zigzag shape along the in-plane direction, as shown in Figure 2-12. Li et al. [104] investigated the dynamic crushing behaviours of origami-modified re-entrant metastructures (Figure 2-12(a)) in all three directions. It was found that the origami-modified re-entrant metastructure exhibits a negative Poisson's ratio in all three directions [104]. The 3D origami metastructures have significantly improved crushing responses under quasi-static crushing in the out-of-plane Z direction by having a predictable deformation [105], tuneable crushing resistance [103], and high tri-directional auxeticity [99,106]. 3D origami-modified double-arrowhead metastructures have also been investigated [51,99,103,106,107], as shown in Figure 2-12(b). By adjusting the folding angle of the pattern, the structure transforms from a stiff honeycomb-like structure with a high peak and strong softening crushing resistance to a collapsible structure with nearly constant crushing resistance [103,107], thereby eliminating the peak crushing force. However, the crushing resistance decreases with an increase in the folding angle, and the peak crushing resistance becomes significant under dynamic crushing in the out-of-plane Z direction [51,99], resulting in reduced crushing efficiency. Therefore, further improvements in its crushing performance in the out-of-plane direction are required to enhance the overall crushing performance and efficiency of the origami metastructure under dynamic loads.

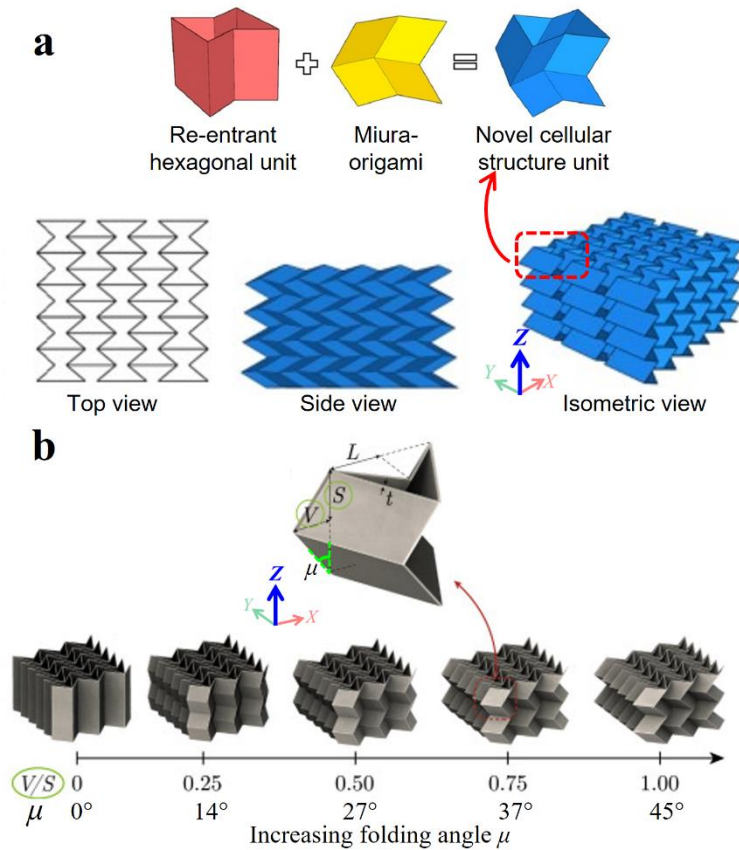


Figure 2-12. 3D origami modified 2D auxetic (a) re-entrant [104] and (b) double arrowhead [51] metastructures.

2.7 Existing nature-inspired structures

Over the past decades, structural features and mechanisms in nature have been imitated to develop new designs and improve conventional energy-absorbing structures [42,108–116]. The improvement in the crushing performance of honeycomb structures has been investigated by implementing various bio-inspired features found in plants and animals [42,115], such as hierarchical structures found in pomelo peel [117], spider-web hierarchical structures [118], horseshoe mesostructures [119], grass stems [120], and the microstructure of vascular bundles in bamboo [121], as shown in Figure 2-13. Bio-inspired hierarchical honeycomb structures have shown improved performance compared to conventional honeycomb structures in terms of crushing resistance and energy-absorbing capability. The hierarchical structures provide more corners and edges for plastic deformation, leading to improved energy absorption performance [117]. Bio-inspired hierarchical honeycombs have higher specific energy absorption capacities than most cellular materials [108]. However, the addition of vertical hierarchical sidewalls also increases the initial buckling resistance [122],

resulting in lower crushing force efficiency, which is not ideal for energy-absorbing and structural protective applications. Furthermore, a high initial peak force is still observed, especially when the structure is subjected to high-rate dynamic loads. In addition to the crushing responses, manufacturing the hierarchical complexity of bio-inspired structures could be challenging and costly, especially on a large scale [42,123]. Therefore, a simple modification and efficient biomimetic approach should be implemented to enhance the performance of conventional structures without complicating the fabrication process.

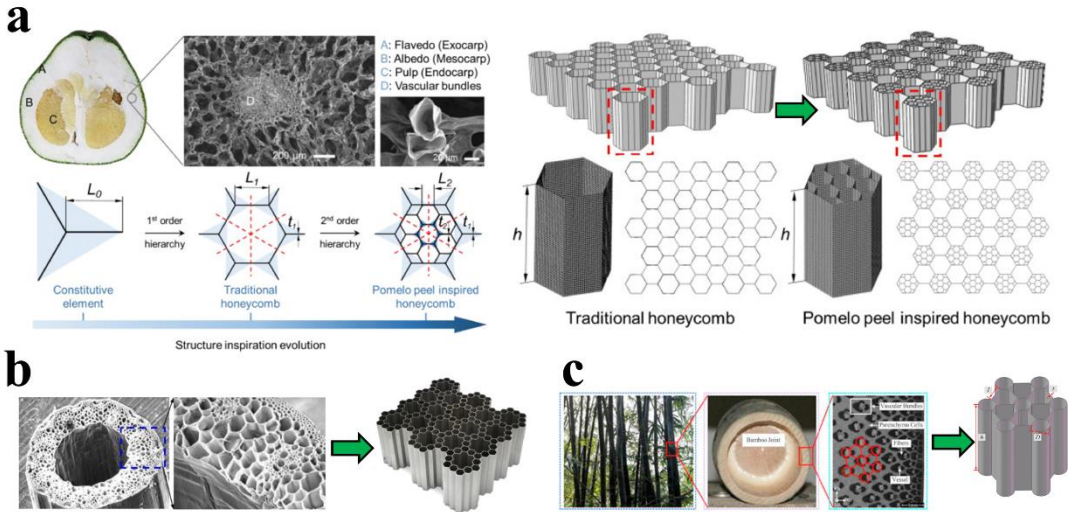


Figure 2-13. Hierarchical honeycomb structures inspired by (a) pomelo peel [117], (b) grass stem [120], and (c) bamboo [121].

The sandwich structures inspired by beetle forewings have been extensively studied and tested under quasi-static compressive loading [124–126]. Hollow trabeculae, found inside beetle forewings, have been mimicked to create bio-inspired structures by adding hollow tubes at the intersections or in the middle of honeycomb walls within the structure’s cores [127,128], as depicted in Figure 2-14(a). The results have shown that trabecular honeycomb core sandwich structures exhibited higher compressive strength and energy absorption compared to conventional honeycomb structures with the same core volume. This is because the hollow tubes reinforce the intersections of the honeycomb walls, requiring a higher load to deform under compression. Meng et al. [126] proposed a sandwich structure inspired by the microstructure of beetle forewing, as illustrated in Figure 2-14(c). Conventional corrugated cores were modified by incorporating the herringbone pattern of a dactyl club [129] to enhance their energy-absorbing characteristics. A double sinusoidal corrugated core, inspired

by the pattern of dactyl club of mantis shrimp, was proposed (Figure 2-14(b)) and tested under quasi-static loading [129]. Due to the bi-directional curvature of the double-sine corrugated skin core, plastic hinges were generated at the vertices, allowing more material in the bio-inspired corrugated core sandwich structures to crush and dissipate more energy than the regular triangle and single sinusoidal sandwich structures [129]. However, most of these bio-inspired structures were investigated under quasi-static loads, a high initial peak force occurs under dynamic loads, and their energy-dissipating mechanisms are mainly through plastic deformation and fracture, which are irrecoverable. A novel honeycomb sandwich structure, inspired by the wavy cell walls of a woodpecker's beak microstructure, was investigated and tested under dynamic crushing conditions [130], as shown in Figure 2-14(d). The introduction of waviness to the cell walls of the honeycomb led to a large number of plastic hinges, resulting in significant deformation and increased energy absorption capacities compared to conventional honeycomb structures. However, a high initial peak force was also observed in this type of bio-inspired honeycomb structure.

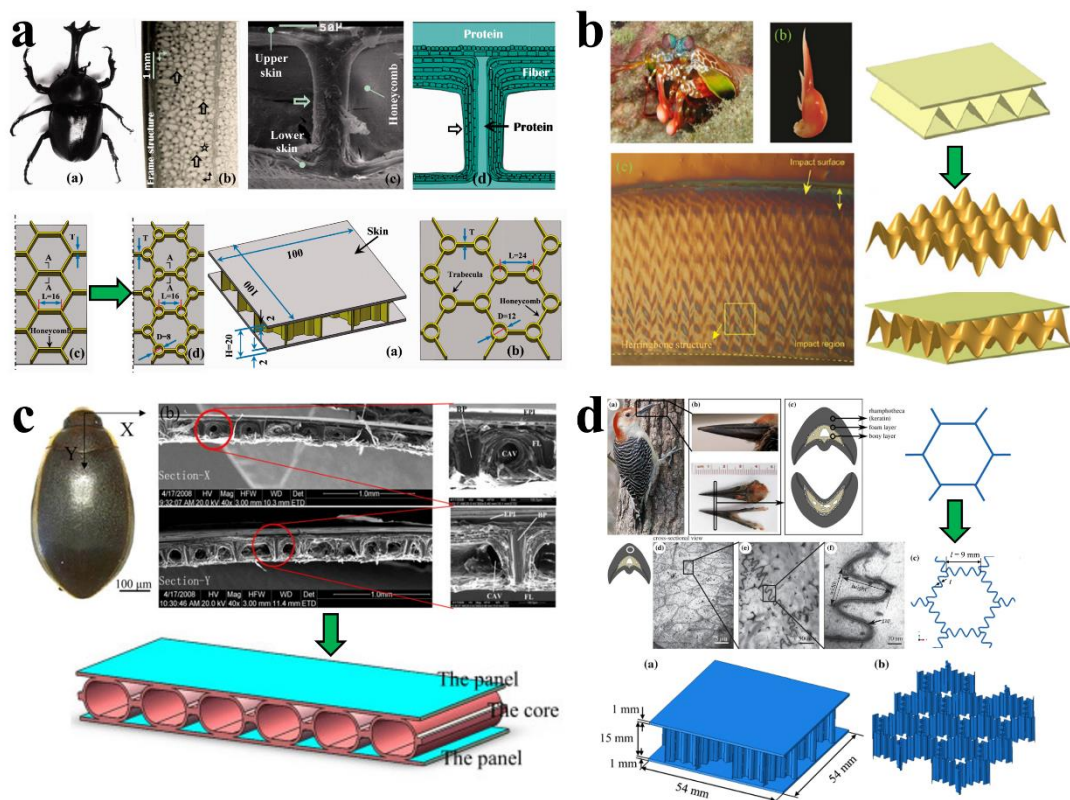


Figure 2-14. Sandwich structures inspired by (a) tubular structure of beetle forewing [124], (b) herringbone pattern of dactyl club [129], (c) microstructure of beetle forewing [126], and (d) wavy pattern of the suture [130].

Even though conventional sandwich structures have been improved by incorporating patterns and mechanisms found in nature, certain drawbacks, such as a complicated manufacturing process and high initial peak forces, still persist and require further improvement. While the protective mechanisms of animals, such as the forewings of beetles, horn sheaths of headbutting animals, and the beaks of woodpeckers, can adapt to various unpredictable loading conditions and resist impact loads without noticeable damage, the structures inspired by these protective mechanisms are constrained by fixed energy absorption capacities specific to their particular designs, which may be either too soft or too stiff for different impact energies or impact speeds. Furthermore, most existing nature-inspired structures absorb and dissipate energy through plastic deformation and fracture, which are irrecoverable. Therefore, it is fascinating to develop novel nature-inspired structures with new mechanisms and enhanced performance, such as adaptive and recoverable capabilities, by incorporating these protective mechanisms found in nature.

2.8 Interesting feature and protective mechanism in nature

Plants and animals have optimised their structures to be lightweight, high-strength, and protective to withstand extreme conditions or protect themselves from predators. Some interesting features and protective mechanisms in nature, such as plant stems, protective structures of animals, and suture structures, can be mimicked to develop innovative energy-absorbing structures with unique mechanisms and enhanced performance.

2.8.1 Structural feature of the cross-section of mint plant stem

The shape of the plant stem provides additional resistance to the structure of the plant against flexural and torsional loads caused by wind and additional weight, such as its leaves, flowers, and fruits [131]. Various transverse cross-sectional outer shapes of plant stems can be found, including triangle, star shape, square, hexagon, circle, and flower shape [132]. These cross-sectional shapes form a tapered geometry whose cross-sectional area decreases from the apex (top) to the base of the plant stem. The mint plant has a hollow stem with a square shape in the transverse section. The outer part of the stem section comprises strengthening tissues, including vascular tissues and collenchyma at the corners and sides of the stem [131], forming a corrugated square

shape as illustrated in Figure 2-15(b). These unconventional stem shapes provide additional buckling resistance to the plant structure when compared to conventional shapes, such as circular or square [132]. Therefore, it is of interest to implement both corrugated and tapered shapes from plant stems to enhance the crushing resistance of square honeycomb core.

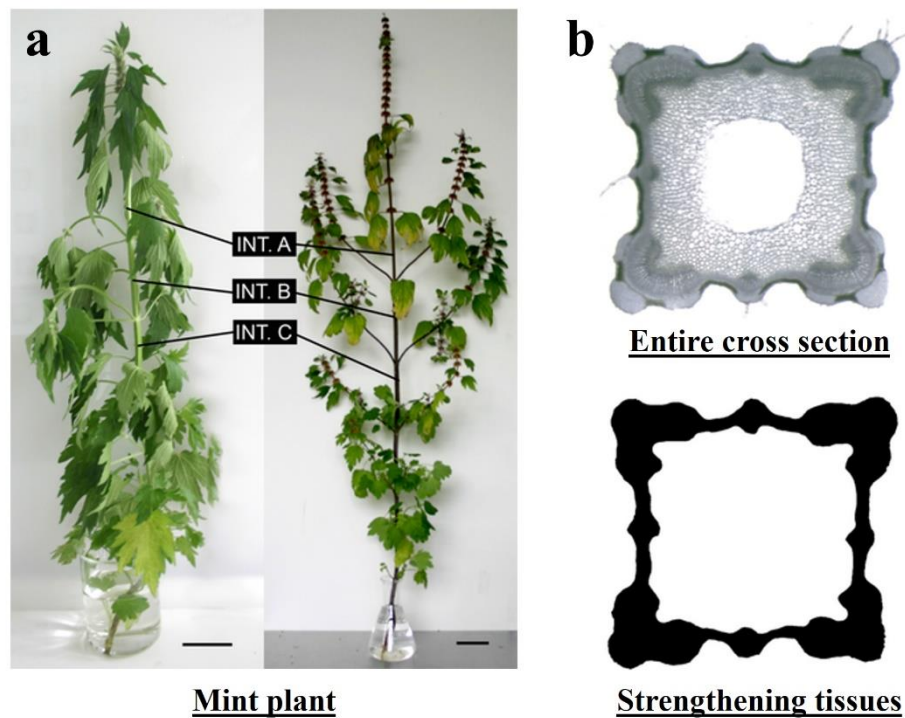


Figure 2-15. (a) Mint plant and (b) its cross-section [131].

2.8.2 Viscoelastic material inside the protective structures of animals

In nature, animals can protect themselves and minimise the transmitted force from various impact and loading conditions by using their unique protective mechanisms. One interesting protective mechanism is the forewings of the beetle, which play an important role as protective covers over the soft wings and body parts against predators [133]. It is observed that viscoelastic materials, such as grease and a protein matrix, exist inside the trabeculae of the beetle forewings [134–137]. Studies of biomaterials have shown that the protein matrix can dissipate input energy and enhance the toughness of the bio-composites through its intrinsic viscoelastic properties [138–140]. Another fascinating protective mechanism exists in the horns of bighorn sheep, which endure various impact conditions during violent clashes with other animals and

predators. Their horns and cranial bones exhibit excellent impact energy absorption and minimise the impact force transmitted to their brains [141,142]. It has been found that the hydrated horn material exhibits strong viscoelastic behaviour under compression, thereby absorbing significant amounts of energy during impacts [141]. The protective mechanisms of these animals share an interesting common feature, which is the presence of a liquid material with viscoelastic behaviour within the trabeculae of beetle forewings [136,138,143] and the tubules of horn sheaths [141], as depicted in Figure 2-16. Therefore, it is fascinating to mimic these protective mechanisms in nature and incorporate the viscoelastic materials to develop novel energy-absorbing protective structures with unique energy-absorbing mechanisms and high crushing efficiency.

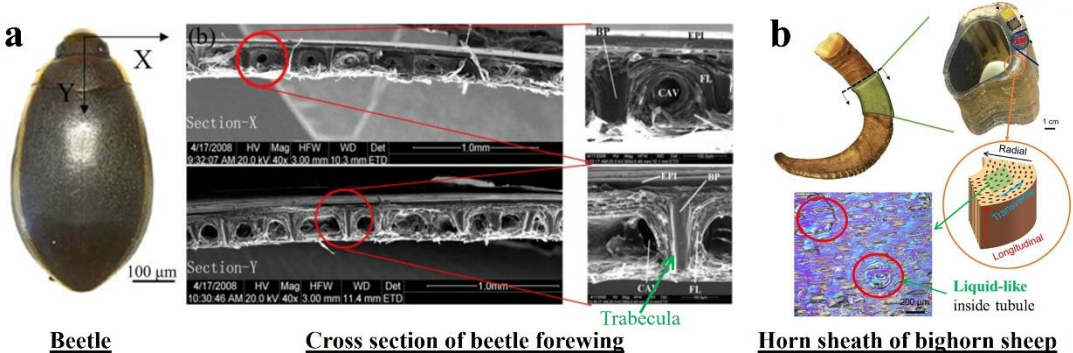


Figure 2-16. (a) Forewing of beetle [126] and (b) horn sheath of bighorn sheep [141].

2.8.3 Viscoelastic material inside the wavy suture interfaces

One interesting bio-inspired mechanism from nature is the suture structure found in the cranial bones of headbutting animals and the beaks of woodpeckers [142,144,145], as shown in Figure 2-17. During violent clashes of headbutting animals, high-impact forces and energy are transferred to the skull, yet no noticeable damage or injury to the animals' brains is observed [142,146]. Results from impact tests on the cranial bones of headbutting animals have shown that sutures and collagen materials between the suture interfaces act as shock absorbers for the skull during impacts [142,144]. Lee et al. [147] investigated the mitigation of stress waves at the interface of the suture. The results show that the viscoelastic collagen material at the suture interface dampens the stress waves and absorbs the impact energy [147]. Woodpecker beaks can also withstand high impacts without damage, despite multiple strikes onto tree trunks [148]. This is due to the highly wavy sutures and collagen between the suture interfaces of

the beak, which function as an energy absorption mechanism through shearing and friction [145]. Therefore, it is interesting to mimic the viscoelastic collagen material for a recoverable energy-absorbing device.

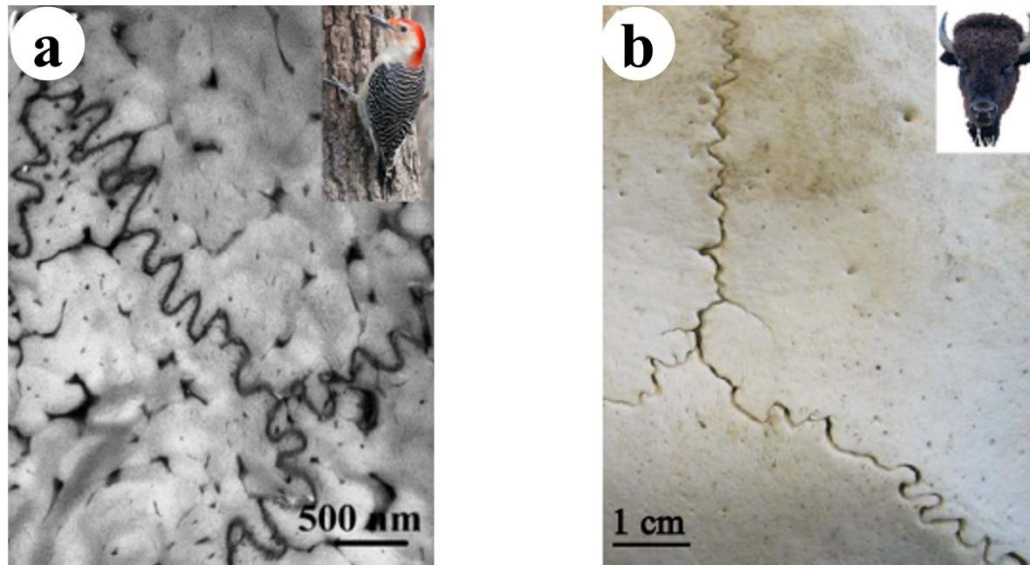


Figure 2-17. Suture structures inside (a) beaks of woodpeckers and (b) cranial bones of headbutting animals [147].

2.8.4 Shear thickening fluid (STF)-viscoelastic material

One interesting viscoelastic material is shear thickening fluid (STF), whose viscosity rapidly increases with the rising shear rates. The viscosity of STF increases due to shear thickening behaviour caused by shear loading [149] and compression thickening behaviour due to compression [150,151], resulting in a transformation from a liquid-to-solid state. STF is a combination of colloidal solid particles, such as silica or styrene/acrylate particles, and an inert carrier liquid, such as ethylene glycol (EG) or polyethylene glycol (PEG) [152,153]. During an impact, STF transforms from a liquid-like material to a solid-like material with high viscosity when resisting a shear up to or greater than its critical rate [54,154]. This transformation occurs due to the jamming of particles, which can provide a significant increase in energy absorption capacity through viscous dissipation and friction between internal particles [54,155,156], as shown in Figure 2-18(a). The viscous energy absorption of STF is associated with its shear thickening behaviour, which depends on factors such as the volume/weight fraction of colloidal particles, particle size, and different carrier liquids [156,157], as shown in Figure 2-18(a).

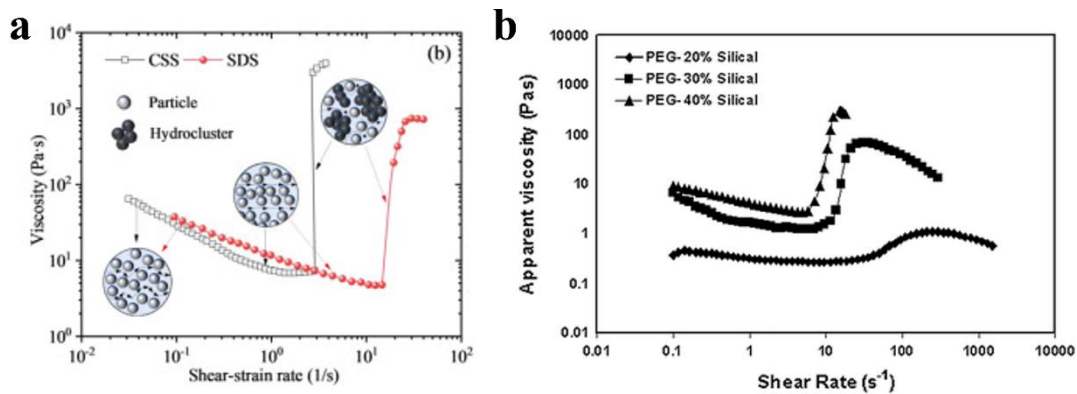


Figure 2-18. (a) Viscosity-shear rate of STF [158] and (b) Viscosity-shear rate of STF with different weight fractions of particles [157].

Intensive research interests in STF have been focused on STF-embedded fabrics for ballistic impact [159–162], stab, and puncture resistance [163–165]. Some studies have also focused on integrating STF with foam and preventing STF from leaking. Caglayan et al. [166] investigated the drop weight impact test of STF-integrated closed-cell PU foam sandwich composites. The STF and foam were integrated during the manufacturing process. This study revealed that STF-integrated foam cores have higher energy absorption compared to their neat counterparts. However, increasing the quantity of STF decreases the overall strength of the polymer foam [166]. Soutrenon and Michaud [167] investigated the impact properties of STF-filled soft foam and used silicone to encapsulate the specimens from the external environment. The impact test results showed that STF-filled soft foam composites reduced the transmitted shock waves and increased energy absorption by up to 85%, which could also recover after several impacts [167]. In another study, Liu et al. [168] investigated the mechanical properties of composite PU foam by mixing STF capsules into the PU foam during the foaming process. The results showed that the STF capsule-filled PU foam was able to reduce the maximum impact acceleration and the corresponding time due to the buffering effect of STF capsules and the support from the PU foam [168].

Recently, the impact and energy absorption behaviours of bulk STF have also been investigated by encapsulating inside silicone gel [169,170], sealing inside rubber [54], or sealing inside grids of PU foam [171,172]. It has been found that STF exhibits excellent impact resistance and energy absorption capacity, which also increases with the increase in impact energy [54,169–172]. STF can also be filled into the cavities or used as interfaces between multi-layer structures to develop structural protection and

shock-absorbing applications [153,173]. It has been implemented by filling inside the honeycomb and lattice structures to enhance dynamic compressive behaviour [54,174,175]. Wu et al. [54] investigated the dynamic compressive behaviour of STF-filled lattice truss cores. The STF was filled into the lattice core and sealed with soft rubber on all four open sides, as shown in Figure 2-19(a). The study revealed that the dynamic compressive strength and energy absorption of the sandwich panel with STF-filled lattice core increased significantly compared to those of the sandwich panel with non-filled or water-filled lattice truss cores. The compressive stress of the STF-filled lattice truss core was three times higher than that of the empty truss core, and it slightly increased with further compression, which was attributed to the shear thickening behaviour of STF [54].

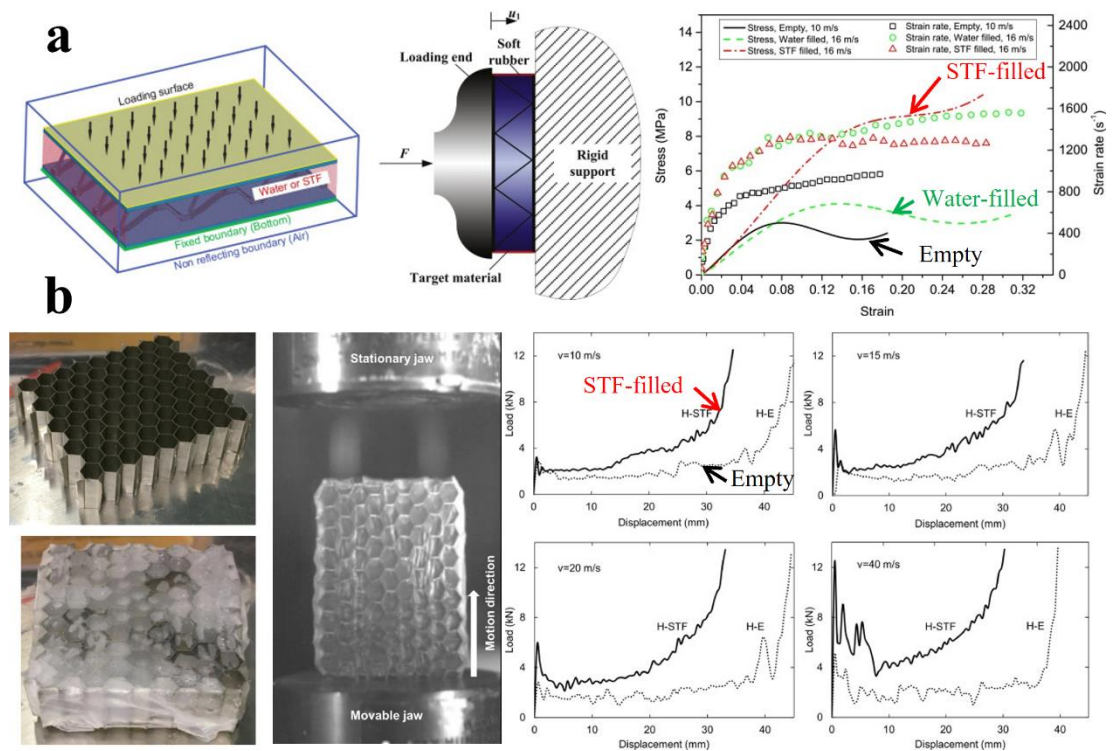


Figure 2-19. Crushing responses of (a) STF-filled lattice structure [54,175] and (b) STF-filled honeycomb structure [174].

Hu et al. [174] investigated the dynamic compressive behaviour of STF-filled honeycomb in the in-plane direction, as shown in Figure 2-19(b). It was observed that the dynamic energy-absorbing capability of the sandwich structures improved with STF implementation. However, a high initial peak force of the structure occurs and becomes more pronounced as the crushing speed increases due to the inertial effect and shear thickening effect of fully filled STF [174]. Therefore, an effective

implementation of STF into the structure is needed to improve the energy absorption of the sandwich structure by incorporating the shear thickening behaviour and averting the full compression of STF. In addition, fully filling the STF inside the cores or integrating the STF with the foams cannot fully utilise the recoverability and repeatability of STF under impact loads [169,170] due to the damage of the internal cores and foams. Therefore, a recoverable energy-absorbing device could be investigated by incorporating the recoverable energy-absorption behaviour of bulk STF with the multiple-impact protective mechanism of animals' suture interface.

2.9 Summary

In this chapter, information regarding the overview of protective structures, the ideal characteristics of energy absorbers for protective structures, conventional energy-absorbing structures, existing nature-inspired structures, and some interesting features and mechanisms in nature are briefly discussed. From the literature, the structural features and protective mechanisms found in nature could be efficiently mimicked to develop novel energy-absorbing structures with unique energy absorption mechanisms and high dynamic crushing efficiency to address the existing non-ideal characteristics of the conventional structures.

Besides the high initial peak crushing resistance, honeycomb structures exhibit good energy-absorbing characteristics in terms of high plateau crushing resistance and specific energy absorption capacity in the out-of-plane direction compared to most cellular structures. However, this significantly high initial peak crushing resistance contributes only a small portion to the energy absorption but can result in unnecessarily high transferred force and severe damage to the protected structures at the back under dynamic loads. Therefore, modifications should be explored to eliminate its crushing peak without compromising its overall crushing resistance.

For most existing energy-absorbing structures, a high peak crushing force occurs during the elastic deformation stage, followed by a significant drop and fluctuation of crushing force during the plastic deformation stage, resulting in undesirable energy-absorbing characteristics. Furthermore, the force-displacement profile of conventional structures, such as foams and honeycombs, scales up insignificantly even though the initial peak drastically increases with the rising crushing rate. In other words, the initial

peak force is highly sensitive to the loading rate, while the overall crushing resistance and energy absorption capacity are not, leading to insufficient energy absorption capacity but a high transmitted force to the protected structures as the impact load increases. Therefore, sandwich protective structures using conventional structures are constrained to a fixed energy absorption capacity, but they may become either too soft or too stiff under different impact energies or impact speeds. For these reasons, it is deemed necessary to design a smart energy-absorbing structure that can maintain a stable crushing resistance without introducing a high initial peak and can adapt its energy absorption capacity to various impact speeds.

Sandwich protective structures with conventional cores have been proved to be able to absorb impact and blast energies through the plastic deformation of their crushable cores. However, through this energy absorption mechanism, these conventional protective structures are unlikely to recover and provide protection in cases where multiple impacts or blast events occur. Therefore, a new design with alternative forms of energy absorption mechanisms and recoverability needs to be developed and investigated.

Chapter 3. Corrugated tilted honeycomb (CTH) core inspired by plant stem

The related work in this chapter was published in *Thin-Walled Structures*:

Lam L, Chen W, Hao H, Li Z. *Crushing behaviour of corrugated tilted honeycomb core inspired by plant stem. Thin-Walled Structures 2023;188:110852.*

<https://doi.org/10.1016/j.tws.2023.110852>

3.1 Introduction

In this chapter, a new corrugated tilted honeycomb (CTH) core for sandwich structure is proposed by implementing the corrugated and tapered shape inspired by plant stems, as illustrated in Figure 3-1. The corrugated tapered shape of the plant stem is incorporated into the sidewalls of each unit cell of the honeycomb core. The crushing responses and energy absorption capacity of the proposed bio-inspired honeycomb cores are numerically investigated using a finite element software LS-DYNA.

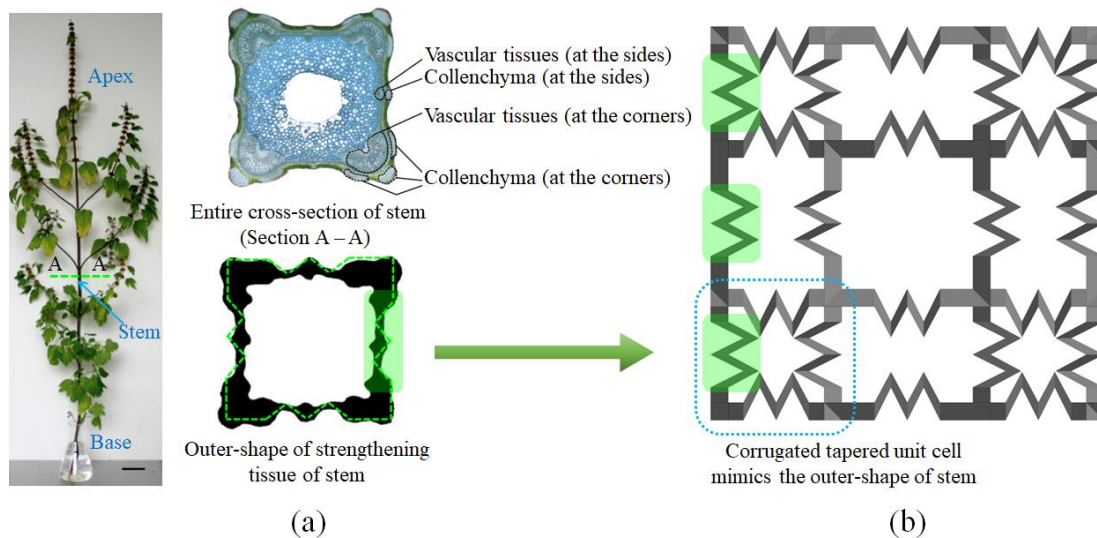


Figure 3-1. (a) Mint plant and its entire cross-section of stem as well as the outer shape of the strengthening tissues of the stem [131] and (b) the proposed bio-inspired corrugated tilted honeycomb (CTH) core with unit cells mimicked the outer shape of the mint stem.

The numerical model is calibrated with the flatwise crushing test of a conventional honeycomb conducted by Li et al. [89] by comparing the crushing response generated

from the numerical simulation with that obtained from the experimental test. Then the same material model and modelling techniques are used to model the proposed bio-inspired corrugated tilted honeycomb core. The crushing and energy absorption efficiencies of the proposed CTH cores are evaluated by comparing them with those of commercially available cores, such as square honeycomb core and aluminium foam of the same mass, as well as other cores of similar material and structural forms found in the literature. The crushing performances of each core are evaluated by using the key indicators of the energy-absorbing structures, such as the peak crushing force (*PCF*), mean crushing force (*MCF*), crushing force efficiency (*CFE*), and the specific energy absorption capacity (*SEA*). The effects of the crushing speed, tilted angle, and relative density on the crushing behaviour of the proposed CTH core are also investigated.

3.2 Numerical model calibration

The quasi-static flatwise crushing test of a conventional honeycomb in out-of-plane direction experimentally tested by Li et al. [89] is used for model calibration. It is made of aluminium 1060 sheets with 0.26 mm wall thickness, resulting in a relative density of 2%. The dimensional details of the conventional honeycomb can be found in the previous study [89]. The numerical model of the conventional honeycomb is developed using finite element software LS-DYNA. The crushing responses generated from the numerical simulation and the experimental test are compared to evaluate the accuracy of the numerical model. Then the same material model and modelling techniques are used to construct the proposed core in the following section.

3.2.1 Numerical model

A default Belytschko-Tsay type shell element with five integration points through the shell thickness and *MAT_PIECEWISE_LINEAR_PLASTICITY material model are used to mesh and model the honeycomb structure made from Aluminium 1060. The mechanical properties of Aluminium 1060 are listed as follows, density of 2710 kg/m³, Young's modulus of 70 GPa, Poisson's ratio of 0.33, and yield stress of 110 MPa. Its true stress-strain curve is shown in Figure 3-2 [89]. The strain rate effect of the aluminium is insignificant [176]. Therefore, it is not considered in this chapter. The honeycomb structure is simply placed on a fixed rigid supporting plate and crushed by

another rigid crushing plate in out-of-plane direction. The honeycomb structure is flatwise crushed at a constant crushing speed of 0.5 m/s until a compressive displacement of 85% of the structural height is reached. It should be mentioned that the loading speed used in the experimental test is 5 mm/min, which is too expensive for explicit simulation. Therefore, the low crushing speed of 0.5 m/s is used in numerical simulation while the quasi-static loading condition and an insignificant dynamic effect are ensured since the calculated kinetic-to-internal energy ratio is less than 5% during the whole crushing process [177–179]. The *CONTACT_AUTOMATIC SINGLE SURFACE is used to model the self-contact of the honeycomb structure. The *CONTACT_AUTOMATIC SURFACE TO SURFACE is used to model the contact interactions between the honeycomb structure and the loading/supporting plates. The friction coefficient of 0.25 is used for all contact interactions [89].

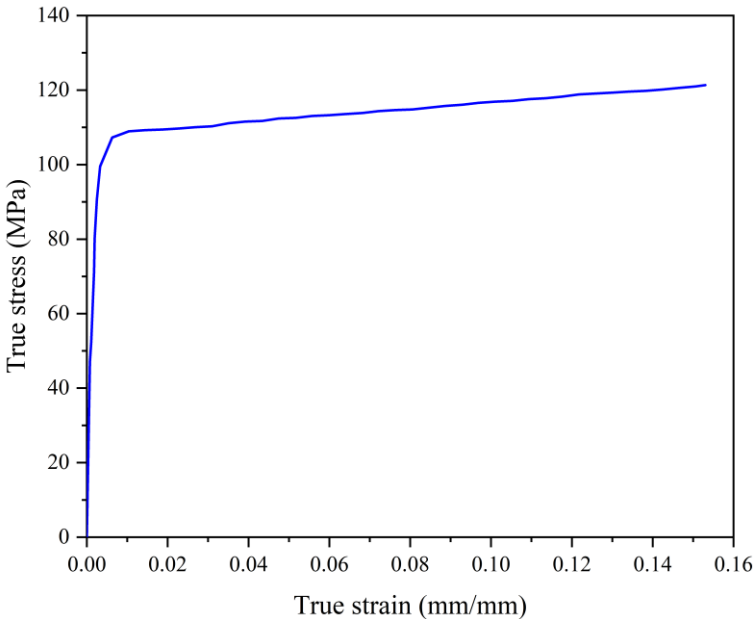


Figure 3-2. True stress-strain curve of aluminium 1060 sheet [89].

3.2.2 Model calibration

The crushing force-displacement responses from the numerical prediction and experiment [89] are plotted and compared in Figure 3-3. Overall, the numerical model predicts well in terms of crushing response during the plateau and densification stages of crushing. The simulated peak force at the initial crushing stage also agrees well with its experimental counterpart.

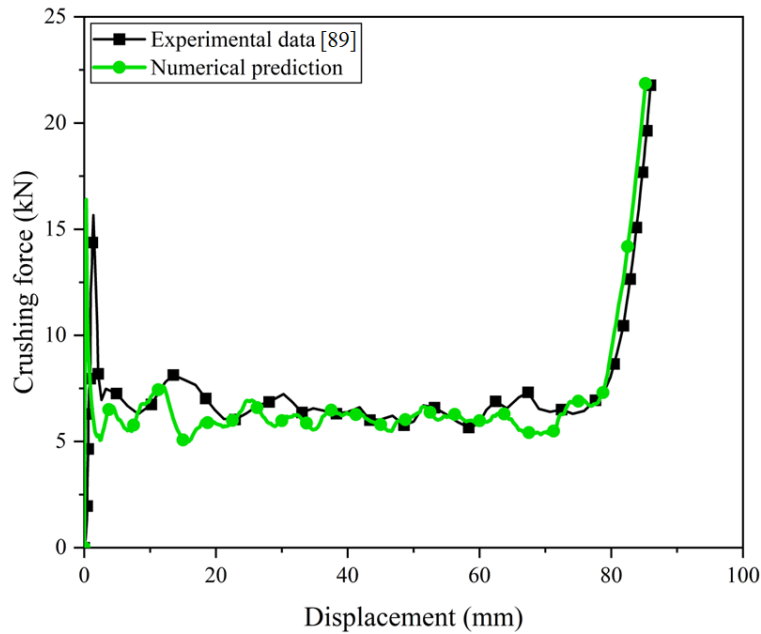


Figure 3-3. Comparison of the crushing force-displacement curves of the honeycomb from numerical simulation and experimental test [89].

The predicted initial peak force is 16.40 kN, which is only 4.7% higher than the initial peak of 15.66 kN obtained from the test. This overestimation is due to the manufacturing imperfection of the honeycomb structure, which is not considered in the FE model. In terms of energy absorption capacity, the difference between simulation and experiment is around 7.4% at the densified distance of 79 mm. Overall, the numerical model generates a good prediction of the crushing response of the aluminium honeycomb structure. Therefore, the same modelling technique and material model are used for the proposed model in the subsequent sections.

3.3 Corrugated tilted honeycomb (CTH) core inspired by plant stem

3.3.1 Geometries and loading conditions

Conventional honeycombs have been widely used as a core for energy absorption because of their high specific energy absorption. However, one significant drawback of this type of core is its high peak resistance at the initial elastic stage compared to its plateau resistance at the plastic deformation stage. This high initial resistance is due to the high stiffness of the vertical cell wall of conventional honeycombs. It may result in a high transmitted force that could cause damage to the protected structures even

before the impact or blast energies are absorbed or dissipated. Therefore, a simple yet effective design that is capable of absorbing high energy and transmitting low initial peak force is crucial. In this chapter, the corrugated tapered shape found in plant stems is implemented onto the cell walls of the conventional square honeycomb core to propose an effective energy-absorbing core. The proposed corrugated tilted honeycomb (CTH) core is illustrated in Figure 3-4(b). It is designed based on the conventional square honeycomb core of the cell size $c = 40$ mm, as shown in Figure 3-4(d). The square honeycomb core consists of 3×3 unit cells and has an overall bottom cross-section of 120×120 mm. The CTH core is constructed by inclining each sidewall to a specific tilted angle (θ), and corrugations are introduced to the centre of each sidewall of the unit cell, as shown in Figure 3-4(d) and (e). As illustrated in Figure 3-4(b), the proposed CTH core can be easily fabricated using the slotting technique, which is widely used for the fabrication of conventional square honeycomb [23]. During the fabrication of each corrugated plate of CTH core shown in Figure 3-4(a), rectangular plate of the same width (w) and length (l) can be slotted and corrugated at the desired location. Then, those corrugated plates are assembled at the interconnections by brazing or bonding to ensure good bonding. Since the corrugated plate is tilted at a specific angle θ , small portions at the bottom edges of the corrugations need to be cut with a cutting angle β ($\beta = 90^\circ - \theta$) to ensure a flat bottom surface of the CTH core, as illustrated in Figure 3-4(a). These corrugated tilted plates also leave the top gaps (corrugated gaps) of the same dimension as the cutting portions as circled in Figure 3-4(e). These top corrugated gaps help decrease the initial stiffness and facilitate the initial bending during the crushing process.

The surface area of each corrugated plate (S) of the CTH core can be calculated by subtracting the cut-out area (A') from the rectangular plate (before folding) having the surface area A . The surface areas A and A' can be calculated as follows:

The surface area of each rectangular plate $A = l \times w$; where l and w are the length and width of the rectangular plate, respectively. The total length of each plate $l = [2a + (2e)n]p$; where n is the number of corrugations on each side of the unit cell, and p is the number of units on each side of the core.

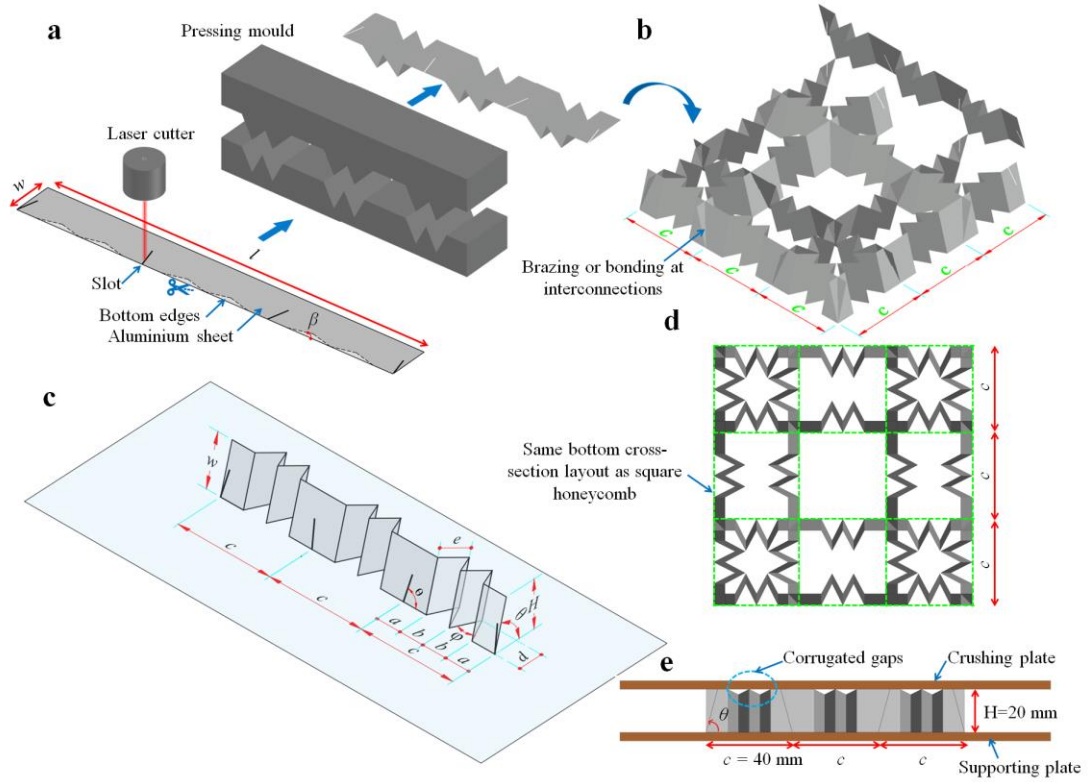


Figure 3-4. Details of the CTH core showing (a) corrugated plate fabrication process, (b) assembling of core, (c) details of corrugated plate, (d) top view, and (e) side view of core.

$$a = \frac{c - nb}{2}; e = \cos \beta \cdot \sqrt{\left(\frac{b}{2}\right)^2 + d^2}; w = \frac{H}{\sin \theta}; \beta = 90^\circ - \theta; \text{ where } H \text{ is the height of the}$$

core, b and d are the width and depth of the corrugation, respectively. The surface area of each plate of square honeycomb and tilted square honeycomb can also be calculated using the same formulae whose $n = 0$, $b = 0$, and $d = 0$.

$$\text{The total cut-out area } A' = \left[2 \left(\frac{e \times e \tan \beta}{2} \right) \right] n \times p = np \cdot e^2 \tan \beta;$$

The volumetric density or relative density of the core can be calculated as

$$\rho_v = \frac{8S \cdot t}{(3c)^2 \cdot H}; \text{ where } t \text{ is the thickness of the plate. This volumetric density is the}$$

ratio of the material volume in the core to the overall volume of the core. All geometric parameters are shown in Figure 3-4(c).

Five different honeycomb cores of the same mass are compared as shown in Figure 3-5. Three CTH cores with different numbers of corrugations, n , (i.e., 1, 2 and 3) on

each side of the unit cell are investigated and denoted as C1, C2, and C3, respectively. These three CTH cores are compared with the conventional square honeycomb core (HC) and tilted square honeycomb core (TC). All CTH cores have the same corrugation depth (d) of 10 mm. C1 and C2 have the same corrugation width (b) of 10 mm, while C3 has a corrugation width (b) of 5 mm to avoid the touching of the corrugations, resulting in a corrugated angle (φ) of 53 degrees for core C1 and C2, and 28 degrees for core C3. It should be mentioned that the tilted angle and overall height of the CTH core are also limited by the corrugations. Therefore, the tilted angle (θ) of 75 degrees is chosen as the baseline-tilted angle of the CTH core as the cell size is fixed for all cores. Each plate of the square honeycomb core HC has a wall thickness (t) of 0.26 mm, resulting in an overall mass of core (m) of 13.5 g and a volumetric density of core (ρ_v) of 1.7%. Since each core has a different plate surface area, its plate wall thickness is adjusted to have the same volume or mass of material in the core. The geometric parameters of all five cores are listed in Table 3-1.

Table 3-1. Geometric parameters of all five cores.

Core	H (mm)	b (mm)	d (mm)	φ (°)	θ (°)	t (mm)
HC	20	0	0	-	90	0.260
TC-T75	20	0	0	-	75	0.251
C1-T75	20	10	10	53	75	0.199
C2-T75	20	10	10	53	75	0.165
C3-T75	20	5	10	28	75	0.124

In this chapter, the same Belytschko-Tsay type shell element with five integration points through the shell thickness and *MAT_PIECEWISE_LINEAR_PLASTICITY material model are used to model all cores, which are made of the same aluminium 1060 sheet as the calibrated model. The energy absorption and crushing performances of each core are investigated by performing flatwise crushing under constant speed. The core is placed between a fixed rigid supporting plate and a rigid crushing plate, as shown in Figure 3-4(e). The rigid crushing plate is set to crush the core at a constant crushing speed in the out-of-plane (Z) direction. The fixed boundary condition is used for the bottom edges of the core to simulate the perfect bond between the core and the external plate, as shown in Figure 3-6, which is commonly used for sandwich

structures. The influence of crushing speed on the energy absorption and crushing performances of each core is studied under three different constant crushing speeds such as 0.5 m/s, 5 m/s, and 15 m/s, which are denoted as V0.5, V5, and V15, respectively. Each core is denoted by its configuration, tilted angle, and crushing speed. As an example, C2-T75-V15 denotes the 2-corrugation honeycomb core with 75-degree tilted angle of the plate, which is crushed under 15 m/s crushing speed. The influences of the tilted angle and wall thickness (relative density) on the performance of the CTH cores are also investigated and discussed in Sections 3.4.2 and 3.4.3, respectively.

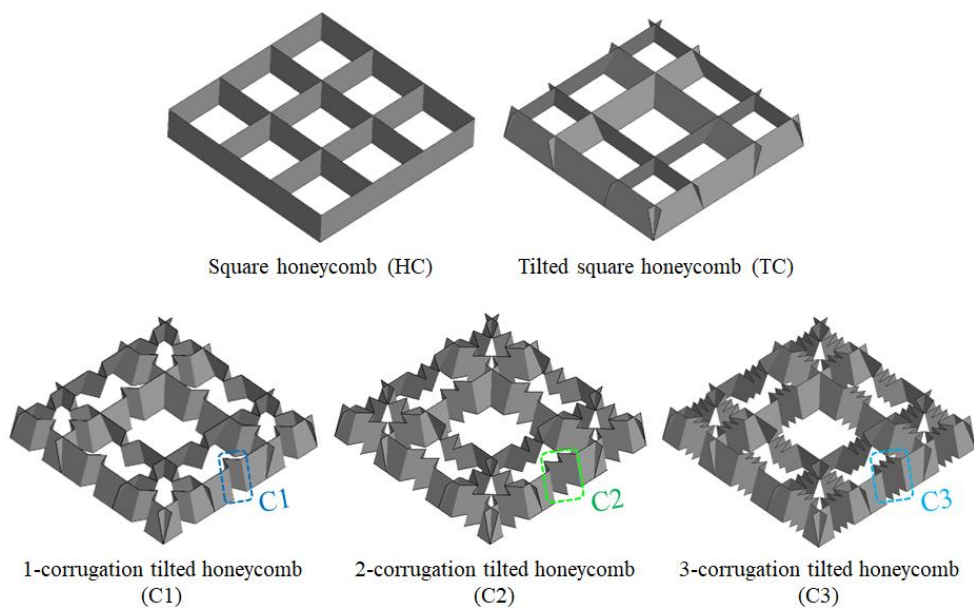


Figure 3-5. Core configurations.

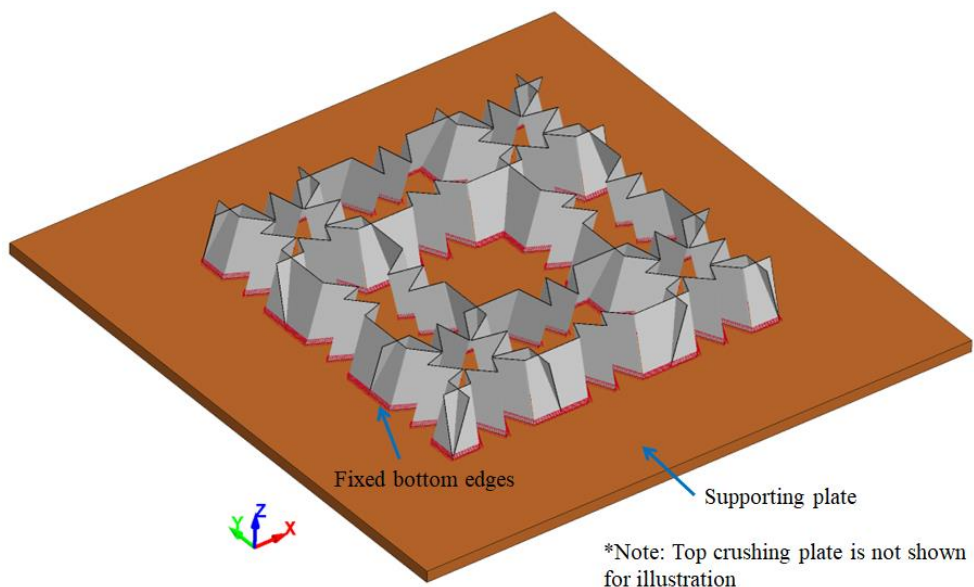


Figure 3-6. Finite element model of C2-T75.

3.3.2 Mesh convergence test

Core C2-T75-V15 with four different mesh sizes (i.e., 0.25 mm, 0.5 mm, 1 mm, and 2 mm) is used for the mesh convergence test to determine a suitable mesh size for the numerical model, which can achieve the balance between simulation accuracy and computation cost. The force-displacement responses obtained from the mesh convergence test are plotted and compared in Figure 3-7. The mesh size significantly affects the densification stage or stroke length, as shown in Figure 3-7. The models with coarse mesh sizes (i.e., 1 mm and 2 mm) generate a smaller stroke length and a higher crushing force. The models with small mesh sizes such as 0.5 mm and 0.25 mm generate similar force-displacement responses and capture similar key indicators, i.e., the initial peak, overall crushing force, and stroke length. Therefore, the mesh size of 0.5 mm is chosen for the FE analysis in the subsequent numerical simulations.

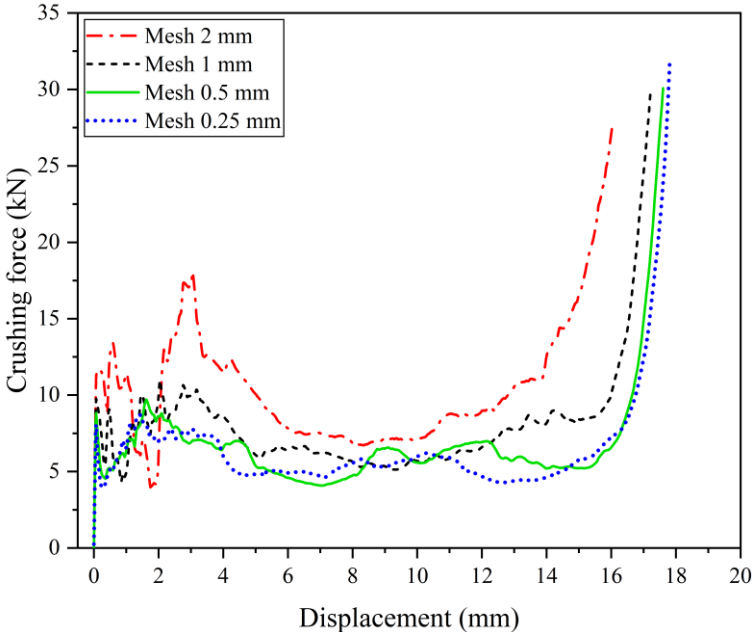


Figure 3-7. Force-displacement curves of C2-T75-V15 with different mesh sizes.

3.4 Results and discussions

The crushing responses and energy absorption performances of each core are assessed and evaluated by using key indicators of the energy-absorbing structure such as peak crushing force (*PCF*), mean or average crushing force (*MCF*), crushing force efficiency (*CFE*), energy absorption capacity (*EA*) and specific energy absorption capacity (*SEA*). A typical crushing force-displacement response of the energy-

absorbing structure showing the PCF , MCF , and EA is illustrated in Figure 3-8. The EA is the total energy that can be absorbed by the core before reaching densification. The area enclosed under the force-displacement curve characterises the EA calculated

as $EA = \int_0^s F(z)dz$, where $F(z)$ is the crushing force exerting on the rigid crushing plate

as a function of its corresponding crushing distance, z . The stroke, s , is the effective crushing distance where the crushing force starts rising steeply as the structure starts to densify. It can be defined by the intersection of two asymptotic lines of the force-displacement curve at the plateau and densification stages [45,58,169,170,180], as shown in Figure 3-8. SEA is the energy absorption capacity per unit mass of the structure, which is calculated as $SEA = \frac{EA}{m}$.

The PCF and MCF are the peak and the mean crushing forces over the stroke. The MCF can be calculated as $MCF = \frac{EA}{s}$.

The CFE is the ratio of mean-to-peak crushing force ($CFE = \frac{MCF}{PCF}$).

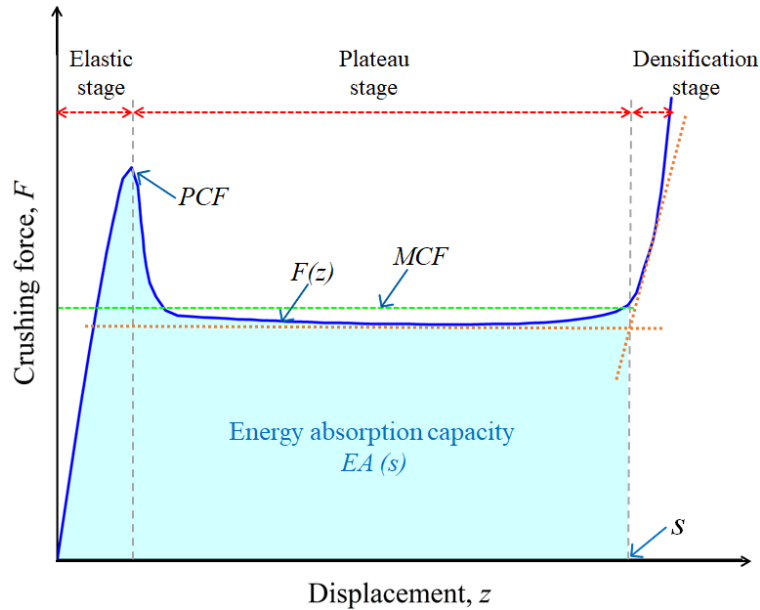


Figure 3-8. Typical crushing force-displacement response of energy-absorbing structure under compression.

3.4.1 Crushing responses of CTH cores under various crushing speeds

In this section, the influences of the crushing speeds on the energy absorption and crushing responses of each CTH core are investigated and compared with those of the

typical square honeycomb core and tilted square honeycomb core. Three crushing speeds of 0.5 m/s, 5 m/s, and 15 m/s are investigated. All cores have the same overall dimension of 120 mm × 120 mm × 20 mm (height) and relative density of 1.7%. All tilted cores have the same tilted angle of 75 degrees.

3.4.1.1 Deformation modes

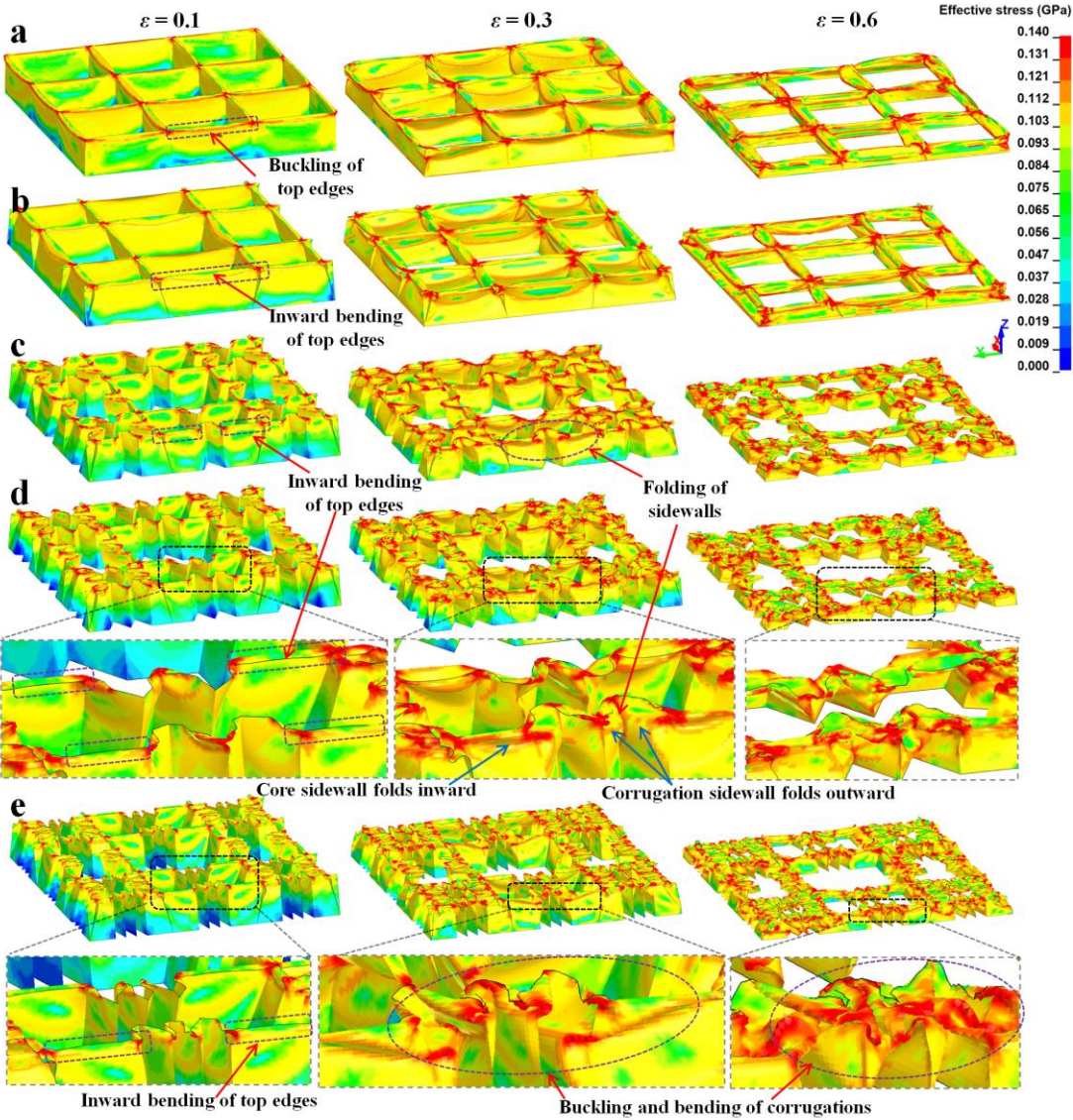


Figure 3-9. Deformation modes of (a) HC, (b) TC-T75, (c) C1-T75, (d) C2-T75, and (e) C3-T75 under 0.5 m/s crushing speed.

The deformation modes under the crushing speeds of 0.5 m/s and 5 m/s are quite similar for all cores. Figure 3-9 illustrates the deformation at the strains of 0.1, 0.3, and 0.6 of all cores crushed under 0.5 m/s crushing speed. The strain is the ratio of the crushing distance to the overall height of the core. At the initial crushing stage of the

square honeycomb core (HC), the buckling appears at the top edges of the vertical wall, causing a sharp rise with an immediate drop in the crushing resistance after the buckling. With further crushing, the core sidewalls are subsequently folded and bent along the crushing direction, as shown in Figure 3-9(a). By tilting the sidewalls of the core, the buckling of the top edges followed by the inward bending of the sidewalls of core TC-T75 occurs, as shown in Figure 3-9(b). The tilted core sidewalls of core TC-T75 require less force to generate the buckling during the initial crushing stage as compared to the vertical core sidewalls of core HC. However, the initial buckling resistance of core TC-T75 is still significantly high owing to the perfectly bonded interconnections between each plate of the core, which results in an overall high stiffness at the contact interface.

For the proposed CTH cores, the implementation of the corrugated tilted design inspired by the plant stem helps eliminate the initial peak at the elastic stage and enhance the plateau crushing resistance of the honeycomb cores HC and TC-T75. As shown in Figure 3-9(c), at the initial crushing stage, the top edges of the core sidewalls bend inward first, followed by folding of the corrugated sidewalls owing to the gaps at the corrugation locations (Figure 3-4(e)). With partial contact between the crushing plate and core sidewalls, the overall stiffness of the core at the contact interface is substantially reduced, resulting in a significant reduction of the initial buckling resistance, elimination of the initial peak force, and easy folding of the core. As the core is further crushed, the corrugated gaps are fully closed at a strain of around 0.1, where the CTH core reaches its crushing peak. With further crushing, the core sidewalls fold inward while the corrugated sidewalls fold outward horizontally towards each other, thus providing horizontal support to the sidewalls, which leads to the increase in plateau crushing resistance as well as more plastic deformation of the folded corrugated sidewalls. Furthermore, with the increase in the number of corrugations (i.e., from C1-T75 to C2-T75), the corrugated gaps increase, resulting in a more significant reduction of its buckling resistance. As shown in Figure 3-9(d), the adjacent side walls of nearby corrugations fold and bend outward towards each other, thus providing further support, which increases the buckling resistance of the sidewalls and results in an enhancement of plateau crushing resistance as well as increases the plastic deformation of the folded corrugated sidewalls. However, core C3-T75 tends to deform more easily because of the ease of buckling of each individual corrugation,

which has smaller corrugated angle (φ) and thinner wall thickness as compared to cores C1-T75 and C2-T75. As shown in Figure 3-9(e), the adjacent corrugations individually buckle and bend without providing support to the sidewalls, resulting in a low crushing resistance of its structure.

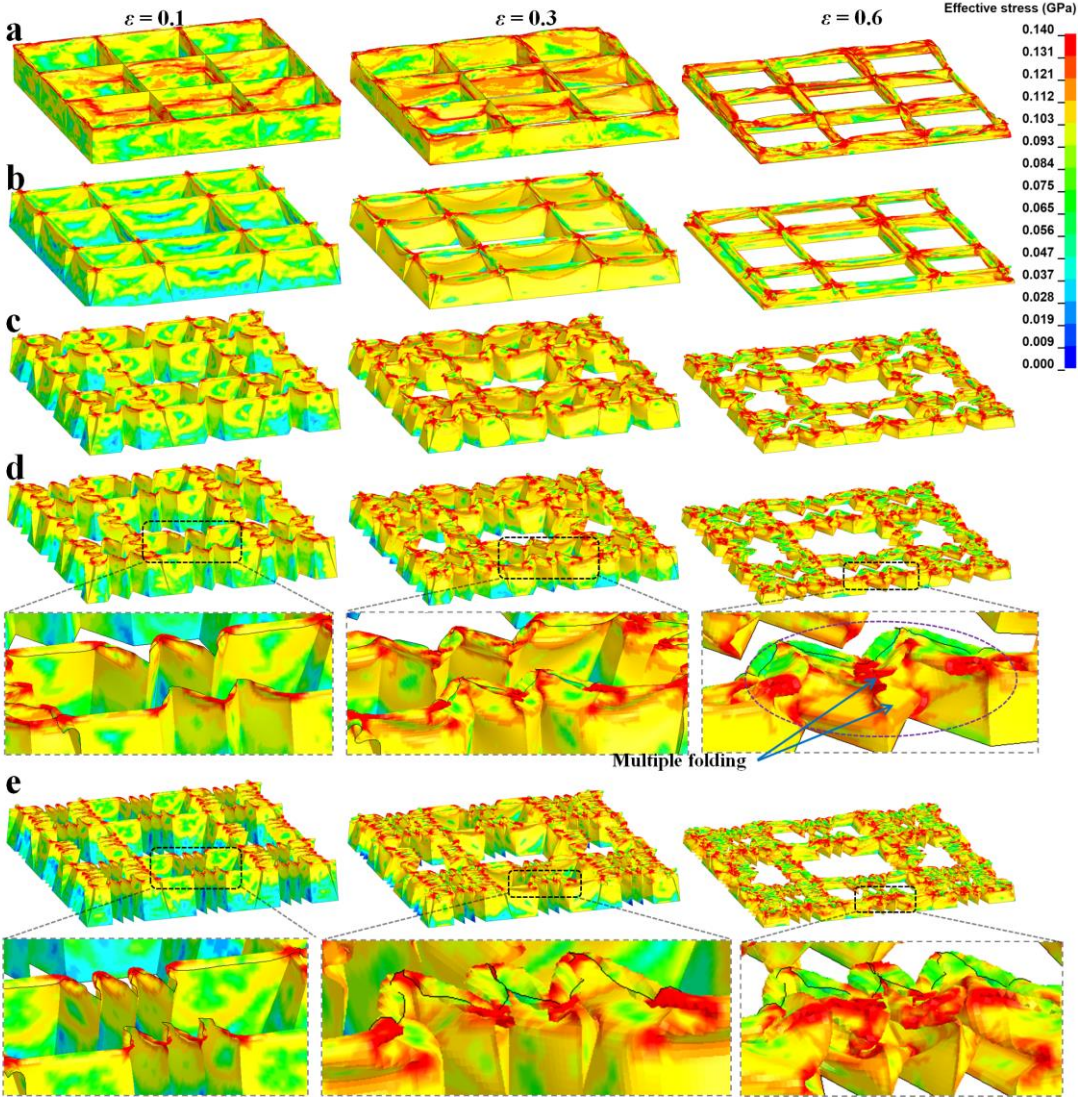


Figure 3-10. Deformation modes of (a) HC, (b) TC-T75, (c) C1-T75, (d) C2-T75, and (e) C3-T75 under 15 m/s crushing speed.

The deformation at the strains of 0.1, 0.3 and 0.6 of all cores crushed under 15 m/s are illustrated in Figure 3-10. With the increase in crushing speed, the buckling of core HC initiates at around mid-height while the top edges of the core sidewalls remain almost vertical, causing the increase in the initial peak and plateau crushing resistances. This increase is due to the initial effect of the core and the initial stabilisation of the core sidewalls [12,45], which is similarly found in the dynamic crushing of the sandwich square honeycomb core and cube strip [12,45]. The increases in the peak and plateau

crushing resistances with the increase in the crushing speed are also observed for the tilted square honeycomb core (TC-T75) and CTH cores. However, the increasing rate of the peak crushing resistance is low for CTH cores as compared with that of core TC-T75. Furthermore, this increasing rate reduces with the increase in the number of corrugations owing to the enlargement of the corrugated gaps at the corrugation locations. With more numbers of corrugations and larger corrugated angle as well as multiple folding of the sidewalls as illustrated in Figure 3-10(d), the plateau crushing resistance of CTH cores is still higher as compared to that of square honeycomb core with higher wall thickness. Therefore, core C2-T75 outperforms other cores of the same mass (i.e., HC, TC-T75, C1-T75, C3-T75) by possessing low buckling resistance and high plateau crushing resistance owing to more numbers of corrugations with large corrugated angle.

3.4.1.2 Force-displacement responses

The force-displacement responses of all CTH cores (i.e., C1, C2, C3), square honeycomb core (HC), and tilted square honeycomb core (TC) under 0.5 m/s crushing speed are plotted in Figure 3-11(a). As expected, the conventional square honeycomb core (HC) has a significantly high peak crushing force at the elastic stage, followed by a relatively low crushing force at the plateau stage, thus resulting in a low crushing force efficiency (*CFE*) of only 0.15. This high initial crushing resistance of HC is due to the high stiffness of its vertical and thick sidewall, which requires a high force to generate buckling of its structure. With the inclined sidewall of the tilted square honeycomb core (TC-T75), the *PCF* is reduced by around 54%. However, the plateau crushing force also decreases because of the easy bending of the tilted plates of TC core. Therefore, TC-T75 still has a low *CFE* of around 0.32. Similar finding was also found in the case of inclined cell honeycomb structure under compression [181]. As compared with HC and TC-T75, the proposed CTH core has a significantly lower initial crushing force at the elastic stage owing to the easy bending of the top edges and the corrugated gaps at the corrugation locations (Figure 3-4(e)). Therefore, it has a delayed *PCF* which occurs in a plateau stage once the crushing plate closes the corrugated gaps and starts crushing the corrugations, thus enhancing the plateau crushing force and improving the crushing efficiency.

As compared in Figure 3-11(b), under the low crushing speed of 0.5 m/s, all CTH cores have a significantly low *PCF*. Core C1-T75 (one-corrugation on each side of unit cell) has a 68% lower *PCF* than core HC. Increasing the number of corrugations, i.e., to two (C2-T75) and three (C3-T75) on each side, leads to a further decrease in the *PCF*, which is around 72% to 80% lower than that of HC, respectively. Therefore, increasing the number of corrugations decreases the *PCF* and increases the *CFE* to around 0.6 to 0.8. However, core C3-T75, with more corrugations but smaller corrugated angle (φ) and thinner wall thickness, tends to bend and deform more easily, thus resulting in a lower *MCF* than cores C1-T75 and C2-T75. In terms of *SEA*, the proposed CTHs have higher *SEA* than the conventional square and tilted square honeycomb cores. Core C2-T75 has the highest *SEA* of 6.29 J/g, around 30% and 36% higher than cores C3-T75 and HC, respectively.

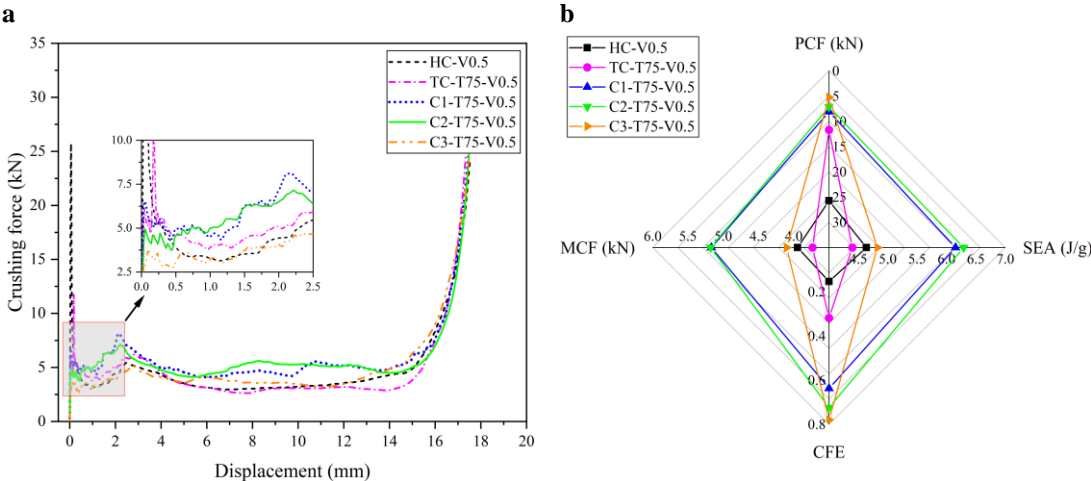


Figure 3-11. (a) Force-displacement curves and (b) comparisons of *PCF*, *MCF*, *CFE*, and *SEA* of all cores under 0.5 m/s crushing speed.

The force-displacement responses of all cores under the crushing speeds of 5 m/s and 15 m/s are plotted in Figure 3-12(a) and Figure 3-13(a), respectively. With the increase in the crushing speed (from 0.5 m/s to 15 m/s), the *PCF* of all cores increases, especially for cores TC and C1, because of the significant inertial effect of the cores. The increasing rate of *PCF* of the CTH core decreases as the number of corrugations increases, owing to the enlargement of the corrugated gaps. All CTH cores outperform the conventional square and tilted square honeycomb cores by having a lower *PCF* and a higher *CFE*. The square honeycomb core shows an undesirably high *PCF* and low *CFE* of around 0.15 to 0.21. Under the high crushing speed of 15 m/s, the introduction of the inclination plates of TC core has less effect on the reduction of the

PCF due to the inertial effect of the core. Therefore, the *PCF* of TC-T75 is only 24% lower than that of HC core. For CTH cores, the *PCF* of C1-T75 is around 52% lower than that of HC. By increasing the number of corrugations, i.e., to two (C2-T75) and three (C3-T75) on each side, the *PCF* further reduces by 68% and 74%, resulting in a high *CFE* of 0.63 and 0.67, respectively. However, because of the small corrugated angle and thin wall thickness, it is easier to bend and deform the corrugations as well as the whole structure of core C3-T75, resulting in a lower *MCF* and *EA* than a core with larger corrugated angle and thicker wall thickness, i.e., cores C1-T75 and C2-T75. As illustrated in Figure 3-12(b) and Figure 3-13(b), core C2-T75 outperforms all cores in all four key indicators by having a relatively high *CFE* with low *PCF* and high *MCF* as well as high *SEA* under various crushing speeds. As the crushing speed increases from 0.5 m/s to 15 m/s, the *CFE* of corrugated tilted core C2 only slightly decreases from 0.72 to 0.63, showing its low and rate-insensitive peak crushing force. Therefore, the CTH core with 2 numbers of corrugations and large corrugated angle (i.e., C2-T75 in this chapter) has the best crushing performance under various crushing speeds, i.e., 0.5 m/s to 15 m/s, as compared with the conventional square honeycomb core of the same mass and relative density.

The *PCF*, *MCF*, *CFE*, *EA*, and *SEA* of all cores under 0.5 m/s, 5 m/s, and 15 m/s crushing speeds are summarised in Table 3-2. The tilted angle and thickness of the corrugated plate affect the stiffness of the CTH core. Therefore, the effects of the tilted angle and wall thickness of the corrugated plate on the crushing performance of core C2 are investigated and discussed in Sections 3.4.2 and 3.4.3, respectively.

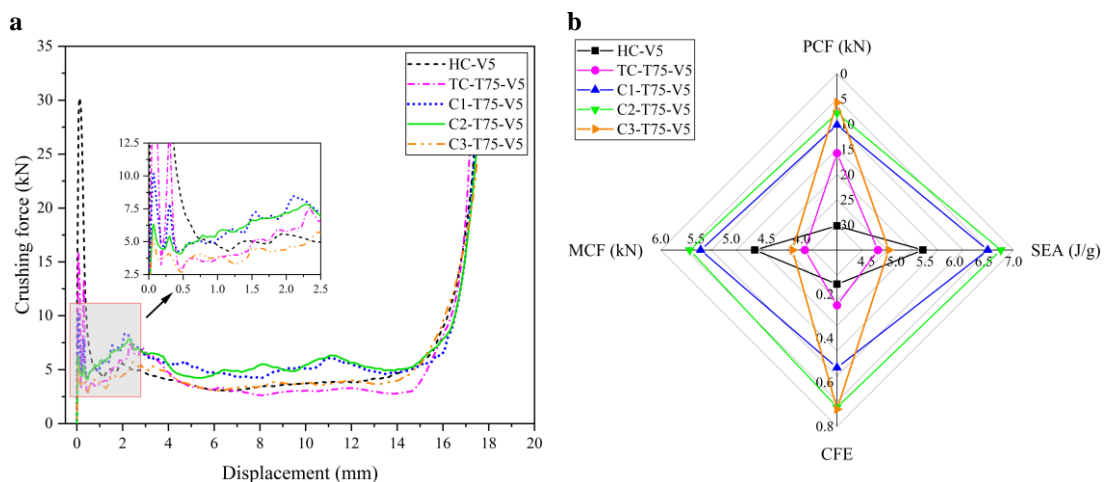


Figure 3-12. (a) Force-displacement curves and (b) comparisons of *PCF*, *MCF*, *CFE*, and *SEA* of all cores under 5 m/s crushing speed.

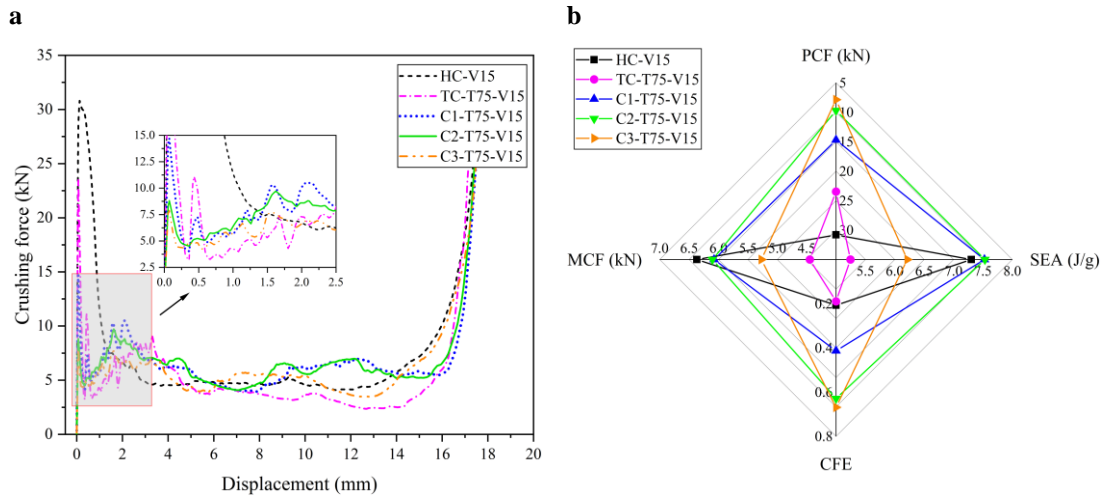


Figure 3-13. (a) Force-displacement curves and (b) comparisons of PCF , MCF , CFE , and SEA of all cores under 15 m/s crushing speed.

Table 3-2. Summary of PCF , MCF , CFE , EA and SEA of all cores under 0.5 m/s, 5 m/s, and 15 m/s crushing speeds.

Core	Stroke s (mm)	PCF (kN)	MCF (kN)	CFE	EA (J)	SEA (J/g)
HC-V0.5	15.89	25.72	3.95	0.15	62.71	4.64
TC-T75-V0.5	15.93	11.73	3.73	0.32	59.48	4.40
C1-T75-V0.5	16.11	8.11	5.17	0.64	83.24	6.15
C2-T75-V0.5	16.43	7.15	5.18	0.72	85.09	6.29
C3-T75-V0.5	15.91	5.26	4.10	0.78	65.26	4.82
HC-V5	15.84	30.20	4.67	0.15	73.91	5.46
TC-T75-V5	16.05	15.80	3.96	0.25	63.52	4.70
C1-T75-V5	16.34	10.19	5.43	0.53	88.81	6.56
C2-T75-V5	16.43	7.84	5.59	0.71	91.83	6.79
C3-T75-V5	15.98	5.72	4.13	0.72	66.02	4.88
HC-V15	15.51	30.80	6.37	0.21	98.79	7.30
TC-T75-V15	15.96	23.48	4.44	0.19	70.95	5.24
C1-T75-V15	16.76	14.72	6.08	0.41	101.81	7.53
C2-T75-V15	16.70	9.71	6.10	0.63	101.93	7.53
C3-T75-V15	15.95	7.88	5.27	0.67	84.05	6.21

3.4.2 Effect of tilted angle on the CTH core

The effect of the tilted angle of the corrugated plates on the crushing performance of core C2 is investigated in this section. As mentioned previously, the tilted angle (θ) of 75 degrees is the baseline-tilted angle of the CTH core as the cell size is fixed for all cores, to avoid touching of the corrugations. Therefore, three different tilted angles, i.e., 75, 80, and 85 degrees, are considered. All cores have the same overall mass of 13.5 g and a volumetric density of core (ρ_v) of 1.7% by adjusting the wall thickness of the corrugated plate. All cores are crushed under 15 m/s crushing speed.

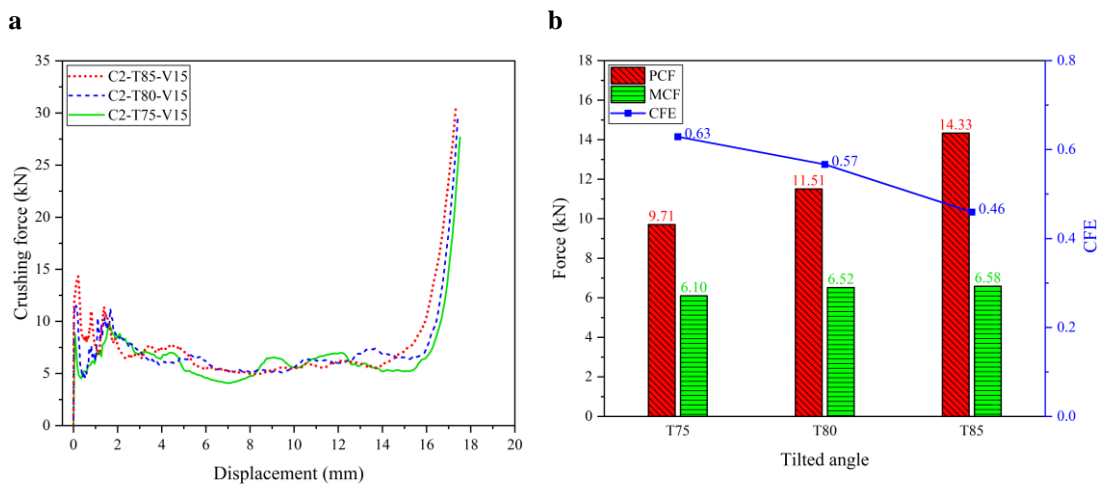


Figure 3-14. (a) Force-displacement curves and (b) comparisons of *PCF*, *MCF*, and *CFE* of corrugated tilted honeycomb core C2 with different tilted angles under 15 m/s crushing speed.

As presented in Figure 3-14(a), the crushing responses of core C2 with different tilted angles are quite similar. However, the *PCF* tends to occur at the initial elastic stage of crushing as the tilted angle increases. It is because the stiffness of the corrugated plate increases and the corrugated gaps become smaller as the tilted angle increases, thus increasing the *PCF*. As compared in Figure 3-14(b), the *PCF* increases by 48% from 9.71 kN to 14.33 kN when the tilted angle increases from 75 degrees to 85 degrees, while the *MCF* only slightly improves by around 8%, resulting in a decrease of the *CFE* from 0.63 to 0.46. Increasing the tilted angle also leads to a slight reduction of the stroke due to the folding of more vertical and thicker corrugated walls of the core with a larger tilted angle. All cores have a similar value of *SEA* between 7.53 J/g and 7.86 J/g. Therefore, increasing the tilted angle of the corrugated plates has a minor effect on the enhancement of the *MCF* and *SEA*, but it leads to an increase in *PCF*,

thus resulting in a decrease in the *CFE*. The *PCF*, *MCF*, *CFE*, *EA*, and *SEA* of core C2 with different tilted angles are summarised in Table 3-3.

Table 3-3. Summary of *PCF*, *MCF*, *CFE*, *EA* and *SEA* of corrugated tilted honeycomb core C2 with different tilted angles under 15 m/s crushing speed.

Core	Stroke <i>s</i> (mm)	<i>PCF</i> (kN)	<i>MCF</i> (kN)	<i>CFE</i>	<i>EA</i> (J)	<i>SEA</i> (J/g)
C2-T75-V15	16.70	9.71	6.10	0.63	101.93	7.53
C2-T80-V15	16.31	11.51	6.52	0.57	106.32	7.86
C2-T85-V15	15.86	14.33	6.58	0.46	104.39	7.72

3.4.3 Effect of relative density on the CTH core

The effect of relative density on the performance of square honeycomb core (HC) and CTH core (C2-T75) is investigated in this section. Three different relative densities, i.e., 1.7%, 3% and 5%, are considered. The cores C2-T75 and HC of the same relative densities of 1.7% and 3% are compared. The relative density of each core is increased by altering the wall thickness of the plates. Core C2-T75 with a higher relative density of 5% is also compared with the commercially used CMATTM aluminium foam of the same density. All cores are crushed under the crushing speed of 15 m/s. The force-displacement responses of C2-T75 and HC with relative densities of 1.7% and 3% are compared in Figure 3-15(a). It is shown that the crushing force of both cores increases with the increase in the relative density. As compared in Figure 3-15(b), the *PCF* of the C2-T75 is 68% lower than that of HC of the same 1.7% relative density, and it is 55% lower than that of HC of the same 3% relative density. In terms of the average crushing force, both cores C2-T75 and HC of the same relative density have quite similar *MCF*. Therefore, C2-T75 has a higher *CFE* than HC of the same density. Core C2-T75 has a *CFE* of 0.63 and 0.67 while core HC has a much lower *CFE* of only 0.21 and 0.28 for the relative density of 1.7% and 3%, respectively. Therefore, the corrugated tilted core C2-T75 outperforms the conventional square honeycomb core HC of the same relative density in all key indicators by having a lower *PCF*, a higher *CFE*, *MCF* and *SEA*.

Core C2-T75 is also compared with aluminium foam which is widely used for energy absorption applications. Both C2-T75 and the aluminium foam have the same overall mass of 39 g and the same relative density of 5%. The aluminium foam is modelled

using solid elements and *MAT_CRUSHABLE_FOAM material model. The compressive stress versus strain curve of the CYMAT™ aluminium foam is shown in Figure 3-16, and the material properties are listed in Table 3-4 [9,182].

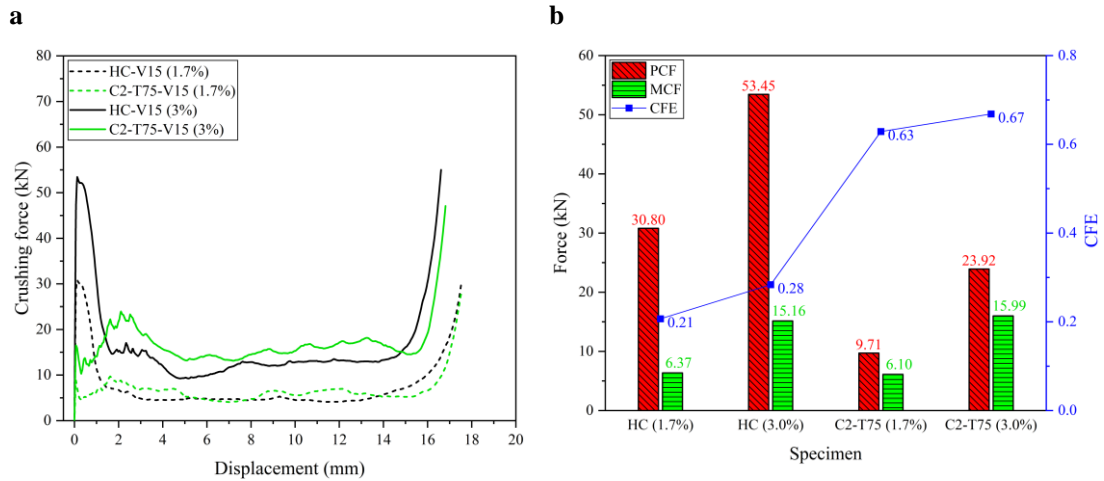


Figure 3-15. (a) Force-displacement curves and (b) comparisons of PCF, MCF, and CFE of HC-V15 and C2-T75-V15 with relative densities of 1.7% and 3% under 15 m/s crushing speed.

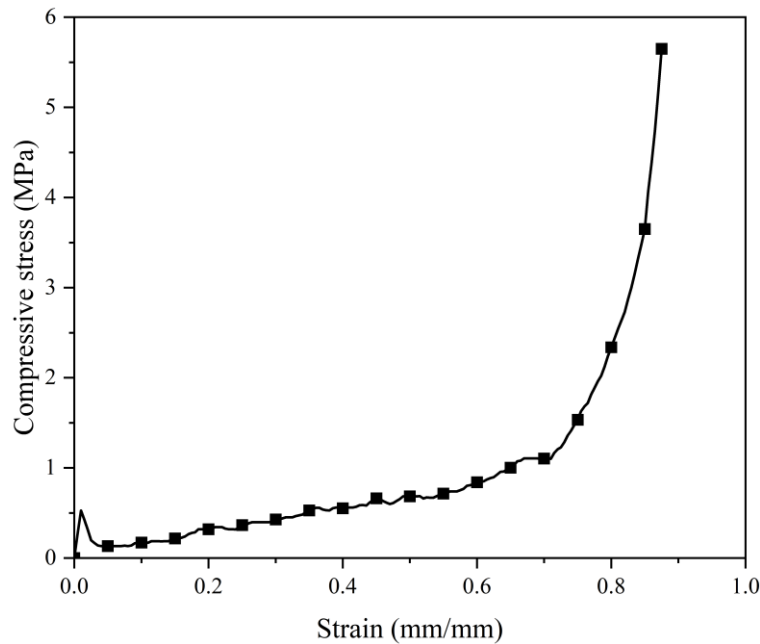


Figure 3-16. Compressive stress-strain curve of CYMAT™ aluminium foam with 5% relative density [9,182].

Table 3-4. Material properties of CYMAT™ aluminium foam [9,182].

Parameter	Density (kg/m ³)	Young's modulus (MPa)	Poisson's ratio	Damping coefficient
value	135.5	53	0	0.1

The force-displacement responses of core C2-T75 and CMATTM aluminium foam are compared in Figure 3-17(a). It is shown that the average crushing force of C2-T75 is higher than that of the aluminium foam of the same mass and relative density. As compared in Figure 3-17(b), the proposed corrugated tilted honeycomb core C2-T75 has four times higher *MCF* and *SEA* than the aluminium foam of the same mass. The *SEA* of C2-T75 is around 13.88 J/g while that of the aluminium foam is only around 3.44 J/g. Therefore, the proposed CTH core can absorb more energy than the conventional cores such as square honeycomb or aluminium foam of the same mass. The *PCF*, *MCF*, *CFE*, *EA*, and *SEA* of HC-V15, C2-T75-V15, and aluminium foam with various relative densities are summarised in Table 3-5.

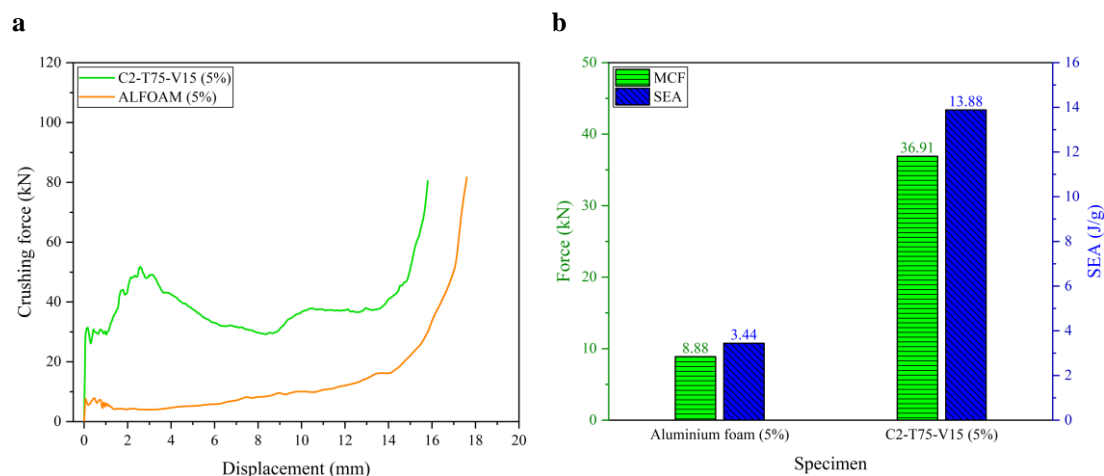


Figure 3-17. (a) Force-displacement curves and (b) comparisons of *MCF* and *SEA* of C2-T75-V15 and aluminium foam of the same 5% relative density under 15 m/s crushing speed.

Table 3-5. Summary of *PCF*, *MCF*, *CFE*, *EA* and *SEA* of HC-V15, C2-T75-V15, and aluminium foam with various relative densities (3% and 5%) under a crushing speed of 15 m/s.

Core	Stroke <i>s</i> (mm)	<i>PCF</i> (kN)	<i>MCF</i> (kN)	<i>CFE</i>	<i>EA</i> (J)	<i>SEA</i> (J/g)
HC-V15 (3%)	15.42	53.45	15.16	0.28	233.77	9.98
C2-T75-V15 (3%)	16.05	23.92	15.99	0.67	256.69	10.96
Aluminium foam (5%)	15.14	-	8.88	-	134.37	3.44
C2-T75-V15 (5%)	14.68	51.79	36.91	0.71	541.86	13.88

Overall, the proposed structure with corrugated tilted design improves the crushing performances of the conventional one by eliminating the initial peak crushing force and enhancing the crushing efficiency as well as *SEA* without introducing complex

manufacturing process of structures, which is still a challenge, especially in a large scale [42,123].

3.5 Comparison of crushing performances of similar cellular structures

In this section, the crushing performances of the proposed bio-inspired CTH core are compared with those of the existing cores having similar material and cellular structures, as shown in Table 3-6. The *SEA* and *CFE* of each core are calculated using the same method discussed in Section 3.4. The comparison of the specific energy absorption (*SEA*) of various cellular cores is illustrated in Figure 3-18. The proposed CTH cores (C2-T75) having three different relative densities (i.e., 1.7%, 3%, and 5%) are selected for the comparison. It is shown that the proposed CTH cores outperform most existing cellular cores made of similar aluminium materials with similar relative density by having a higher *SEA*. Furthermore, the proposed CTH cores even have higher *SEA* than the other cores of higher relative density, illustrating the capability of absorbing higher energy by utilising less material, which is ideal for energy-absorbing applications.

Table 3-6. Material properties and illustration of each cellular structure.




Crushing speed and material properties	Illustration
Truncated square pyramid foldcore [179] Aluminium 1060 $\rho_v = 2.5\%$ $V = 0.5 \text{ m/s}$	
Truncated triangular pyramid foldcores [84] Aluminium 1060 $\rho_v = 2.7\%$ $V = 0.05 \text{ m/s}$	
Truncated pentagonal pyramid foldcores [84] Aluminium 1060 $\rho_v = 2.7\%$ $V = 0.05 \text{ m/s}$	

Table 3-6 (Continued)

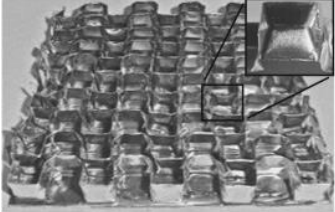
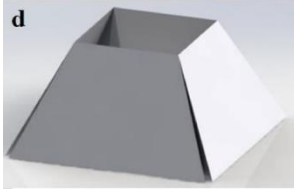

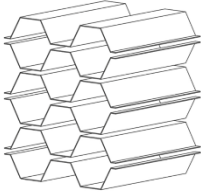
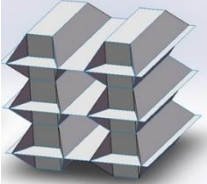
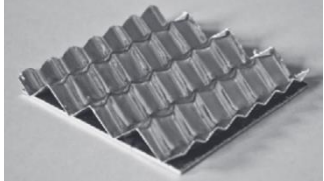

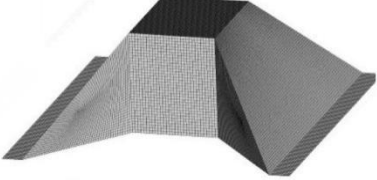
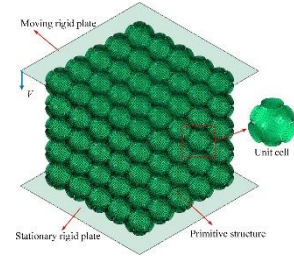

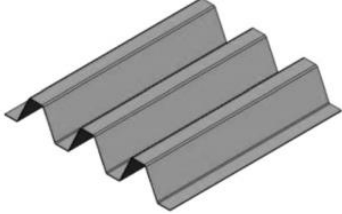
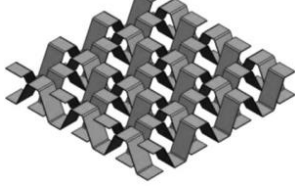


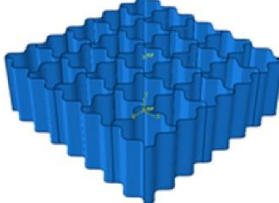
Crushing speed and material properties	Illustration
<p>Diamond strip [43] aluminium 1100-0 $\rho_v = 2.7\%$ Quasi-static</p>	
<p>Open top square dome foldcore [45] aluminium 1100-0 $\rho_v = 3\%$ $V = 0.05 \text{ m/s}$</p>	
<p>Square antiprism structure [87] aluminium 1100-0 $\rho_v = 5.6\%$ $V = 0.05 \text{ m/s}$</p>	
<p>Hexagonal honeycomb structure [89] aluminium 1060 $\rho_v = 2\%$ Quasi-static</p>	
<p>Kirigami modified honeycomb structure [89] aluminium 1060 $\rho_v = 2.3\%$ Quasi-static</p>	
<p>Miura-ori foldcore [80] aluminium 1100-0 $\rho_v = 3\%$ Quasi-static</p>	
<p>Curved-crease tessellation-two foldcore [80] aluminium 1100-0 $\rho_v = 3.2\%$ Quasi-static</p>	
<p>Kirigami corrugated structure [183] aluminium 1060 $\rho_v = 2.5\%$ $V = 0.5 \text{ m/s}$</p>	

Table 3-6 (Continued)

Crushing speed and material properties	Illustration
<p>Primitive structure [184] aluminium alloy $\rho_v = 2\%, 5\%$ Quasi-static</p>	
<p>Kirigami modified triangular structure [185] aluminium 1060 $\rho_v = 1.3\%$ Quasi-static</p>	
<p>Trapezoidal corrugated core [186] aluminium 1050 H14 $\rho_v = 4.55\%$ Quasi-static</p>	
<p>Trapezoidal corrugated sliced core [186] aluminium 1050 H14 $\rho_v = 6.45\%$ Quasi-static</p>	
<p>Horseshoe-shaped square honeycomb [119] aluminium AA3003 H18 $\rho_v = 4.5\%$ $V = 1 \text{ m/s}$</p>	
<p>Aluminium foam [5] Closed-cell aluminium foam $\rho_v = 4.2\%$ Quasi-static</p>	
<p>Sinusoidal square honeycomb [187] aluminium AA6061O $\rho_v = 2.7\%$ $V = 1 \text{ m/s}$</p>	

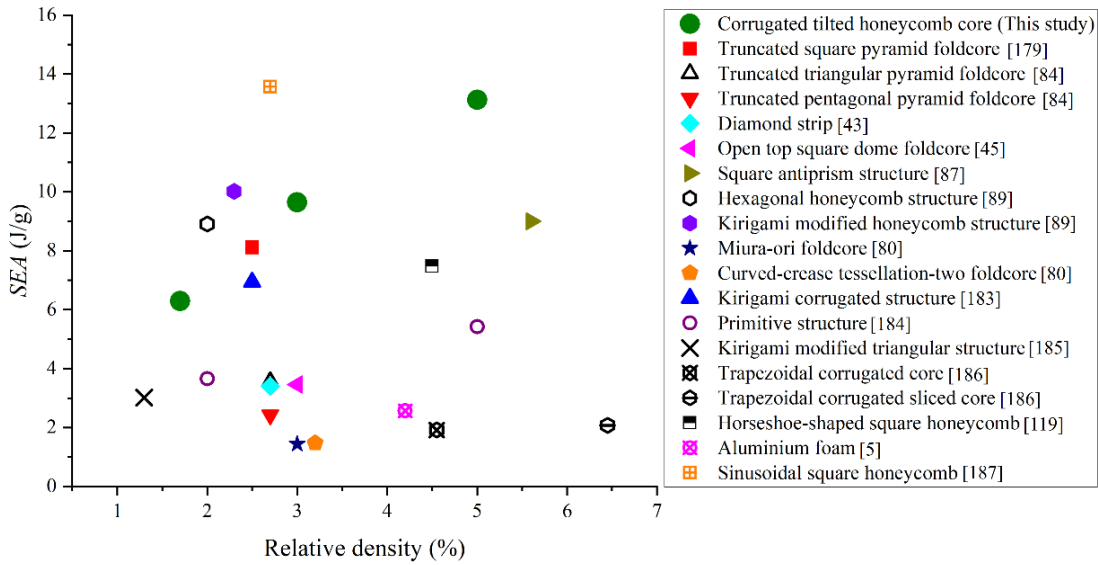


Figure 3-18. Comparison of *SEA* of similar cellular structures.

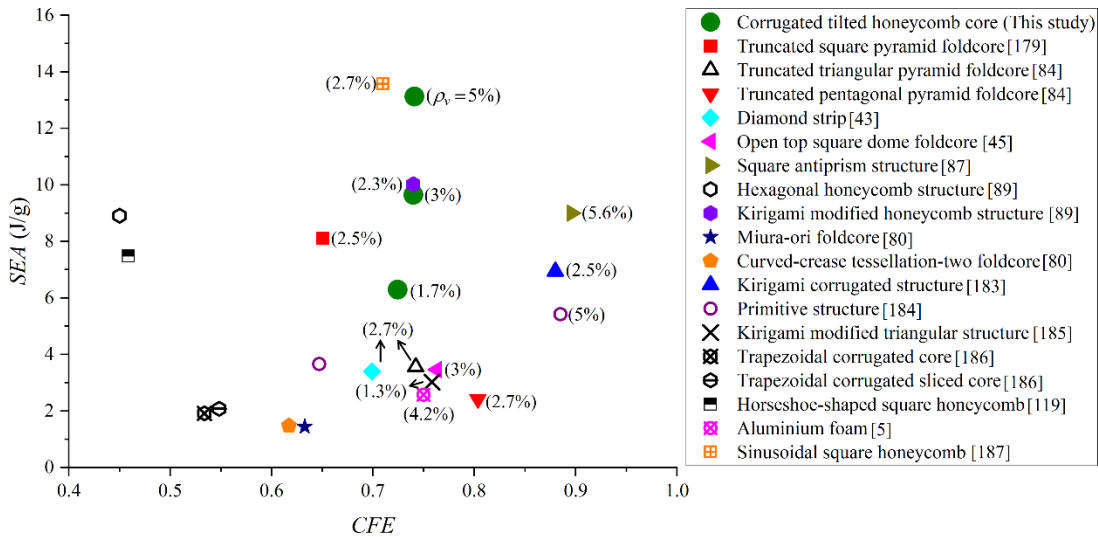


Figure 3-19. Comparison of *SEA* versus *CFE* of similar cellular structures (the value in the parentheses is the relative density of the core).

Another important factor for the energy-absorbing structure is the crushing force efficiency (*CFE*) which indicates the fluctuation between the average crushing force and the highest peak crushing force during the whole crushing process of the core. As shown in Figure 3-19, most of the cores with higher *CFE* tend to have lower *SEA* than the proposed CTH core of similar relative density. It is due to the ease of bending and deformation of those cores, which reduces not only the initial buckling force but also the crushing force in the plateau stage. It should be pointed out that the kirigami modified honeycomb [89] and sinusoidal square honeycomb [187] have smaller relative density but higher *SEA* than CTH core. However, CTH core seems to have

higher *CFE* than those cores under similar crushing speeds, while the *CFE* of the kirigami modified honeycomb decreases as the crushing speed increases [48,89]. Furthermore, the *CFE* of the CTH core is still high under higher crushing speed (i.e., 15 m/s), showing its loading rate insensitivity of the peak crushing force as well as its uniform crushing efficiency. Overall, the proposed CTH core outperforms most of the cores compared in this chapter by having higher *SEA* and *CFE* as compared to other cores of similar relative density owing to its structural form, which helps eliminate the initial buckling force without affecting the overall crushing force as well as *SEA* of the core.

3.6 Summary

In this chapter, a new corrugated tilted honeycomb (CTH) core is proposed by mimicking the corrugated tapered shape found in plant stems, and its crushing performance is investigated by using a finite element software LS-DYNA. This chapter aims to propose a simple yet effective energy-absorbing core with a high energy-absorbing capacity and high crushing force efficiency. The crushing responses and energy absorption performance of the proposed CTH cores are compared with the conventional square honeycomb cores under various crushing speeds. The effects of the tilted angle of the corrugated plate and the relative density of the CTH cores are also investigated and compared with the conventional square honeycomb core and aluminium foam of the same mass. The main findings are summarised as follows.

- The high initial peak force of the conventional honeycomb core can be eliminated without sacrificing the plateau crushing force by implementing the corrugated tilted design to the cell walls. The peak crushing force of the proposed CTH cores is delayed during crushing.
- The proposed CTH cores have a higher specific energy absorption capacity (*SEA*) and a higher crushing force efficiency (*CFE*) than the conventional square and tilted square honeycomb cores of the same relative density under various crushing speeds, i.e., 0.5 m/s to 15 m/s. The proposed CTH core has higher *SEA* and *CFE* than most of the existing structural forms of cores with similar relative density. It has a significantly improved *SEA*, which is four times higher than aluminium foam, up to 142% higher than the primitive structure,

and 46% higher than the square antiprism structure, showing a better performing core for the energy-absorbing sandwich structures.

- The CTH core with two corrugations (C2) outperforms the conventional square honeycomb core and other corrugated tilted honeycomb cores by having a higher *CFE* and a higher *SEA* due to its more numbers of corrugations with large corrugated angle. Its loading rate insensitivity with respect to the peak crushing force and crushing force efficiency is also demonstrated.
- The tilted angle of the corrugated plate significantly influences the *PCF* of the CTH core since it affects the overall stiffness of the core. Increasing the tilted angle leads to a significant increase in *PCF* but only a slight increase in *MCF*, resulting in a decrease in the *CFE* of the CTH core.
- Increasing the wall thickness/relative density of the core leads to an increase in the crushing resistance and energy absorption capacity. The CTH core outperforms the conventional square and tilted square honeycomb cores of the same relative density by having a lower *PCF*, higher *MCF*, *CFE* and *SEA*.

Chapter 4. Impact performance of sandwich cladding with CTH core

The related work in this chapter was published in Structures:

Lam L, Chen W, Hao H, Huang Z, Li Z. Impact performance of sandwich cladding with corrugated tilted honeycomb core. Structures 2024;61:106072.

<https://doi.org/10.1016/j.istruc.2024.106072>

4.1 Introduction

As demonstrated in Chapter 3, the CTH core inspired by plant stems demonstrates excellent energy-absorbing performance with a low initial peak and high crushing resistances [188]. In this chapter, its impact mitigation performance as a sacrificial core of the sandwich cladding is investigated using a pendulum impact testing facility. Large-scale sandwich claddings are fabricated and tested. The impact mitigation performances of CTH cladding are compared with those of conventional square honeycomb and corrugated square honeycomb claddings of the same mass. Four types of cladding with different cores are investigated, including square honeycomb (SH), corrugated square honeycomb (CSH), and two types of corrugated tilted honeycomb (CTH). The impact mitigation performances are evaluated by comparing the impact force and the transmitted forces recorded at various locations, as well as the deformation mode among each cladding. The impact force is recorded by the load cell attached to the impactor head, while the transmitted forces at various locations are recorded by a custom-made load cell system placed at the back of the sacrificial cladding. Various impact scenarios with different impact masses and velocities are considered to investigate the effect of impact velocity and impact mass-velocity combinations on the impact performances of each cladding.

4.2 Specimen configurations and preparation

4.2.1 Core configurations

Four core configurations of the sandwich cladding are investigated, including one square honeycomb (SH) core, one corrugated square honeycomb (CSH) core and two

proposed corrugated tilted honeycomb (CTH) cores, as shown in Figure 4-1. The SH core has a vertical sidewall (T90) with no corrugation (C0) on each unit-cell side, thereby designated as C0-T90. The CSH core, which has one corrugation on each unit-cell side, is denoted as C1-T90. The CTH cores with one and two corrugations on each unit-cell side have the same tilted angle of 80 degrees (T80) and are denoted as C1-T80 and C2-T80, respectively. This tilted corrugated sidewall was chosen since a high energy absorption capacity with a low initial peak crushing force was achieved for the CTH core as reported in Chapter 3. All cores consist of a 5×5 unit-cell with an 80 mm cell size along with a 15 mm extension at both ends to accommodate the slots and have the same height of 40 mm, resulting in an overall core dimension of 430×430×40 mm, as shown in Figure 4-1(a) and (c). Each corrugation of the same dimension is introduced to the centre of each unit cell of the CSH and CTH cores, as marked out in Figure 4-1(b) and (d). The CTH cores (i.e., C1-T80 and C2-T80) are designed by tilting each nearby corrugated sidewall toward each other, as illustrated in Figure 4-1(c) and (d).

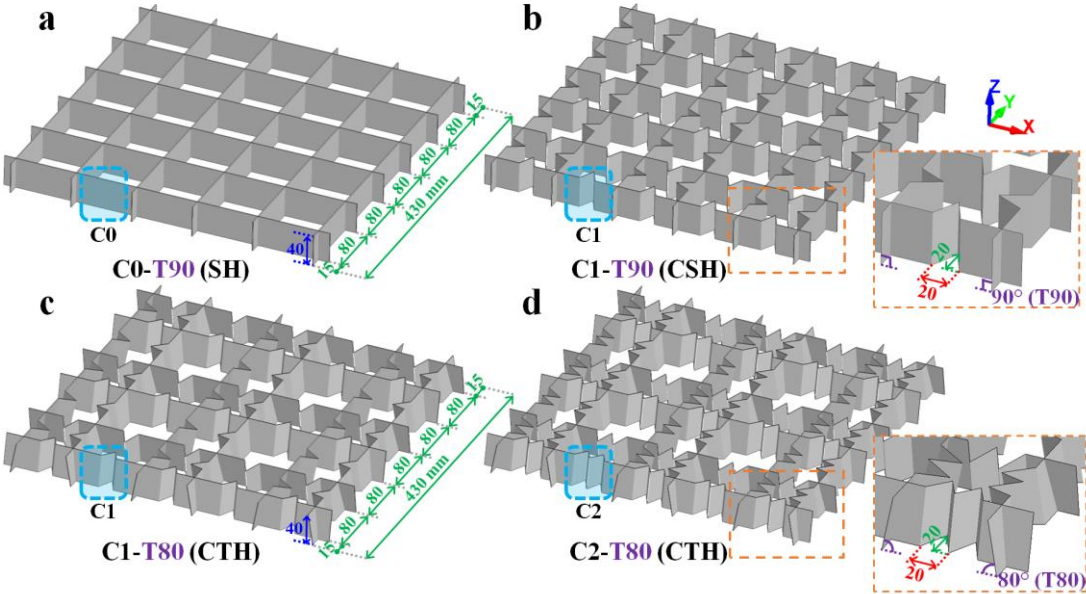


Figure 4-1. Core details of (a) C0-T90, (b) C1-T90, (c) C1-T80, and (d) C2-T80.

4.2.2 Cladding preparation and material property

A total of 11 specimens were prepared. Each cladding specimen consists of an internal core sandwiched between two external plates, as illustrated in Figure 4-2. The core was fabricated by assembling each aluminium sidewall using slotting and bonding

techniques. Each core sidewall was slotted up to its mid-width at the interconnecting locations, and the corrugations were fabricated using pressing moulds, as shown in Figure 4-2(a). The sandwich cladding specimen was then fabricated by bonding the assembled core to the front and rear external plates, each with a thickness of 2 mm, as illustrated in Figure 4-2(b). For the corrugated tilted honeycomb (CTH) core, each core sidewall was trimmed at the bottom edge of each corrugation, as indicated in Figure 4-2(a), allowing a flat bottom surface for bonding with the rear external plate. Therefore, by tilting the corrugated sidewalls, the corrugated gaps between the core and the front external plate of the CTH claddings were generated, as shown in Figure 4-2(c) and (d), thereby reducing the buckling resistance and facilitating the initial bending of the core during impact [188].

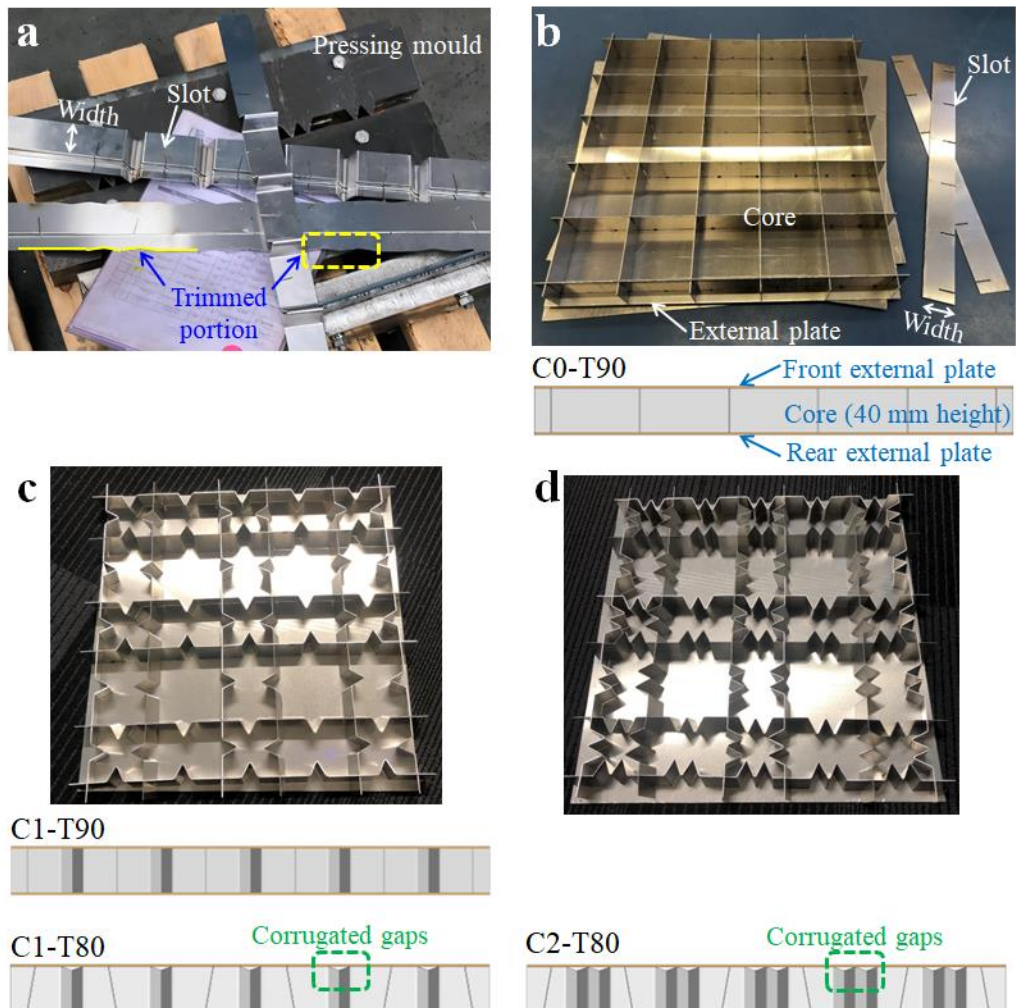


Figure 4-2. (a) Pressing mould and corrugated sidewall preparation, (b) assembling of core and side view of C0 configuration, (c) C1 configurations, and (d) C2 configuration.

The core of the cladding specimen was made of aluminium 5005 sheet with a density of 2680 kg/m³. The aluminium sheet with a thickness, t , of 1.2 mm was used to fabricate the core of C0-T90, resulting in a volumetric density of the core (ρ_v) of 3.3% and a mass of around 0.66 kg. For a fair comparison, the masses of other cores were kept the same by using different thicknesses of the aluminium sheets. However, a slightly thinner thickness than the calculated one was used based on the availability of the aluminium sheet in the market. A 0.9 mm sheet was used for the core of C1-T90 and C1-T80, thus having a similar volumetric density of the core of around 3.2% and a mass of around 0.64 kg. The core of C2-T80 was made of a 0.7 mm sheet, thus having a volumetric density of the core of around 3.0% and a mass of around 0.60 kg. Each core was bonded with front and rear external plates made of the same aluminium 5005. Each external plate had a dimension of 430×430×2 mm and a weight of around 1 kg. The wall thickness and mass of each component of all claddings are summarised in Table 4-1. The external plates and internal core were bonded at the interconnecting interfaces using the 3MTM Impact Resistant Structural Adhesive 07333, which has an ultimate tensile strength of 35 MPa as reported by the manufacturer. The coupon tensile test of the aluminium 5005 sheet was carried out according to the standard ASTM E8/8M-13 standard [189] under a quasi-static loading condition. It has a yield strength of 151 MPa and a Young's modulus of 69 GPa.

Table 4-1. Wall thickness and mass of each component of claddings.

Cladding	Front external plate		Core			Rear external plate		Total mass (kg)
	t (mm)	Mass (kg)	t (mm)	Mass (kg)	ρ_v (%)	t (mm)	Mass (kg)	
C0-T90 (SH)	2	1	1.2	0.66	3.3	2	1	2.66
C1-T90 (CSH)	2	1	0.9	0.64	3.2	2	1	2.64
C1-T80 (CTH)	2	1	0.9	0.64	3.2	2	1	2.64
C2-T80 (CTH)	2	1	0.7	0.60	3.0	2	1	2.60

4.3 Experimental program

4.3.1 Impact test setup and instrumentation

The setup of the pendulum impact test is shown in Figure 4-3(a). The pendulum consists of the pendulum arm and the impact steel frame, where steel blocks can be

added to increase the total impact mass. The pendulum arm has a mass of 42 kg. The impact steel frame has a total mass of 76.3 kg, which includes the steel frame, load cell, square impact head, and installation accessories. The pendulum has a total length of 2.8 m from the rotating point to the centre of the impact steel frame.

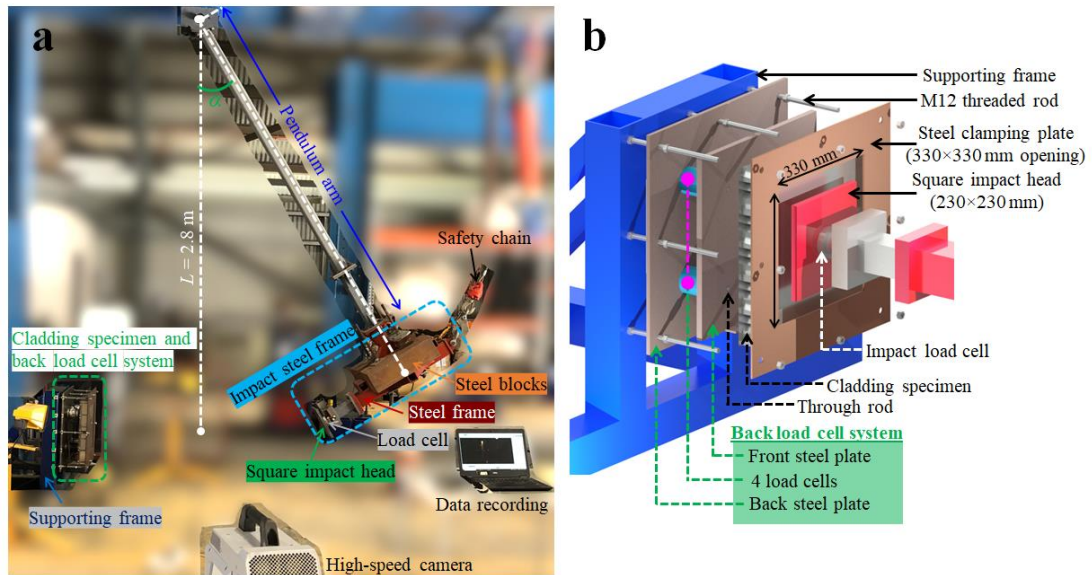


Figure 4-3. (a) Setup of pendulum impact test and (b) schematic diagram showing the fixation of the back load cell system and the tested cladding specimen.

Each cladding specimen was impacted by a 16 mm thick flat frontal impact head with a dimension of 230×230 mm, as shown in Figure 4-3(b). One load cell was attached to the impact head to record the impact force time history. The cladding specimen was placed vertically and clamped by a steel clamping plate (with a 330×330 mm opening) onto a rigid supporting frame using 8 M12 threaded rods, as illustrated in Figure 4-3(b). The cladding specimen was simply placed in front of a custom-made back load cell system, which was used to measure the transmitted force to the protected structure. This back load cell system consists of four load cells sandwiched between 10 mm thick front and back steel plates, which are connected by four rods passing through the load cells. It is then fixed to the supporting frame through its back steel plate using the existing 8 M12 threaded rods, as shown in Figure 4-3(b).

The load cell locations of the back load cell system are illustrated in Figure 4-4(a). The four load cells are symmetrically placed one and a half units away from the centre along the diagonal lines of the specimen. The centre of each unit cell is located beneath the inner corner of the edged unit cell, which is positioned 95 mm away from each side

of the cladding specimen. The two load cells located at the top left and top right positions are denoted as TL (1) and TR (2), respectively. The other two load cells, located at the bottom left and bottom right, are denoted as BL (3) and BR (4), respectively. The square impact head is set to crash horizontally at the centre of the cladding specimen along the out-of-plane direction, as illustrated in Figure 4-4.

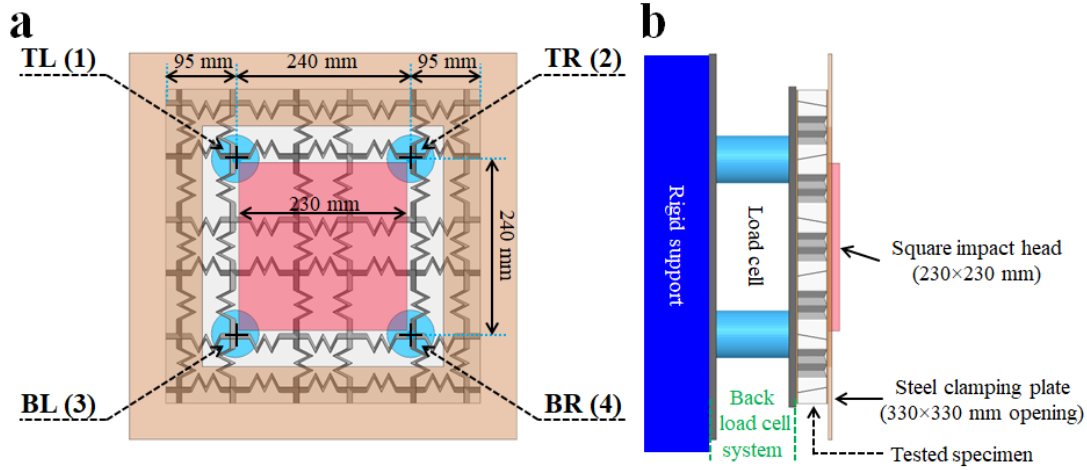


Figure 4-4. (a) Front view and (b) side view showing the load cell locations of the back load cell system and the impacting area.

In this chapter, different impact scenarios were performed using various combinations of impact mass and impact velocity. Different impact masses were achieved by using steel blocks as additional weights to the impact steel frame. Hence, the total impact mass comprises the mass of the pendulum arm ($m_{arm} = 42$ kg), the mass of the impact steel frame ($m_{frame} = 76.3$ kg), and the mass of the added steel block (m_{add}). The impact steel frame and the added steel block are considered as a concentrated mass impacting the centre of the cladding specimen at the impact velocity, V . However, the tangential velocities of the pendulum arm are not uniform along its length but rather linearly increase from zero at the rotating point to the impacting velocity, V , at the bottom end [11]. The mass of the pendulum arm is assumed to be equally distributed along its length and travels at an average velocity of $\frac{V}{2}$. Therefore, the equivalent impact mass, M , can be calculated as

$$\frac{1}{2}MV^2 = \frac{1}{2}(m_{frame} + m_{add})V^2 + \frac{1}{2}m_{arm}\left(\frac{V}{2}\right)^2 \quad (4-1)$$

$$M = m_{frame} + m_{add} + \frac{m_{arm}}{4} \quad (4-2)$$

The impact velocity (V) is the velocity at which the impact head is about to impact the specimen, coinciding with the moment the pendulum reaches its vertical position. Various impact velocities can be achieved by raising the pendulum to different release angles α . By using the principle of energy conservation (friction is neglected), the impact velocity can be calculated as

$$V = \sqrt{2gL(1 - \cos \alpha)} \quad (4-3)$$

where g is the gravity, and L is the pendulum length.

4.3.2 Impact scenarios

A total of 11 specimens and their impact scenarios are summarised in Table 4-2. Two add-on steel blocks with a total weight of 300 kg and 500 kg were used, resulting in two equivalent impact masses of 387 kg and 587 kg, calculated using Equation (4-2). The pendulum was raised to the release angles of 40° and 50°, resulting in impact velocities of 3.6 m/s and 4.43 m/s, respectively. In this chapter, the impact tests were divided into three impact scenarios, i.e., S1, S2, and S3, based on the combination of the equivalent impact mass (M) and impact velocity (V). Each scenario is identified by its corresponding equivalent impact mass and impact velocity. For example, S1 (M387-V4.43) represents the impact scenario 1 with the equivalent impact mass of 387 kg and impact velocity of 4.43 m/s. To identify each tested specimen, cladding type and impact scenario are used for notation. For example, C2-T80-S1 represents the cladding C2-T80 which is impacted under impact scenario S1.

In scenario S1 (M387-V4.43), four claddings with different cores were tested to investigate and compare the impact performances of the claddings. In scenario S2 (M387-V3.6), three claddings (C0-T90, C1-T80, and C2-T80) were impacted at a different velocity of 3.6 m/s (same impact mass as S1) to investigate the effect of impact velocity as well as impact energy on the performance of each cladding. In scenario S3 (M587-V3.6), four types of cladding were tested under approximately the same impact energy as S1 (around 3800 J) but were impacted by a higher equivalent impact mass of 587 kg and a lower impact velocity of 3.6 m/s, thereby investigating

the effect of impact mass-velocity combination on the impact performances of the claddings.

Table 4-2. Summary of impact scenarios.

Impact scenario	Specimen notation	Cladding type	Equivalent impact mass M (kg)	Impact velocity V (m/s)	Release angle α	Momentum (kg.m/s)	Impact Energy (J)
S1 (M387-V4.43)	C0-T90-S1	C0-T90	387	4.43	50°	1714	3797
	C1-T90-S1	C1-T90	387	4.43	50°	1714	3797
	C1-T80-S1	C1-T80	387	4.43	50°	1714	3797
	C2-T80-S1	C2-T80	387	4.43	50°	1714	3797
S2 (M387-V3.6)	C0-T90-S2	C0-T90	387	3.6	40°	1393	2508
	C1-T80-S2	C1-T80	387	3.6	40°	1393	2508
	C2-T80-S2	C2-T80	387	3.6	40°	1393	2508
S3 (M587-V3.6)	C0-T90-S3	C0-T90	587	3.6	40°	2113	3804
	C1-T90-S3	C1-T90	587	3.6	40°	2113	3804
	C1-T80-S3	C1-T80	587	3.6	40°	2113	3804
	C2-T80-S3	C2-T80	587	3.6	40°	2113	3804

4.4 Results and discussions

4.4.1 Impact performances of claddings with different cores

In this section, the impact performances of all four types of cladding are assessed and compared in terms of the impact force and transmitted force, as well as the deformation mode of the internal core. Four cladding specimens were tested under the same scenario S1, including the square honeycomb SH cladding (C0-T90), the corrugated square honeycomb CSH cladding (C1-T90), and the proposed corrugated tilted honeycomb CTH claddings (C1-T80, C2-T80). The impact scenario S1 (M387-V4.43) indicates an equivalent impact mass of 387 kg and an impact velocity of 4.43 m/s.

4.4.1.1 Impact force

The impact force time histories of all four claddings with different cores tested under S1 (M387-V4.43) are plotted in Figure 4-5. The impact force profiles show two peak

impact forces due to the impact interactions between the impactor and the cladding. At the initial stage, the impact head struck the front external plate of the cladding, and the impact force sharply increased and reached its first peak. After that, the impactor slightly slowed down while the cladding oscillated, causing an immediate separation between the impact head and the front external plate, which resulted in a decrease or unloading of the impact force [190]. However, the large inertia of the heavy impactor made it difficult to completely bounce off or separate from the cladding, leading to an immediate second contact between the impact head and the front external plate of the tested cladding [191]. Therefore, the impactor caught up with the front external plate after oscillation and impacted the cladding for a second time, thereby resulting in a second peak of the impact force. A similar two-peak impact force profile caused by a double-strike event was also observed for a flat frontal impact of soft material, as well as sandwich cladding with rigid back support [5,190,192].

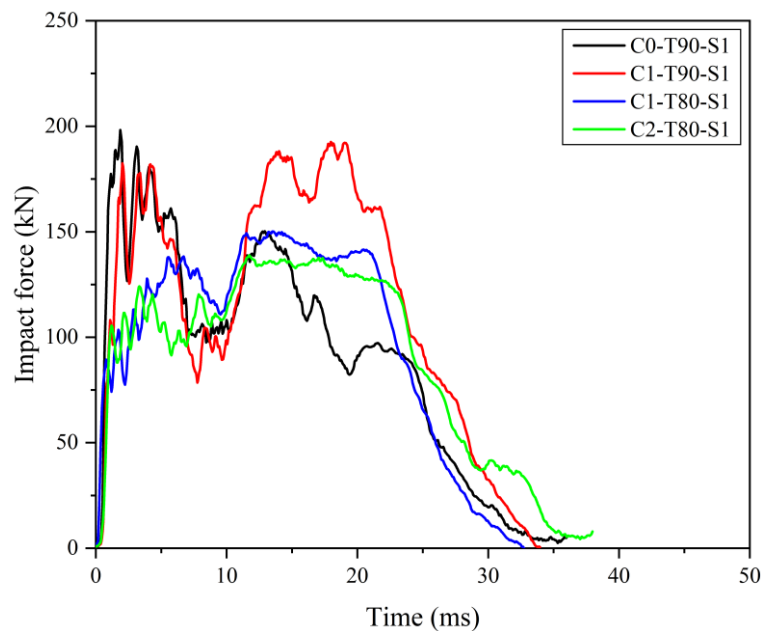


Figure 4-5. Impact force time histories of the four claddings under S1 (M387-V4.43).

As shown in Figure 4-5, the C0-T90 and C1-T90 claddings reached their first peaks immediately after the initial contact between the impactor and the front external plate. The first peak impact force is associated with the local contact stiffness of the cladding at the impacting location. Therefore, C0-T90 has the highest first peak impact force of 198.2 kN, followed by C1-T90, which has a slightly lower first peak of 182.4 kN. These high peaks are attributed to the thick vertical sidewalls of core C0-T90 and the vertical corrugation sidewalls of core C1-T90, which result in a high initial contact

stiffness at the impacting location. In contrast, the proposed C1-T80 has a significantly lower initial peak force, and its first peak is reached at a later stage compared to those of C0-T90 and C1-T90. The first peak impact force of C1-T80 cladding is around 138.3 kN, which is 30% and 24% lower than that of C0-T90 and C1-T90, respectively. This reduction in peak force is attributed to the lower contact stiffness in the impacting area, which occurs due to the presence of corrugated gaps between the front external plate and the internal core, as circled in Figure 4-2(c), as well as the tilted sidewalls of the core. C2-T80 cladding has the lowest first peak impact force of 124.1 kN, which is 37%, 32%, and 10% lower than that of C0-T90, C1-T90, and C1-T80, respectively. This significant reduction is attributed to the presence of more corrugated gaps and thinner tilted core sidewalls of C2-T80, resulting in a lower initial contact stiffness and a more easily deformable core. After the first peak, the second peak of the impact force occurs. Among all four claddings, C1-T90 cladding has the highest second peak. This is because debonding occurs between the front external plate and core during the initial impact. However, the integrity of the core is still maintained owing to the vertical corrugations, which stiffen the sidewalls of the core, as shown in Figure 4-6(b). Therefore, a high second peak occurs once the impactor restrikes the cladding. The second peak impact force of C0-T90 cladding is significantly lower than that of C1-T90. As observed in Figure 4-6, the impactor seems to be slightly twisted and rotated clockwise during its oscillation with respect to the front plate, causing asymmetric deformation to the left, as well as individual buckling of the core sidewalls of C0-T90, as circled in Figure 4-6(a). Furthermore, the sharp corners of the impactor head and the vertical core sidewalls also caused the rupture of the front external plate due to high-stress concentration. Therefore, the contact stiffness at the impacting area between the impactor and C0-T90 is significantly reduced, resulting in a low second peak impact force [193]. For the corrugated tilted honeycomb (CTH) cladding, the peak during the second impact is not obvious and is quite similar in value to its corresponding first peak. The second peak of C1-T80 and C2-T80 is around 150.1 kN and 138.8 kN, respectively, which is around 9% and 12% higher than their corresponding first peak. This increase in the crushing force during the second impact is due to the crushing of tilted corrugated core sidewalls, which occurs after the corrugated gaps are closed by the impactor. As shown in Figure 4-6(c) and (d), the front external plate and internal core of the CTH cladding were significantly deformed, particularly those of C2-T80, which experienced the largest impact depth of around 20

mm compared to C1-T90 and C0-T90 with impact depths of around 2 mm and 12 mm, respectively, demonstrating its uniform deformation and high energy absorption during the impact.

As shown in Figure 4-5, C2-T80 has the longest impact duration, lasting approximately 37 ms, followed by C0-T90 with a duration of 35 ms. C1-T80 and C1-T90 have impact durations of around 33 ms and 34 ms, respectively. The longer impact duration of C2-T80 is attributed to its less stiff and easy-to-deform core, which also leads to greater deformation and a more stable impact crushing force throughout the entire impact duration. However, for C0-T90, its long impact duration is due to the low impact force during the second impact, resulting from the asymmetric deformation discussed previously. C1-T90 and C1-T80 have shorter impact duration because of their relatively stiff cores, which can be attributed to the thick corrugated core sidewalls as well as fewer corrugated gaps of C1-T80. Under the same impact scenario S1, C0-T90, C1-T80, and C2-T80 are subjected to similar impacting impulses, which are 3215 N.s, 3257 N.s, and 3345 N.s, respectively. However, C1-T90 is subjected to a higher impacting impulse of around 3932 N.s. This is because the strength and integrity of its core are still maintained after the first impact, resulting in a high impact force during the second impact.

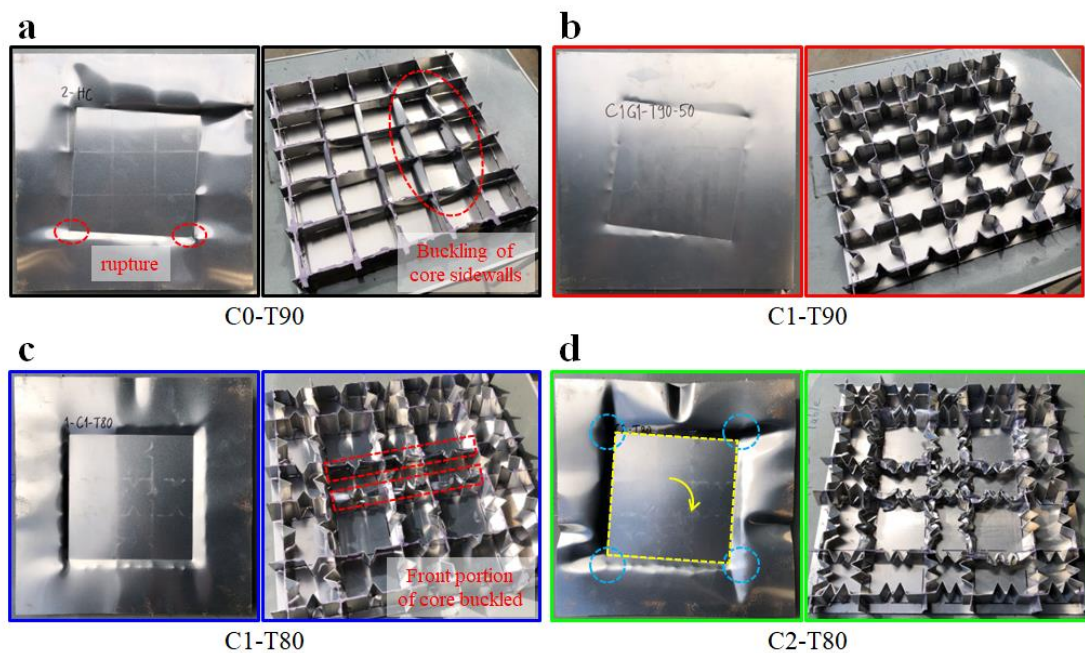


Figure 4-6. Deformation of the front external plate and core of claddings (a) C0-T90, (b) C1-T90, (c) C1-T80, and (d) C2-T80 under S1 (M387-V4.43).

4.4.1.2 Transmitted force

The overall transmitted force time histories of the four claddings are plotted in Figure 4-7(a). This overall transmitted force is obtained by summing the transmitted forces recorded by the four load cells of the back load cell system in the time domain [5]. The peak of the overall transmitted force of C1-T90 cladding is around 156.7 kN, which is the highest among all claddings. This is caused by its stiff core with high buckling resistance, which results in a high transmitted force to the back structure. The peak of the overall transmitted force of C0-T90 is around 118.5 kN, which is quite similar to 121.7 kN of C1-T80. The lowest overall transmitted force is observed for the C2-T80 cladding with a peak of 96.8 kN, which is 18%, 20%, and 38% lower than that of C0-T90, C1-T80, and C1-T90, respectively. Furthermore, its overall transmitted force response is more uniform and lower throughout the entire impact duration compared to the double-peak transmitted force responses of the other claddings. This is due to its low initial contact stiffness and easy folding of the internal core under the impacting area. The peak transmitted forces at each load cell location of the four claddings are also compared and summarised in Figure 4-7(b) and Table 4-3, respectively. Even though all four load cells are symmetrically placed at each corner, both to the centre of the cladding and the impact location, the peak transmitted forces at each location are slightly different. During the impact, the front external plate and the internal core of the cladding deformed and debonded from each other, leading to a slight clockwise twist and rotation of the front impact head, as illustrated in Figure 4-6(d). This results in different peak forces between each corner of the same cladding.

Overall, under the same impact scenario, the peak transmitted forces of the C2-T80 cladding at all four locations are the lowest compared to those of the other three claddings. Therefore, the proposed corrugated tilted honeycomb (CTH) design exhibits excellent impact performance, with a stable crushing force without obviously high peaks, lower transmitted force, larger deformation, and an easy-folding core compared to the SH and CSH claddings of similar mass. The C2-T80 cladding outperforms the C1-T80 due to its higher number of corrugations and larger corrugated gap. However, further increasing the number of corrugations, such as C3 or C4, associates with a difficult fabrication when using the pressing technique introduced herein.

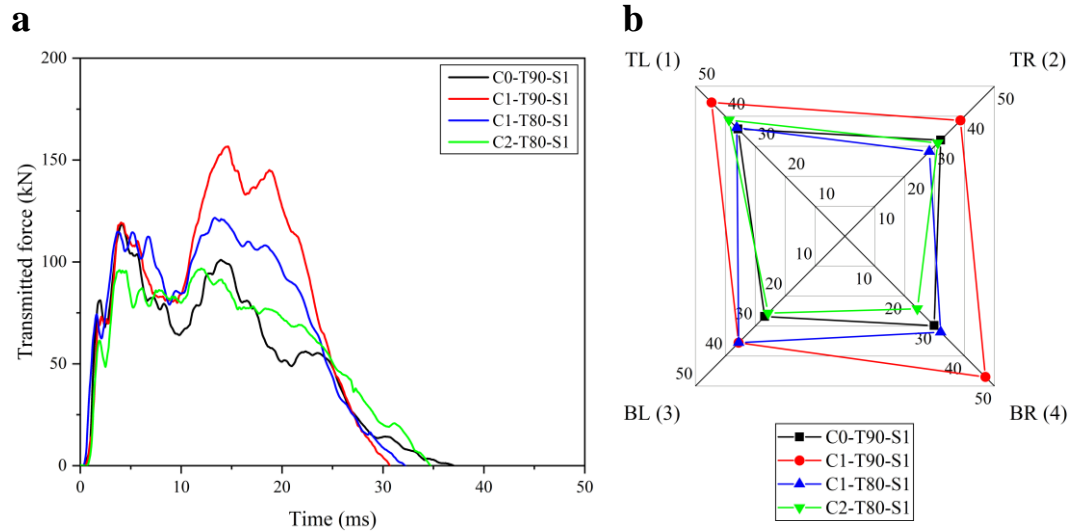


Figure 4-7. (a) Overall transmitted force time histories and (b) comparisons of peak transmitted forces at each load cell location of the four claddings under S1 (M387-V4.43).

Table 4-3. Peak impact force and peak transmitted forces at each load cell location of the four claddings under S1.

Cladding	Impact scenario	Peak impact force (kN)	Peak transmitted force at different locations (kN)			
			TL (1)	TR (2)	BL (3)	BR (4)
C0-T90	S1 (M387-V4.43)	198.2	35.7	32.0	26.8	29.8
C1-T90		192.6	44.6	38.6	35.6	47.0
C1-T80		150.1	36.2	28.2	35.5	32.0
C2-T80		138.8	38.7	31.1	25.7	24.2

Note: Load cell locations (TL, TR, BL, BR) are shown in Figure 4-4.

4.4.2 Effect of impact velocity

In this section, the impact performances of three claddings (C0-T90, C1-T80, C2-T80) are investigated under different impact-velocity scenarios, i.e., S1 and S2. Each sandwich cladding is impacted by different velocities (3.6 m/s and 4.43 m/s) from an impactor with an equivalent mass of 387 kg. Scenario S1, with a higher impact velocity of 4.43 m/s, generates greater impacting energy and impacting impulse compared to scenario S2, which has a lower impact velocity of 3.6 m/s. The impact force time histories and the peak transmitted forces at different locations of each cladding under both scenarios are plotted and compared in Figure 4-8 and Figure 4-10, respectively. The key parameters are summarised in Table 4-4.

4.4.2.1 Impact force

Two peaks of the impact force profile are observed for all claddings under both impact scenarios, as plotted in Figure 4-8. The peak and overall impact force increase for all types of cladding when the impact velocity increases from 3.6 m/s to 4.43 m/s. This is because the impact force is influenced by the impact energy and the contact stiffness [191]. A higher impact velocity of the same impactor leads to a larger impact energy and deeper indentation on the tested specimen [194], which results in a larger deforming area and thus increases the contact stiffness [191]. Similar impact responses with the increase in impact velocity are also observed for various sandwich structures under impact loads [11,190].

As the impact velocity increases from 3.6 m/s to 4.43 m/s, the impact force profile of the CTH cladding increases and becomes more stable without a significant drop in the impact force right after the first peak, as shown in Figure 4-8(b) and (c). This is due to the faster velocity and larger inertia of the impactor, resulting in a faster catch-up between the impactor and the front external plate. Under both impact-velocity scenarios, besides the drop in the impact force, the impact crushing force of the CTH cladding gradually increases and reaches its highest peak at a later stage during the second impact pulse. Furthermore, the difference between the first and second peaks is low, especially for C2-T80, due to its larger corrugated gaps as well as thinner and easy folding of core sidewalls [188]. The CTH core design led to a low initial contact stiffness and increased crushing resistance through the core thickness along the impact direction, owing to the corrugated gap and the tilted corrugation sidewalls, respectively.

However, the impact force profiles of the SH cladding under both impact-velocity scenarios are quite different, as shown in Figure 4-8(a). The impact crushing force of C0-T90 reaches its highest peak during the second impact pulse under scenario S2 with a 3.6 m/s impact velocity, while its highest peak is reached immediately after the initial impact of scenario S1 with a 4.43 m/s impact. This difference is due to the varying interactions between the impactor and the cladding that occurred during the tests. Besides the impact velocity, the peak impact force depends on the contact stiffness at the impact zone, which is associated with the flexural stiffness of the external plate as well as the stiffness and strength of the core [11]. As shown in Figure

4-9(a), a large indentation is observed at the bottom left of the impact zone of C0-T90 under an impact velocity of 3.6 m/s. This demonstrates a slightly inclined impact angle between the impactor and the front external plate of the cladding, resulting in a smaller contact area and lower contact stiffness, leading to a lower peak during the initial impact. After the first impact, the impactor comes into full contact with the almost undeformed core, causing a significant rise in the second peak impact force. Under a higher impact velocity of 4.43 m/s, the impact force significantly increases after the initial contact due to the high initial contact stiffness of the thick vertical core sidewalls and front external plate. However, the contact stiffness at the impacting area between the impactor and C0-T90 is significantly reduced during the second impact due to asymmetric deformation of the core sidewalls and rupture of the front external plate (Figure 4-6(a)), resulting in a low second peak impact force.

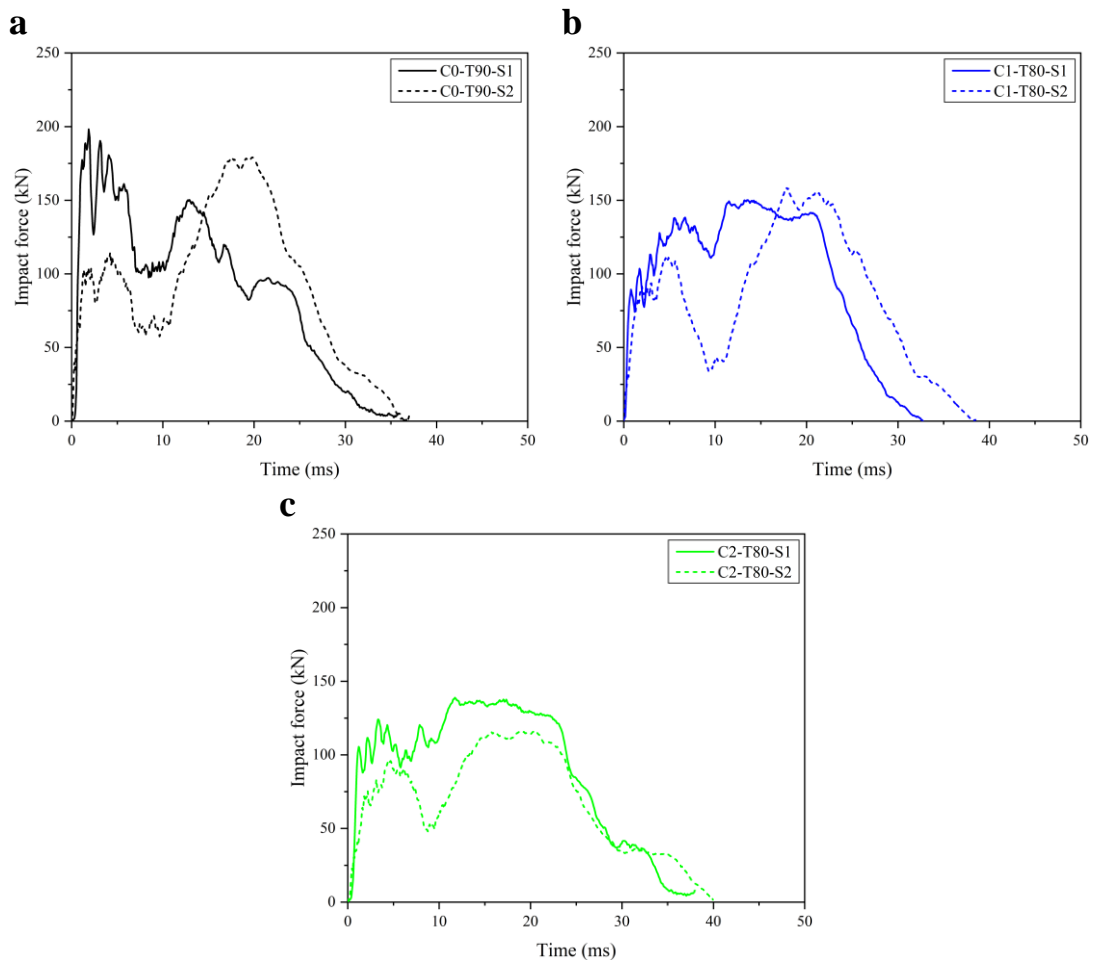


Figure 4-8. Impact force time histories of (a) C0-T90, (b) C1-T80, and (c) C2-T80 under S1 (M387-V4.43) and S2 (M387-V3.6) of the same impact mass.

Besides the different impact interactions during the impacts of C0-T90, the peak impact force of the square honeycomb cladding under each impact scenario is significantly high once the impactor fully contacts its stiff vertical core sidewalls, as compared to a more uniform and lower impact crushing of the corrugated tilted honeycomb (CTH) claddings, i.e., C1-T80 and C2-T80. Therefore, the CTH cladding outperforms the SH cladding by having a lower peak impact force under both impact velocities tested in this chapter. The C2-T80 Cladding is capable of absorbing the impact energy under a lower crushing force, with a peak of just 116 kN. This represents a 35% reduction compared to the 179.1 kN peak impact force of the conventional square honeycomb SH cladding (C0-T90) under the same impact velocity of 3.6 m/s. As the impact velocity increases to 4.43 m/s, the peak impact force of C2-T80 increases to around 138.8 kN, which is around 30% lower than the 198.2 kN peak impact force of C0-T90.

It is also observed that the impact duration is also affected by the impact velocity. As shown in Figure 4-8, the impact duration decreases as the impact velocity increases for C1-T80 cladding. This is because only the front portion of the core under the impacting area buckled, while the remaining core sidewalls remained intact and barely deformed, as circled in Figure 4-6(c) and Figure 4-9(b), demonstrating its stiff core during impacts. Therefore, this stiff core leads to an increase in the impact force and a decrease in the impact duration as the impact velocity increases [191]. However, C0-T90 and C2-T80 deformed significantly and reached plastic deformation as the impact velocity increased to 4.43 m/s, resulting in the influence of the impact velocity on the impact duration less prominent [191].

Under the same impact scenario, the front external plate and internal core of C2-T80 cladding deform significantly under both impact velocities, showcasing its high energy absorption. This is different from the other three cores of the same volumetric density, which are stiff and only deform slightly, as observed in Figure 4-6 and Figure 4-9. Moreover, the CTH core design outperforms many existing structural forms of the core, as well as aluminium foam with a similar volumetric density [188], demonstrating its potential for use as the sacrificial core of sandwich cladding, which can also be easily fabricated using slotting and pressing techniques.

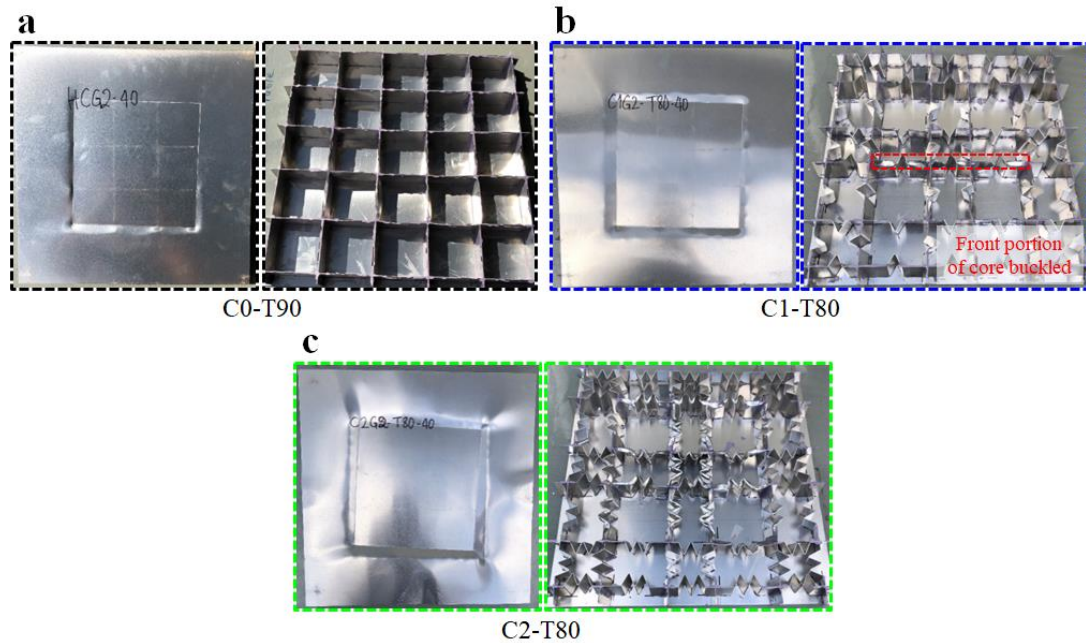


Figure 4-9. Deformation of the front external plate and core of claddings (a) C0-T90, (b) C1-T80, and (c) C2-T80 under S2 (M387-V3.6).

4.4.2.2 Transmitted force

The peak transmitted forces at each load cell location of C0-T90, C1-T80, and C2-T80 under the impact velocities of 3.6 m/s and 4.43 m/s are compared in Figure 4-10 and summarised in Table 4-4. It should be mentioned that the transmitted force at the top right (TR) was not recorded for C1-T80 under the 3.6 m/s impact velocity due to a malfunction of the load cell. It is observed that, for the same cladding, the peak transmitted forces at the top locations (TL and TR) increase as the impact velocity increases from 3.6 m/s to 4.43 m/s. However, the peak transmitted forces at the bottom locations (BL and BR) under a 4.43 m/s impact tend to be lower than those under a 3.6 m/s impact. This is because, in scenario S2 with a 3.6 m/s impact velocity, a slight clockwise twist and rotation of the impactor head occurred. As a result, the impact head impacted more on the bottom load cells, especially on the right, leading to a higher peak transmitted force at the BR location. Furthermore, as the impactor significantly crushed the cladding, i.e., C1-T80 and C2-T80, the impactor head became slightly inclined, causing a slightly upward impact due to the swing motion of the pendulum. This resulted in a slightly deeper indentation at the bottom of the impacting area, as observed in Figure 4-9. Therefore, the peak transmitted forces at the bottom locations tend to be larger than those at the top locations under a 3.6 m/s impact. Under a higher impact velocity of 4.43 m/s in scenario S1, the twist of the impact head

became more pronounced, resulting in a smaller impacting area on the bottom load cells and thus lower peak transmitted forces at the bottom locations.

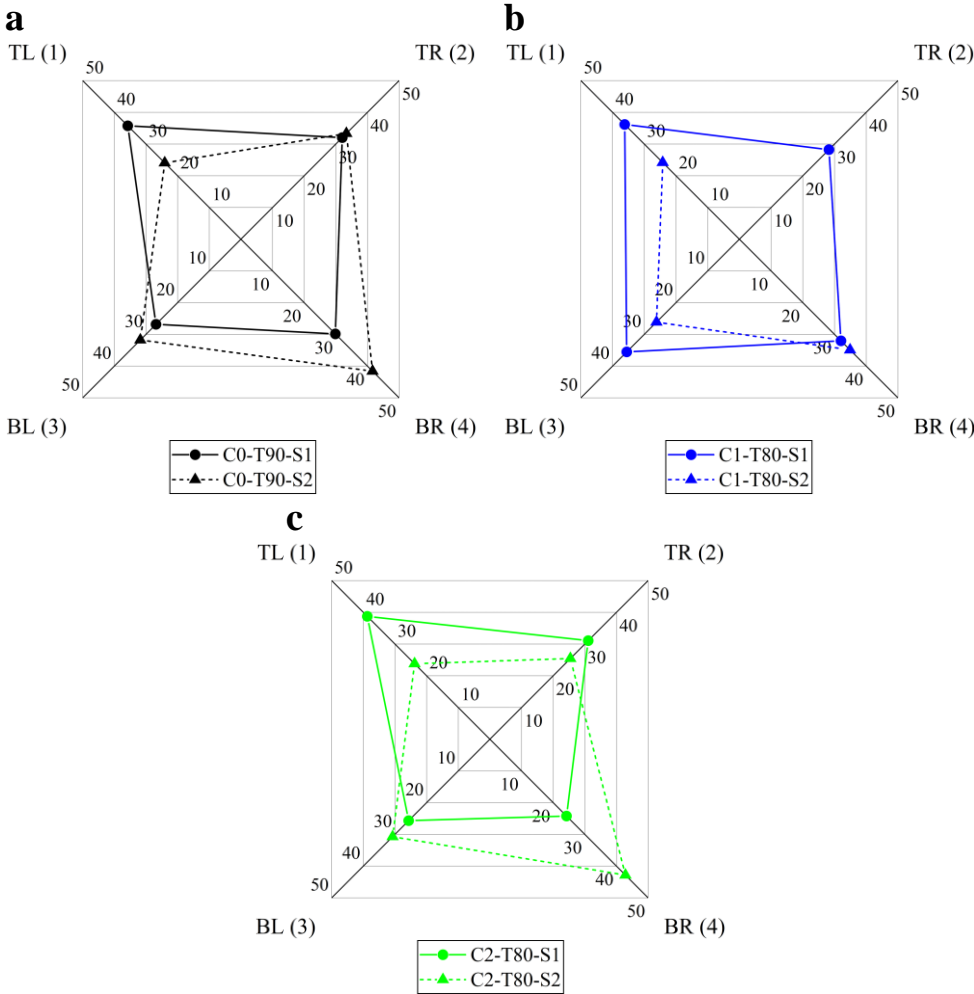


Figure 4-10. Comparisons of peak transmitted forces at each load cell location of (a) C0-T90, (b) C1-T80, and (c) C2-T80 under S1 (M387-V4.43) and S2 (M387-V3.6) of the same impact mass.

Under the same impact velocity (either 3.6 m/s or 4.43 m/s), the CTH cladding generates a lower peak transmitted force than the conventional square honeycomb cladding at the same location. Under a lower impact velocity of 3.6 m/s, the stiff core of C0-T90 with thick vertical sidewalls remains intact and only slightly deforms, resulting in a high transmitted force to the back structure. Unlike C0-T90, which remains stiff under the low-velocity impact of 3.6 m/s, C1-T80 and C2-T80 experience more deformation during the impact. However, by increasing the impact velocity to 4.43 m/s, C1-T80 tends to have a slightly higher peak transmitted force than C0-T90 at the same location, especially at the bottom location (BL and BR). This is caused by the stiff core with thick corrugated sidewalls of C1-T80. On the other hand, under the

4.43 m/s impact of C0-T90, the impactor head twisted, causing asymmetric and large deformation to the bottom left of the core, resulting in lower transmitted forces at the bottom location of C0-T90. In contrast, C2-T80 cladding generates the lowest transmitted force at most of the recorded locations under both impact velocities, compared to the other two claddings (C0-T90 and C1-T80), owing to its large deformation and easy folding core, which leads to high energy absorption and low transmitted force. Furthermore, its corrugated tilted sidewall design is similar to the load-self-cancelling square dome structure [29], which reduces the reaction force by cancelling it through the in-plane directions of the structure, thereby reducing the transmitted force.

Table 4-4. Peak impact force and peak transmitted forces at each load cell location of the claddings under S1 and S2.

Cladding	Impact scenario	Peak impact force (kN)	Peak transmitted force at different locations (kN)			
			TL (1)	TR (2)	BL (3)	BR (4)
C0-T90		179.1	24.0	33.3	31.7	41.6
C1-T80	S2 (M387-V3.6)	158.3	24.2	N/A	26.1	34.9
C2-T80		116.0	23.8	25.4	30.7	42.8
C0-T90		198.2	35.7	32.0	26.8	29.8
C1-T80	S1 (M387-V4.43)	150.1	36.2	28.2	35.5	32.0
C2-T80		138.8	38.7	31.1	25.7	24.2

4.4.3 Effect of combination of various impact masses and velocities

The effect of the combination of various impact masses and velocities on the impact performances of claddings is investigated in this section. Four claddings with different core types are tested under scenario S3, with an equivalent impact mass of 587 kg and an impact velocity of 3.6 m/s (M587-V3.6). Scenario S3 is selected to have a similar impact energy of around 3800 J as scenario S1, which has a lower equivalent impact mass of 387 kg but a higher impact velocity of 4.43 m/s (M387-V4.43). The impact force time histories and the peak transmitted forces at different locations of each cladding under both scenarios are plotted and compared in Figure 4-11 and Figure 4-12, respectively. The key parameters are summarised in Table 4-5.

4.4.3.1 Impact force

As shown in Figure 4-11, the impact force profiles of the same type of cladding are different when subjected to different combinations of impact mass and impact velocity, even though the initial impact energy is the same. For the same cladding, the impact force decreases while the impact duration increases with decreasing impact velocity, along with increasing impact mass of the identical impact energy, i.e., changing from scenario S1 to S3 and vice versa. This is because the impact force is more sensitive to the impact velocity than to the impact mass [193]. Therefore, the impact force of the cladding under scenario S3 (M587-V3.6) is lower than that under scenario S1 (M387-V4.43) due to its lower impact velocity. Furthermore, even though the initial kinetic energies of both scenarios S1 and S3 are similar, the impactor in scenario S3, with a heavier equivalent impact mass and lower impact velocity, has a higher initial momentum than that in scenario S1, which has a lighter equivalent impact mass and higher impact velocity. Since the impulse is directly proportional to the initial momentum of the impactor [193,195], the cladding under impact scenario S3 experiences a higher impulse compared to the same cladding under impact scenario S1. Under scenario S3, claddings C0-T90, C1-T90, C1-T80, and C2-T80 are subjected to the impulses of 3536 N.s, 4776 N.s, 3377 N.s, and 3473 N.s, respectively, which are derived from Figure 4-11. Under scenario S1, claddings C0-T90, C1-T90, C1-T80, and C2-T80 are subjected to lower impulses of 3215 N.s, 3932 N.s, 3257 N.s, and 3345 N.s, respectively. Therefore, a lower impact velocity of a heavier impactor in scenario S3 leads to a lower impact force and higher initial momentum of the impactor, as well as a higher impulse imposed on the cladding during the impact. This results in a longer impact duration compared to that in scenario S1.

Overall, similar to impact scenarios S1 and S2 discussed previously, the proposed CTH claddings, i.e., C1-T80 and C2-T80, outperform the SH and CSH claddings (C0-T90 and C1-T90) by having lower peak impact forces when crushed under the same impact scenario S3, as shown in Figure 4-11. The C1-T90 cladding has the highest peak impact force of 197.2 kN, followed by C0-T90 cladding with a peak of 140.7 kN, which is attributed to their stiff cores with vertical corrugated sidewalls in the case of C1-T90 and thick vertical sidewalls in the case of C0-T90. The C1-T80 cladding exhibits a lower peak force of 127.1 kN, which is around 10% and 36% lower than

that of C0-T90 and C1-T90, respectively. The C2-T80 demonstrates the lowest peak of 122.1 kN, which is around 13% and 38% lower than that of C0-T90 and C1-T90, respectively.

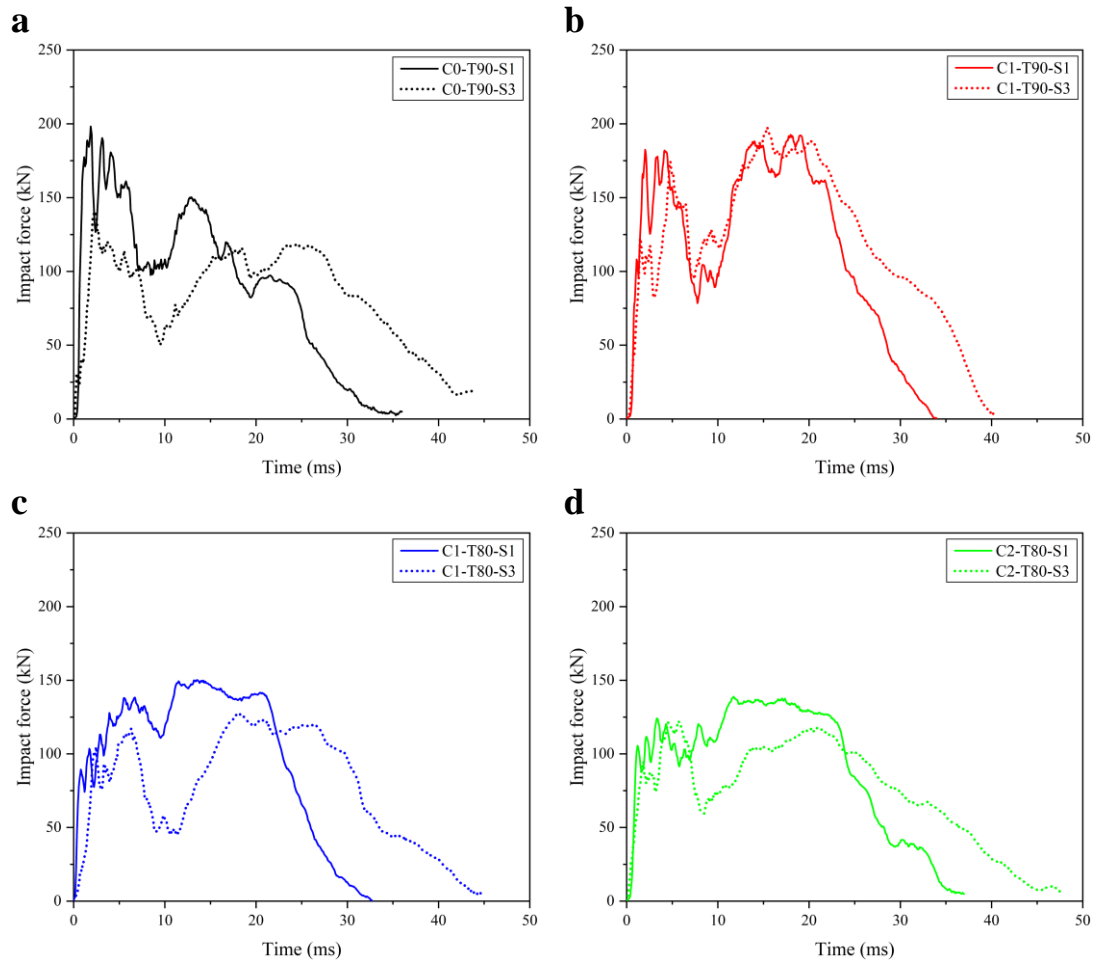


Figure 4-11. Impact force time histories of (a) C0-T90, (b) C1-T90, (c) C1-T80, and (d) C2-T80 under S1 (M387-V4.43) and S3 (M587-V3.6) of the same impact energy.

4.4.3.2 Transmitted force

The peak transmitted forces at each location for all four types of cladding under scenarios S1 and S3 are compared in Figure 4-12 and summarised in Table 4-5. It is observed that the peak transmitted forces at each location for the same cladding decrease when changing from a higher impact velocity and lower impact mass in scenario S1 (M387-V4.43) to a lower impact velocity and higher impact mass in scenario S3 (M587-V3.6) due to the decrease in the impact force. However, the peak impact force at the bottom left (BL) location is only slightly different and even higher at the bottom right (BR) location under scenario S3 compared to that under scenario S1 for the same cladding. This difference is attributed to the twisting and rotating

clockwise of the square impact head during high-energy impact. In scenario S3, which has a lower impact velocity, the twist is minimal, as observed in Figure 4-13. Conversely, in scenario S1, with a higher impact velocity, the twist is more pronounced, as seen in Figure 4-6. As a result, the impact areas on the BR load cell in scenario S3 are larger than those in scenario S1, leading to higher peak transmitted forces at the bottom locations, especially the BR location, in scenario S3 compared to scenario S1. Similar to scenario S2, in scenario S3, the peak impact forces at the bottom locations (BL and BR) are larger than those at the top locations (TL and TR) for the same cladding. This is because as the impactor crushed the cladding and moved forward, the impact head became slightly inclined, causing a slight upward impact due to the swing motion of the pendulum, thus resulting in lower peak transmitted forces at the top locations.

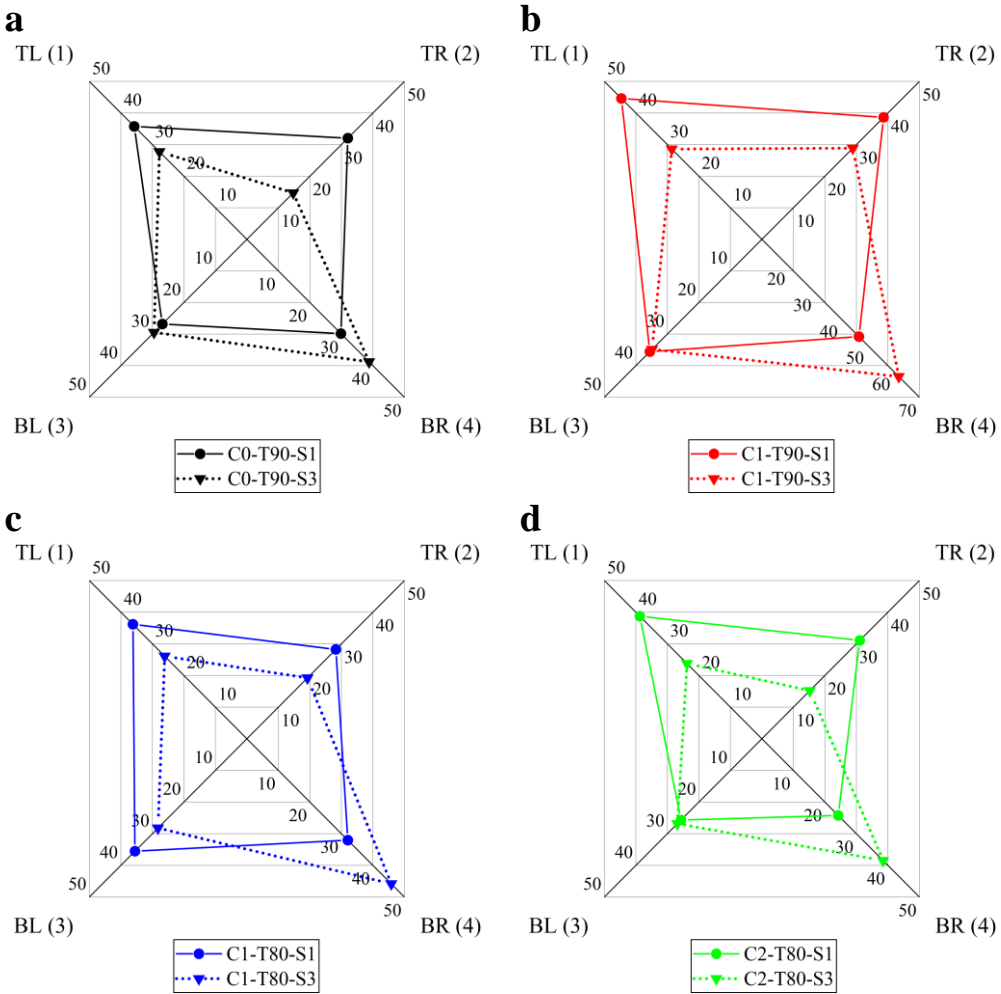


Figure 4-12. Comparisons of peak transmitted forces at each load cell location of (a) C0-T90, (b) C1-T90, (c) C1-T80, and (d) C2-T80 under S1 (M387-V4.43) and S3 (M587-V3.6) of the same impact energy.

Overall, under the same impact scenario, the proposed CTH cladding has a lower peak transmitted force than the SH and CSH claddings at the same location. The C2-T80 cladding exhibits the lowest peak transmitted forces among all types of cladding, demonstrating its excellent performance as protective sacrificial cladding, owing to its stable impact crushing force without an obvious peak, low peak transmitted force, high energy absorption, and an easy-folding core.

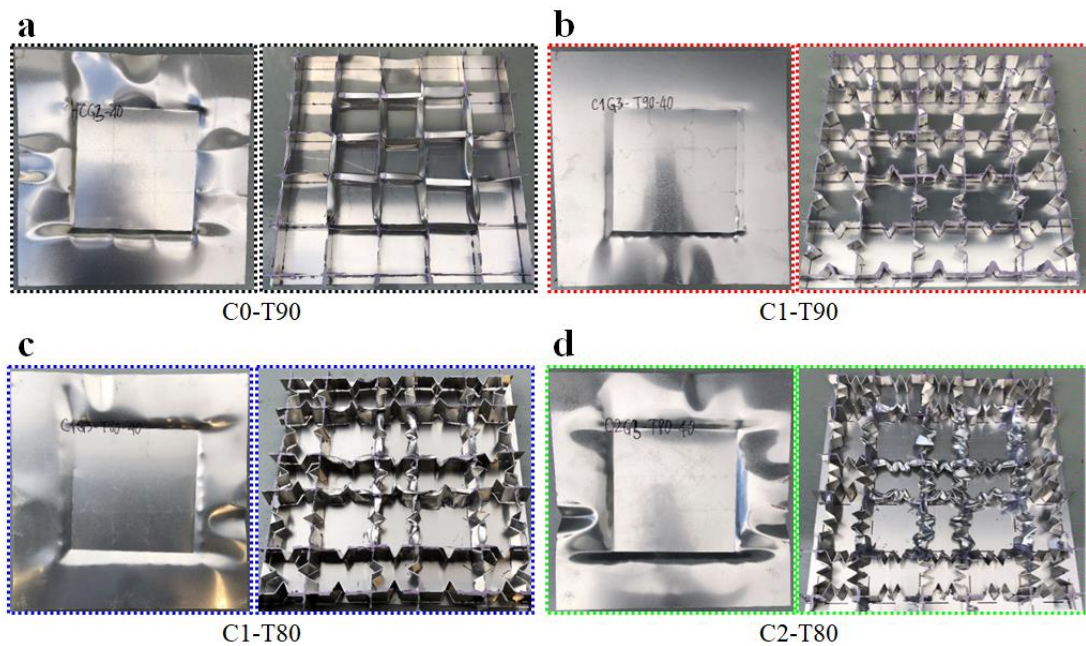


Figure 4-13. Deformation of the front external plate and core of claddings (a) C0-T90, (b) C1-T90, (c) C1-T80, and (d) C2-T80 under S3 (M587-V3.6).

Table 4-5. Peak impact force and peak transmitted forces at each load cell location of the four claddings under S1 and S3.

Cladding	Impact scenario	Peak impact force (kN)	Peak transmitted force at different locations (kN)			
			TL (1)	TR (2)	BL (3)	BR (4)
C0-T90	S1 (M387-V4.43)	198.2	35.7	32.0	26.8	29.8
C1-T90		192.6	44.6	38.6	35.6	47.0
C1-T80		150.1	36.2	28.2	35.5	32.0
C2-T80		138.8	38.7	31.1	25.7	24.2
C0-T90	S3 (M587-V3.6)	140.7	27.7	14.7	29.5	38.8
C1-T90		197.2	28.6	28.8	34.8	62.1
C1-T80		127.1	26.1	19.2	28.2	45.8
C2-T80		122.1	23.7	15.2	26.8	38.4

4.5 Summary

In this chapter, the impact mitigation performances of a novel sandwich cladding with a corrugated tilted honeycomb (CTH) core were experimentally investigated using pendulum impact testing system. The impact mitigation performances of the CTH cladding were evaluated and compared with those of the square honeycomb (SH) and corrugated square honeycomb (CSH) claddings of the same mass. Various impact scenarios were considered by combining different impact masses and velocities. The main findings are outlined below.

- The proposed CTH cladding exhibits excellent impact mitigation performances under various investigated impact scenarios. The CTH cladding demonstrates an increased crushing resistance, more stable crushing force without obviously high peaks, lower transmitted force, larger deformation, and an easy-folding core compared to the SH and CSH claddings of similar mass. These characteristics demonstrate its excellent impact mitigation performances as a protective sacrificial cladding, which can be easily fabricated using conventional slotting and pressing techniques.
- The CTH cladding with C2-T80 core outperforms all types of cores investigated in this chapter due to its larger corrugated gaps and thinner corrugated tilted core sidewalls. This results in a lower peak impact force, a more stable crushing force, and an easy-folding core, as compared to C1-T80. However, further increasing the number of corrugations, such as C3 or C4, may make the fabrication difficult when using the pressing technique introduced herein.
- With the increase in impact velocity from 3.6 m/s to 4.43 m/s, the initial peak impact force of the SH cladding significantly increases due to its stiff vertical sidewalls. However, the impact crushing force of the CTH cladding gradually increases till its highest peak at a later stage of impact, owing to its corrugated tilted core design.
- Different combinations of impact mass and impact velocity significantly affect the impact force profiles and the peak transmitted forces of all claddings investigated in this chapter. Under the same impact energy, the impact scenario

with a higher impact mass and lower impact velocity leads to a lower impact force and a longer impact duration due to its higher initial momentum.

Chapter 5. Sandwich structures inspired by beetle forewing (SSBF)

The related work in this chapter was published in International Journal of Impact Engineering:

Lam L, Chen W, Hao H, Li Z, Ha NS. Dynamic crushing performance of bio-inspired sandwich structures with beetle forewing cores. International Journal of Impact Engineering 2023;173:104456.

<https://doi.org/10.1016/j.ijimpeng.2022.104456>

5.1 Introduction

In Chapter 3, the high initial peak force of the conventional honeycomb core can be eliminated without sacrificing the plateau crushing force by implementing the structural feature of the plant stems [188]. Furthermore, the initial peak of the proposed CTH design remains insensitive to the loading rate, showcasing an excellent energy-absorbing core. However, the CTH core with a specific wall thickness may be suitable for only certain impact scenarios or energy levels since its energy absorption capacity remains quite similar under various crushing speeds. Therefore, in this chapter, an innovative structure with adaptive energy-absorbing capability to address the uncertainties of real impact scenarios is numerically proposed by mimicking the internal structure of beetle forewings, as shown in Figure 5-1. The microstructure of beetle forewings consists of circular cavities made of fibre layers [134], between which there are a series of trabecula tube-like structures connecting the upper and lower layers of the forewing [133,137]. The sandwich structure is proposed by mimicking and simplifying the complexity of the forewing-internal structure, as shown in Figure 5-1(b). One unit between two circular cavities is used to mimic one unit of the proposed SSBF structure. The semi-arch cores are used to mimic the arch shape of the hollow cavity inside the forewing. PU foam is used to divide the inside of the core into cells to mimic the series of trabeculae, and STF is filled inside those cells to mimic the viscoelastic material inside the trabecula. The proposed SSBF is designed by partially filling each cell with the STF, and the bending deformation of the curved cores is used to trigger the thickening behaviour of the STF. The coupling interaction between fluid

and structural components is analysed using a fluid-structure interaction (FSI) technique in LS-DYNA. The dynamic compressive test on the STF specimen conducted by Wu et al. [54] is used for numerical model calibration of the STF specimen by comparing the generated numerical prediction of the stress-strain curve of the STF specimen with the existing experimental data [54]. Then the numerical model of the proposed SSBF structure is constructed by implementing the same modelling technique as the calibrated model. The mean crushing force, crushing force efficiency and energy absorption capacity are used to assess the performance of the proposed SSBF structure.

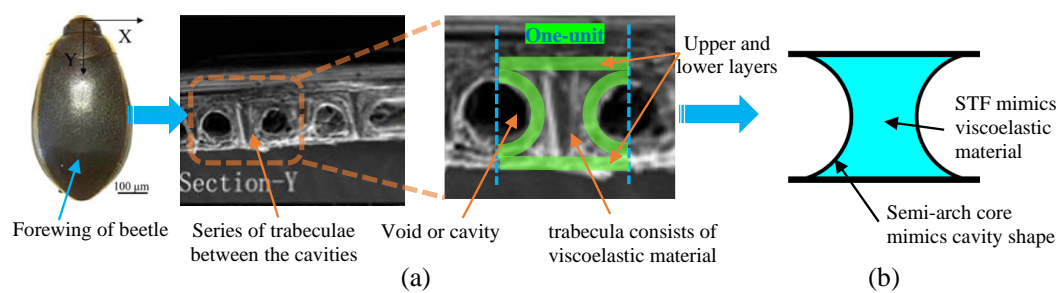


Figure 5-1. (a) Beetle and its cross-section showing the internal structure of forewing [126] and (b) schematic diagram of the sandwich structure inspired by beetle forewing (SSBF).

5.2 Numerical model calibration

The dynamic compressive test of STF conducted by Wu et al. [54] is used for model calibration of the STF specimen under impact loading. A series of dynamic compression tests with various impact velocities were performed to compress the STF using a gas gun. The STF specimen was fabricated by filling the STF into a predetermined cylindrical rubber container, which has a diameter and height of 52 mm and 9.4 mm, respectively. The wall thickness of the rubber is 0.1 mm. The STF has a density of 1,600 kg/ m³. It is a mixture of silica particles and polyethylene glycol 200 (PEG 200) with a weight ratio (Silica/PEG 200) of 70/30 [54]. The dimensional details of the striker and loading bar can be found in the previous study [54,175]. The impact test of the STF specimen subjected to the impact speed of 8 m/s is used for model calibration in this chapter. The schematic diagram showing the testing setup of the dynamic compressive test of STF is illustrated in Figure 5-2(a).

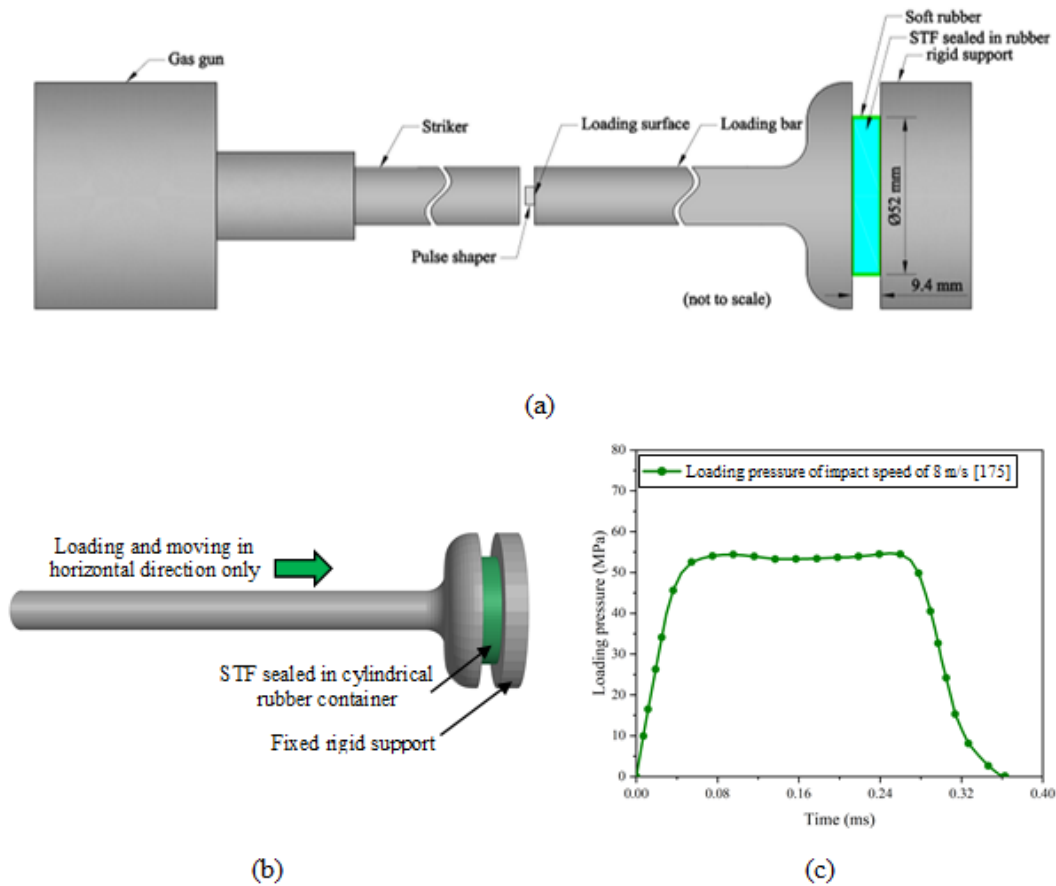


Figure 5-2. (a) Schematic diagram showing the testing setup of dynamic compressive test of STF [54,175], (b) loading and boundary conditions of ALE-FE model of STF compressive test, and (c) loading pressure-time history of the impact speed of 8 m/s [175].

5.2.1 Boundary conditions and contact

In the numerical model, the STF specimen is simply placed on a rigid support and totally crushed by a trumpet-shaped loading bar. The rigid support is fully constrained, while the loading bar is allowed to move in the horizontal direction only. The loading pressure of the impact speed of 8 m/s, measured from the experimental test [54,175], is perpendicularly applied on the loading surface of the loading bar. The numerical model and loading pressure history of the impact speed of 8 m/s are shown in Figure 5-2(b) and (c), respectively.

The FSI coupling algorithm and Arbitrary Lagrangian-Eulerian (ALE) method are used to model the compressive test of this STF specimen. The *CONSTRAINED_LAGRANGE IN SOLID command is used to model the coupling interaction between the structural components and fluid materials [65,111,175]. The contact between the rubber and loading bar/support is defined by

*CONTACT_AUTOMATIC SURFACE TO SURFACE with soft constraint formulation for the interaction between the dissimilar materials in the contact [36,65]. The contact force between the STF specimen and rigid support is extracted and divided by the contact area of the specimen to obtain the compressive stress of the STF. The compressive strain is simply calculated by dividing the displacement of the loading bar by the total height of the specimen. The compressive stress-strain curve of STF generated from the calibrated model is compared with that of STF measured in the experimental test [54] to validate the accuracy and reliability of the numerical simulation. Then the numerical model of the proposed SSBF structure is constructed by implementing the same modelling technique as the calibrated model.

5.2.2 Element types and material models

To model the test, the rigid loading bar and support are meshed using hexahedral solid element, while the rubber is modelled using Belytschko-Tsay type shell element. STF and air are modelled by ALE formulation. In ALE method, the fluid elements are externally covered by the mesh of air domain, which allows fluid materials to flow through [196,197]. Shear thickening fluid (STF) is a non-Newtonian fluid whose viscosity increases with the rising shear rate. Therefore, it is modelled using *MAT_ALE_VISCOUS which allows the modelling of fluids with variable viscosity. This variable viscosity of STF is characterised as [198]:

$$\eta = RK \cdot \dot{\gamma}^{RN-1} \quad (5-1)$$

where η is the dynamic viscosity, $\dot{\gamma}$ is the applied shear rate, RK is the variable viscosity multiplier, and RN is the variable viscosity exponent. The material properties and equation of state (EOS) parameters of the STF are adopted from the previous study of Gu et al. [175]. The hydrostatic behaviour of STF is described by the EOS_GRUNEISEN, whose pressure is described as [175,198]:

$$p = \frac{\rho_0 C_v^2 \mu \left[1 + \left(1 - \frac{\gamma_0}{2} \right) \mu - \frac{a}{2} \mu^2 \right]}{\left[1 - (S_1 - 1) \mu - S_2 \frac{\mu^2}{\mu + 1} - S_3 \frac{\mu^3}{(\mu + 1)^2} \right]^2} + (\gamma_0 + a\mu) E_1 \quad (5-2)$$

where $\mu = \frac{\rho}{\rho_0} - 1$, μ is a volumetric parameter, ρ_0 and ρ are the original and current density, respectively, C_v is the intercept of shock velocity-particle velocity curve, S_1, S_2, S_3 are the coefficients of the slope of shock velocity-particle velocity curve, γ_0 is the Gruneisen-gamma, a is the first order volume correction to γ_0 , E_I is the internal energy per initial volume. Air is modelled using *MAT_NULL material model. The hydrostatic behaviour of air is described by the EOS_LINEAR_POLYNOMIAL, whose pressure is given by [175,198]:

$$p = C_0 + C_1\mu + C_2\mu^2 + C_3\mu^3 + (C_4 + C_5\mu + C_6\mu^2)E_I \quad (5-3)$$

where $C_0 \sim C_6$ are the polynomial equation coefficients. The loading bar and support are assumed rigid and modelled using *MAT_RIGID. A two-parametric material model (*MAT_MOONEY-RIVLIN_RUBBER) is used to model the container of STF [199,200]. The details of material properties and EOS parameters are summarised in Table 5-2.

5.2.3 Model calibration

The stress-strain curves obtained from the numerical simulation and experimental data in [54] are compared and plotted in Figure 5-3.

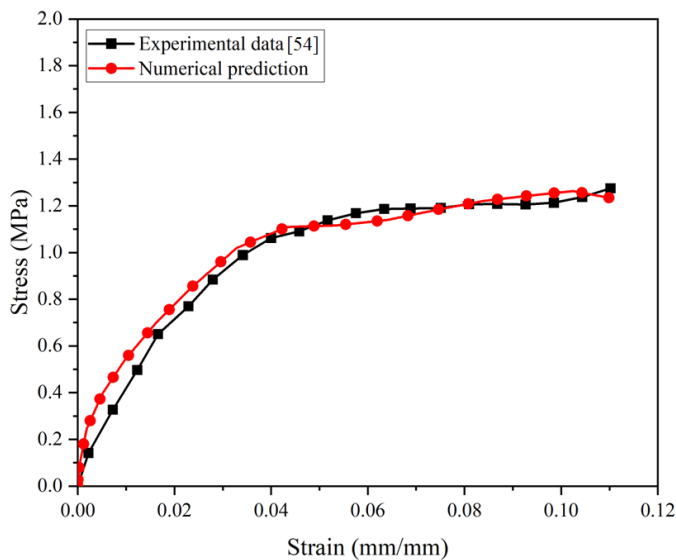


Figure 5-3. Comparison of numerical prediction and experimental data [54] of compressive stress-strain response of STF under 8 m/s impact speed.

It is shown that the numerical prediction agrees well with the experimental result. It is concluded that the numerical model yields a reasonably accurate prediction of the compressive response of STF under impact loading. Therefore, the modelling technique of the calibrated model is used to construct the numerical model of the proposed SSBF structure in the subsequent sections.

5.3 Sandwich structure inspired by beetle forewing (SSBF)

5.3.1 Geometries and loading conditions

The proposed prototype represents one unit of energy-absorbing structure which consists of two external plates and two semi-circular-shaped cores curved inward, forming a concave shape as shown in Figure 5-4(a). The prototype has a cross-section of 76 mm by 50 mm and a total height of 120 mm. The concave-shaped core has a curved radius of 25.6 mm with a middle thinner gap of 26 mm. Three PU foams in concave shape with a thickness of 20 mm are arrayed 50 mm apart from their centres, forming two cells inside the core to contain fluid, as shown in Figure 5-4(b). These PU foams can be physically connected to the cores and external plates by using adhesive. The contact and tapered lengths of around 5 mm are for the connections between the core sheets and external plates as well as the feasibility of cornered joints of PU foams for fabrication. In the numerical simulation, a tied contact is used to connect the PU foam to the core and external plates, and the connections between cores and external plates are assumed perfectly tied by using common nodes. For fluid-filled specimens, two types of fluid, i.e., STF, and Newtonian viscous fluid with a constant viscosity (e.g., silicone oil), are used. The fluid is partially filled inside each cell to 10 mm in height, thus leaving an air gap of 20 mm, which allows fluid to flow during crushing.

The proposed structure is designed to be placed in the vertical position, thus resisting the crushing load in the horizontal direction as shown in Figure 5-4(d). The specimen is simply attached to the rigid support which is constrained in both translation and rotation in all directions. The rigid loading plate is translated at a constant crushing speed in the horizontal direction only. The *CONTACT_AUTOMATIC SURFACE TO SURFACE contact algorithm is adopted, and the friction coefficient of 0.2 is used for all contact interactions [201,202]. The contact force between the specimen and the support, and the displacement of the front plate are used to construct the force-

displacement curve, from which the energy absorption capacity of each specimen can be obtained.

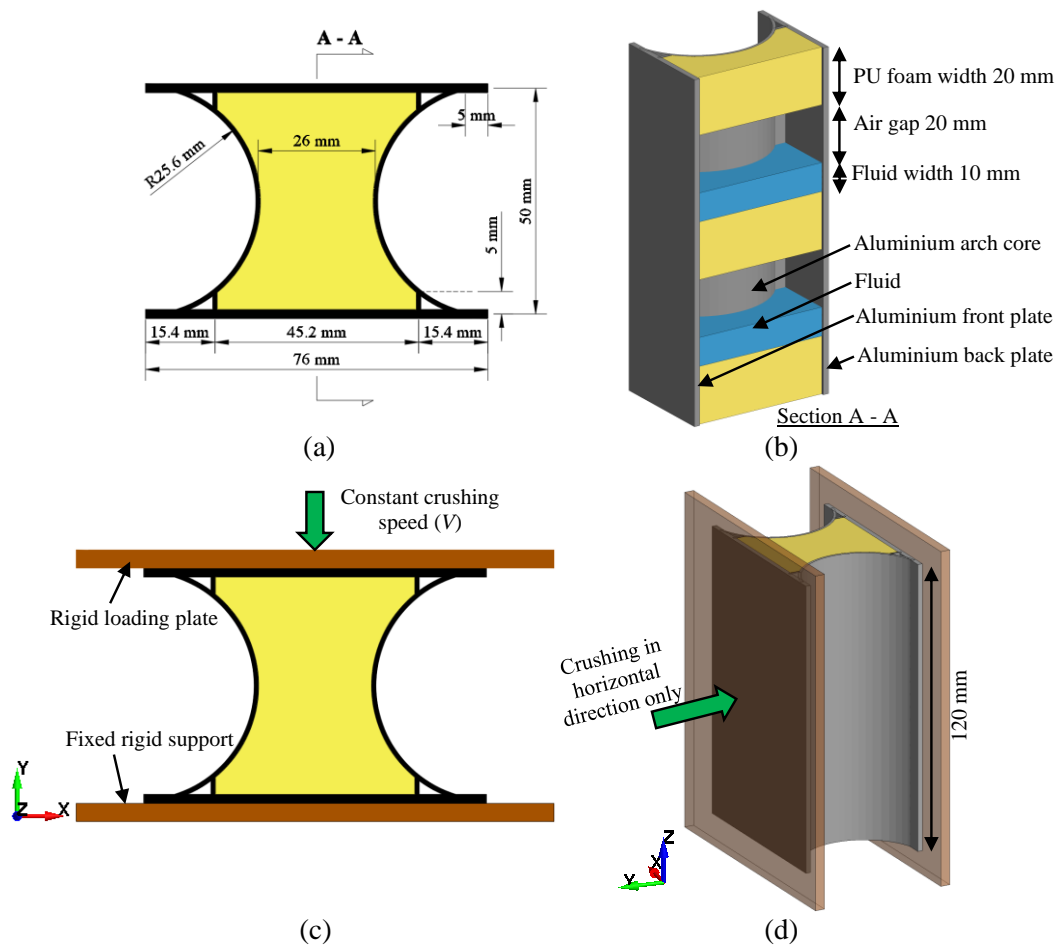


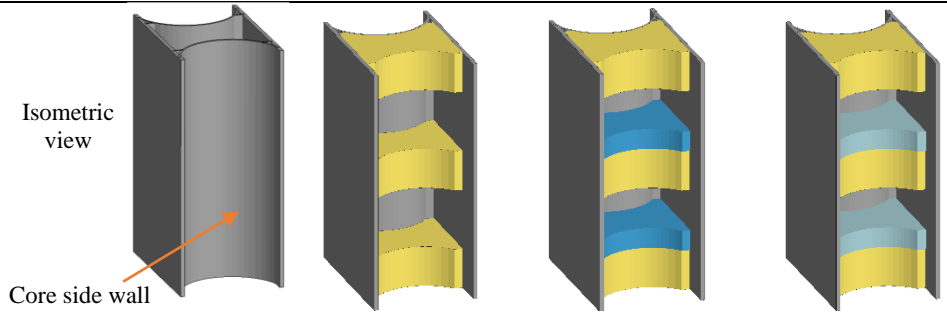
Figure 5-4. (a) Details of specimen in top view, (b) cross-section A-A showing internal details of the specimen, (c) boundaries and loading condition, and (d) isometric view of the specimen.

The effect of loading rate on the dynamic crushing performance of the specimen is investigated under three constant crushing speeds (i.e., 10 m/s, 20 m/s, and 30 m/s). The specimens tested under the same crushing speed are grouped together as summarised in Table 5-1. In each group, there are four specimens such as empty, partially filled PU foam only, PU foam and viscous fluid-filled, and PU foam and STF-filled (SSBF) specimens. All specimens have the same 2 mm thickness of the external plate. To easily identify the specimen, its core wall thickness, infilled material, and crushing speed are used for specimen designation. The core wall thickness of 1 mm is denoted by C1. The core wall thickness of 2 mm, denoted by C2, is also used to investigate the effect of core wall thickness in Section 5.4.3. The infilled materials such as empty, partially filled PU foam, PU foam and viscous fluid (Newtonian fluid),

and PU foam and STF are denoted by E, PP, VF, and STF, respectively. V10, V20, and V30 denote the crushing speeds of 10 m/s, 20 m/s, and 30 m/s, respectively. Therefore, C1-STF-V10 is the STF-filled specimen that is crushed under the crushing speed of 10 m/s.

Table 5-1. Specimen configurations.

Group	Filling material				Crushing speed (m/s)
	Empty (E)	Partial filled PU foam (PP)	Partial PU foam with viscous fluid (VF)	Partial PU foam with STF (STF)	
1	C1-E-V10	C1-PP-V10	C1-VF-V10	C1-STF-V10	10
2	C1-E-V20	C1-PP-V20	C1-VF-V20	C1-STF-V20	20
3	C1-E-V30	C1-PP-V30	C1-VF-V30	C1-STF-V30	30



*Note: one core side wall is removed for illustration.

5.3.2 Material models

In this chapter, the curved core and external plates of the proposed structure are made of aluminium 5052 H32 plates. These components are modelled by using the Belytschko-Tsay type shell element with five integration points through the shell thickness. The *MAT_PIECEWISE_LINEAR_PLASTICITY material model is used for the aluminium material whose true stress-strain curve [11] is plotted in Figure 5-5. Since the strain rate effect of aluminium is insignificant [203], it is not considered in the simulation of this chapter. The rigid polyurethane (PU) foam with a density of 35 kg/m³ is used and modelled by using solid element and *MAT_CRUSHABLE_FOAM material model with a damping coefficient of 0.5 [204]. The *MAT_ADD_EROSION option with the maximum principal failure strain of 0.1 [205] and the keyword *CONTACT_INTERIOR are utilised for PU foam [58,204] to avoid the negative volume error of soft material under large deformation. The measured compressive engineering stress versus strain curve of PU foam [58] is shown in Figure 5-6. To

compare the effect of fluid type, a viscous fluid (Newtonian fluid) made of silicone oil is used. It has a constant dynamic viscosity of 10 Pa.s [169], which is four orders higher than that of water. It is modelled using *MAT_NULL material model and *EOS_GRUNEISEN by altering its viscosity as conducted in the previous study of Wang et al. [206]. The keyword *MAT_RIGID is used for the loading plate and supporting plate. The same material properties and EOS parameters of STF and air in Section 5.2.2 are used to model the proposed SSBF structure. The input parameters of material properties and EOS of all materials for the numerical simulations are listed in Table 5-2.

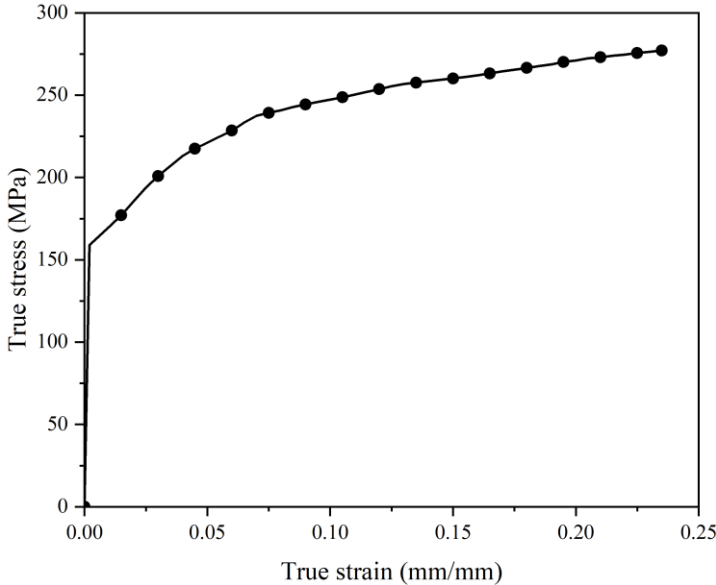


Figure 5-5. True stress-strain curve of Aluminium 5052 H32 plate [11].

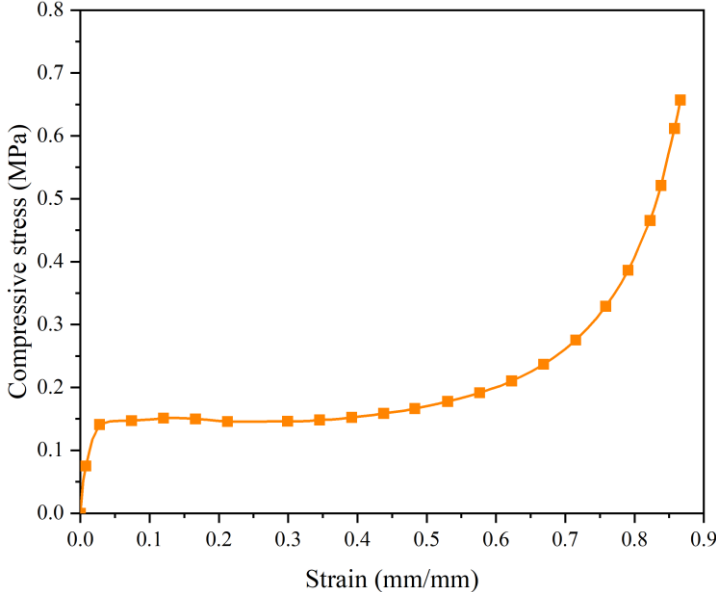


Figure 5-6. Compressive stress-strain curve of PU foam [58].

Table 5-2. Material properties and EOS parameters of all materials used in the calibrated and proposed models.

Component	Material	Input data in LS-DYNA						
Cylindrical-shaped rubber	Rubber [206]	*MAT_027 MOONEY-RIVLIN_RUBBER						
		Density (kg/m ³)	Poisson's ratio	A (MPa)	B (MPa)			
		1143	0.495	0.5113	2.563			
Infilled material	STF [150,175]	*MAT_ALE_VISCOUS						
		Density (kg/m ³)	<i>RK</i>	<i>RN</i>				
		1600	72	1.35				
		*EOS_GRUNEISEN						
		<i>C_v</i> (m/s)	<i>γ₀</i>	<i>S₁</i>	<i>S₂</i>	<i>S₃</i>	<i>a</i>	
		2050	2	5.324	0	0	0	
	Viscous fluid [169,206]	*MAT_009 NULL						
		Density (kg/m ³)	Dynamic viscosity (Pa.s)					
		970	10					
		*EOS_GRUNEISEN						
		<i>C_v</i> (m/s)	<i>γ₀</i>	<i>S₁</i>	<i>S₂</i>	<i>S₃</i>	<i>a</i>	
		1480	0.5	2.56	1.986	1.2268	0	
Air domain	Air [175]	*MAT_009 NULL						
		Density (kg/m ³)						
		1.29						
		*EOS_LINEAR_POLYNOMIAL						
		<i>C₀</i>	<i>C₁</i>	<i>C₂</i>	<i>C₃</i>	<i>C₄</i>	<i>C₅</i>	<i>C₆</i>
		0	0	0	0	0.4	0.4	0
Aluminium core and external plates	Aluminium 5052 H32 [11]	*MAT_024 PIECEWISE_LINEAR_PLASTICITY						
		Density (kg/m ³)	Young's modulus (GPa)	Poisson's ratio	Yield stress (MPa)			
		2680	70	0.33	159			

Table 5-2 (Continued)

Component	Material	Input data in LS-DYNA			
Core divider	PU foam [58]	*MAT_063 CRUSHABLE_FOAM			
		Density (kg/m ³)	Young's modulus (MPa)	Poisson's ratio	Damping coefficient
		35	13.68	0	0.5

5.3.3 Mesh convergence test

A mesh convergence test was carried out to determine the mesh sizes for the numerical model. The response of the C1-STF-V30 specimen with three different Lagrangian/Eulerian-element pairs of mesh size such as (6 mm, 4 mm), (3 mm, 2 mm), and (2 mm, 1 mm) was examined. The force-displacement curves of the C1-STF-V30 with different pairs of mesh sizes are shown in Figure 5-7.

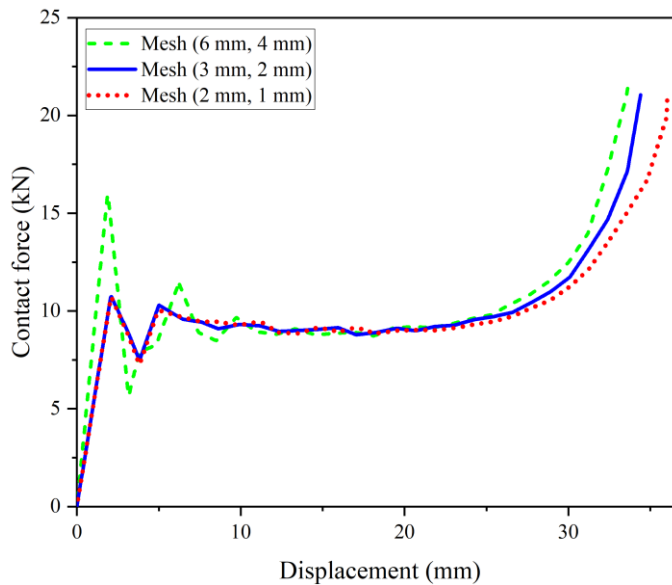


Figure 5-7. Mesh convergence test results on the force-displacement response of C1-STF-V30 with different pairs of mesh sizes.

It is shown that the numerical models of these different mesh sizes generate a similar force-displacement profile. However, the model with coarse mesh sizes (6 mm, 4 mm) yields a higher initial peak force and smaller stroke length. The numerical models using the element sizes of (3 mm, 2 mm) and (2 mm, 1 mm) generate a similar force-displacement profile, initial peak force, and stroke length. Therefore, by considering both the simulation accuracy and computational cost, the Lagrangian/Eulerian-element pair of (3 mm, 2 mm) is adopted for the subsequent numerical simulations.

5.4 Results and discussions

5.4.1 Force-displacement and energy absorption of SSBF under various crushing speeds

Peak crushing force (*PCF*), Mean crushing force (*MCF*), crushing force efficiency (*CFE*), energy absorption capacity (*EA*), and specific energy absorption capacity (*SEA*) are used to assess and evaluate the performance of the proposed SSBF structure. The details of each key evaluating criterion can be found in Section 3.4.

5.4.1.1 Group 1 (10 m/s)

The performances of empty, PU foam-filled, PU foam and viscous fluid-filled, and PU foam and STF-filled specimens under the same 10 m/s crushing speed (i.e., Group 1) are investigated and compared in this section. The force-displacement curves of all specimens are plotted in Figure 5-8. It is observed that the force-displacement response of the empty specimen shows a high initial peak force followed by a low fluctuating crushing force during the crushing process, leading to a low *CFE* of 36%. By adding the PU foam, the crushing force is improved owing to the crushing of PU foam and the interaction between the curved cores and PU foams while the initial peak force remains almost unchanged, thus increasing the *CFE* to 46%. However, filling the Newtonian viscous fluid inside the gaps of the specimen does not significantly improve the crushing resistance because of the relatively low support and easy flow of the fluid. In addition, the crushing force slightly increases, and the densification occurs earlier at the later stage of the crushing process due to the full compression of the viscous fluid. Overall, similar force-displacement profiles with a high initial peak and a low fluctuating crushing force for the three sandwich structures are observed. In particular, by partially filling the empty specimen with PU foam, the specimen C1-PP-V10 has an improved *MCF* of 2.53 kN which is around 30% higher than the empty specimen C1-E-V10. However, for the specimen C1-VF-V10 partially filled with PU foam and Newtonian viscous fluid, the *MCF* only increases by 10% as compared with C1-PP-V10. On the other hand, replacing the Newtonian viscous fluid by STF, i.e., partially filling the specimen C1-PP-V10 with STF leads to a large enhancement on *MCF*, a more stable crushing process without a noticeably high initial peak force, as plotted in Figure 5-8. The *CFE* of the specimen C1-STF-V10 is 83%. In summary, at 10 m/s

crushing, the SSBF specimen has the highest MCF of 5.39 kN which is around 176%, 113%, and 93% higher than that of C1-E-V10, C1-PP-V10, and C1-VF-V10 specimens, respectively, and has the most uniform and stable crushing process among the four types of designs considered in this chapter. However, the SSBF specimen has the smallest consolidation displacement among the considered specimens, which may compromise its energy absorption capacity.

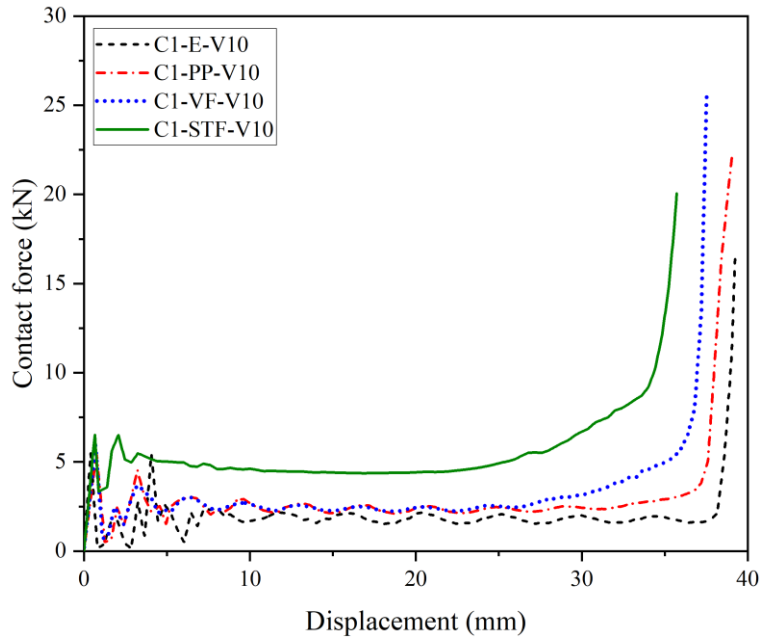


Figure 5-8. Force-displacement profiles of specimens in Group 1 under 10 m/s crushing speed.

In terms of energy absorption, the empty specimen (C1-E-V10) has a total EA of around 75 J, which is mostly dissipated through the plastic deformation of the curved core. For C1-PP-V10 specimen, its EA increases to 94.72 J, which is around 26% higher than that of empty specimen. This additional increase in energy absorption capacity is contributed mostly by the crushing of PU foam. By further filling the specimen with the Newtonian viscous fluid, the total EA of C1-VF-V10 is only around 8% higher than that of C1-PP-V10 specimen due to the contribution of viscous dissipation of the Newtonian viscous fluid. For SSBF, C1-STF-V10 has the highest EA of 188.42 J, which is 151%, 99%, and 84% higher than C1-E-V10, C1-PP-V10, and C1-VF-V10, respectively because of the increased crushing resistance although its crushing distance is the smallest. The total EA of C1-STF-V10 is largely contributed by the viscous dissipation of STF, which is around 48.1%. The remaining contribution is from the deformation of the core and crushing of PU foam, which is 39.2% and

11.8% of the total energy absorption capacity, respectively. Therefore, SSBF exhibits desirable energy-absorbing characteristics of stable and high crushing resistance without a noticeably high initial peak. The absorbed energy contributed by each component of specimens in Group 1 is shown in Figure 5-9. The energy absorbed by each component, *PCF*, *MCF*, *CFE*, and *EA* of the specimens in Group 1 are summarised in Table 5-3.

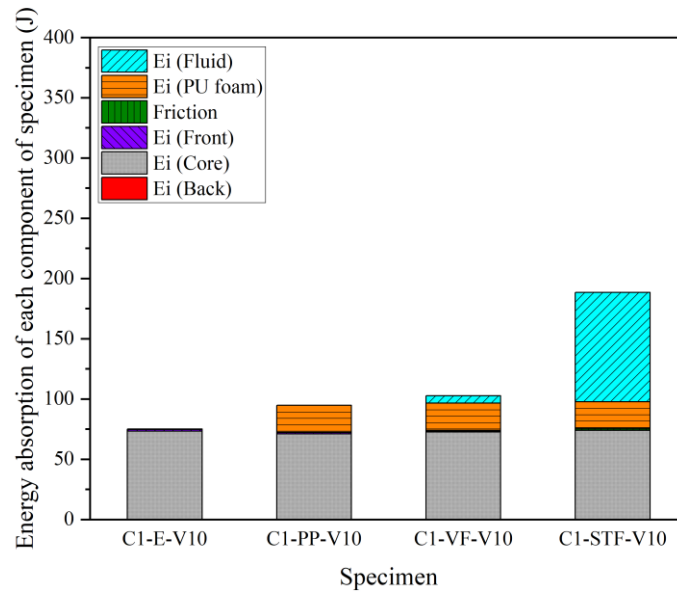


Figure 5-9. Energy absorbed by each component of specimens in Group 1 under crushing speed of 10 m/s.

5.4.1.2 Group 2 (20 m/s) and Group 3 (30 m/s)

The force-displacement responses of specimens in Group 2 and Group 3 are plotted in Figure 5-10(a) and (b), respectively. It is shown that the crushing force-displacement responses of the empty and PU foam-filled specimens are quite similar under the same crushing speed, except that the crushing resistance of the PU foam-filled specimen is higher than that of the empty specimen. There still exists a high initial peak force followed by a low fluctuating crushing force during the crushing process. Furthermore, the initial peak force substantially increases while the crushing force-displacement profile remains similar as the crushing speed increases. Therefore, the empty specimen still has a low *CFE* of 34% and 41%, and the PU foam-filled specimen also has a low *CFE* of 41% and 46%, when the crushing speed increases from 20 m/s to 30 m/s. It is due to the inertial effect of the structure of the empty and PU foam-filled specimens since aluminium plates and PU foam are made of rate-insensitive materials. By filling the Newtonian viscous fluid, the crushing force-displacement profile remains similar

to that of the PU foam-filled specimen since the fluid only provides little support to the core, resulting in a similar *CFE* of 43% and 46% under the crushing speeds of 20 m/s and 30 m/s, respectively. Furthermore, as the crushing rate increases, the crushing force is not substantially improved because the Newtonian viscous fluid is still in the same viscous state under different rates, thus dissipating a similar amount of energy.

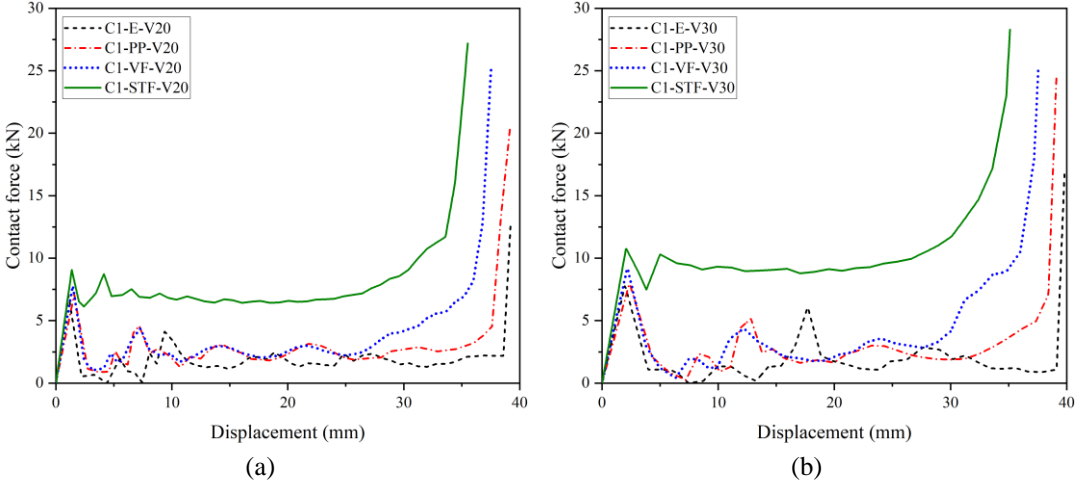


Figure 5-10. Force-displacement profiles of specimens in (a) Group 2 under crushing speed of 20 m/s and (b) Group 3 under crushing speed of 30 m/s.

The *MCF* of the empty specimen remains similar as the crushing speed increases from 20 m/s to 30 m/s. For the partially filled PU foam specimen, its *MCF* only slightly increases to 2.92 kN and 3.68 kN, i.e., 23% and 17% higher than that of the empty specimen under the crushing speeds of 20 m/s and 30 m/s, respectively. By partially filling with Newtonian viscous fluid, the enhancement of *MCF* increases further by 14% and 16% compared with the partially filled PU foam specimen under the same crushing speeds of 20 m/s and 30 m/s, respectively. For SSBF, the crushing resistance increases with the increase of crushing speed without a noticeably high initial peak force, resulting in the highest *CFE* of 87% and 92% under the crushing speeds of 20 m/s and 30 m/s, respectively. When the loading speed increases from 10 m/s to 20 m/s, the *MCF* of SSBF increases by 46% from 5.39 kN to 7.86 kN, which is 231%, 169%, and 136% higher than that of the empty (C1-E-V20), partial filled PU foam (C1-PP-V20), and the viscous fluid-filled (C1-VF-V20) specimens under 20 m/s crushing speed, respectively. At a higher 30 m/s crushing speed, the *MCF* of SSBF increases by 84% to around 9.94 kN, which is 215%, 170%, and 134% higher than that of C1-E-V30, C1-PP-V30, and C1-VF-V30, respectively.

Figure 5-11 shows the absorbed energy contributed by each component of specimens under the crushing speeds of 20 m/s and 30 m/s. The total EA of empty and PU foam-filled specimen increases mainly because of the deformation of the front plate as the crushing speed becomes higher. For the Newtonian viscous fluid-filled specimen, its EA increases by 18% and 49% when the crushing speed increases from 10 m/s to 20 m/s, and then 30 m/s, respectively. For SSBF, its EA is significantly enhanced when the crushing speed increases. It is enhanced by 40% from 188.42 kN to 264.41 kN when the crushing speed increases from 10 m/s to 20 m/s. It is further enhanced by 73%, which is around 325.12 kN as the crushing speed further increases to 30 m/s. This increase is mainly contributed by the viscous dissipation of STF which is around 58.6% and 62.7% of the total EA of SSBF under the crushing speeds of 20 m/s and 30 m/s, respectively, as shown in Figure 5-11. As the crushing rate increases, the curved cores generate a high shear rate on STF, thus leading to the rise of viscosity and viscous dissipation of STF. As illustrated in Figure 5-9 and Figure 5-11, the energy absorbed by STF increases by 70.9% from 90.63 kN to 154.86 kN when the crushing speed increases from 10 m/s to 20 m/s. It significantly increases by 125.1% as the crushing speed increases up to 30 m/s. Therefore, as the crushing speed increases, STF becomes more viscous, leading to the enhancement of the crushing resistance and energy absorption capacity of SSBF. The energy absorbed by each component, PCF , MCF , CFE , and EA of the specimens in Group 2 and Group 3 are summarised in Table 5-3.

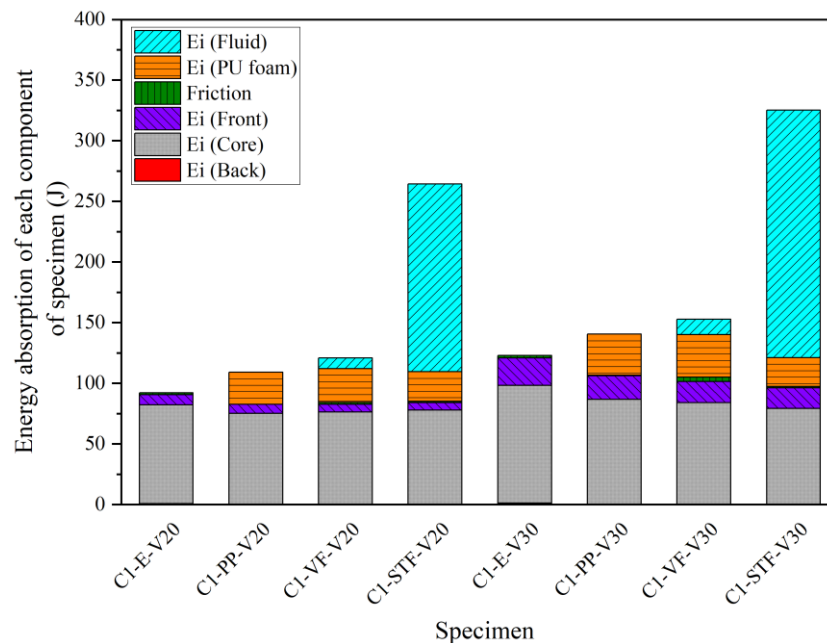


Figure 5-11. Energy absorption by each component of specimens under crushing speeds of 20 m/s (Group 2) and 30 m/s (Group 3).

Table 5-3. Summary of *PCF*, *MCF*, *CFE*, *EA* and *SEA* of empty, PU foam-filled, viscous fluid-filled, and STF-filled (SSBF) specimens in Group 1, Group 2, and Group 3.

Specimen	Stroke <i>d</i> (mm)	Mass (kg)	<i>PCF</i> (kN)	<i>MCF</i> (kN)	<i>CFE</i> (%)	Internal Energy E_i (J)					Friction (J)	Total <i>EA</i> (J)	<i>SEA</i> (J/kg)
						Front	Core	Back	PU foam	Fluid			
C1-E-V10	38.41	0.149	5.48	1.95	36	1.34	73.02	0.22	-	-	0.43	75.00	504.54
C1-PP-V10	37.40	0.152	5.48	2.53	46	0.99	70.92	0.12	22.42	-	0.27	94.72	623.26
C1-VF-V10	36.80	0.185	5.92	2.79	47	0.55	72.51	0.04	22.58	6.19	0.81	102.68	553.62
C1-STF-V10	34.95	0.207	6.52	5.39	83	0.40	73.83	0.02	22.21	90.63	1.33	188.42	909.26
C1-E-V20	38.79	0.149	7.01	2.37	34	8.37	81.53	0.74	-	-	1.47	92.11	619.61
C1-PP-V20	37.41	0.152	7.08	2.92	41	7.36	75.09	0.10	26.51	-	0.11	109.18	718.47
C1-VF-V20	36.20	0.185	7.77	3.34	43	6.27	76.36	0.01	27.79	8.73	1.62	120.78	651.23
C1-STF-V20	33.63	0.207	9.06	7.86	87	6.04	77.81	0.06	24.38	154.86	1.27	264.41	1,275.99
C1-E-V30	39.02	0.149	7.75	3.15	41	22.68	97.00	1.24	-	-	2.03	122.94	827.05
C1-PP-V30	38.19	0.152	7.94	3.68	46	19.30	86.46	0.31	33.82	-	0.59	140.47	924.35
C1-VF-V30	35.91	0.185	9.18	4.25	46	17.59	83.87	0.02	35.03	12.66	3.64	152.81	823.91
C1-STF-V30	32.71	0.207	10.75	9.94	92	17.10	79.10	0.04	23.70	204.00	1.18	325.12	1,568.95

5.4.1.3 Energy absorption capacity of SSBF under various crushing speeds

As observed in Figure 5-12, SSBF is a crushing-rate sensitive structure, whose energy absorption capacity increases with the increase of crushing speed. When the crushing speed increases from 10 m/s to 20 m/s, the *SEA* of SSBF increases by 40% from 909.26 J/kg to 1,275.99 J/kg, which is 106%, 78%, and 96% higher than that of C1-E-V20, C1-PP-V20, and C1-VF-V20, respectively. The *SEA* of SSBF increases up to 73% when the crushing speed increases to 30 m/s, which is 90%, 70%, and 90% higher than that of C1-E-V30, C1-PP-V30, and C1-VF-V30 under the same 30 m/s crushing, respectively. This significant enhancement of *EA* of SSBF is due to the shear thickening behaviour of STF. As the loading increases, the STF/core-wall shear interactions become higher, leading to higher apparent viscosity and viscous dissipation of STF as well as the energy absorption capacity of SSBF. Hence, the energy absorption capacity of SSBF increases with the increase of impact energy, showing the adaptability to the uncertainty of real impact scenarios and avoiding the fixed energy absorption capacity of conventional energy absorption structures (i.e., empty, or PU foam-filled specimens in this chapter).

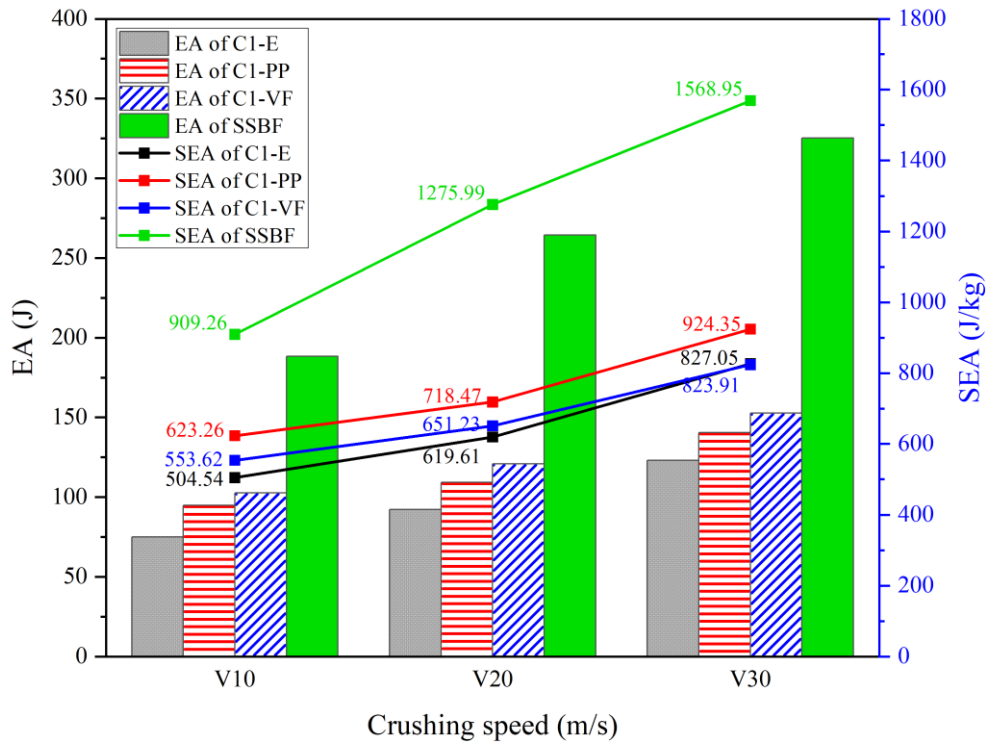


Figure 5-12. Comparison of *EA* and *SEA* of empty, PU foam-filled, viscous fluid-filled, and STF-filled specimens under various crushing speeds.

5.4.2 Deformation mode of SSBF

Figure 5-13(a) and (b) show the deformation of empty (C1-E-V10) and partially filled PU foam (C1-PP-V10) under 10 m/s crushing speed, respectively. It is observed that the deformation of empty and PU foam-filled specimens is quite similar during the crushing process. As the loading plate crushes the front plate of the specimen, the curved cores plastically deform inward, thus dissipating the energy through plastic deformation.

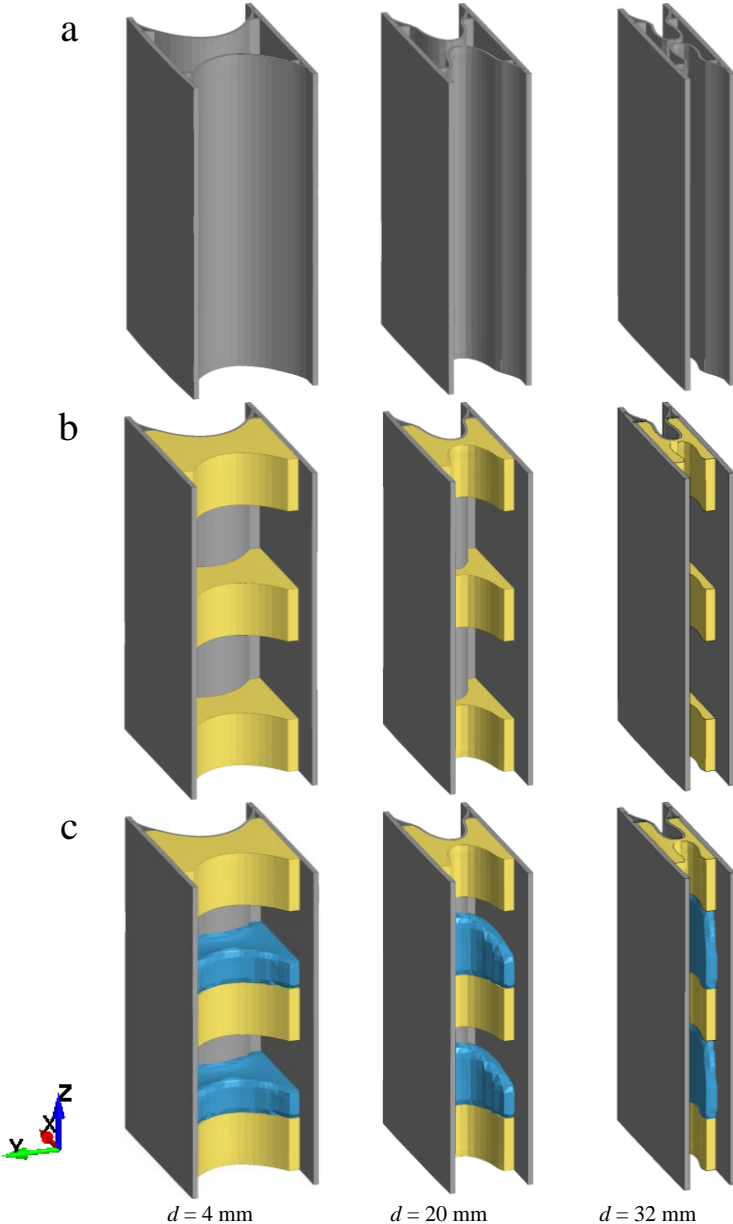


Figure 5-13. Deformation of (a) empty, (b) partially filled PU foam, and (c) viscous fluid-filled specimens.

In case of PU foam-filled specimen, the PU foam is crushed horizontally in both X- and Y-direction by the curved core wall and external plates, respectively. Therefore, the crushing resistance and energy absorption capacity of PU foam-filled specimen are enhanced by the curved core wall/PU foam interaction and the crushing of PU foam.

Similarly, for the deformation of viscous fluid-filled specimen shown in Figure 5-13(c), the bending of curved cores generates shear and compression deformation on the fluid, which lead to a viscous dissipation of the fluid. However, after the bending of the curved cores, the PU foams and viscous fluid provide little support to the core, causing a low and fluctuating crushing force. Furthermore, as the crushing speed increases, the crushing force remains similar to that under lower crushing speed because of the invariable viscosity of the Newtonian viscous fluid. Therefore, adding Newtonian viscous fluid only slightly improves the crushing force but increases the overall weight of the specimen, making it an ineffective choice for enhancing the energy absorption capacity.

During the crushing process of SSBF with STF, the deformations of core walls generate shear force and jamming front on STF along X-direction, which trigger the shear thickening behaviour and high normal stress of STF [149,207]. This jamming front causes the rise of the effective stress at the centre of the cross-section of STF, as shown in Figure 5-14(a). As the core further deforms, STF is squeezed out and flows upward inside the gaps, generating further STF/core-wall shear interactions in the vertical Z-direction, as illustrated in Figure 5-14(b). During this flow, the effective stress of STF near the external plates increases while that of STF at the centre decreases, leading to a high and stable crushing force of SSBF, as shown in Figure 5-8. Therefore, the STF/core-wall interactions and STF jamming front trigger the shear thickening and solid-like transformation of STF due to the rise of viscosity, thus increasing the viscous dissipation of STF and enhancing the crushing resistance of SSBF. Furthermore, with the increase in loading rate, the viscosity and viscous dissipation of STF become even higher, leading to a further enhancement of crushing resistance and energy absorption performance of SSBF without a high initial crushing force. It should be noted that the internal gaps inside the core allow the deformation of STF during crushing, thus preventing the full compression of the incompressible STF

fluid. With further compression, the STF is confined between the external plates and the core walls, leading to the densification of SSBF.

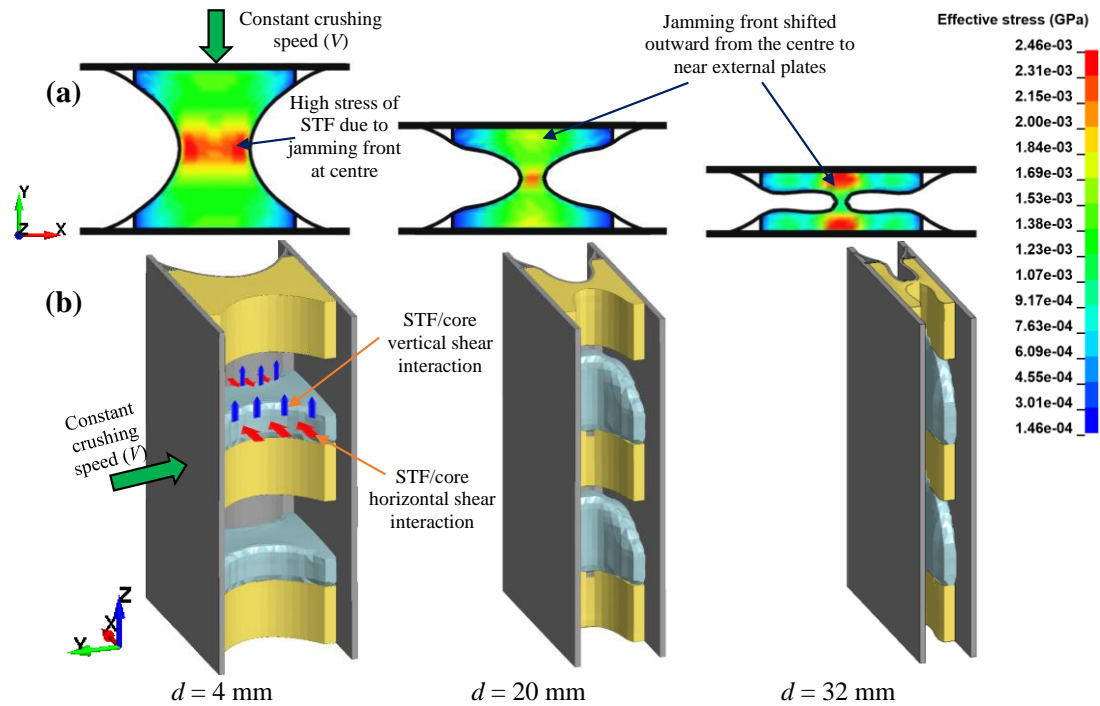


Figure 5-14. (a) Cross-section showing the distribution of effective stress of the STF and (b) isometric view showing the deformation of SSBF specimen.

5.4.3 Comparison between SSBF and conventional specimen with comparable mass

In this section, for a fair comparison, the empty specimen denoted by C2-E with an increased core wall thickness of 2 mm, based on C1-E, is selected so that its mass is comparable to that of SSBF specimen. It should be mentioned that the details of SSBF and loading conditions are the same as those described in Section 5.3. Both specimens are tested under two different crushing speeds of 10 m/s and 30 m/s. As shown in Figure 5-15, by increasing the core wall thickness, the initial peak force of the empty specimen (i.e., C2-E-V10, C2-E-V30) substantially increases as the crushing speed increases because of its stiffness and inertial effect, while the crushing force profiles remain similar. Once the core buckles, the crushing force substantially decreases and fluctuates along the crushing process. Therefore, the *CFE* of the empty specimen decreases from around 64% to 44% as the crushing speed increases from 10 m/s to 30 m/s. In contrast, the force-displacement profile of SSBF (i.e., C1-STF-V10, C1-STF-V30) remains relatively constant throughout the compression without a noticeable

initial peak force. Furthermore, this constant crushing force increases with the increase of crushing speed, showing a good behaviour for energy absorption [6]. As the crushing speed increases from 10 m/s to 30 m/s, the *CFE* of SSBF increases from 87% to 92%. In terms of energy absorption capacity, under 10 m/s crushing speed, the *MCF* of SSBF is lower than that of the empty specimen, resulting in a lower *EA*. However, as the crushing speed increases to 30 m/s, the *MCF* of SSBF increases almost two-fold, while that of the empty specimen remains similar, leading to a higher *EA* than that of the empty specimen. Therefore, the proposed SSBF is capable of absorbing various impact energy inputs and adapting to a variety of impact speeds, owing to the enhanced shear thickening behaviour of STF at a high crushing rate.

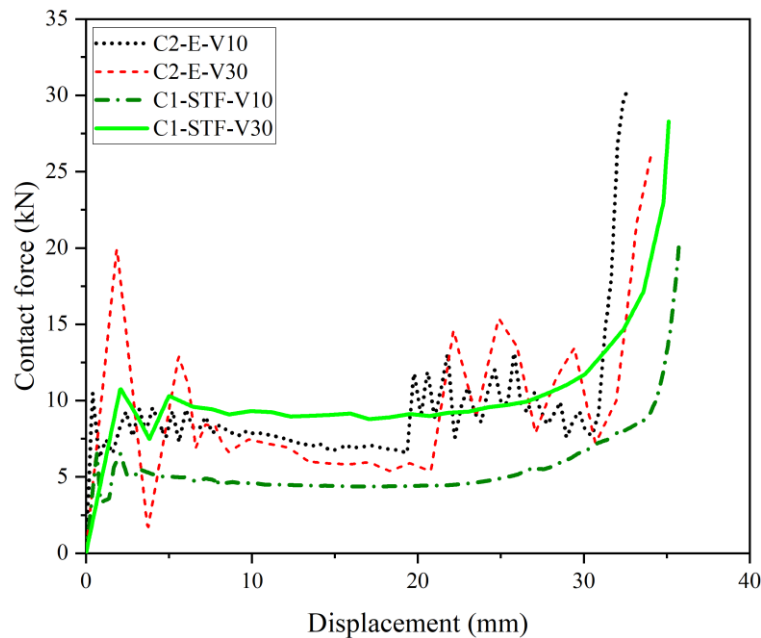


Figure 5-15. Force-displacement profiles of SSBF and empty specimen with thick core (C2-E) under two crushing speeds.

5.5 Summary

In this chapter, a novel Sandwich Structure inspired by Beetle Forewing (SSBF) is proposed by mimicking the internal structure of beetle forewing and its crushing performance is numerically investigated by using LS-DYNA. The viscoelastic material and the arch shape of hollow cavity structures of the beetle forewing are mimicked by utilising STF and semi-arch cores, respectively. The mean crushing force and energy absorption capacity of SSBF under various crushing speeds are investigated, and the following conclusions can be drawn.

- The proposed SSBF design can enhance the mean crushing force, stabilise the crushing force profile and increase the crushing force efficiency compared with the conventional empty, PU foam-filled, or Newtonian viscous fluid-filled specimens.
- The effect of crushing speed on the specific energy absorption capacity (*SEA*) of SSBF structure is also investigated. When the crushing speed increases from 10 m/s to 30 m/s, the *SEA* of empty, PU foam-filled, and Newtonian viscous fluid-filled specimens remains similar. In contrast, the *SEA* of SSBF increases with the increase of crushing speed, showing its ability to adapt to various impact scenarios.
- The proposed SSBF is compared with an empty specimen with a thick core and hence comparable mass. When the crushing speed increases, the initial peak force of the empty specimen substantially increases but the mean crushing force remains almost unchanged, while the mean crushing force of SSBF increases with the crushing speed and its force-displacement profile remains constant throughout the compression process without a noticeable initial peak force, showing ideal behaviour for energy absorption.

Chapter 6. Bio-inspired shear thickening fluid-filled origami metastructure (STF-OM)

The related work in this chapter was published in Engineering Structures:

Lam L, Chen W, Hao H, Li Z. Dynamic crushing and energy absorption of bio-inspired shear thickening fluid-filled origami metastructure. *Engineering Structures* 2024;299:117122

<https://doi.org/10.1016/j.engstruct.2023.117122>

6.1 Introduction

In Chapter 5, an innovative energy-absorbing structure is proposed, and adaptive energy-absorbing capability is achieved by implementing the protective mechanism of the beetle. Its crushing resistance and energy-absorbing capacity significantly enhance as the crushing speed increases, i.e., enhanced by approximately 80% as the crushing speed increases from 10 m/s to 30 m/s. This enhancement results from the inward bending of its curved cores, which generate high shear interaction with the STF. However, this inward bending of curved cores leads to a slight drop in crushing resistance at the initial stage, resulting in a slightly lower crushing efficiency of the structure. In this chapter, a novel approach is proposed to develop an innovative nature-inspired design with ideal crushing efficiency and adaptive crushing resistance. The shear thickening fluid (STF) is incorporated into the cells of the origami metastructure to mimic the existence of the viscoelastic material found inside the protective mechanism in nature, such as inside the tubules in the horn sheath of bighorn sheep [141], between the sutures in the beak of woodpeckers [145,147], and in the forewings of beetle [136,138], as shown in Figure 6-1. The dynamic crushing and energy-absorbing performances of the proposed STF-filled origami metastructure are numerically investigated using the commercial software LS-DYNA. The coupling between the infilled fluid and structure parts is simulated using the FSI method. The compression test of the origami metastructure under dynamic loads, conducted by Harris and McShane [51], is adopted for model calibration. The numerical results are validated with the testing data by comparing the compressive stress-time response and the deformation process. Then, the same modelling technique is used to construct the

origami metastructure in this chapter. The same FSI approach and material model of STF as in Chapter 5 [112] are adopted to model the proposed STF-filled origami metastructure (STF-OM). The crushing performances of STF-OM are assessed by comparing the peak crushing force (*PCF*), mean crushing force (*MCF*), crushing force efficiency (*CFE*), energy absorption capacity (*EA*), and specific energy absorption capacity (*SEA*) with the non-filled and viscous fluid-filled counterparts under various crushing velocities. The influences of the filled height of STF, the viscosity of STF, and the origami folding angle on the crushing performances of STF-OM are also investigated.

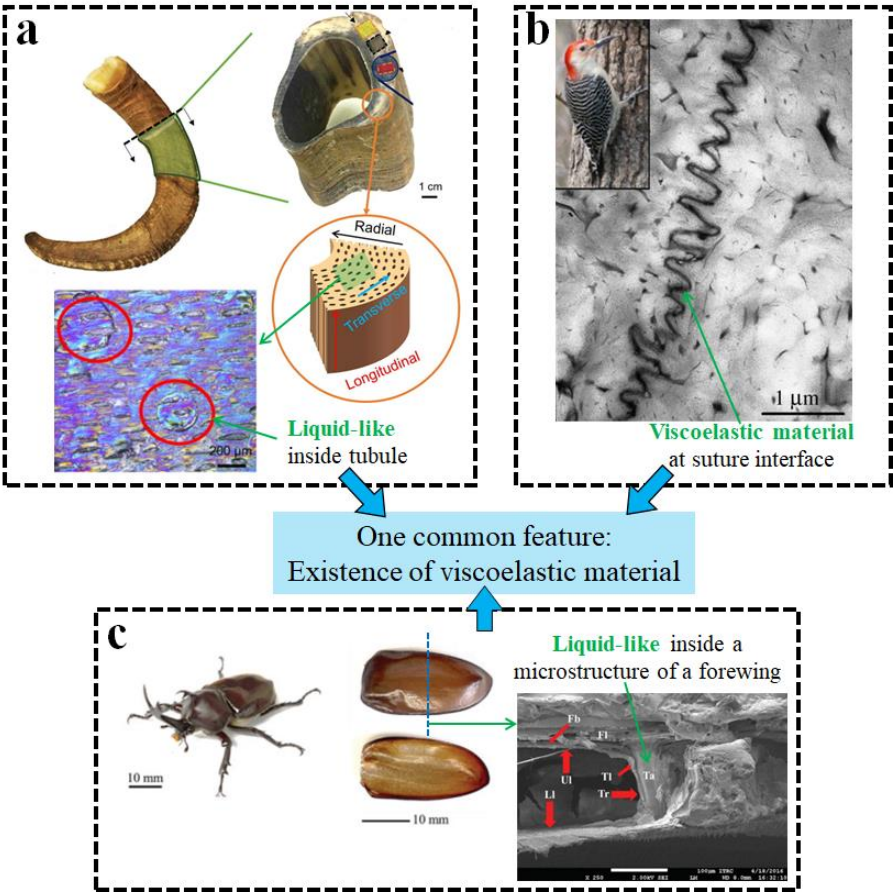


Figure 6-1. Existence of viscoelastic material found inside the (a) horn sheath of bighorn sheep [141], (b) suture interface of woodpecker [145], and (c) forewing of the beetle [136].

6.2 Numerical model calibration

The dynamic compression test of origami metastructure carried out by Harris and McShane [51] is adopted for model calibration. Several tests were performed by using a gas gun to crush the specimen under various dynamic crushing speeds. The origami

metastructure consists of $3 \times 5 \times 2$ unit cells along X , Y , and Z directions. Each unit cell has a width ($2l$) \times height (h_c) \times length ($2s$) of $6.5 \text{ mm} \times 6.5 \text{ mm} \times 6.5 \text{ mm}$, resulting in an overall dimension of $19.5 \text{ mm} \times 19.5 \text{ mm} \times 13.0 \text{ mm}$, as shown in Figure 6-2(a) and (b). Each unit cell has a folding angle μ of 37° , and top α and bottom β intersection angles of 90° and 53° , respectively, as marked out in Figure 6-2(b). The origami metastructure was made of stainless steel 316L with a wall thickness of 0.16 mm using selective laser melting (SLM) system. It was attached to the stationary Hopkinson bar and crashed by a steel projectile using a gas gun, as illustrated in Figure 6-2(c). The dynamic crushing test of the origami metastructure at the crushing speed of 50 m/s is selected for model calibration. The accuracy of the numerical model is validated by comparing the dynamic compressive stress-time history and the deformation process of the origami metastructure obtained from the numerical simulation and the experimental test [51]. The compressive stress of the experimental test is obtained by dividing the transient force measured at the supported face (Hopkinson bar) by the base area of the specimen, as marked out in Figure 6-2(a) [51]. Similarly, the predicted compressive stress of the numerical simulation is calculated by dividing the contact force by the base area of the model.

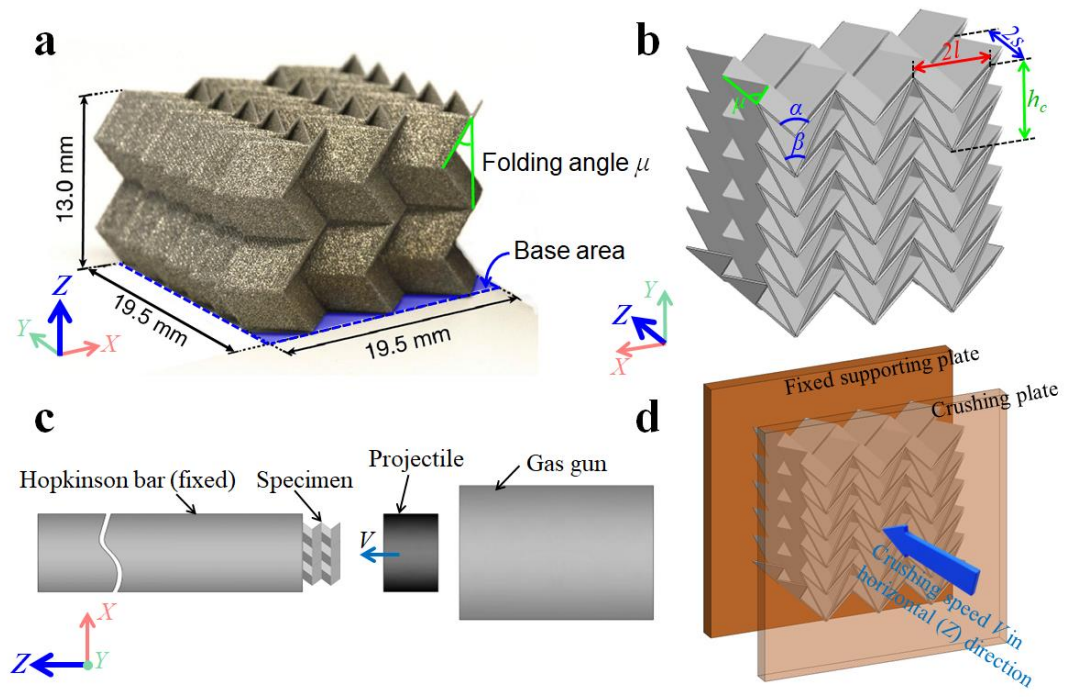


Figure 6-2. (a) Origami metastructure [51], (b) FE model, (c) setup of the dynamic compression test of the origami metastructure [51], and (d) boundary and loading conditions of FE model.

6.2.1 Numerical model

The numerical model of the origami metastructure is established using LS-DYNA. A default Belytschko-Tsay type shell element with five integration points through the shell thickness is used to model the origami metastructure. An elasto-plastic material model, *MAT_PIECEWISE_LINEAR_PLASTICITY, is used for the SLM stainless steel 316L material whose mechanical properties are listed in Table 6-3. Its true plastic stress-strain curve can be obtained from [107]. The boundary and loading conditions of the finite element (FE) model are depicted in Figure 6-2(d). The origami metastructure is simply supported by a fixed rigid plate, which replicates the stationary Hopkinson bar, and compressed by another rigid crushing plate replicating the steel projectile. The speed of the projectile is assumed to be constant for the whole crushing process [51]. Therefore, the specimen is constantly crushed by the crushing plate under the crushing velocity of 50 m/s in the horizontal (Z) direction only. The *CONTACT_AUTOMATIC_SINGLE_SURFACE and *CONTACT_AUTOMATIC_SURFACE_TO_SURFACE keywords are used to simulate the self-contact of the origami metastructure and the contacts between the origami metastructure and the rigid plates, respectively. The friction coefficient for all contact interfaces is set to 0.2 [208].

6.2.2 Model calibration

The comparison of compressive stress-time responses of the origami metastructure generated from the test [51] and FE simulation is shown in Figure 6-3(a). It is shown that the FE simulation accurately predicts the dynamic compressive response of the origami metastructure as compared to the experimental result [51]. The difference between the average compressive stress obtained from the simulation and the experiment is only approximately 6%. However, discrepancies in the compressive stress and densification at the later stage of crushing are observed. It may be due to the excess material in the fold lines and the inconsistent wall thickness of the real specimen [51], resulting in early densification and the rise of the crushing force. The FE model also predicts well the deformation process observed in the test, as illustrated in Figure 6-3(b). Overall, the FE model accurately predicts the dynamic crushing response of the origami metastructure. Hence, the same modelling technique is employed for the proposed structures in the following sections.

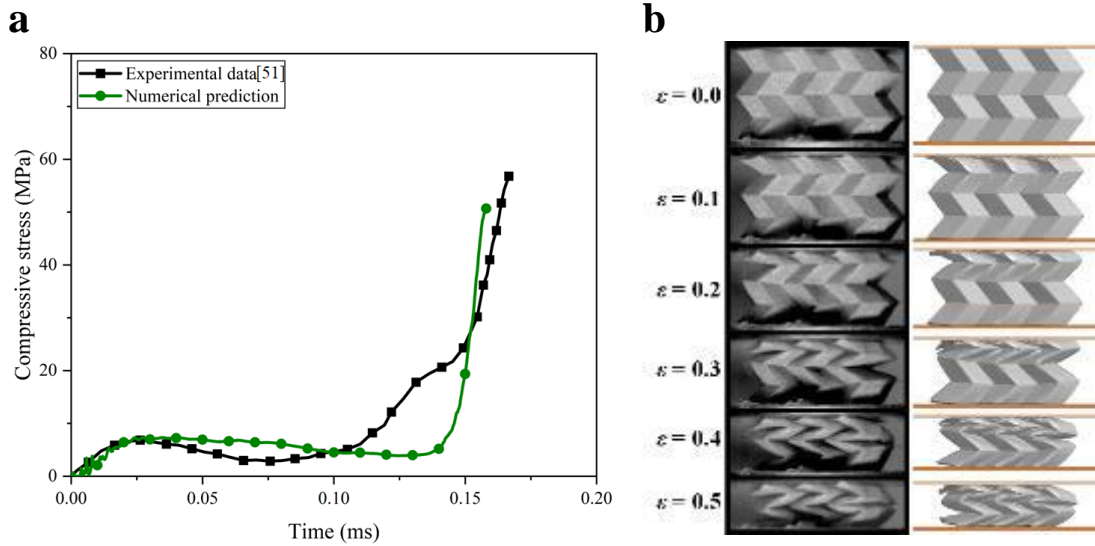


Figure 6-3. Comparison of (a) the compressive stress-time responses and (b) the deformation process of the origami metastructure obtained from the experiment [51] and numerical simulation.

6.3 Shear thickening fluid-filled origami metastructure (STF-OM)

6.3.1 Geometries and loading conditions

Figure 6-4(a) illustrates the isometric view of the origami metastructure (OM), whose structure can be fabricated by alternating stacked two types of standard aluminium Miura-origami panels with intersection angles α and β [99], denoted as panels A and B, respectively. In this chapter, the structure of OM is constructed by stacking three layers of stacked panels A and B with a folding angle μ , as shown in Figure 6-4(a) and (b). These contiguous panels are assumed to be perfectly bonded in the numerical model by using the common nodes. The origami metastructure consists of $3 \times 3 \times 3$ unit cells along X , Y , and Z directions. The unit cell is adopted from the previous study by Yang et al. [99], as illustrated in Figure 6-4(c). The geometric parameters of the origami metastructure are summarised in Table 6-1.

Table 6-1. Geometric parameters of origami metastructure [99].

$\mu(^{\circ})$	$\alpha(^{\circ})$	$\beta(^{\circ})$	h_c (mm)	l (mm)	s (mm)	v (mm)	H (mm)	W (mm)	L (mm)	t (mm)	ρ_v (%)
30	120	60	15.87	9.17	10	5.77	37	55	60	0.29	8

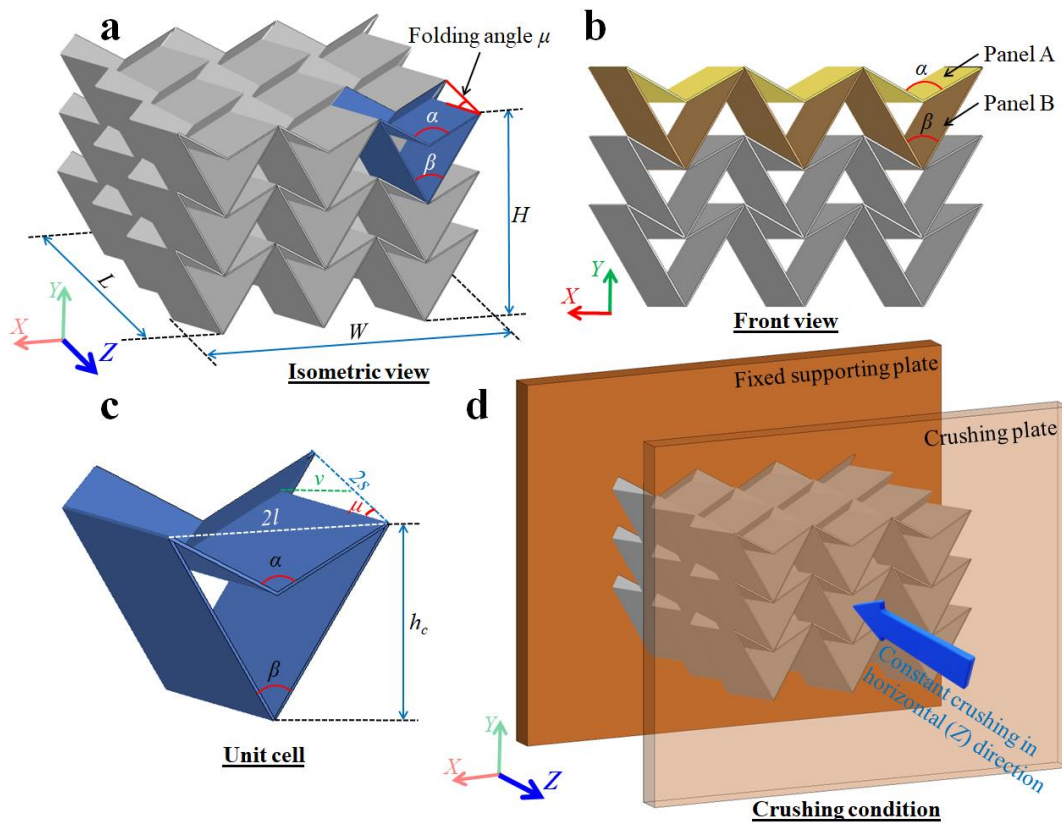


Figure 6-4. (a) Isometric view of origami metastructure (OM), (b) front view, (c) unit cell of OM [99], and (d) crushing condition.

The shear thickening fluid (STF) filled origami metastructure (OM) is proposed by partially filling the STF inside each layer, and thin rubber of 0.1 mm thickness is used to seal the opening side at both ends of the structure, as illustrated in Figure 6-5(a). This STF-filled origami metastructure is denoted as STF-OM. Newtonian viscous fluid (i.e., silicone oil) is also chosen as a filler of the OM for comparison. The non-filled (empty) and viscous fluid-filled origami metastructures are denoted as E-OM and VF-OM, respectively. The origami metastructure (E-OM) is made of the aluminium 1060 sheet with a wall thickness (t) of 0.29 mm and a folding angle (μ) of 30° , resulting in a volumetric density ρ_v (ratio of the material volume in the structure to the overall volume of the structure) of 8%. In this chapter, this aluminium sheet is chosen because it allows the origami metastructure to be made using the mould-pressing technique [99,209], and the folding angle of 30° is initially chosen because high compressive strength and stiffness with low softening of the structure can be obtained within this range of the folding angle [103,107]. The fluid-filled origami metastructure (VF-OM or STF-OM) is formed by partially filling E-OM with the corresponding fluid to the height h of 7.5 mm, as shown in Figure 6-5(b), corresponding to around 41% of the

internal volume of E-OM. The remaining internal volume, around 59%, allows the fluid to flow and deform during compression, thus preventing it from being fully compressed. The overall masses of E-OM, VF-OM, and STF-OM are 0.027 kg, 0.057 kg, and 0.077 kg, respectively.

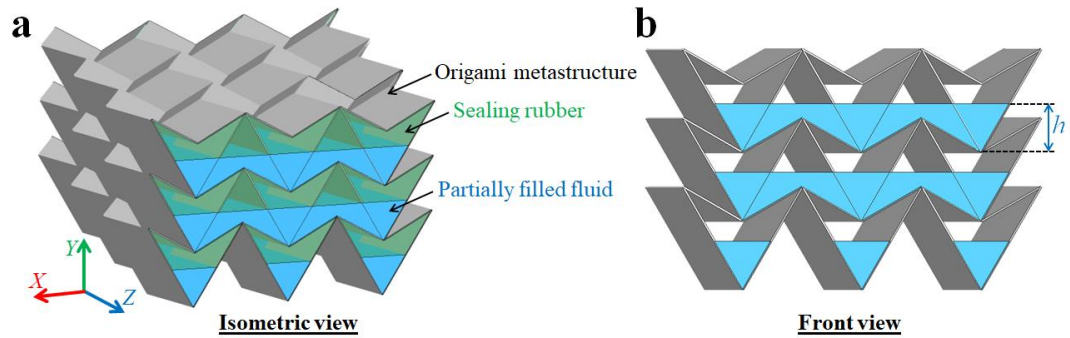


Figure 6-5. (a) Isometric view of fluid-filled origami metastructure and (b) front view (sealing rubber is not shown for illustration).

In this chapter, the proposed structure is designed to resist horizontal loads along its out-of-plane direction. Thus, it is crushed by a rigid crushing plate, which is translated in the horizontal (Z) direction only, as illustrated in Figure 6-4(d). It should be mentioned that this origami metastructure has a larger negative Poisson's ratio when it is crushed in its out-of-plane (Z) direction than when it is crushed in the other two (X or Y) directions [99,106]. This large negative Poisson's ratio or high contraction during the crushing may generate more flow of fluid and shear/compression interactions between its folding structure and infilled STF, thus resulting in the increase in shear thickening [149] and compression thickening behaviours [150,151], as well as viscous dissipation of the STF [54,155,156]. Therefore, this out-of-plane direction is chosen as the crushing direction in this chapter.

Three different constant crushing velocities of 10 m/s, 20 m/s, and 40 m/s (denoted as V10, V20, and V40, respectively) are considered to investigate the crushing-rate effect on the crushing performances of the structure, which is discussed in Section 6.4. Each structure is denoted by its filling material and crushing velocity. For example, STF-OM-V40 denotes the origami metastructure, which is filled with STF and crushed at the speed of 40 m/s. The notations of all specimens are summarised in Table 6-2. The effects of the filled height (h) of STF, viscosity of STF, and folding angle (μ) on the crushing performances of STF-OM are also carried out and discussed in Sections 6.5.1, 6.5.2, and 6.5.3, respectively.

Table 6-2. Specimen configurations.

Filling material	Crushing velocity V (m/s)		
	10	20	40
Empty (E)	E-OM-V10	E-OM-V20	E-OM-V40
Viscous fluid (VF)	VF-OM-V10	VF-OM-V20	VF-OM-V40
Shear thickening fluid (STF)	STF-OM-V10	STF-OM-V20	STF-OM-V40

6.3.2 Material models and FE modelling techniques

The origami metastructure is made of thin aluminium 1060 sheet, and it is modelled using a default Belytschko-Tsay shell element. The material properties of the aluminium 1060 sheet are listed in Table 6-3, and its true plastic stress-strain curve is obtained from the previous study [99]. For fluid-filled origami metastructure, the Eulerian element is used to mesh the fluid, which is enclosed by the Eulerian mesh of the air domain, thus allowing the Eulerian material of fluid to flow through during deformation [196,197]. The interactions between the infilled fluid (i.e., STF or viscous fluid) and the structure parts (i.e., origami structure and rubber) are modelled using the same FSI technique via the keyword *CONSTRAINED_LAGRANGE IN SOLID in LS-DYNA as described in Section 5.2. For the material models, material properties, and EOS parameters of STF, viscous fluid, air, and rubber, please refer to Table 5-2 in Section 5.3.2. After performing the mesh size convergence test, the 2 mm mesh size of Lagrangian elements and the finer 1 mm mesh size of Eulerian elements are determined, ensuring both simulation accuracy and computational time.

Table 6-3. Material properties of SLM stainless steel 316L and aluminium 1060 sheet.

Material	Material model and EOS	Parameter	Value
SLM stainless steel 316L [51,107]	*MAT_PIECEWISE_LINEAR_PLASTICITY	ρ (kg/m ³)	8000
		E (GPa)	131
		ν	0.3
		σ_y (MPa)	376
Aluminium 1060 [99]	*MAT_PIECEWISE_LINEAR_PLASTICITY	ρ (kg/m ³)	2710
		E (GPa)	70
		ν	0.33
		σ_y (MPa)	145

6.4 Results and discussions

Peak crushing force (*PCF*), average or mean crushing force (*MCF*), crushing force efficiency (*CFE*), energy absorption capability (*EA*), and specific energy absorption capacity (*SEA*) are used as the key evaluating criteria of the crushing performances of the proposed structure. The details of each key evaluating criterion can be found in Section 3.4.

6.4.1 Dynamic crushing of STF-OM under different velocities

The influence of the crushing velocities on the crushing responses and energy-absorbing performances of the proposed STF-filled origami metastructure (STF-OM) are investigated and compared with those of non-filled (E-OM) and viscous fluid-filled (VF-OM) origami metastructures. Three different crushing velocities of 10 m/s, 20 m/s, and 40 m/s are used for the investigation. The OM structure of all the specimens has the same wall thickness of 0.29 mm and folding angle μ of 30°, and the fluids are filled to the same height h of 7.5 mm for the structures filled with fluid.

6.4.1.1 Deformation mode comparison

The damage modes of E-OM, VF-OM, and STF-OM under 20 m/s are very similar to those under 40 m/s. Therefore, only the damage modes under 10 m/s and 40 m/s are shown. The damage modes at different compressive strains of E-OM under 10 m/s and 40 m/s are illustrated in Figure 6-6(a) and (b), respectively. The compressive strain is the ratio of the crushing distance to the overall length (L) of the specimen. Under 10 m/s, the stress concentrations initially occur along the crease lines and distribute uniformly through the crushing length, showing its uniform bending deformation throughout the crushing process. Similar deformation behaviour is also observed in the compressions of the stacked origami-based cellular materials [51,99,107,210]. Under a higher crushing speed of 40 m/s, the stress concentrations mostly occur at the crushing end at the initial crushing stage, showing that the deformation of the structure is localised at the crushing end, while the deformation at the supporting end is minimal. It is due to the inertial resistance of the structure and the inertial stabilization of its sidewalls, thus delaying the drop of the crushing resistance to a larger crushing distance than under a lower crushing speed [12]. However, the crushing resistance

significantly drops after buckling because of the easy bending of the pre-exhibit creases, thus resulting in a low bending resistance [99].

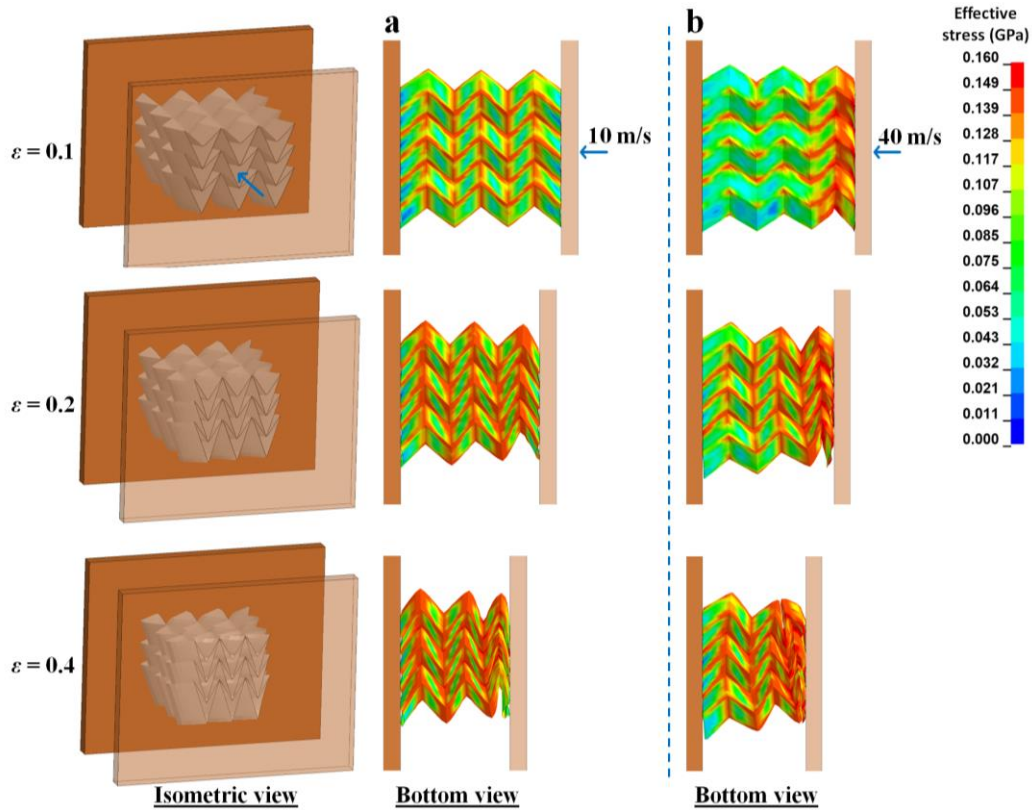


Figure 6-6. Damage modes of E-OM at the compressive strains of 0.1, 0.2, and 0.4 under (a) 10 m/s and (b) 40 m/s.

The deformation mode of VF-OM is quite similar to that of E-OM under the same crushing speed, as shown in Figure 6-7. During crushing, the folding and contracting of the structure of VF-OM cause the squeeze and slosh of the viscous fluid, which provides additional support to the folding sidewalls of the structure. With further compression, the fluid flows and fills up the internal space, causing the densification of the structure. Under a higher crushing speed of 40 m/s, the severe deformation at the crushing end still occurs because of the insufficient supports provided by the viscous fluid, causing the abrupt reduction of the empty space, which results in the early occurrence of densification.

The damage modes of STF-OM under 10 m/s and 40 m/s are illustrated in Figure 6-8(a) and (b), respectively. During the crushing of STF-OM, the compression and contraction of the origami metastructure generate the flow of STF, as well as the compression/shear interactions between its folded shape structure and STF, triggering the thickening behaviour of the STF. Under 10 m/s, the structure of STF-OM uniformly

folds and contracts along the crease lines, transforming the STF into a solid-like material with high viscosity and high stress, as shown in Figure 6-9(a), which provides support to the bending sidewalls, thus increasing the crushing resistance of the structure. During crushing, the solid-like STF deforms and gradually flows to the empty space of the unit cells, leading to viscous energy dissipation during this flow and deformation. With further crushing, STF-OM reaches its densification due to the shear thickening effect and high viscosity of the STF. A similar finding of early densification was also observed in the dynamic compression test of an STF-filled honeycomb [174]. Under a higher crushing speed of 40 m/s, the deformation at the crushing end triggers the thickening effect of the STF at a higher rate which causes the viscosity and stress of the STF to be even higher as shown in Figure 6-9(b), thus preventing the severe localised deformation and further enhancing the crushing resistance of the structure. As the crushing continues, the deformed sidewalls along the crushing direction trigger shear thickening of the surrounding STF, thereby providing further support to the deformed sidewalls and stabilising the crushing resistance of the structure.

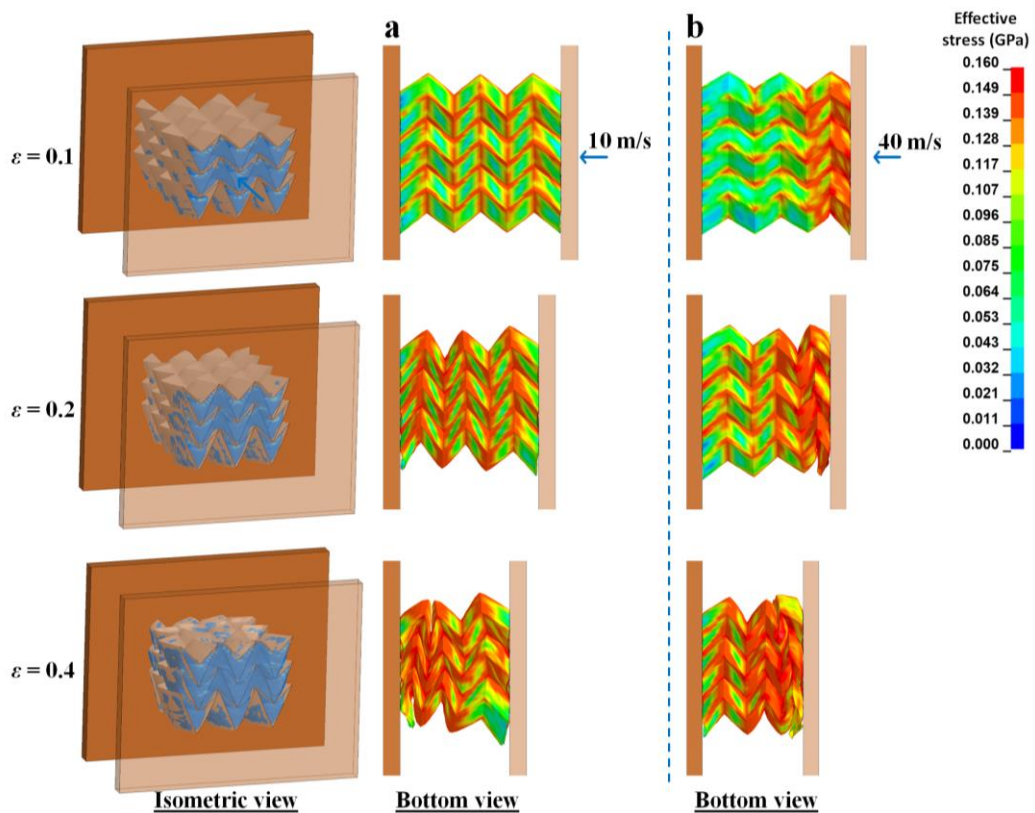


Figure 6-7. Damage modes of VF-OM at the compressive strains of 0.1, 0.2, and 0.4 under (a) 10 m/s and (b) 40 m/s.

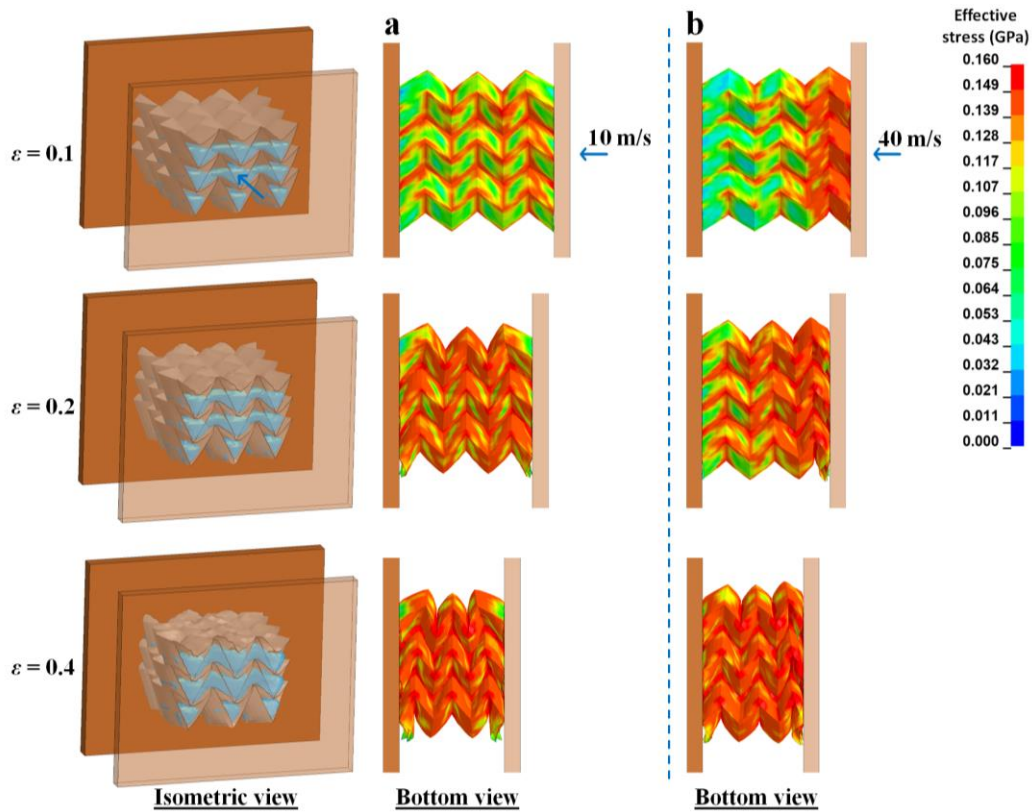


Figure 6-8. Damage modes of STF-OM at the compressive strains of 0.1, 0.2, and 0.4 under (a) 10 m/s and (b) 40 m/s.

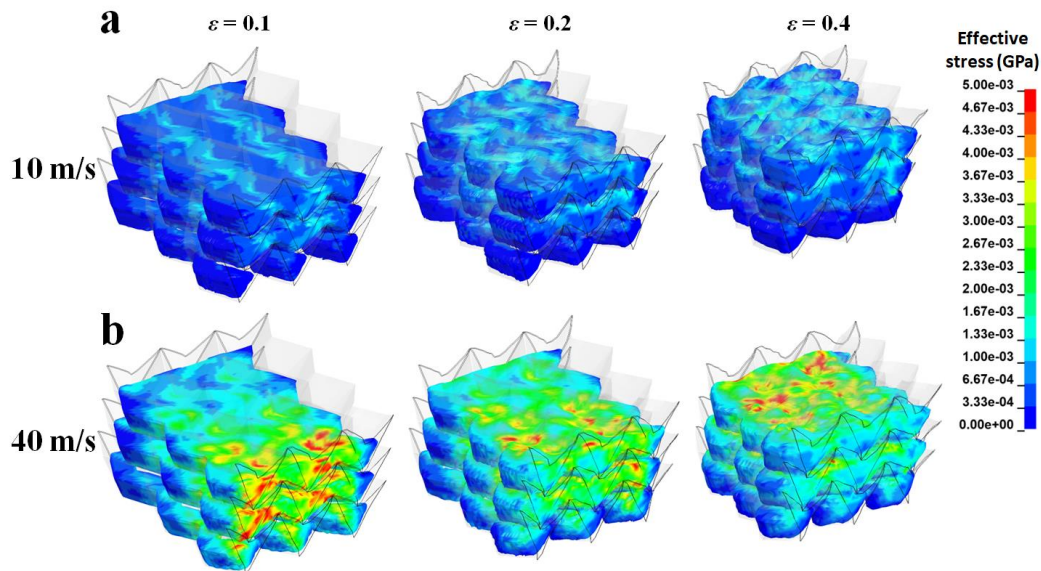


Figure 6-9. Effective stress distributions of the STF at 0.1, 0.2, and 0.4 compressive strains of STF-OM under (a) 10 m/s and (b) 40 m/s.

6.4.1.2 Crushing response and energy-absorbing capacity

The force-displacement curves of E-OM, VF-OM, and STF-OM under different crushing speeds are shown in Figure 6-10(a), (b), and (c), respectively. The crushing

force profiles of all specimens show three deformation stages of energy-absorbing structures such as the elastic stage, followed by a long plateau stage, and the densification stage where the crushing force rises significantly [40]. As shown in Figure 6-10(a) and (b), the crushing force profiles of E-OM and VF-OM show a similar trend under the same crushing speed by having a high *PCF* at the initial elastic stage, followed by a significant drop of the crushing force due to the buckling and bending of the structure along the crease lines. With further crushing, E-OM (non-filled) further folds and contracts in its in-plane directions. Then, its structure condenses and densifies at around 35 mm to 40 mm of the crushing distance, thus reaching its densification stage. However, for VF-OM (viscous fluid-filled), the crushing force starts to increase after the drop in its plateau stage because the viscous fluid flows to the empty space during the compression and contraction, thus providing support to the contracted sidewalls. However, since the fluid is incompressible, VF-OM reaches its densification stage (at around 28 mm to 33 mm of the crushing distance) earlier than E-OM. As the crushing velocity rises from 10 m/s to 40 m/s, there is no significant change in the crushing forces of E-OM and VF-OM in the plateau regime, except that the dropping rate (softening) of crushing force after the buckling reduces owing to the change of the deformation mode.

For STF-OM, the crushing force is enhanced and stabilised without a significant drop, as shown in Figure 6-10(c). During the crushing of STF-OM, the compression and contraction of the origami metastructure trigger the shear thickening behaviour of the STF, which transforms the STF into a highly viscous fluid, thus providing support to the bending sidewalls of the structure. With further crushing, the STF is squeezed into the empty space, thus stabilising the crushing force, and dissipating the energy through viscous dissipation. This similar crushing enhancement of the structure after buckling has also been observed in the investigation of the lattice sandwich panel filled with STF under dynamic crushing [54,175]. Finally, the STF-OM densifies, and its onset of densification is earlier than that of E-OM and VF-OM, owing to the shear thickening effect and high viscosity of the STF. As the crushing speed increases, the viscosity of STF also increases, resulting in the further enhancement of the crushing force, as well as earlier densification of STF-OM.

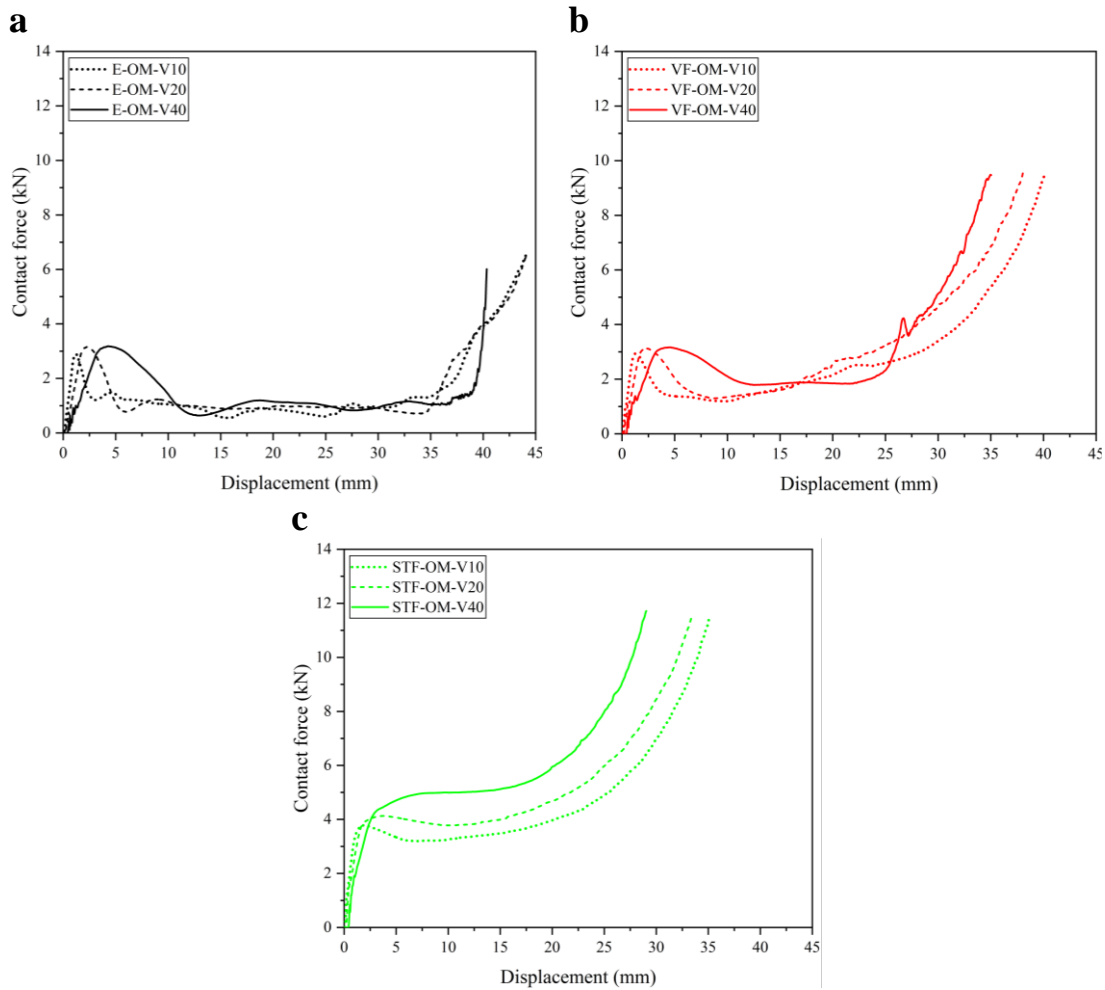


Figure 6-10. Force-displacement responses of (a) E-OM, (b) VF-OM, and (c) STF-OM under 10 m/s, 20 m/s and 40 m/s crushing speeds.

The energy absorption of each component of E-OM, VF-OM, and STF-OM under different crushing speeds is shown in Figure 6-11. Under the same crushing speeds, partial filling with fluid (i.e., VF or STF) enhances the total energy absorption of E-OM, which is contributed by the viscous dissipation of fluid and the increase in plastic deformation of OM owing to the interaction with the infilled fluid. This energy absorption enhancement is even more significant when filling with the STF, owing to its shear thickening effect. For STF-OM-V10, the viscous dissipation of STF contributes around 39.2%, while the plastic deformation of OM contributes around 57.9% and the small remaining is contributed by the deformation of rubber and friction. As the crushing velocity rises from 10 m/s to 40 m/s, the energy absorbed by STF increases by around 45% from 45.10 J to 65.31 J, which is around 51.4% of the total energy absorbing capacity of STF-OM-V40.

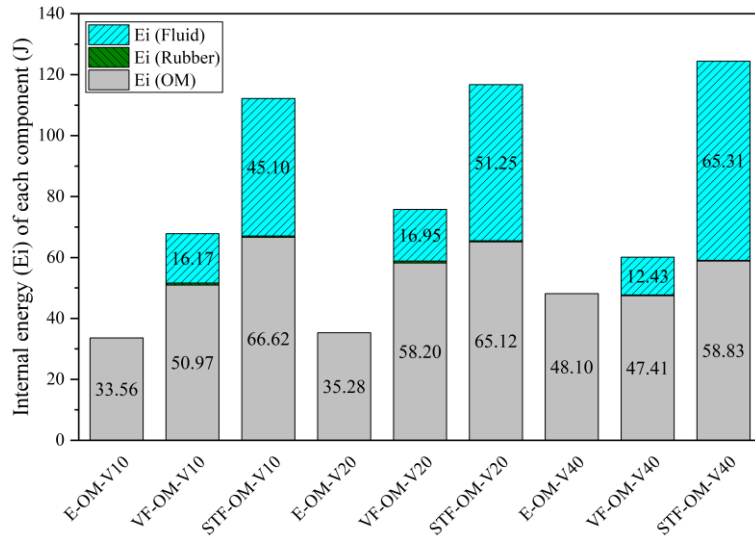


Figure 6-11. Energy absorption of each component of E-OM, VF-OM, and STF-OM under different crushing speeds.

6.4.2 Comparison of the crushing performances under various crushing velocities

The crushing performances of all the specimens under 10 m/s, 20 m/s, and 40 m/s crushing speeds are compared in Figure 6-12(a), (b), and (c), respectively. The key evaluating criteria are summarised in Table 6-4. Under 10 m/s, the non-filled specimen (E-OM) has a high *PCF* of around 2.89 kN, which is almost three times higher than its *MCF*. Therefore, it has a low *CFE* of only around 0.36. By filling with the viscous fluid, the *MCF* of VF-OM is around two times higher than that of E-OM. Therefore, its *CFE* is improved to around 0.73. By filling with STF, the proposed STF-OM has the highest *MCF* of around 3.90 kN, which is 81% and 279% higher than VF-OM and E-OM, respectively. It also has the highest *CFE* of around 0.98, demonstrating its stable crushing force without a significant high peak during the whole crushing process. The total energy absorption capacity of E-OM-V10 is significantly improved by filling with fluid, i.e., improved by 96% and 216% when filled with viscous fluid (VF-OM-V10) and STF (STF-OM-V10), respectively. However, the *SEA* of VF-OM-V10 is around 8% lower than that of E-OM-V10 owing to the heavy and incompressible viscous fluid, which leads to the increase in the overall mass and the reduction of the crushing stroke of the structure. STF-OM-V10 has the highest *SEA* of around 1,504.23 J/kg, which is 11% and 20% higher than E-OM-V10 and VF-OM-V10, respectively, owing to its high shear thickening viscosity, even though its fluid is almost twice as heavy as that of VF-OM-V10.

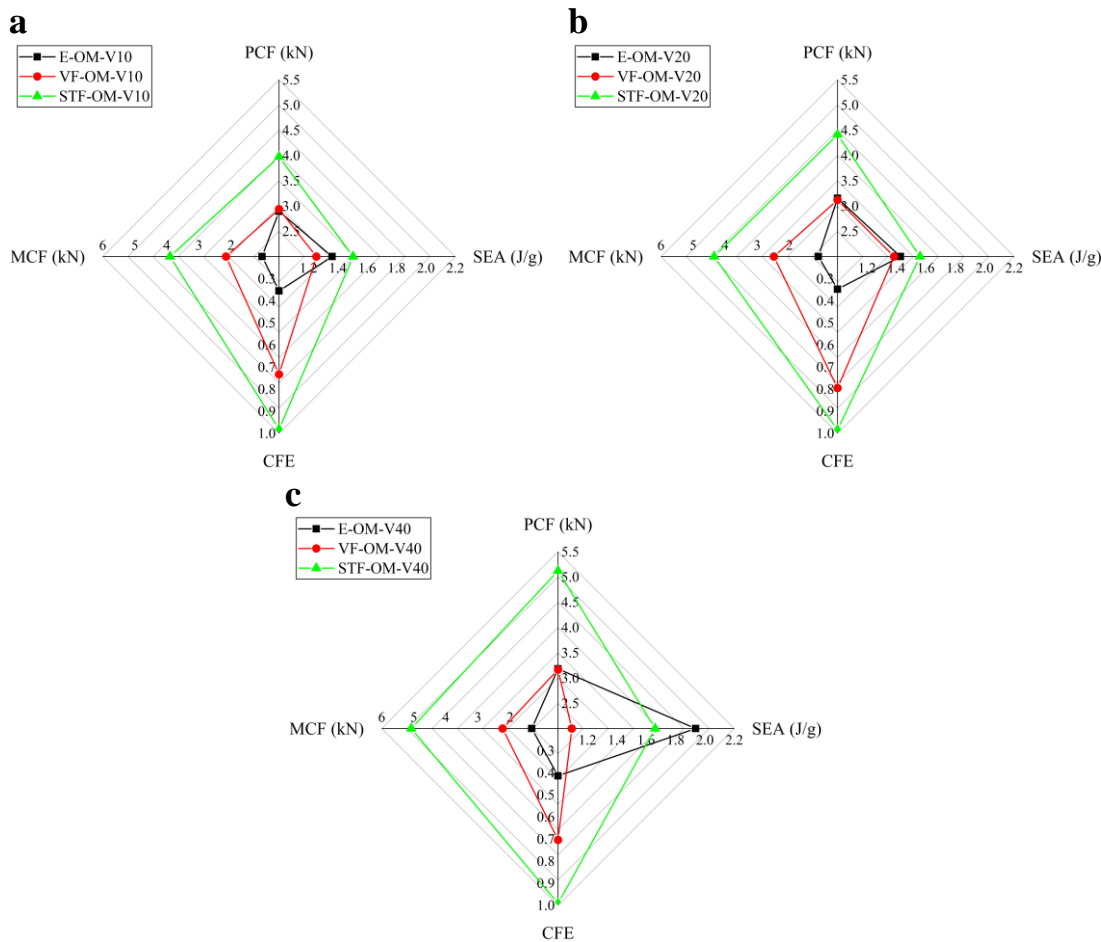


Figure 6-12. Comparisons of key evaluating criteria of specimens under (a) 10 m/s, (b) 20 m/s, and (c) 40 m/s crushing speeds.

As the crushing velocity rises, i.e., from 10 m/s to 40 m/s, the *MCF* and *SEA* of E-OM increase as a result of the change in deformation mode, which leads to a large enclosed area of the crushing force after the initial buckling. However, its crushing force after buckling remains similar under various crushing speeds, thus resulting in a slightly improved but low *CFE* of only 0.41. Similar to that of E-OM, the crushing force of VF-OM after buckling is not significantly improved as the crushing speed increases since its viscous fluid does not provide sufficient support to the deformed structure at the crushing end. Therefore, the nonuniform deformation with the early buckling at the crushing end still occurs, resulting in an abrupt reduction in the internal volume, which leads to a further decrease in its crushing stroke. As a result, the *SEA* of VF-OM-V40 reduces to around 1,093.78 J/kg, which is 44% lower than that of E-OM-V40. Unlike VF-OM, the *MCF* of the proposed STF-OM increases by around 30% to around 5.08 kN as the crushing velocity rises from 10 m/s to 40 m/s. As illustrated in Figure 6-8, the deformation at the crushing end is not observed, and the uniform

deformation is maintained under 40 m/s crushing owing to the squeeze of the STF, which triggers the thickening behaviour as well as the rise of the STF viscosity. During the deformation, STF transforms into a solid-like material of high viscosity, which provides support to the deformed sidewalls, thus generating a more stable deformation than E-OM and VF-OM under high crushing velocity, i.e., 40 m/s. STF-OM-V40 has a 145% and 104% higher EA than E-OM-V40 and VF-OM-V40, respectively. As shown in Figure 6-12, STF-OM has the highest MCF , CFE , and SEA among all structures under the same crushing speed of 10 m/s and 20 m/s. Under the high crushing speed of 40 m/s, the EA of STF-OM is higher than that of E-OM; however, its SEA is slightly lower because of its heavy weight.

Table 6-4. Key evaluating criteria of all specimens under various crushing velocities.

Specimen	m (kg)	d (mm)	PCF (kN)	MCF (kN)	CFE	EA (J)	SEA (J/kg)
E-OM-V10	0.027	35.39	2.89	1.03	0.36	36.39	1,361.23
VF-OM-V10	0.057	33.13	2.94	2.15	0.73	71.36	1,254.03
STF-OM-V10	0.077	29.51	3.97	3.90	0.98	115.08	1,504.23
E-OM-V20	0.027	34.83	3.15	1.10	0.35	38.18	1,427.87
VF-OM-V20	0.057	31.74	3.12	2.48	0.80	78.78	1,384.37
STF-OM-V20	0.077	27.48	4.41	4.34	0.98	119.35	1,560.05
E-OM-V40	0.027	39.29	3.18	1.32	0.41	51.78	1,936.79
VF-OM-V40	0.057	27.93	3.17	2.23	0.70	62.24	1,093.78
STF-OM-V40	0.077	25.02	5.12	5.08	0.99	127.09	1,661.25

Overall, the crushing efficiency and the energy absorption performance of origami metastructure can be significantly improved by incorporating the STF into its structure. Furthermore, the crushing resistance and energy absorption capability of the proposed structure increase with the increase in crushing velocity, showing its adaptive crushing resistance and energy absorption capability to various impact scenarios. Therefore, the proposed structure has the potential to be used as energy absorbers in protective applications. It should be mentioned that improving the performance of the origami metastructure by increasing the wall thickness is not always achievable due to the difficulty in folding the thick plates. Furthermore, thick-walled origami metastructures may also lead to an increase in the buckling resistance and early densification [51], as

well as unnecessarily high transmitted force to the protected structure at the back, which is a drawback for protective applications such as sacrificial cladding.

6.5 Parametric studies of STF-OM

The infilled shear thickening fluid significantly affects the crushing performance and the densification stage of STF-OM. Therefore, the effects of different filled heights (fluid volume) and viscosity of STF, as well as the origami folding angle on the shear thickening behaviour and crushing performance of STF-OM are investigated in this section. The same crushing speed of 40 m/s is used for all specimens. The force-displacement responses and crushing performances of each specimen are compared and discussed.

6.5.1 Effect of the filled height of STF

The effect of the filled height of STF on the crushing response of STF-OM is investigated in this section. Three different filled heights (h) of 6 mm, 7.5 mm, and 9 mm of the same STF ($RK=72$, $RN=1.35$) are considered, as illustrated in Figure 6-13(a). All three specimens have the same OM structure with 0.29 mm wall thickness and 30° folding angle, as described in Section 6.3.1. Increasing the filled height of the STF from 6 mm to 9 mm increases the filled volume of the STF from approximately 30% to 55%, respectively, thereby reducing the empty space within the structure from around 70% to 45%.

As shown in Figure 6-13(b), increasing the filled height of STF leads to an increase in the crushing resistance of the STF-OM due to a larger contact area between the sidewalls and STF, as well as more support to the bending sidewalls. However, it also causes the early densification of the structure due to the reduction of the empty space, thus compromising the total energy absorption capability of the structure. The key evaluating criteria of STF-OM with various filled heights are summarised in Table 6-5. By increasing the filled height of STF from 6 mm to 9 mm, the MCF of STF-OM-V40 increases by 53% from 3.93 kN to 6.06 kN, respectively, and its EA increases by 27%. However, its SEA slightly decreases by around 18% from 1,696.81 J/kg to 1,397.23 J/kg owing to the heavy mass of the fluid and early densification of the structure. STF-OM-V40 with a 7.5 mm filled height has the most stable crushing force and the highest

CFE among the three specimens. Overall, increasing the filled height/volume of STF enhances the energy absorption and crushing performances of the STF-filled origami metastructure. However, too much filling of fluid leads to a heavy and early densified structure.

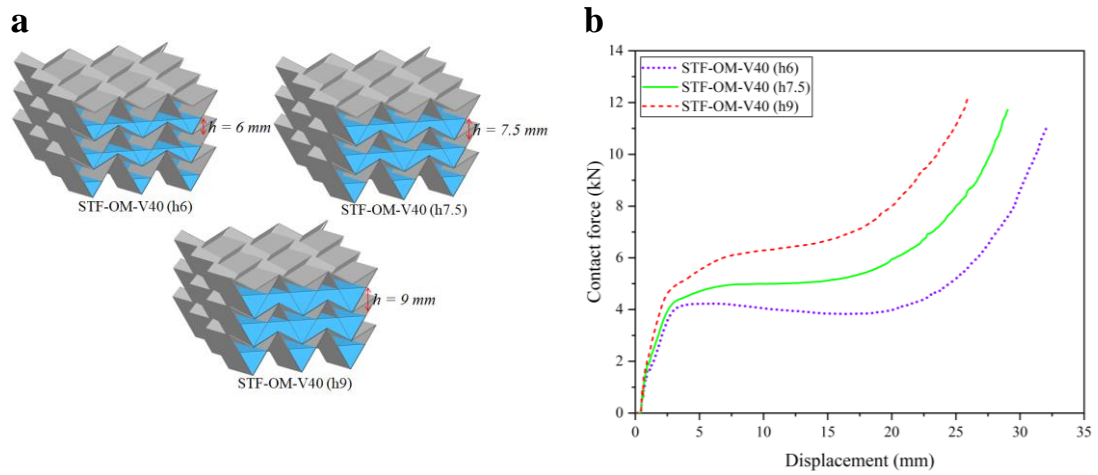


Figure 6-13. (a) Illustration and (b) force-displacement responses of STF-OM with various heights of STF.

Table 6-5. Key evaluating criteria of STF-OM with various heights of STF.

Specimen	m (kg)	d (mm)	PCF (kN)	MCF (kN)	CFE	EA (J)	SEA (J/kg)
STF-OM-V40 (h6)	0.060	26.03	4.23	3.93	0.93	102.37	1,696.81
STF-OM-V40 (h7.5)	0.077	25.02	5.12	5.08	0.99	127.09	1,661.25
STF-OM-V40 (h9)	0.094	21.66	6.34	6.06	0.96	131.23	1,397.23

6.5.2 Effect of viscosity of STF

In this section, three specimens are filled with STF of various shear-thickening viscosities, as plotted in Figure 6-14(a). All STF-OM specimens have the same OM structure with 0.29 mm wall thickness and 30° folding angle as described in Section 6.3.1, and the STF is filled into the specimens to the same height of 7.5 mm.

As compared in Figure 6-14(b), the crushing resistance of STF-OM-V40 increases when it is filled with STF of high shear thickening property, which results in higher viscosity and stress of the STF at the same loading rate [175], thus enhancing the crushing response and energy absorption performance of the structure. However, the STF-OM-V40 with higher shear thickening behaviour experiences early densification due to the high viscosity and early solidification of STF [174]. As shown in Table 6-6,

both *MCF* and *SEA* of STF-OM-V40 are enhanced by using higher shear thickening behaviour of the same filled quantity STF, which does not significantly affect the empty space and the overall mass of the structure. Therefore, the energy absorption and crushing performances of the origami metastructure can be efficiently improved by partially filling with STF of high shear thickening property, instead of increasing its volume.

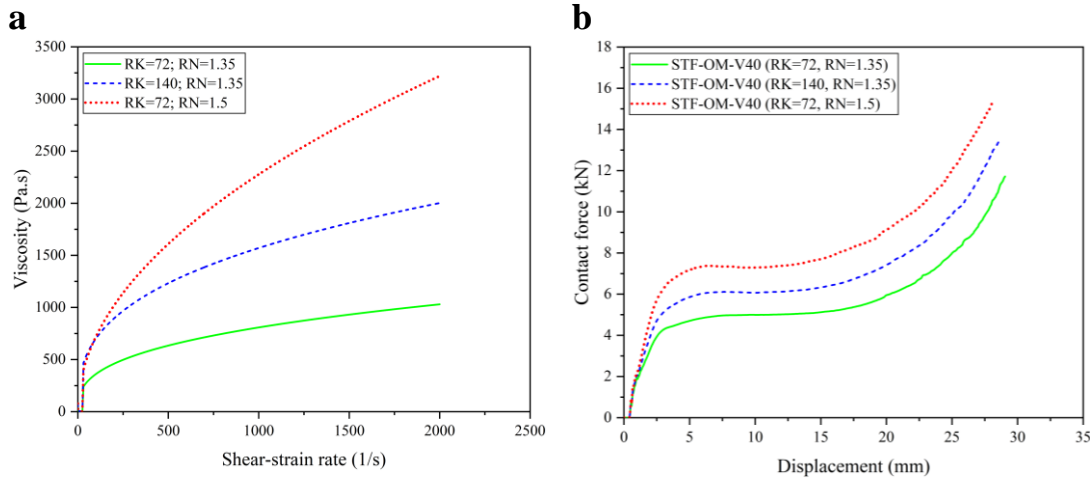


Figure 6-14. (a) Viscosity-shear rate relationships of STF with different shear thickening viscosities [175] and (b) force-displacement responses of STF-OM filled with STF of various shear thickening viscosities.

Table 6-6. Key evaluating criteria of STF-OM filled with STF of various shear thickening viscosities.

Specimen	<i>m</i> (kg)	<i>d</i> (mm)	<i>PCF</i> (kN)	<i>MCF</i> (kN)	<i>CFE</i>	<i>EA</i> (J)	<i>SEA</i> (J/kg)
STF-OM-V40 (<i>RK</i> =72, <i>RN</i> =1.35)	0.077	25.02	5.12	5.08	0.99	127.09	1,661.25
STF-OM-V40 (<i>RK</i> =140, <i>RN</i> =1.35)	0.077	23.54	6.27	6.08	0.97	143.08	1,870.22
STF-OM-V40 (<i>RK</i> =72, <i>RN</i> =1.5)	0.077	22.72	7.38	7.27	0.99	165.19	2,159.32

6.5.3 Effect of origami folding angle

The influence of the folding angle of the origami metastructure on the crushing performance of STF-OM is discussed herein. As illustrated in Figure 6-15(a), four different folding angles μ of 10° , 20° , 30° , and 40° are considered and denoted as A10, A20, A30, and A40, respectively. The width, length, and height of all OM structures are kept the same. Therefore, the wall thickness of each specimen is adjusted to have

the same mass as the OM structure with 0.29 mm wall thickness and 30° folding angle (A30) in Section 6.3.1. The same STF ($RK=72$, $RN=1.35$) is filled into each STF-OM specimen to the same filled height of 7.5 mm.

The force-displacement responses of non-filled (E-OM) and STF-filled (STF-OM) origami metastructures with various folding angles are plotted in Figure 6-15(b). Decreasing the folding angle leads to the increase in the *PCF* and *MCF* of E-OM because the cell walls of the origami metastructure become almost straight, thus resulting in a similar crushing response of the honeycomb structures in the out-of-plane direction [99]. The difference between *PCF* and *MCF* is even more pronounced for the origami metastructure with a small folding angle, i.e., A10. The crushing response of STF-OM is quite similar to that of E-OM, except that its crushing force is higher than that of E-OM of the same folding angle. STF-OM-V40 (A10) with a small folding angle exhibits a significantly high *PCF* because the STF mainly resists the compression from the loading plate, transforming the STF into a solid-like material. This transformation leads to a further increase in the buckling resistance of the almost vertical sidewalls, as well as the direct transfer of load to the support, thus resulting in an increase in the initial peak crushing force. For STF-OM with a large folding angle (A20, A30), the initial peak force is not obvious, and the balancing between the *PCF* and *MCF* is observed, especially for STF-OM-V40 (A30), which has the highest *CFE*. STF-OM-V40 (A20) and STF-OM-V40 (A30) have relatively high *CFE* of around 0.83 to 0.99 owing to a relatively high and stable crushing force and low initial peak force. However, as the folding angle is further increased, i.e., A40, the *MCF* and *SEA* of STF-OM-V40 (A40) reduce owing to the large prebend cell wall, which results in an easy folding structure. The *SEA* of STF-OM-V40 (A40) is 1,350.39 J/kg, which is around 20% and 40% lower than that of STF-OM-V40 (A30) and STF-OM-V40 (A20), respectively. The key evaluating criteria of STF-OM with various folding angles are summarised in Table 6-7. Overall, partially filling STF into the OM structure enhances the energy absorption and crushing efficiency by enhancing and stabilising the crushing resistance. The OM structure with a folding angle between 20° to 30° should be chosen as the enclosed structure of the proposed design to obtain a good compromise between high plateau and low peak crushing resistances.

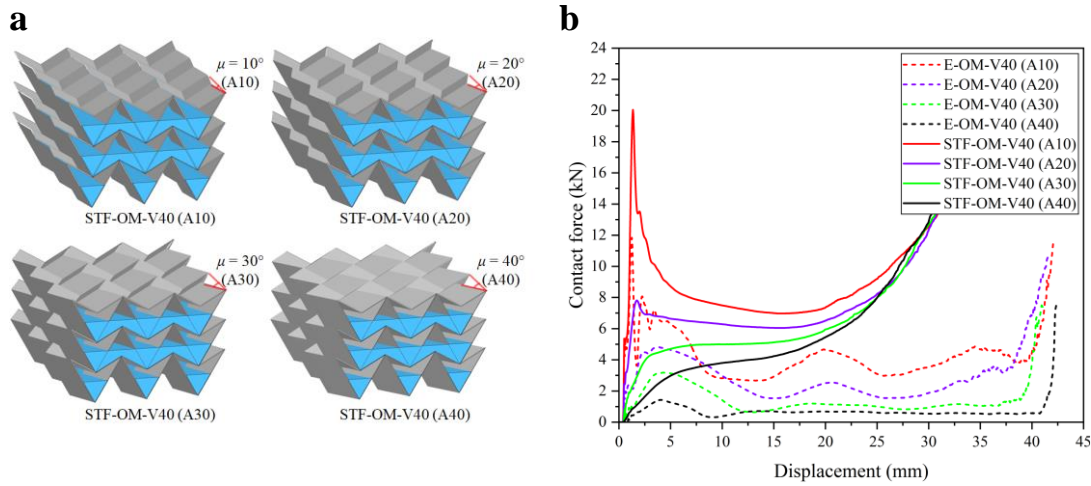


Figure 6-15. (a) Illustration and (b) force-displacement responses of STF-OM with various folding angles.

Table 6-7. Key evaluating criteria of STF-OM with various folding angles.

Specimen	m (kg)	d (mm)	PCF (kN)	MCF (kN)	CFE	EA (J)	SEA (J/kg)
STF-OM-V40 (A10)	0.077	26.66	20.05	8.17	0.41	217.90	2,848.44
STF-OM-V40 (A20)	0.077	26.55	7.81	6.50	0.83	172.69	2,257.31
STF-OM-V40 (A30)	0.077	25.02	5.12	5.08	0.99	127.09	1,661.25
STF-OM-V40 (A40)	0.077	25.23	4.18	4.09	0.98	103.30	1,350.39

6.6 Summary

In this chapter, a novel approach is proposed to enhance the crushing efficiency and energy absorption performance of origami metastructure by incorporating the shear thickening fluid (STF), which mimics the existence of the viscoelastic material found inside the protective mechanism in nature. The dynamic crushing and energy-absorbing performances of the proposed structure are numerically investigated using the commercial software LS-DYNA. The crushing performances of the proposed STF-filled origami metastructure (STF-OM) are investigated and compared with the non-filled and viscous fluid-filled counterparts under various crushing velocities. The influences of filled height and viscosity of STF, and origami folding angle on the crushing performances of STF-OM are also investigated, and the main findings are summarised as follows.

- The crushing response and energy absorption performance of the origami metastructure can be significantly enhanced by incorporating the STF into its

structure. Furthermore, the crushing resistance of the proposed STF-OM increases by 30% as the crushing velocity increases from 10 m/s to 40 m/s, while remaining a high *CFE* of 0.98, demonstrating its adaptive crushing performances for various impact scenarios.

- As compared with the non-filled and viscous fluid-filled counterparts, the proposed STF-OM generates a more stable and higher crushing resistance without a significantly high peak during the whole crushing process owing to the shear thickening behaviour of the STF, which is triggered by the contraction of OM structure. This contraction causes the squeezing flow and deformation of the highly viscous STF, thereby providing support and preventing the localised deformation of the structure.
- Increasing the filled height of STF enhances the crushing resistance and energy absorption capability of the STF-OM. However, too much filling of fluid leads to a heavy and early densified structure due to the increase in the quantity of fluid and the reduction of the empty space of the structure, thereby compromising the *SEA* of the structure.
- The crushing performances of the proposed STF-OM can be efficiently improved by using STF with higher shear thickening behaviour, which does not significantly affect the overall mass of the structure.
- The folding angle of the OM structure significantly affects the crushing resistance and energy absorption efficiency of STF-OM. The STF-OM structure of a small folding angle may lead to a significantly higher peak crushing resistance, whereas a large folding angle may result in a lower plateau crushing resistance.

Chapter 7. Recoverable bio-inspired energy-absorbing device (BIEAD)

The related work in this chapter was published in International Journal of Impact Engineering:

Lam L, Chen W, Hao H, Li Z, Ha NS, Pham TM. Numerical study of bio-inspired energy-absorbing device using shear thickening fluid (STF). International Journal of Impact Engineering 2022;162:104158.

<https://doi.org/10.1016/j.ijimpeng.2022.104158>

7.1 Introduction

In Chapters 5 and 6, innovative energy-absorbing structures with adaptive energy absorption and crushing performances are proposed by mimicking the protective mechanisms of animals. However, in cases where protection against multiple loadings or impacts is required, these protective designs are unsuitable due to the irrecoverable plastic deformation of the structural parts that occurs during loading. Therefore, in this chapter, a recoverable bio-inspired energy-absorbing device (BIEAD) utilising the shear thickening behaviour of STF is proposed by mimicking the suture interface found inside the beak of woodpeckers, as shown in Figure 7-1. The STF is used to mimic the viscous material at the suture interfaces of the animals. To mimic the suture geometry, a simple rectangular tube is used to represent the single tooth of the suture interface. A cross-section view of the woodpecker's beak showing the suture structure and a schematic diagram of BIEAD are illustrated in Figure 7-1. The thickening behaviour of the STF is utilised as the main energy absorption mechanism of the proposed device, while the spring is used to restore the original shape of the device. Finite element software LS-DYNA is used in this chapter to analyse the impact force and energy absorption capacity of the proposed device. The same FSI approach as in Chapter 5 [112] is adopted to model the interaction between the fluid and the structural components. A water-filled corrugated beam, which was experimentally tested and numerically modelled by Wang et al. [206], is used for model calibration. The impact force and displacement time histories generated from the numerical model are compared with the existing numerical and experimental data. The calibrated numerical

model is then used to perform the numerical investigations of the proposed BIEAD. The viscosity behaviour as a function of the shear rate representing the shear thickening behaviour is considered in the numerical model of the STF. The crushing resistance and energy absorption capacity are used as criteria for evaluating the performance of the proposed device.

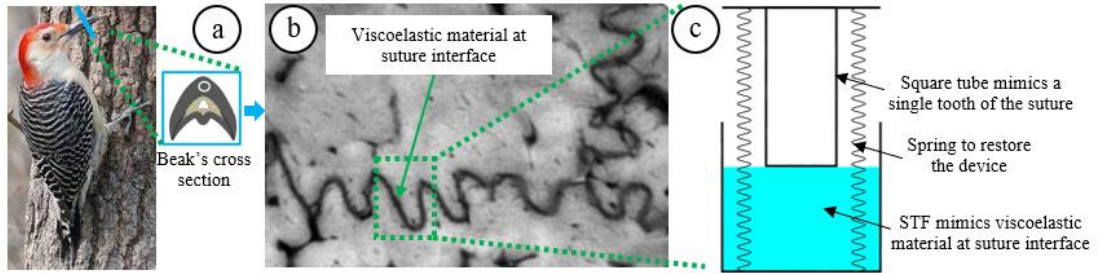


Figure 7-1. (a) A red-bellied woodpecker [145], (b) a section view of a woodpecker's beak showing the suture [145], and (c) a BIEAD mimicked the suture structure.

7.2 Numerical model calibration

In this chapter, the available commercial software LS-Prepost is used to generate the models of both empty and fluid-filled (water or STF) specimens, and the LS-DYNA solver is used to conduct the numerical simulation. The impact test of water-filled corrugated beam conducted by Wang et al. [206] is used to validate the Fluid-Structure-Interaction approach and calibrate the numerical model. A series of impact tests of different impact speeds were conducted by impacting an aluminium-foam projectile at the mid span of the corrugated beam using a gas gun. The test setup of projectile impact onto the corrugated beam is illustrated in Figure 7-2.

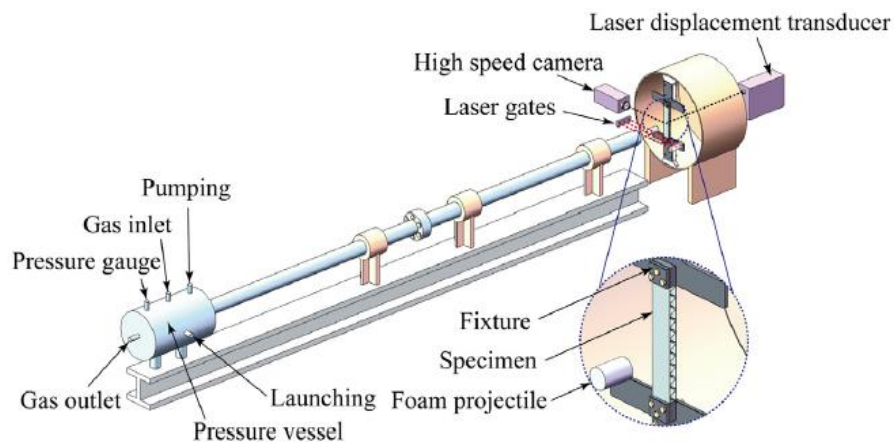


Figure 7-2. Testing setup of projectile impact of corrugated beam [206].

The water-filled specimen with an overall clear span of 300 mm was clamped at both sides and sealed at the other two sides to contain the water, as shown in Figure 7-3. The detail geometric parameters of the corrugated beam can be found in the previous study [206]. A water-filled corrugated beam subjected to impact at its mid span by a foam projectile with an initial velocity of 277 m/s is used to calibrate the numerical model in this chapter.

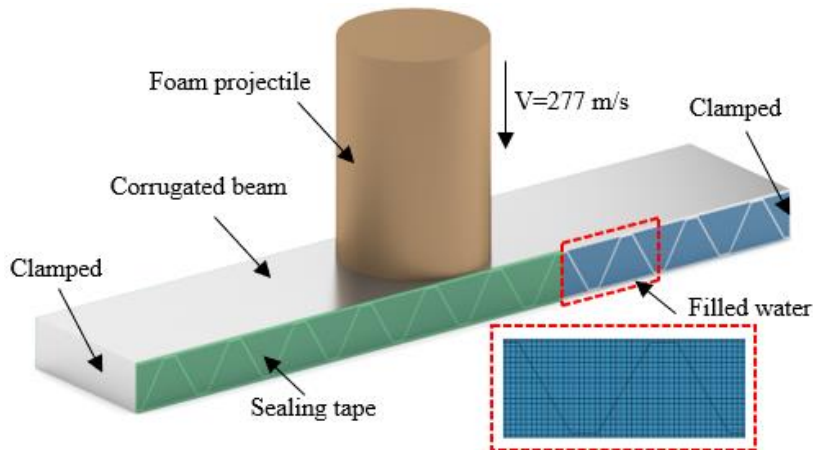


Figure 7-3. ALE-FE model of water-filled corrugated beam.

The Arbitrary Lagrangian-Eulerian (ALE) method and Fluid-Structure Interaction (FSI) coupling algorithm are utilised to calibrate the water-filled corrugated beam under projectile impact. The contact between the projectile and top face sheet is defined by *CONTACT_AUTOMATIC NODES TO SURFACE. The contacts between the corrugated core and top/bottom plates are modelled by *CONTACT_AUTOMATIC SURFACE TO SURFACE. The welded connections between core and top/bottom plates are modelled using the tied contact. The accuracy and reliability of the numerical simulation are verified by comparing its generated mid-span displacement time histories of top and bottom plates with the existing numerical and experimental data. Then the calibrated numerical model is used to perform the numerical simulations of the proposed water and STF-filled specimens of this chapter.

7.2.1 Element, mesh, and boundary condition of the tested beam model

The two external face sheets and the corrugated core of the sandwich beam are modelled using Belytschko-Wong-Chiang type shell elements, while the foam projectile is meshed using hexahedral solid elements. Water and air are meshed and

modelled using the ALE-multi-material solid elements. The rubber is meshed using the fully integrated shell element to minimize the hourglass energy [211]. The corrugated sandwich beam is clamped and constrained in all degrees of freedom on both ends. To ensure the accuracy and balanced computational cost in the finite element analysis, a mesh sensitivity test is carried out for the water-filled corrugated sandwich beam under the projectile impact of 277 m/s. To model the Eulerian materials such as water and air, the Eulerian elements should be the same size or smaller than the Lagrangian elements to prevent the leakage at the coupling interfaces [175,196]. Therefore, three pairs of Lagrangian and Eulerian-element sizes such as (4 mm, 2 mm), (2 mm, 1 mm), and (1 mm, 0.5 mm) were used for the mesh-convergence test. The mid-span displacement-time histories and residual deflection of top and bottom plates obtained from the numerical model are compared with the numerical and experimental data conducted by Wang et al. [206] and discussed in Section 7.2.4 below.

7.2.2 Material models

The elastic-plastic material model *MAT_PLASTIC_KINEMATIC is used to model the AISI 304 stainless steel of the corrugated beam. The strain rate effect is also considered in this material model via Cowper-Symonds model in LS-DYNA, as defined by [198]:

$$\frac{\sigma_d}{\sigma_s} = 1 + \left(\frac{\dot{\epsilon}}{C} \right)^{\frac{1}{P}} \quad (7-1)$$

σ_s is the static yield stress and σ_d is the dynamic yield stress corresponding to the strain rate $\dot{\epsilon}$; C and P are the Cowper Symonds strain rate parameters. The *MAT_CRUSHABLE_FOAM material model is used to model the aluminium-foam projectile with a damping coefficient of 0.1 [206,212]. The compressive stress-strain curve of aluminium foam can be found in [206]. One point ALE multi-material solid element is used to model the Eulerian materials such as water and air. In the ALE method, Eulerian domain representing the surrounding air is required to overlap the Lagrangian elements and cover the water elements, thus allowing the movement of water during impact. Water is modelled using *MAT_NULL material model. The hydrostatic behaviour of the water is defined by the GRUNEISEN equation of state (EOS) [206]. The rubberised tape used to seal the water inside the corrugated sandwich

beam is modelled using a two-parameter rubber model (*MAT_MOONEY-RIVLIN_RUBBER). The input parameters of material properties and equation of states (EOS) for the numerical simulations are summarised in Table 7-3. For the material properties and EOS parameters of air and rubber, please refer to Table 5-2 in Section 5.3.2.

7.2.3 Fluid-Structure-Interaction (FSI) approach

For the ALE method, the Eulerian mesh of fluid is surrounded by the space domain of air or void which allows the fluid material to flow during the simulation process [197]. To ensure the continuity of fluid movement, the fluid and air-domain meshes share the same nodes at the fluid-air interface [175]. The same Fluid-Structure-Interaction (FSI) technique as described in Section 5.2 is employed to analyse the interaction between the Lagrangian elements of the structural components and the Eulerian elements of fluids.

7.2.4 Model calibration

The mid-displacement time histories of top and bottom plates obtained from the numerical simulations are comparable with the numerical data given in [206], as shown in Figure 7-4. The mid-span deflection time histories converge as the mesh sizes decrease, and the pair of Lagrangian and Eulerian element sizes (2 mm, 1mm) generates similar results as the numerical data provided in [206]. The recorded experimental [206] and calculated numerical results of residual mid-span deflections of top and bottom plates of water-filled corrugated beam with the mesh sizes of (2 mm, 1mm) are compared in Table 7-1. It is shown that the predicted numerical results agree well with those from the test, in which only the residual displacement was recorded. It can be concluded that the calibrated numerical model using ALE method provides reasonably accurate predictions of the responses of structures subjected to impact loads with the fluid and structure interaction. Therefore, the calibrated numerical model and the mesh size of (2 mm, 1 mm) are used to conduct the simulations in the subsequent sections. Same material models and equation of states are used for empty and water-filled specimens. For STF-filled specimen, the input parameters of material model and equation of state of the STF are based on the previous work of Gu et al. [175] and discussed in detail in Section 7.3.2.

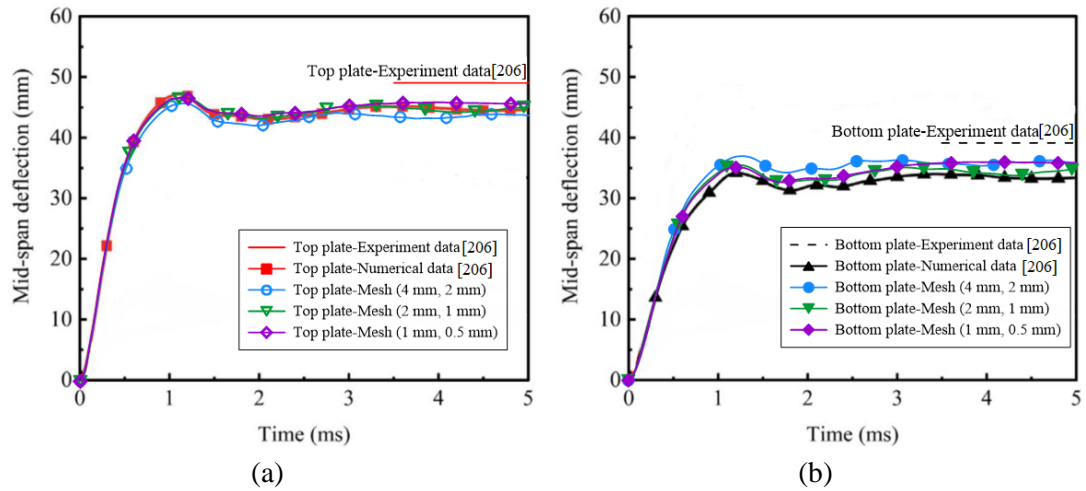


Figure 7-4. Mesh convergence results of mid-span deflection time curves of (a) top and (b) bottom plates using three different pairs of Lagrangian and Eulerian element sizes.

Table 7-1. Experimental and numerical results of residual mid-span deformation of top and bottom plates.

Residual displacement	Experimental data [206]	Numerical simulation	Error
Top plate	49.0 mm	44.5 mm	-9.2%
Bottom plate	39.0 mm	34.5 mm	-11.5%

7.3 Bio-inspired energy-absorbing device (BIEAD)

7.3.1 Geometries and loading conditions

Figure 7-5 shows the isometric view and cross section of the prototype bio-inspired energy-absorbing device (BIEAD) proposed in this chapter, representing one cell in an energy absorption protective panel. The empty specimen has the overall height of 120 mm with a bottom cross section of 72 by 72 mm. The height of the container is 68 mm, thus leaving a movable gap of 52 mm between the top plate and container. Four springs are used to support and connect the top plate to the bottom of the container. All four sides of the gap are wrapped around using the rubber to prevent the leakage and splash of the fluid during loading. The rubber is assumed to be perfectly bonded to the top plate and the top of container's walls by using the common nodes. A closed-square-tube core with a cross section of 32 by 32 mm is fixed to the centre of the top plate, leaving a shear gap of 20 mm between the core's side wall and container's wall. The thicknesses of all the steel components and rubber are 1 mm and 0.5 mm, respectively. For the fluid-filled specimens, the water or STF is filled into the container up to the height of 48 mm, touching the base of the tube core.

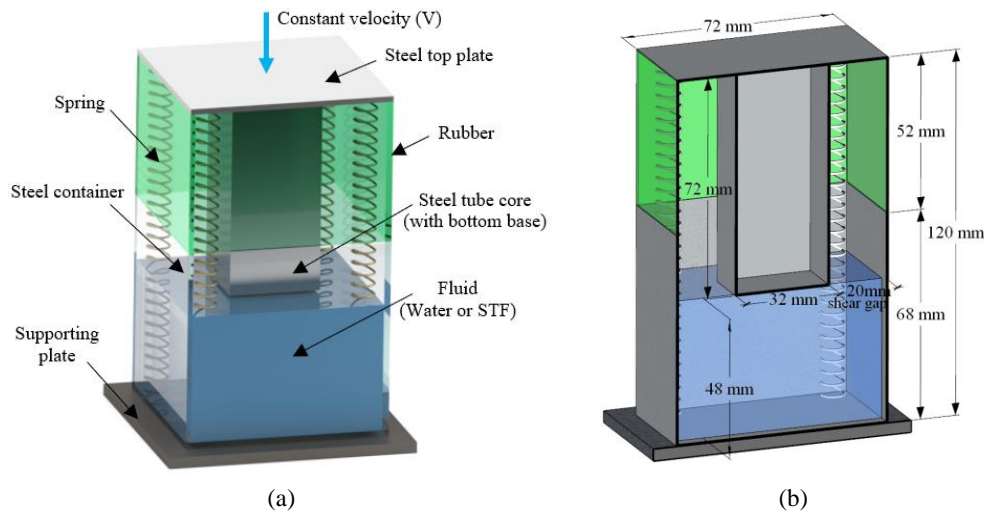


Figure 7-5. (a) Specimen details and (b) cross section of the specimen.

The specimen is simply rested on the rigid supporting plate. The supporting plate is fixed in all degrees of freedom while the top plate is set to have one-degree of freedom in the vertical direction only. A quarter model is implemented because of the symmetry in geometry and loading conditions. Two symmetry planes of boundary condition are applied at the central interfaces of the model. The rubber self-contact is modelled by the keyword `*CONTACT_AUTOMATIC SINGLE SURFACE` and the contact between the bottom of the container and the supporting plate is modelled by the keyword `*CONTACT_AUTOMATIC SURFACE TO SURFACE`. The friction coefficient of 0.2 is used for the contact interactions [208].

The flatwise crushing of the specimen is simulated by moving the top plate downward at a constant speed and stopping at 43 mm before the core reaches the bottom of the container. Three crushing speeds, i.e., 1.25 m/s, 2.50 m/s, and 6.25 m/s are used to study the effect of loading rate on the energy absorption capacity of the specimen. In this chapter, the shear rate during crushing is defined by dividing the crushing speed by the shear gap between the tube core and container. Therefore, the crushing speed of 1.25 m/s is expected to generate the shear rate of 62.5 /s for the specimen with the shear gap of 20 mm. This shear rate is higher than the critical shear rate of the STF which is equal to 25 /s [54], thus activating the shear thickening behaviour of the STF material.

All specimens are divided into three groups based on the crushing speed and summarised in Table 7-2. To facilitate the identification of the specimen, its filler material and crushing speed are used to denote each specimen. The Empty, Water-

filled, and STF-filled specimens are labelled as E, W, and S, respectively. The crushing speeds of 1.25 m/s, 2.50 m/s, and 6.25 m/s are denoted by V1.25, V2.50, and V6.25, respectively. For instance, specimen S-V1.25 represents the STF-filled specimen tested under the crushing speed of 1.25 m/s.

Table 7-2. Specimen configurations.

Group	Specimen	Filling material	Crushing speed (m/s)
1	E-V1.25	Empty (E)	1.25
	W-V1.25	Water (W)	1.25
	S-V1.25	STF (S)	1.25
2	W-V2.50	Water (W)	2.50
	S-V2.50	STF (S)	2.50
3	W-V6.25	Water (W)	6.25
	S-V6.25	STF (S)	6.25

7.3.2 Material model of STF

The parameters of material models and EOS of water and steel described in Section 7.2.2 are listed in Table 7-3 and used to model the Empty and Water-filled specimens in this chapter. The same parameters of material model and EOS of STF described in Section 5.2.2 and listed in Table 5-2 are used for STF-filled specimen. The spring with the stiffness of 1 kN/m is simply modelled as a discrete element with *MAT_SPRING ELASTIC [213].

Table 7-3. Input parameters of material models and EOS of water, steel, and aluminium foam for the numerical simulations.

Component	Material	Input data in LS-DYNA				
Sandwich beam (face sheets and core)	304 Stainless steel	*MAT_003 PLASTIC_KINEMATIC				
	[206,214,215]	Density (kg/m ³)	Young's modulus (GPa)	Poisson's ratio	Yield stress (MPa)	Tangent modulus (GPa)
		7800	200	0.3	200	2
		Hardening parameter, β	C (1/s)	P		
	0	2623.57	5.06			

Table 7-3 (Continued)

Component	Material	Input data in LS-DYNA				
Projectile	Aluminium foam [206,212]	*MAT_063 CRUSHABLE_FOAM				
		Density (kg/m ³)	Young's modulus (GPa)	Poisson's ratio	Tensile stress cut-off (GPa)	Damping coefficient
		378.3	1	0	0.0071	0.1
Filling material	Water [206]	*MAT_009 NULL				
		Density (kg/m ³)	Pressure cutoff (MPa)	Viscosity coefficient (Pa.s)		
		1000	-0.1	0.00089		
		*EOS_GRUNEISEN				
		C_v (m/s)	γ_0	S_1	S_2	S_3
1480	0.5	2.56	1.986	1.2268	0	

7.4 Results and discussions

7.4.1 Deformation mode of BIEAD

Figure 7-6 illustrates the deformation of water-filled and STF-filled specimens under the loading rate of 6.25 m/s. The deformation modes of all the water-filled specimens under various loading rates are quite similar. Since water-filled specimen is partially filled with water, the water splashes and provides negligible crushing resistance due to its low viscosity. Unlike water-filled specimen, during the crushing process of BIEAD, the interfacial-shear forces at the tube-core/STF contact interfaces activate the shear thickening behaviour of STF, leading to the increases of the viscosity of STF and crushing resistance of BIEAD. These increases are due to the high internal-shear stress and jamming front of STF [149,207], as shown in Figure 7-7. Thus, the impact energy can be dissipated through the viscous dissipation and internal friction inside the STF material. In addition, as the tube core almost reaches the bottom of the container, the jamming front of STF causes the deformation of the tube core.

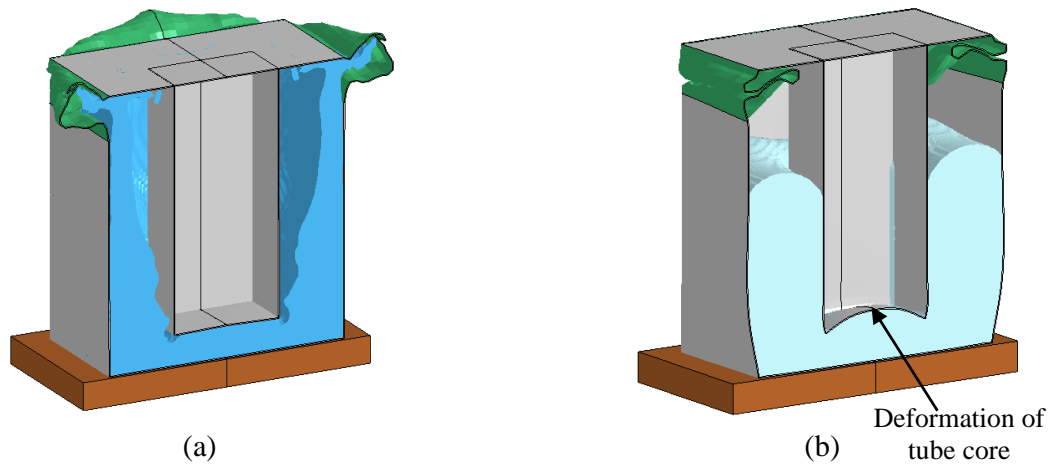


Figure 7-6. Cross sections showing the deformations of (a) water-filled specimen and (b) STF-filled specimen.

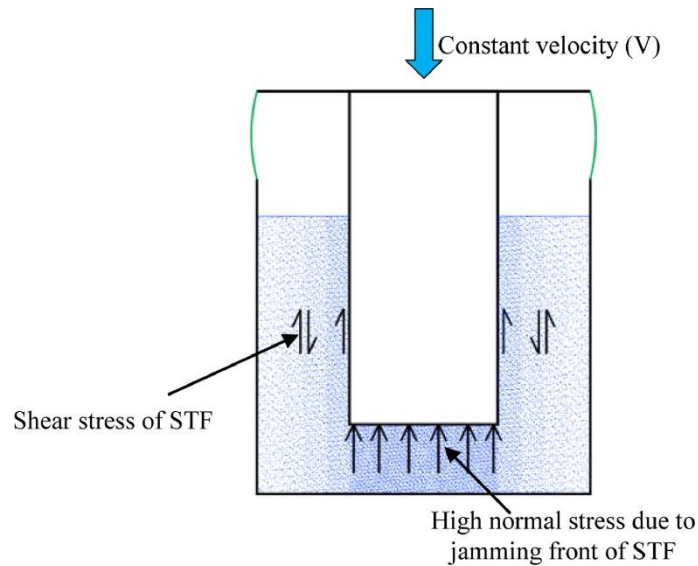


Figure 7-7. Cross section showing shear stress and normal stress of STF.

The distributions of the effective stress of STF along the longitudinal section at the compressive displacement of 4.4 mm and 39 mm are illustrated in Figure 7-8(a) and (b), respectively. The movement of the top plate generates the shear interaction between the tube core and the STF, which leads to the increase of effective stress of the STF. With further penetration of the tube core, the effective stress of STF surrounding the tube core significantly increases, thus leading to the increase of crushing resistance of BIEAD. As illustrated in Figure 7-9, the flow velocity of STF is high at the contact interfaces between the STF and tube core. Then it decreases significantly as the STF further flows outward because of the high viscosity of STF, thus showing the solid-state transformation of the STF during impact.

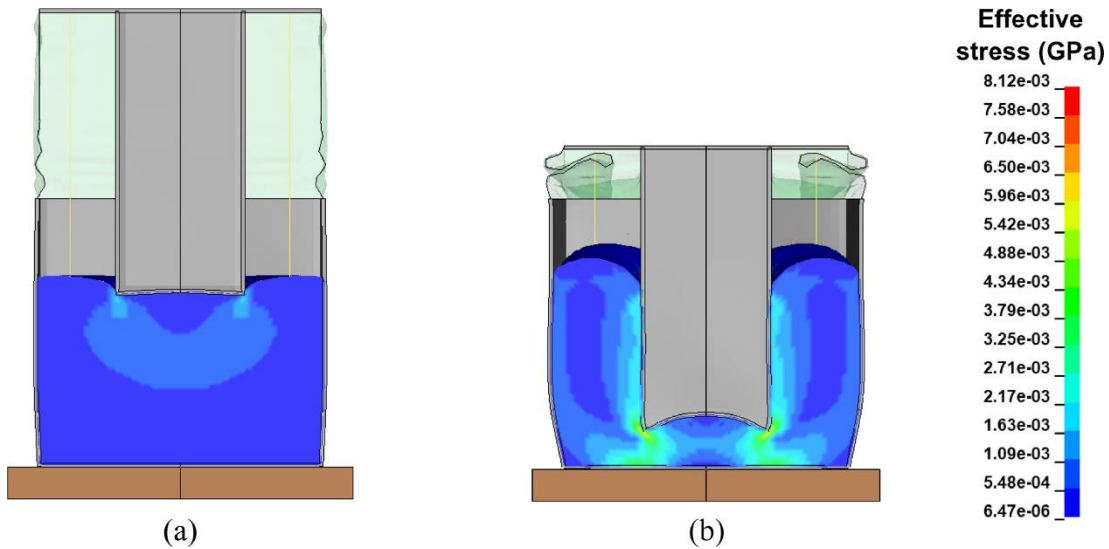


Figure 7-8. Longitudinal-cross sections showing the effective stress distributions of the STF at the compressive displacement of (a) 4.4 mm and (b) 39 mm at the crushing speed of 6.25 m/s.

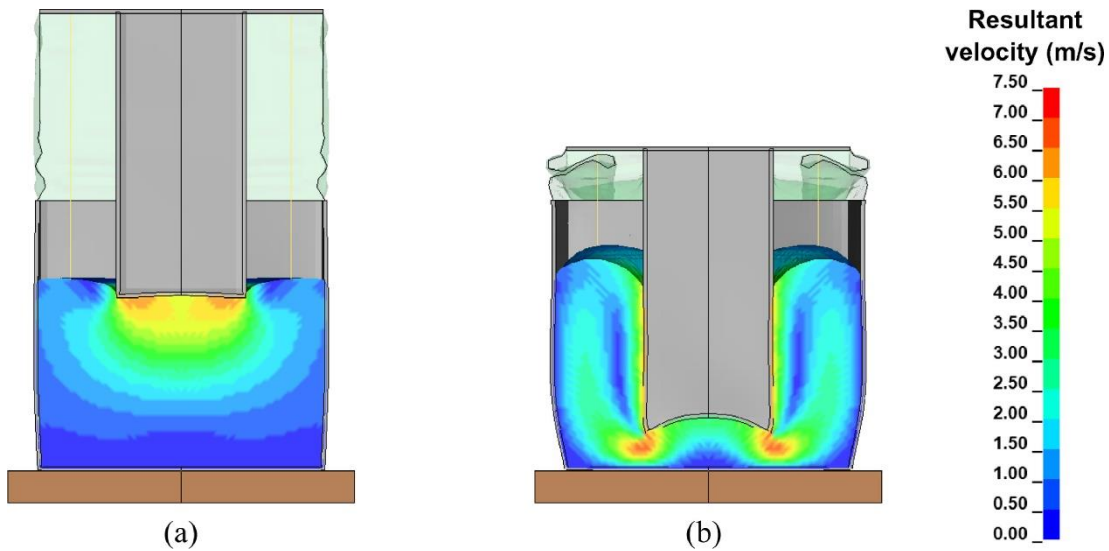


Figure 7-9. Longitudinal-cross sections showing flow velocity distributions of the STF at the compressive displacement of (a) 4.4 mm and (b) 39 mm at the crushing speed of 6.25 m/s.

7.4.2 Force-displacement and energy absorption of BIEAD under various loading rates

The force-displacement curves obtained from the numerical simulations are used to analyse and evaluate the structural performance and energy absorption capacity of each specimen. The force is obtained by extracting the contact force between the bottom of the container and the rigid-supporting plate while the displacement is directly obtained from the top plate.

7.4.2.1 Group 1

As shown in Figure 7-10, the force-displacement curve of water-filled specimen has similar trend to that of empty specimen despite a slight increase of contact force and few spike forces due to the impact between the tube core and water. For STF-filled specimen, the contact force gradually increases as the tube core penetrates the STF. As the tube core further penetrates the STF, the interfacial-contact surface between the STF and tube core becomes larger, leading to more deformation and higher viscous shear stress of STF, and thus increasing the crushing resistance. The energy absorbed by STF contributed up to 94% of the total energy of specimen S-V1.25, while the remaining is contributed by the deformation of tube core, container, and rubber. The specific energy absorption capacity (*SEA*) defined by a total energy absorption capacity of a structure per unit mass is also compared. At low crushing speed of 1.25 m/s, the *SEA* of S-V1.25 is around 136.60 J/kg which is 116 and 99 times higher than that of empty and water-filled specimens, i.e., E-V1.25, W-V1.25, respectively.

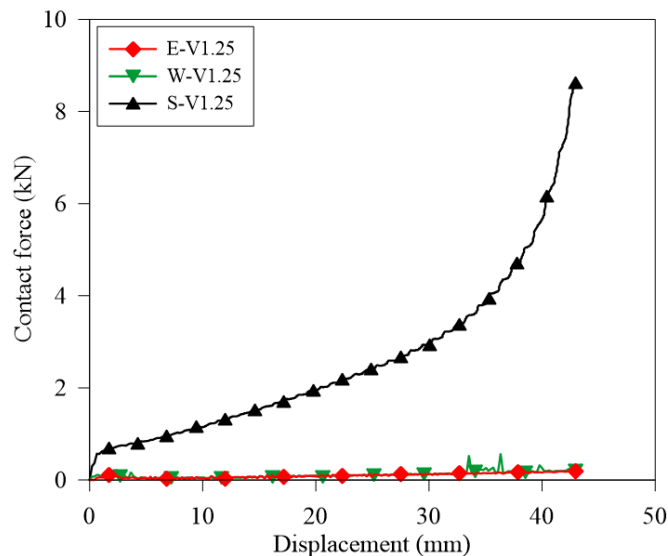


Figure 7-10. Force-displacement curves of empty, water-filled, and STF-filled specimens under crushing velocity of 1.25 m/s.

7.4.2.2 Group 2 and 3

When the crushing speed increases from 1.25 m/s to 6.25 m/s, the responses of water-filled specimens remain quite similar except that the contact force slightly increases with few higher spike forces as the crushing speed increases. For STF-filled specimens, the crushing resistance of BIEAD significantly increases, as shown in Figure 7-11. As the crushing speed increases, the crushing resistance become higher

because high crushing speed initiates higher applied shear rate which activates the shear thickening effect and increases the shear resistance of the STF. The energy absorbed by STF contributes the largest share of total energy of the specimen which is around 85% to 90%, as shown in Figure 7-12 and Table 7-4. The internal energy contributed by the tube core and container is depended on the viscosity and normal stress via jamming front of STF, which is related to the loading rate on the specimen. As the loading rate increases, the viscosity of the STF also increases, thus leading to the deformation of tube core and container. The STF-filled specimen has the highest *SEA* compared with the empty and water-filled specimen under the same crushing rate as given in Table 7-4.

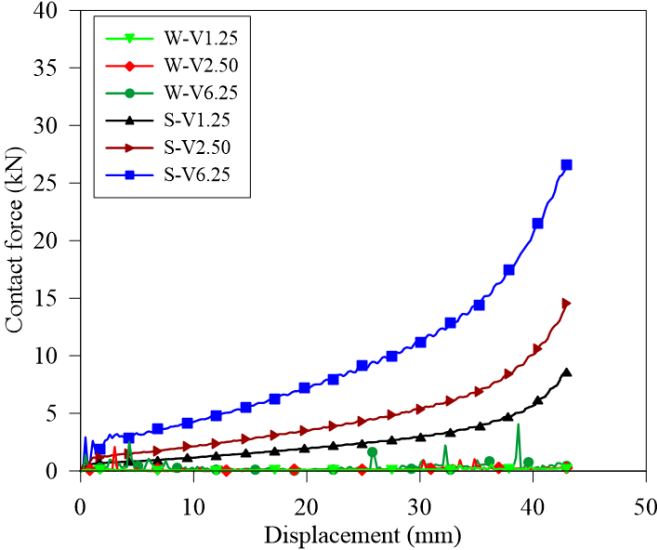


Figure 7-11. Force-displacement curves of Water-filled and STF-filled specimens under different crushing velocities.

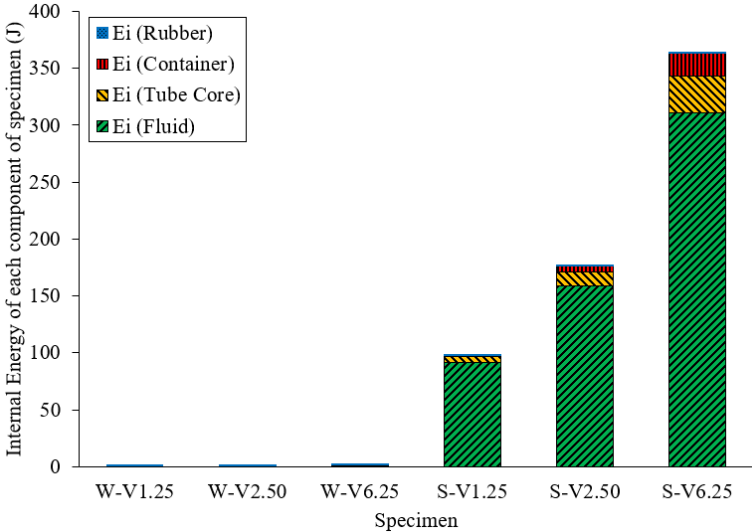


Figure 7-12. Internal energy absorption by each component of specimen.

Table 7-4. Internal energy and SEA of each specimen under various loading rates.

Specimen	Filled Material	Velocity (m/s)	Internal Energy E_i (J)		E_i (STF)/ $E_{i,t}$ (%)	SEA (J/kg)
			E_i (STF)	$E_{i,t}$ (Total)		
E-V1.25	Empty (E)	1.25	-	0.38	-	1.18
W-V1.25	Water (W)	1.25	0.36	0.78	46.1%	1.37
W-V2.50	Water (W)	2.50	0.38	1.01	37.5%	1.78
W-V6.25	Water (W)	6.25	0.60	2.74	21.7%	4.80
S-V1.25	STF (S)	1.25	92.00	98.38	93.5%	136.60
S-V2.50	STF (S)	2.50	158.80	176.64	90.0%	245.27
S-V6.25	STF (S)	6.25	311.20	364.61	85.4%	506.27

7.4.2.3 Energy absorption capacity of BIEAD under various loading rates

The energy absorption capacity (EA) of BIEAD is sensitive to the crushing speed, as observed in Figure 7-13. As the crushing speed increases, the crushing resistance also increases which leads to large enhancement of the energy absorption capacity. The SEA of STF-filled specimen increases by 80 % from 136.60 J/kg to 245.27 J/kg when the loading rate increases from 1.25 m/s to 2.50 m/s. Further increasing the speed to 6.25 m/s, the SEA increases by 271 %, which is around 506.27 J/kg.

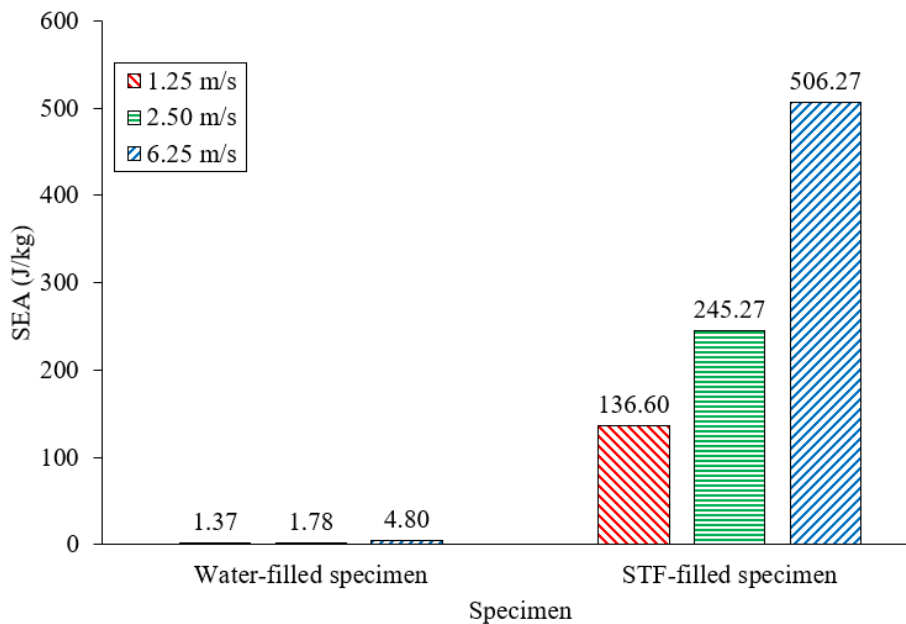


Figure 7-13. SEA of water-filled and STF-filled specimens under various crushing rates.

The increase of energy absorption of STF-filled specimen is due to the shear thickening effect of the STF. The rise of loading rate causes the increase of the viscosity and the viscous shear stress of STF, thus dissipating energy through viscous dissipation. Beside the loading rate, some other parameters such as the shear gap and the shear-thickening constants also influence the behaviours of the STF. Therefore, the effects of the shear gaps, contact area, and shear-thickening constants of STF on the performance of the BIEAD are further investigated and discussed in Section 7.5.

7.4.3 Recoverability of BIEAD

STF is a type of fluid that can transform from its resting liquid-state to solid-state during loading and recover back to its original state during unloading due to its shear-thickening behaviour and recoverability, respectively. During the loading process, the top plate is set to move 43 mm downward at the imposed velocity of 6.25 m/s and then released before the tube core almost touches the bottom of the container. Therefore, the rebound of the top plate occurs due to the existence of the springs during unloading.

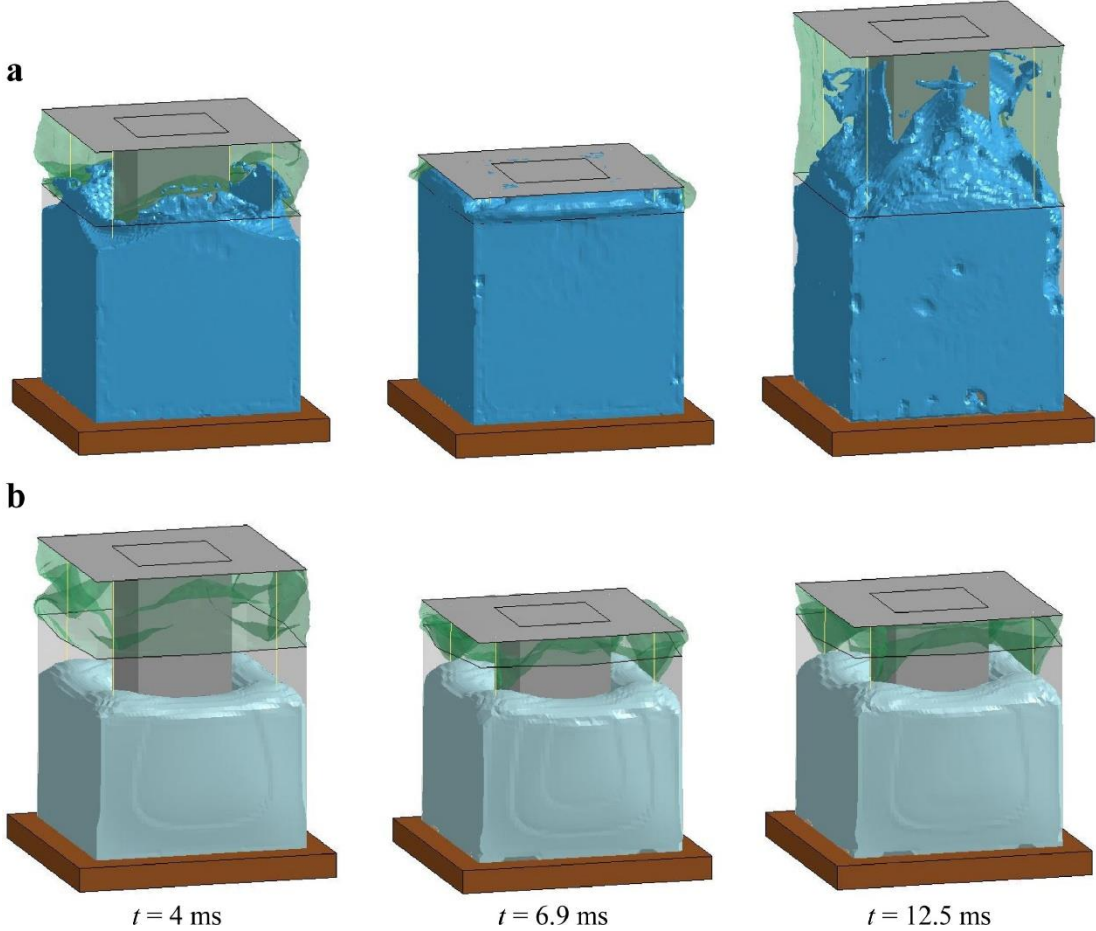


Figure 7-14. Recoverability of (a) water-filled specimen and (b) STF-filled specimen.

As observed in Figure 7-14(a), splashes of water inside water-filled specimen (W-V6.25) occur during loading process. Once unloaded, the top plate quickly bounces back since there is very little constraint between the tube core and the water. In the case of STF-filled specimen (S-V6.25), the quick rebound of the top plate is prevented by the traction of the tube core due to the sticky behaviour of STF. Therefore, the top plate slowly recovers its position, as illustrated in Figure 7-14(b). The top plate of the water-filled specimen bounces back quickly during unloading while that of STF-filled specimen slowly recovers. This steady recovery characteristic allows the proposed device to absorb the impact energy and slowly recover after the impact or blast events. It is noted that the water-filled specimen recovers quickly and excessively with less energy dissipation, which is unfavourable for an ideal absorber.

7.4.4 Comparison of energy absorption capacities of BIEAD, aluminium foam and honeycomb

In this session, the energy absorption performance of the proposed BIEAD (S-V6.25) is compared with the conventional aluminium foam and honeycomb available in the market. The CMATTM aluminium foam [182] and expanded aluminium honeycomb are used as the core of cladding for comparison, as shown in Figure 7-15. The CMATTM aluminium foam has a relative density of 5%. The expanded aluminium honeycomb has a cell size of 18 mm and wall thickness of 0.05 mm, corresponding to a relative density of 0.72%. These two claddings have the same external steel plates and overall dimension of $72 \times 72 \times 120$ mm as BIEAD. The external steel plates are connected to the aluminium foam and honeycomb cores using tied contact. The same loading condition and crushing speed of 6.25 m/s are applied to both claddings and the proposed BIEAD.

The Belytschko-Tsay shell element and material model *MAT_PIECEWISE LINEAR PLASTICITY are used to model the aluminium honeycomb. The aluminium honeycomb is made of Aluminium 1060 which has a yield stress of 67.7 MPa and Young's modulus of 69 GPa. The aluminium foam is modelled using *MAT_CRUSHABLE FOAM. It has a density of 135.5 kg/m^3 . The detail of the input material properties of the Aluminium 1060 and CMATTM aluminium foam can be found in [9,182].

As the cell wall of the aluminium honeycomb starts to buckle and cells of aluminium foam collapse, these two types of cores gradually deform and dissipate the crushing energy through plastic deformation of the cores. For BIEAD, the contact force of S-V6.25 gradually increases as its tube core penetrates further into the STF, as shown in Figure 7-16. This is due to the increase of contact area between the STF and tube core's side walls, which leads to more deformation and higher viscous shear stress of STF.

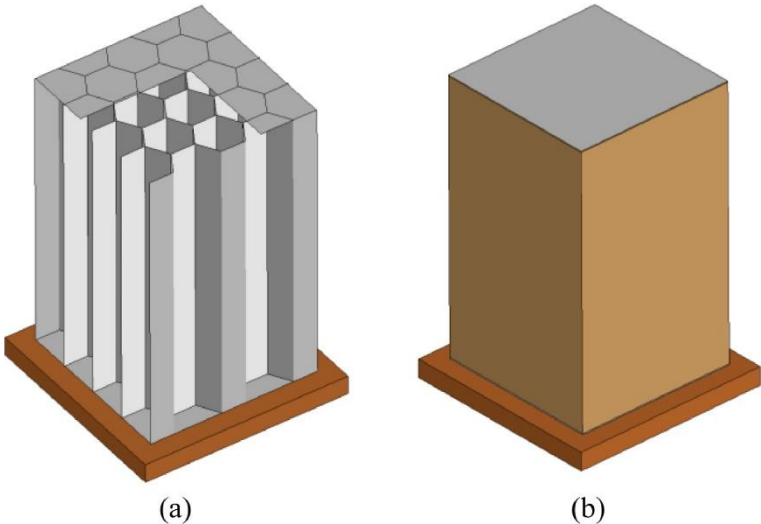


Figure 7-15. Isometric views of (a) aluminium honeycomb and (b) aluminium foam claddings.

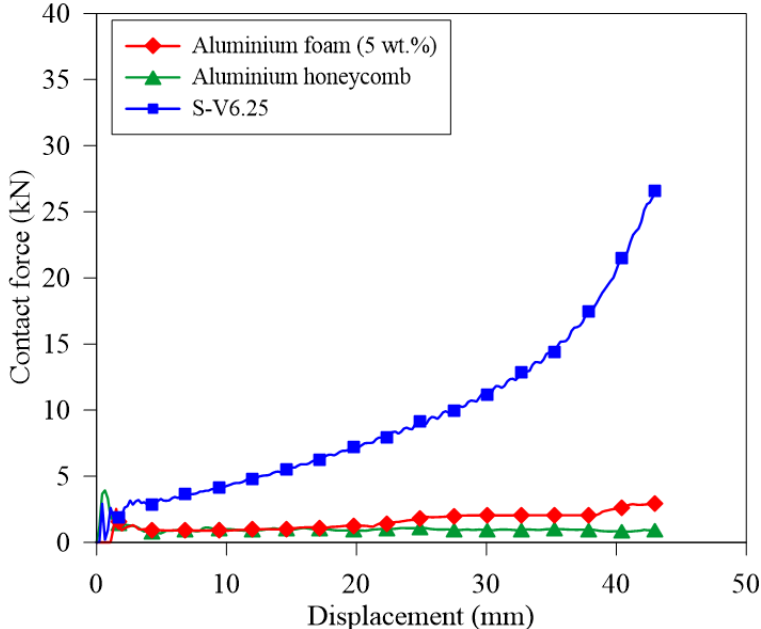


Figure 7-16. Comparison of force-displacement curves of S-V6.25, aluminium foam, and honeycomb (crushing speed $V = 6.25$ m/s).

The comparisons of *EA* and *SEA* of the aluminium foam, honeycomb and S-V6.25 are shown Figure 7-17. In terms of specific energy absorption capacity, since BIEAD has

higher mass than aluminium honeycomb and foam, the *SEA* of S-V6.25 is around 17% and 24% higher than that of aluminium honeycomb and foam, respectively.

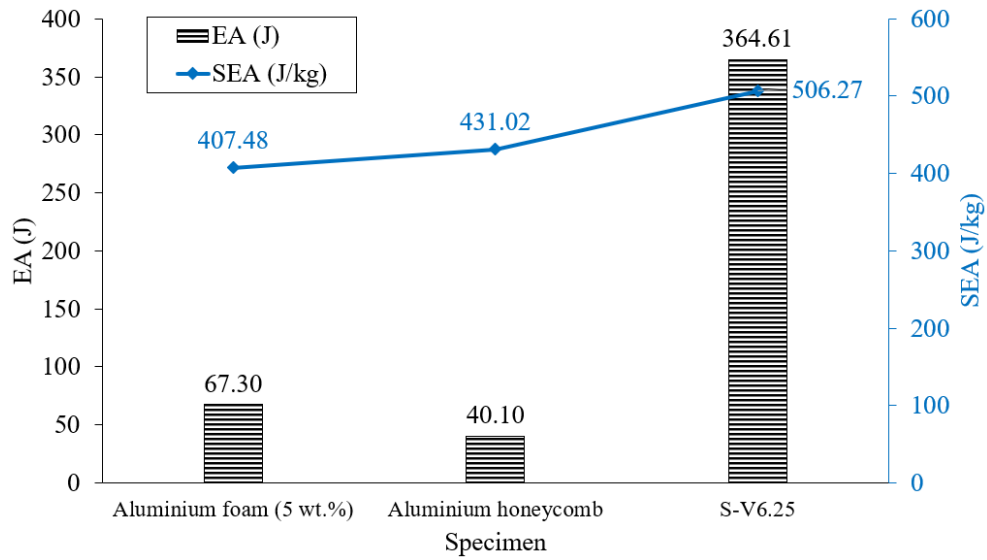


Figure 7-17. Comparison of energy absorption (*EA*) and *SEA* of the S-V6.25, aluminium foam, and honeycomb (crushing speed $V = 6.25$ m/s).

7.5 Parametric studies of BIEAD

As discussed in Section 7.4, the crushing resistance and energy absorption of BIEAD greatly depend on the apparent viscosity of the STF, which is influenced by the shear rate applied on the STF. In this section, parametric studies are carried out to investigate the effects of different shear thickening viscosities of STF, shear gaps and contact area on the energy absorption capacity of BIEAD. The same crushing velocity of 6.25 m/s is applied for all the FE models. The crushing resistance, energy absorbed by STF, and energy absorption capacity are compared for these specimens.

7.5.1 Effect of viscosity

Three STFs with different shear thickening viscosities, i.e., ($RK=72$, $RN=1.35$), ($RK=140$, $RN=1.35$), and ($RK=72$, $RN=1.5$), and the same critical shear rate as described in Section 7.3.2 are considered in this chapter. The viscosity versus shear rate relationships of these STFs are shown in Figure 7-18. In this group, all BIEADs have the same square-tube core of 32×32 mm cross section, thus having the same shear gap of 20 mm along the loading direction.

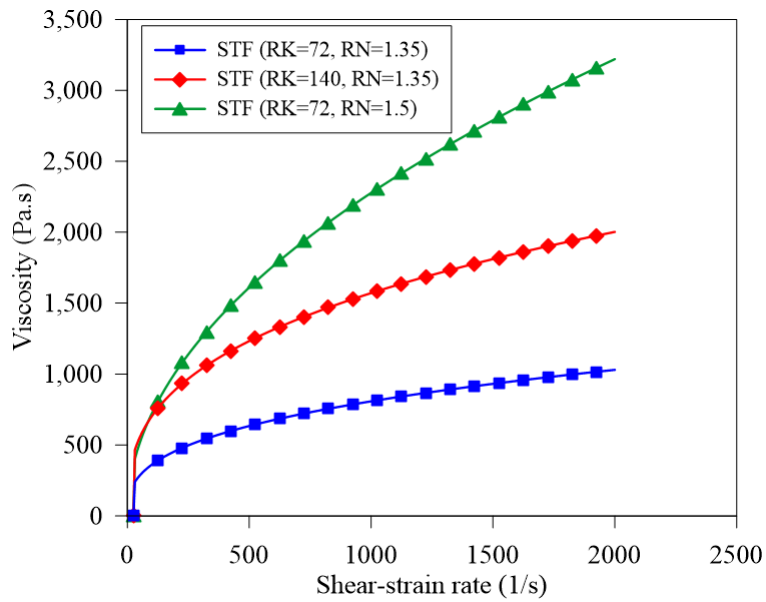


Figure 7-18. Viscosity versus shear strain-rate relationships of STF with different shear-thickening regime constants RK and RN .

As shown in Figure 7-19, the crushing resistance of the specimen increases as the viscosity of the STF increases. Under the same shear rate, the STF with higher viscosity has more intensive shear thickening behaviour, which leads to higher viscous shear stress and viscous dissipation of STF during crushing process. The specimen S-V6.25 ($RK=72$, $RN=1.5$) with higher viscosity STF has the SEA of 990.44 J/kg, which is 96% higher than that of specimen S-V6.25 ($RK=72$, $RN=1.35$) with lower viscosity STF under the same loading rate.

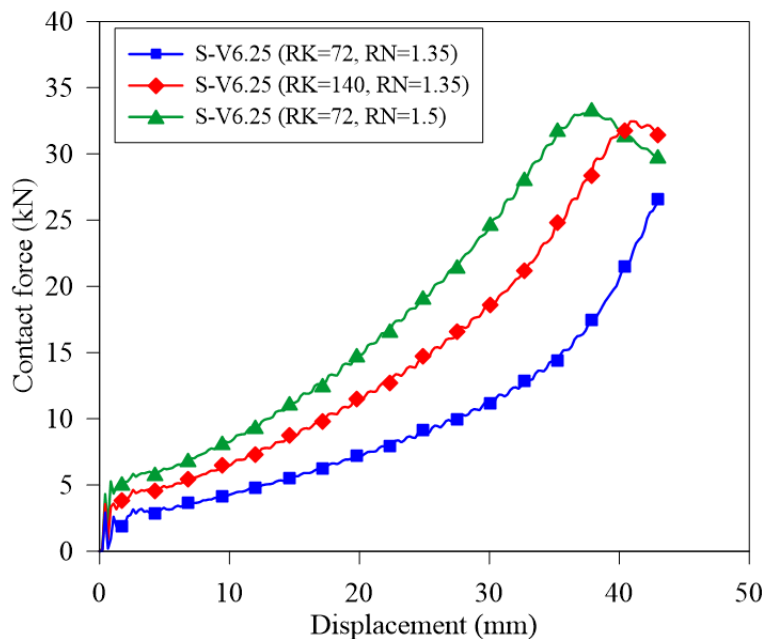


Figure 7-19. Force-displacement curves of specimen filled with STF of different shear-thickening constants under the crushing velocity of 6.25 m/s.

As shown in Figure 7-20 and Table 7-5, the energy dissipated by the STF contributes the largest share of the total energy which is around 79% to 85%, while the remaining is contributed by the steel components. The STF of high viscosity transforms to be solid-like and generates higher shear resistance which leads to the deformation of the tube core during the penetration of the core. Therefore, the EA of BIEAD can be increased by using STF with high shear thickening behaviour. However, high viscosity and jamming front STF can also cause the excessive deformation of the tube core.

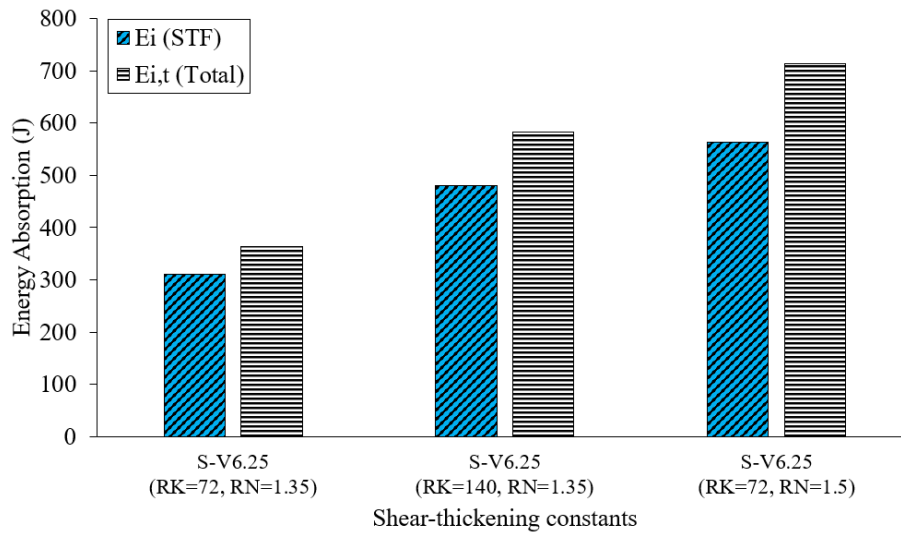


Figure 7-20. Internal energy absorption of STF and total internal energy absorption of specimens with different shear-thickening constants under the crushing velocity of 6.25 m/s.

Table 7-5. Internal energy and SEA of each specimen with various shear-thickening constants.

Specimen	Shear-thickening constants [175]		Internal Energy (J)		E_i (STF)/ $E_{i,t}$ (%)	SEA (J/kg)
	RK	RN	E_i (STF)	$E_{i,t}$ (Total)		
S-V6.25 ($RK=72, RN=1.35$)	72	1.35	311.20	364.61	85.4%	506.27
S-V6.25 ($RK=140, RN=1.35$)	140	1.35	480.00	582.45	82.4%	808.75
S-V6.25 ($RK=72, RN=1.5$)	72	1.5	564.00	713.30	79.1%	990.44

7.5.2 Effect of shear gap

Three specimens with different shear gaps (16 mm, 20 mm, and 24 mm) between the tube core and container wall are considered herein. These shear gaps are obtained by varying the widths of the container in both horizontal directions while the width of

tube core remains as 32 mm, as illustrated in Figure 7-21(a). All specimens are filled with STF of the same shear thickening properties ($RK=72$, $RN=1.35$).

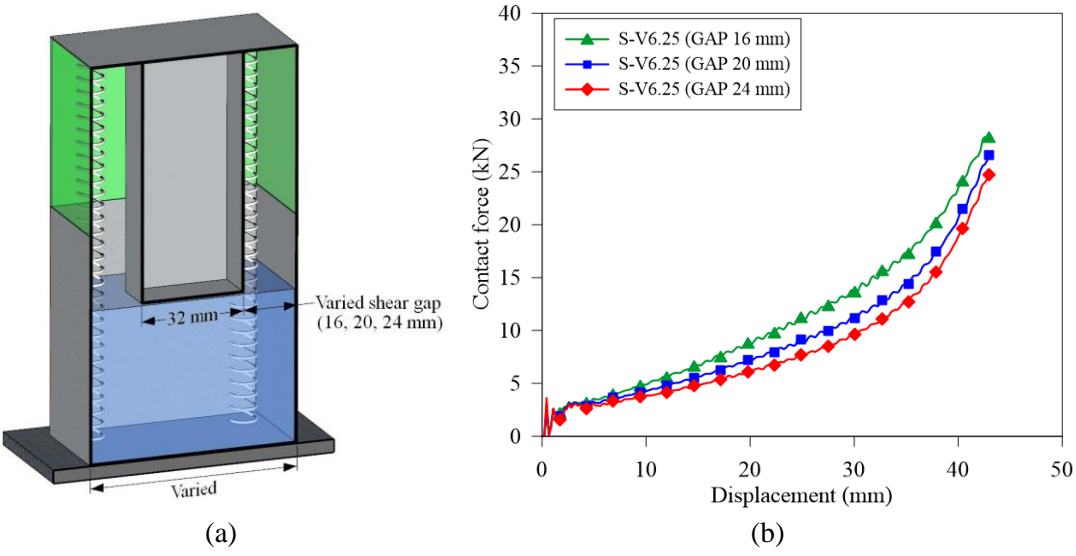


Figure 7-21. (a) Cross section showing the variation of shear gap and (b) force-displacement curves of specimens with different shear gaps.

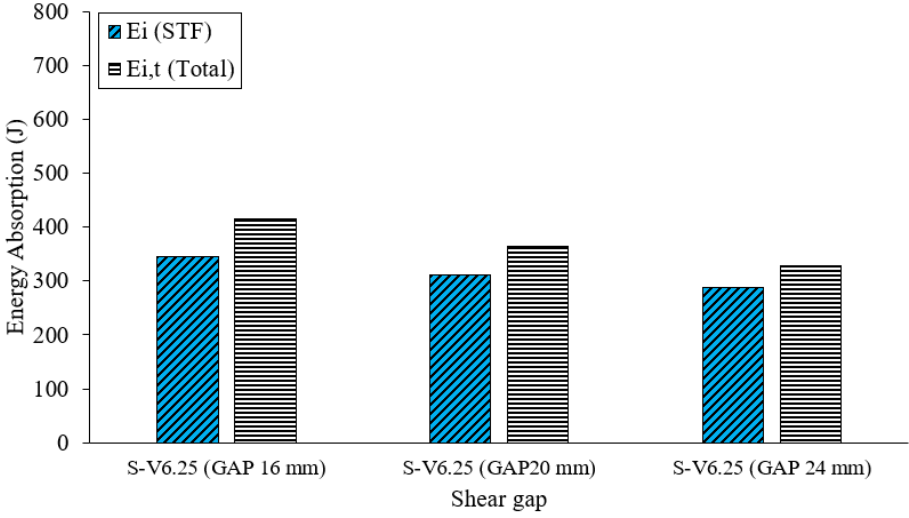


Figure 7-22. Internal energy absorption of STF and total internal energy absorption of specimens with different shear gaps.

As shown in Figure 7-21(b), reducing the shear gap leads to the increase of crushing resistance due to higher shear rate. During the penetration of the tube core, STF of specimen with small shear gap resists higher shear rate, thus leading to high viscous shear stress of STF and crushing resistance of BIEAD. The EA of S-V6.25 (GAP 16 mm) is around 27% higher than that of S-V6.25 (GAP 24 mm). Reducing the shear gap by changing the dimension of the container lightens the overall mass of specimen. Thus, S-V6.25 (GAP 16 mm) has 79% higher SEA than S-V6.25 (GAP 24 mm). The

energy absorbed by STF is around 82% to 87% of the total energy of the specimen, as shown in Figure 7-22 and Table 7-6. It can be concluded that reducing the shear gap not only increases of EA and SEA but also decreases the overall mass of BIEAD.

Table 7-6. Internal energy and SEA of each specimen with different shear gaps.

Specimen	Shear gap	Internal Energy (J)		E_i (STF)/ $E_{i,t}$ (%)	SEA (J/kg)
		E_i (STF)	$E_{i,t}$ (Total)		
S-V6.25 (GAP 16 mm)	16 mm	344.40	416.22	82.7%	691.70
S-V6.25 (GAP 20 mm)	20 mm	311.20	364.61	85.4%	506.27
S-V6.25 (GAP 24 mm)	24 mm	287.60	328.95	87.4%	386.80

7.5.3 Effect of contact area

The contact area between the tube core and STF is varied by changing the base widths of the tube core while the width of the container is kept the same as 72 mm, as illustrated in Figure 7-23(a). Three specimens with different base widths of tube cores (24 mm, 32 mm, and 40 mm) having the bottom contact areas of 576 mm², 1,024 mm², and 1,600 mm² are denoted by S-V6.25 (B 24 mm), S-V6.25 (B 32 mm), and S-V6.25 (B 40 mm), respectively. The width of the container is kept the same so that these three specimens have the same amount of STF. Therefore, increasing the width of the tube core, the shear gaps of S-V6.25 (B 24 mm), S-V6.25 (B 32 mm), and S-V6.25 (B 40 mm) decrease and are equal to 24 mm, 20 mm, and 16 mm, respectively, which correspond to the ratio of shear gap to contact length of 1.0, 0.625, 0.4. All specimens are filled with STF of the same shear thickening properties ($RK=72$, $RN=1.35$) and tested under the same crushing speed of 6.25 m/s.

As shown in Figure 7-23(b), the crushing resistance of the specimen significantly increases with the increase of contact area. As the width of the tube core increases, the interfacial contact area between the STF and tube core becomes larger which leads to higher jamming front and deformation of STF, thus, increasing the crushing resistance of the BIEAD. It should be noted that the reduced shear gap also contributes to this increase due to the increased shear rate as reported in Section 7.5.2. However, the effect of shear gap on the crushing resistance is marginal as shown in Figure 7-21(b).

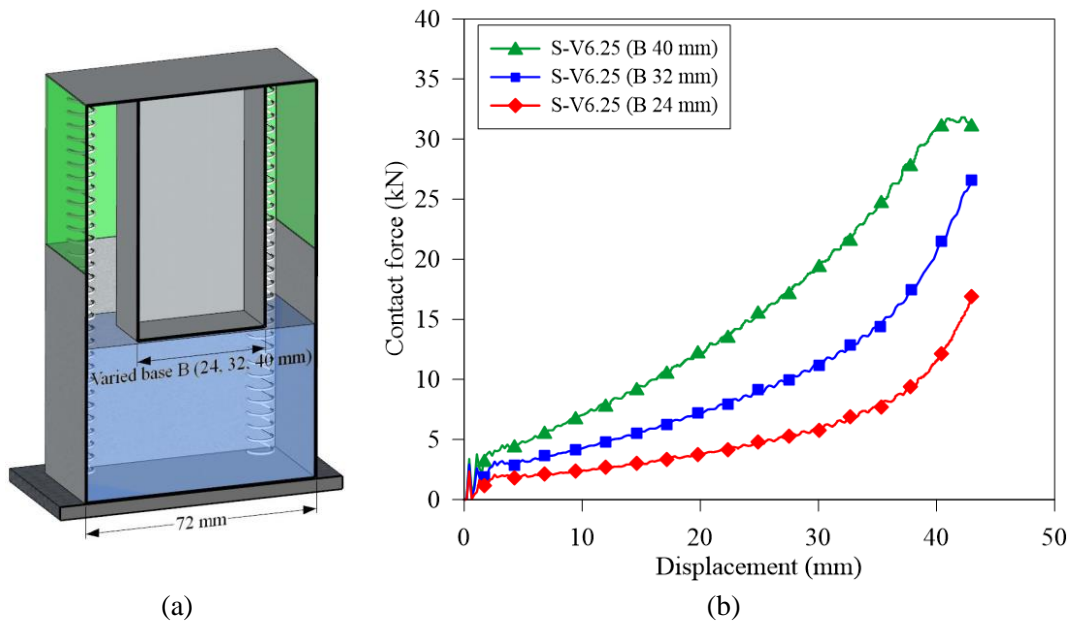


Figure 7-23. (a) Cross section showing the varied base length of tube core and (b) force-displacement curves of specimens with different contact areas.

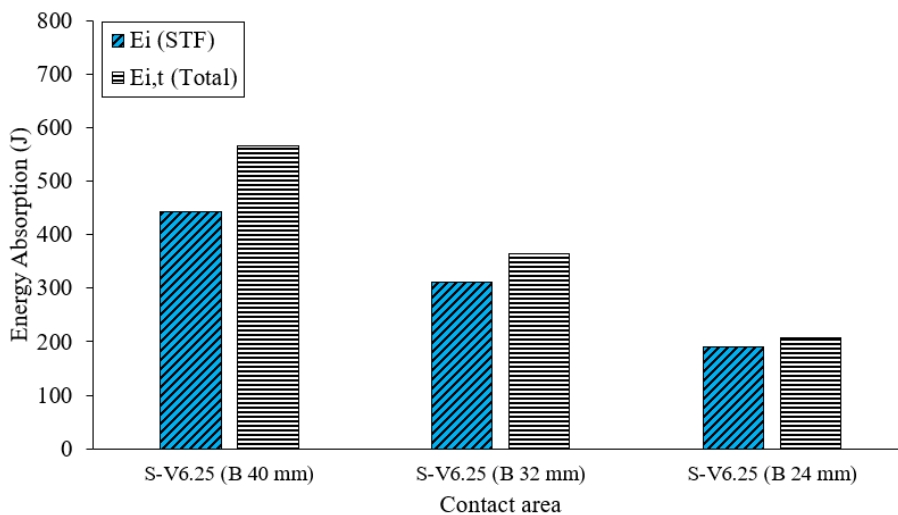


Figure 7-24. Internal energy absorption of STF and total internal energy absorption of specimens with different contact areas.

The *SEA* of the BIEAD increases by 157% from 297.14 J/kg to 763.35 J/kg with the increase of base width of tube core from 24 mm to 40 mm. As shown in Figure 7-24 and Table 7-7, STF absorbs most impact energy, and its energy absorption counts for 78% to 92% of the total energy absorption, while the remaining is absorbed by the steel parts of the specimens. As illustrated in Figure 7-25, the square-tube core of S-V6.25 (B 40 mm) deforms more than that of S-V6.25 (B 24 mm) because of its lower aspect ratio (height/width) of tube core [75]. Under the same height, the square-tube core of S-V6.25 (B 40 mm) has larger width than S-V6.25 (B 24 mm), thus having less

constraint on the cross-section, which leads to larger deformation of the core. Hence, increasing the contact area between the STF and tube core leads to higher EA of BIEAD. However, the deformation of the tube core may occur.

Table 7-7. Internal energy and SEA of each specimen with different contact areas.

Specimen	Square tube core		Internal Energy (J)		E_i (STF)/ $E_{i,t}$ (%)	SEA (J/kg)
	width B	Bottom area (mm ²)	E_i (STF)	$E_{i,t}$ (Total)		
S-V6.25 (B 40 mm)	40 mm	1,600	444.00	566.90	78.3%	763.35
S-V6.25 (B 32 mm)	32 mm	1,024	311.20	364.61	85.4%	506.27
S-V6.25 (B 24 mm)	24 mm	576	191.20	207.62	92.1%	297.14

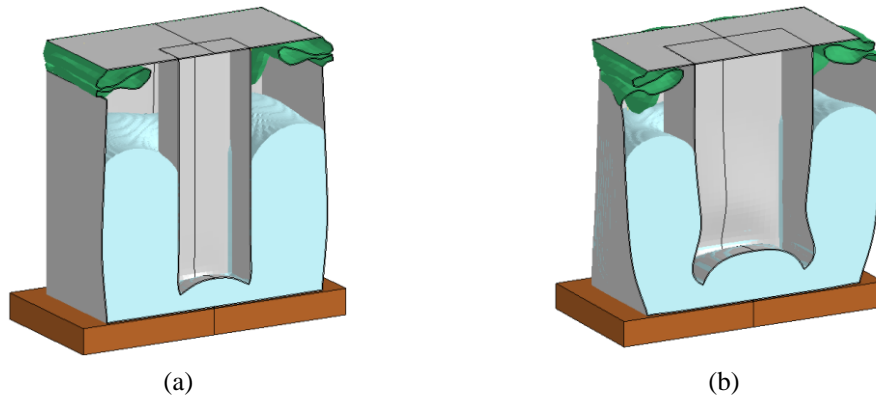


Figure 7-25. Cross sections showing core deformations of (a) S-V6.25 (B 24 mm) and (b) S-V6.25 (B 40 mm).

7.6 Summary

In this chapter, a new Bio-Inspired Energy-Absorbing Device (BIEAD) to mimic the suture and viscoelastic material between the suture interfaces is proposed and investigated by using finite element software LS-DYNA. STF is used to represent the viscoelastic material while the tube core is used to mimic a single tooth of the suture. BIEAD is constructed by filling with the STF whose shear thickening behaviour is activated by the penetration of the tube core. Various parameters such as the loading rates, viscosities of STF, shear gaps and contact areas are studied to investigate the crushing resistance and energy absorption capacities of both STF and BIEAD. The main findings are summarised as follows.

- BIEAD can absorb the impact energy and slowly recover its original position after dynamic loading due to the shear thickening behaviour, sticky characteristic of the STF, and the elastic springs in the prototype design.
- Energy absorption capacity of the BIEAD is sensitive to the loading rate. As the loading rate increases, the rise of the viscosity or the thickening behaviour of the STF occurs, thus dissipating the impact energy through the viscous dissipation of the STF.
- Unlike the aluminium foam and honeycomb which dissipate the energy through plastic deformation, BIEAD dissipates the energy primarily through viscous dissipation and is capable of recovering after impact. BIEAD of the same dimension has a specific energy absorption capacity of 17% and 24% higher than aluminium honeycomb and foam, respectively.
- The performance of the BIEAD depends on the shear thickening behaviour of STF. The crushing resistance and energy absorption capacity of the BIEAD can be enhanced by using STF with high shear-thickening behaviour or reducing the shear gap.
- Increasing the contact area between the STF and tube core significantly increases the EA of BIEAD. However, excessive deformation of the tube core may occur due to high viscosity and normal stress via jamming front of STF.

Chapter 8. Conclusion and recommendations

8.1 Main findings

In this thesis, four innovative energy-absorbing structures for protective applications are proposed and developed by mimicking the structural features and protective mechanisms found in nature. The first nature-inspired energy-absorbing structure is proposed by mimicking the structural feature of a cross-section of the plant stem. This proposed structure demonstrates excellent crushing performance compared to conventional structures, such as aluminium foam and honeycomb cores of the same mass. Additionally, it exhibits exceptional impact mitigation performance as the internal core of the sacrificial cladding against impact loads when compared to sacrificial cladding with conventional square or corrugated square honeycomb cores. The second innovative sandwich structure, with adaptive energy-absorbing capability, is numerically investigated and proposed by mimicking the protective mechanism of the beetles. This adaptive energy-absorbing structure demonstrates high crushing resistance and energy-absorbing capacity, which increase with the crushing speed, demonstrating its ability to adapt to the uncertainties of real impact scenarios. The third innovative nature-inspired design is proposed and numerically investigated by incorporating shear thickening fluid into the cells of an origami metastructure, imitating the existence of the viscoelastic material found inside the protective mechanisms in nature. This design achieves a more stable crushing force without a high initial peak force, resulting in an excellent energy-absorbing structure with ideal crushing efficiency and adaptive crushing resistance. The fourth innovative nature-inspired structure is proposed and numerically investigated to develop a recoverable energy-absorbing device by mimicking the suture interface found inside woodpecker beaks. This energy-absorbing device exhibits a good energy-absorbing capacity and can recover after the impact.

Chapter 3 presents the dynamic crushing response and energy absorption performance of the proposed corrugated tilted honeycomb (CTH) core, inspired by the corrugated and tilted/tapered shape of the cross-section of a plant stem. The proposed CTH core demonstrates excellent crushing performance, exhibiting higher crushing resistance without a high initial peak force under various crushing speeds, when compared to

aluminium foam and honeycomb cores of the same mass. The proposed CTH core also has a higher energy absorption capacity and greater crushing force efficiency than most existing structural core forms with similar relative density.

Chapter 4 presents the impact mitigation performance of the sacrificial cladding with the proposed CTH core as its internal core. The CTH claddings, featuring one and two corrugations on each unit-cell, are investigated under various impact scenarios and compared with conventional square honeycomb and corrugated square honeycomb claddings of the same mass. The proposed CTH cladding exhibits excellent impact mitigation performance, demonstrating a more stable crushing force without obvious high peaks, lower transmitted force, and larger deformation compared to sacrificial cladding with conventional square honeycomb and corrugated square honeycomb cores.

Chapter 5 presents a novel sandwich structure inspired by beetle forewing (SSBF) with adaptive energy-absorbing capability. By mimicking the internal structure of beetle forewing with the existence of viscoelastic material, the proposed SSBF exhibits high crushing resistance and a high energy absorption capacity, which also increases with the increase in crushing speed, demonstrating its ability to adapt to the uncertain fluctuations of real impact scenarios. As compared to an empty specimen with a thick core having a comparable mass, the initial peak crushing resistance of the empty specimen significantly increases as the crushing speed rises. However, its overall crushing resistance remains almost unchanged. In contrast, the crushing resistance of the SSBF enhances with the increase in crushing speed and remains stable throughout the crushing process without a noticeable initial peak, demonstrating its ideal and adaptive energy-absorbing behaviour under different impact scenarios.

Chapter 6 proposes an innovative nature-inspired design with adaptive crushing resistance and ideal crushing efficiency by imitating the viscoelastic behaviour found inside the protective mechanism in nature, i.e., inside the tubules in the horn sheaths of bighorn sheep. The proposed design is developed by incorporating the shear thickening fluid into the cells of an origami metastructure. This nature-inspired STF-filled origami metastructure (STF-OM) generates a higher and more stable crushing force without a high initial peak, resulting in an excellent energy-absorbing structure with ideal crushing efficiency. Furthermore, its crushing resistance increases with the

increase in crushing velocity, demonstrating its adaptive crushing performance for different impact scenarios.

Chapter 7 proposes a novel recoverable bio-inspired energy-absorbing device (BIEAD) by mimicking the wavy suture and viscoelastic behaviour observed between the suture interfaces inside the beak of woodpeckers. This proposed energy-absorbing device exhibits excellent energy-absorbing capacity and possesses the capability to recover its original shape after impact. This recovery is made possible through the combination of shear thickening behaviour and the elastic springs in the prototype design, demonstrating its effectiveness in energy absorption and post-impact recovery.

Overall, this thesis presents four innovative energy-absorbing structures, each characterised by unique energy absorption mechanisms. Excellent energy-absorbing capability with high crushing force without a significantly high peak is achieved for the proposed structure inspired by the structural feature of a plant stem. Moreover, it can be easily fabricated using a simple pressing technique, making it suitable for applications such as energy absorbers and protective sacrificial claddings against impact and blast loads. Adaptive energy-absorbing capacity and crushing resistance with ideal crushing efficiency are observed for the structures inspired by the protective mechanisms of animals. These structures show promising potential for use in protective applications, where the ability to withstand a wide range of uncertain loading scenarios is essential. Furthermore, the proposed recoverable energy-absorbing device has the potential to serve as a protective structure capable of withstanding multiple blast or impact events.

8.2 Recommendations for future work

In this thesis, one unit consisting of three cells of the proposed SSBF design has been numerically investigated. Performances of a planar-array SSBF structure with multiple unit cells could be numerically and experimentally investigated subjected to blast and impact loads in the future. Furthermore, the structural components of SSBF, including the arch core and external plates, can be made from recoverable materials, such as silicone elastic material [216], to explore the development of recoverability and adaptivity of energy-absorbing structures.

A full-sized STF-OM design with a greater number of unit cells could be fabricated and investigated against localised impact and blast loads to further verify its impact mitigation performance. The peak transmitted force of the proposed STF-OM may be compared with that of conventional structures, such as aluminium foam and honeycomb structures, under various loading scenarios.

The proposed BIEAD in this thesis represents one unit in an energy-absorbing structure. A full-sized recoverable BIEAD with multiple tube cores could be investigated numerically and experimentally under various impact speeds. The effects of tube-core shape and spring stiffness on energy-absorption performance and recovery speed could be further studied. Additionally, strong and lightweight materials, such as fibre-reinforced polymer (FRP) composites, could be also explored and used as structural components (i.e., container and tube core) of the BIEAD to develop a lightweight and recoverable energy-absorbing structure.

References

- [1] Shirbhate PA, Goel MD. A Critical Review of Blast Wave Parameters and Approaches for Blast Load Mitigation. *Arch Comput Methods Eng* 2021;28:1713–30.
- [2] Hao H. Predictions of structural response to dynamic loads of different loading rates. *Int. J. Prot. Struct.*, vol. 6, 2015, p. 585–605.
- [3] Li Z, Wen Y, Wen X, Hao H, Chen W. Single and double-layered kirigami corrugated sandwich panels against impact loads. *Structures* 2023;51:402–14.
- [4] Lu G, Yu T. *Energy Absorption of Structures and Materials*. Cambridge, England: Woodhead Publishing Limited; 2003.
- [5] Li Z, Fang R, Yang Q, Chen W, Hao H, Kong Q, et al. Performance of sandwich cladding with modular truncated square pyramid foldcore under projectile impact. *Int J Impact Eng* 2022;166:104258.
- [6] Fanton M, Alizadeh HV, Domel AG, Devlin M, Kurt M, Mungal MG, et al. Variable area, constant force shock absorption motivated by traumatic brain injury prevention. *Smart Mater Struct* 2020;29:085023.
- [7] Nagy A, ko WL, Lindholm US. Mechanical Behavior of Foamed Materials Under Dynamic Compression. *J Cell Plast* 1974;10:127–34.
- [8] Moss WC, King MJ, Blackman EG. Towards reducing impact-induced brain injury: Lessons from a computational study of army and football helmet pads. *Comput Methods Biomech Biomed Engin* 2014;17:1173–84.
- [9] Li Z, Chen W, Hao H. Blast mitigation performance of cladding using square dome-shape kirigami folded structure as core. *Int J Mech Sci* 2018;145:83–95.
- [10] Aparecida Diniz C, Brighenti Bortoluzzi D, Luiz Junho Pereira J, Simões da Cunha Junior S, Ferreira Gomes G. On the influence of manufacturing parameters on buckling and modal properties of sandwich composite structures. *Structures* 2022;46:664–80.

- [11] Li Z, Yang Q, Chen W, Hao H, Matenga C, Huang Z, et al. Impact response of a novel sandwich structure with Kirigami modified corrugated core. *Int J Impact Eng* 2021;156:103953.
- [12] Xue Z, Hutchinson JW. Crush dynamics of square honeycomb sandwich cores. *Int J Numer Methods Eng* 2006;65:2221–45.
- [13] Xu S, Beynon JH, Ruan D, Lu G. Experimental study of the out-of-plane dynamic compression of hexagonal honeycombs. *Compos Struct* 2012;94:2326–36.
- [14] Rejab MRM, Cantwell WJ. The mechanical behaviour of corrugated-core sandwich panels. *Compos Part B Eng* 2013;47:267–77.
- [15] Hou S, Shu C, Zhao S, Liu T, Han X, Li Q. Experimental and numerical studies on multi-layered corrugated sandwich panels under crushing loading. *Compos Struct* 2015;126:371–85.
- [16] Cao BT, Hou B, Zhao H, Li YL, Liu JG. On the influence of the property gradient on the impact behavior of graded multilayer sandwich with corrugated cores. *Int J Impact Eng* 2018;113:98–105.
- [17] Kiliçaslan C, Güden M, Odaci IK, Taşdemirci A. Experimental and numerical studies on the quasi-static and dynamic crushing responses of multi-layer trapezoidal aluminum corrugated sandwiches. *Thin-Walled Struct* 2014;78:70–8.
- [18] Imbalzano G, Tran P, Ngo TD, Lee PVS. A numerical study of auxetic composite panels under blast loadings. *Compos Struct* 2016;135:339–52.
- [19] McShane GJ, Radford DD, Deshpande VS, Fleck NA. The response of clamped sandwich plates with lattice cores subjected to shock loading. *Eur J Mech A/Solids* 2006;25:215–29.
- [20] Ozdemir Z, Hernandez-Nava E, Tyas A, Warren JA, Fay SD, Goodall R, et al. Energy absorption in lattice structures in dynamics: Experiments. *Int J Impact Eng* 2016;89:49–61.

- [21] Ousji H, Belkassem B, Louar MA, Reymen B, Martino J, Lecompte D, et al. Air-blast response of sacrificial cladding using low density foams: Experimental and analytical approach. *Int J Mech Sci* 2017;128–129:459–74.
- [22] Wang Y, Liew JYR, Lee SC, Wang W. Experimental and analytical studies of a novel aluminum foam filled energy absorption connector under quasi-static compression loading. *Eng Struct* 2017;131:136–47.
- [23] Wadley HNG. Multifunctional periodic cellular metals. *Philos Trans R Soc A Math Phys Eng Sci* 2006;364:31–68.
- [24] Zhu F, Lu G, Ruan D, Wang Z. Plastic deformation, failure and energy absorption of sandwich structures with metallic cellular cores. *Int J Prot Struct* 2010;1:507–41.
- [25] Gibson LJ, Ashby MF. *Cellular solids structure and properties*. Cambridge University Press; 1999.
- [26] Ingrole A, Hao A, Liang R. Design and modeling of auxetic and hybrid honeycomb structures for in-plane property enhancement. *Mater Des* 2017;117:72–83.
- [27] Mauko A, Fíla T, Falta J, Koudelka P, Rada V, Neuhäuserová M, et al. Dynamic deformation behaviour of chiral auxetic lattices at low and high strain-rates. *Metals (Basel)* 2021;11:1–15.
- [28] Chen W, Hao H. Numerical study of a new multi-arch double-layered blast-resistance door panel. *Int J Impact Eng* 2012;43:16–28.
- [29] Li Z, Chen W, Hao H. Numerical study of sandwich panel with a new bi-directional Load-Self-Cancelling (LSC) core under blast loading. *Thin-Walled Struct* 2018;127:90–101.
- [30] Palanivelu S, Van Paepegem W, Degrieck J, De Pauw S, Vantomme J, Wastiels J, et al. Low velocity axial impact crushing performance of empty recyclable metal beverage cans. *Int J Impact Eng* 2011;38:622–36.
- [31] Choudhary NS, Goel MD, Panchal S. Numerical Analysis of Innovative

- Sacrificial Protection System under Blast Loading. *Pract Period Struct Des Constr* 2022;27:04021075.
- [32] Tarlochan F, Ramesh S, Harpreet S. Advanced composite sandwich structure design for energy absorption applications: Blast protection and crashworthiness. *Compos Part B Eng* 2012;43:2198–208.
- [33] Chatys R, Panich A, Jurecki RS, Kleinhofs M. Composite materials having a layer structure of “sandwich” construction as above used in car safety bumpers. 11th Int. Sci. Tech. Conf. Automot. Safety, Automot. Saf. 2018, 2018, p. 1–8.
- [34] Pan J, Fang H, Xu MC, Wu YF. Study on the performance of energy absorption structure of bridge piers against vehicle collision. *Thin-Walled Struct* 2018;130:85–100.
- [35] Levadnyi I, Awrejcewicz J, Zhang Y, Goethel MF, Gu Y. Finite Element Analysis of Impact for Helmeted and Non-helmeted Head. *J Med Biol Eng* 2018;38:587–95.
- [36] Wang Y, Lu J, Zhai X, Xue B, Zhi X. Response of energy absorbing connector with polyurethane foam and multiple pleated plates under impact loading. *Int J Impact Eng* 2019;133:103356.
- [37] Vieira CM, Almeida HA, Ferreira IS, Vasco JO, Bártolo PJ, Ruben B, et al. DEVELOPMENT OF AN IMPACT ABSORBER FOR ROADSIDE BARRIERS Summary : LS-DYNA Anwenderforum 2008:25–36.
- [38] Bohara RP, Linforth S, Nguyen T, Ghazlan A, Ngo T. Anti-blast and -impact performances of auxetic structures: A review of structures, materials, methods, and fabrications. *Eng Struct* 2023;276:115377.
- [39] Imbalzano G, Linforth S, Ngo TD, Lee PVS, Tran P. Blast resistance of auxetic and honeycomb sandwich panels: Comparisons and parametric designs. *Compos Struct* 2018;183:242–61.
- [40] Zhang J, Lu G, You Z. Large deformation and energy absorption of additively manufactured auxetic materials and structures: A review. *Compos Part B Eng*

2020;201:108340.

- [41] Rebelo HB, Cismasiu C. Robustness assessment of a deterministically designed sacrificial cladding for structural protection. *Eng Struct* 2021;240:112279.
- [42] Mohammadi H, Ahmad Z, Petru M, Mazlan SA, Faizal Johari MA, Hatami H, et al. An Insight from Nature: Honeycomb Pattern in Advanced Structural Design for Impact Energy Absorption. *J Mater Res Technol* 2022.
- [43] Fathers RK, Gattas JM, You Z. Quasi-static crushing of eggbox, cube, and modified cube foldcore sandwich structures. *Int J Mech Sci* 2015;101–102:421–8.
- [44] Bohara RP, Linforth S, Thai HT, Nguyen T, Ghazlan A, Ngo T. Experimental, numerical, and theoretical crushing behaviour of an innovative auxetic structure fabricated through 3D printing. *Thin-Walled Struct* 2023;182:110209.
- [45] Li Z, Chen W, Hao H. Crushing behaviours of folded kirigami structure with square dome shape. *Int J Impact Eng* 2018;115:94–105.
- [46] Li Z, Chen W, Hao H, Cui J, Shi Y. Experimental study of multi-layer folded truncated structures under dynamic crushing. *Int J Impact Eng* 2019;131:111–22.
- [47] Li Z, Chen W, Hao H. Dynamic crushing and energy absorption of foam filled multi-layer folded structures: Experimental and numerical study. *Int J Impact Eng* 2019;133:103341.
- [48] Li Z, Yang Q, Chen W, Hao H, Fang R, Cui J. Dynamic compressive properties of reinforced and kirigami modified honeycomb in three axial directions. *Thin-Walled Struct* 2022;171:108692.
- [49] Wang Y, Zhai X, Yan J, Ying W, Wang W. Experimental, numerical and analytical studies on the aluminum foam filled energy absorption connectors under impact loading. *Thin-Walled Struct* 2018;131:566–76.
- [50] Wang Y, Zhai X, Ying W, Wang W. Dynamic crushing response of an energy absorption connector with curved plate and aluminum foam as energy absorber.

- Int J Impact Eng 2018;121:119–33.
- [51] Harris JA, McShane GJ. Impact response of metallic stacked origami cellular materials. Int J Impact Eng 2021;147:103730.
- [52] Li X, Lu F, Zhang Y, Lin Y, Meng Y. Experimental study on out-of-plane mechanical and energy absorption properties of combined hexagonal aluminum honeycombs under dynamic impact. Mater Des 2020;194:108900.
- [53] Baker WE, Togami TC, Weydert JC. Static and dynamic properties of high-density metal honeycombs. Int J Impact Eng 1998;21:149–63.
- [54] Wu X, Xiao K, Yin Q, Zhong F, Huang C. Experimental study on dynamic compressive behaviour of sandwich panel with shear thickening fluid filled pyramidal lattice truss core. Int J Mech Sci 2018;138–139:467–75.
- [55] Radford DD, McShane GJ, Deshpande VS, Fleck NA. Dynamic compressive response of stainless-steel square honeycombs. J Appl Mech Trans ASME 2007;74:658–67.
- [56] Wang X, Qin R, Chen B. Laser-based additively manufactured bio-inspired crashworthy structure: Energy absorption and collapse behaviour under static and dynamic loadings. Mater Des 2021;211:110128.
- [57] Zhang S, Zhu Z, Li S, Yu F, Tian C, Yao L. A Simulation Methodology for Analyzing the Energy-Absorption Capabilities of Nanofluidic-System-Filled Tube under Split Hopkinson Pressure Bar Experiment. Materials (Basel) 2022;15:7030.
- [58] Li Z, Chen W, Hao H. Numerical study of blast mitigation performance of folded structure with foam infill. Structures 2019;20:581–93.
- [59] Das S, Brenkus NR, Tatar J. Strategies for Prevention, Protection, and Repair of Bridge Girders Vulnerable to Over-height Vehicle Impacts: A State-of-the-Art Review. Structures 2022;44:514–33.
- [60] Wu C, Huang L, Oehlers DJ. Blast Testing of Aluminum Foam-Protected Reinforced Concrete Slabs. J Perform Constr Facil 2011;25:464–74.

- [61] Qi C, Remennikov A, Pei LZ, Yang S, Yu ZH, Ngo TD. Impact and close-in blast response of auxetic honeycomb-cored sandwich panels: Experimental tests and numerical simulations. *Compos Struct* 2017;180:161–78.
- [62] Rebelo HB, Lecompte D, Cismasiu C, Jonet A, Belkassem B, Maazoun A. Experimental and numerical investigation on 3D printed PLA sacrificial honeycomb cladding. *Int J Impact Eng* 2019;131:162–73.
- [63] Ousji H, Belkassem B, Pyl L, Vantomme J. Air-blast loading on empty metallic beverage can used as sacrificial cladding: Experimental, analytical and numerical study. *Eng Struct* 2020;204:109979.
- [64] Palanivelu S. Energy Absorption of Crushable Tubes for Protective Structures under Static, Impact and Blast Loading. Ghent University, 2011.
- [65] Gladman B. LS-DYNA keyword user's manual-Volume I. Livermore, CA: Livermore Software Technology Corporation; 2020.
- [66] Mahesh P, Varinder S, Regalla SP, Gupta AK, Bera TC, Simhachalam B, et al. The effect of ultrasonic vibrations on residual stresses and material properties of steel tubes during the cold tube drawing process. *Adv Mater Process Technol* 2022.
- [67] Wu Y, Fang J, Wu C, Li C, Sun G, Li Q. Additively manufactured materials and structures: A state-of-the-art review on their mechanical characteristics and energy absorption. *Int J Mech Sci* 2023;246:108102.
- [68] Yang X, Ma J, Wen D, Yang J. Crashworthy design and energy absorption mechanisms for helicopter structures: A systematic literature review. *Prog Aersp Sci* 2020;114:100618.
- [69] Wierzbicki T. Crushing analysis of metal honeycombs. *Int J Impact Eng* 1983;1:157–74.
- [70] Sun G, Chen D, Zhu G, Li Q. Lightweight hybrid materials and structures for energy absorption: A state-of-the-art review and outlook. *Thin-Walled Struct* 2022;172:108760.

- [71] Xu P, Xiao X, Yao S, Kong L. Study on effect of offset defect on mechanical property of honeycomb structures. *Structures* 2021;34:275–85.
- [72] Zhang J, Ashby MF. The out-of-plane properties of honeycombs. *Int J Mech Sci* 1992;34:475–89.
- [73] Xu G, Wang Z, Li Z, Liang X. Theoretical and numerical analyses on mechanical performance of octagonal honeycomb structures subjected to out-of-plane compression. *Mech Adv Mater Struct* 2020;27:1461–72.
- [74] Deqiang S, Weihong Z, Yanbin W. Mean out-of-plane dynamic plateau stresses of hexagonal honeycomb cores under impact loadings. *Compos Struct* 2010;92:2609–21.
- [75] Côté F, Deshpande VS, Fleck NA, Evans AG. The out-of-plane compressive behavior of metallic honeycombs. *Mater Sci Eng A* 2004;380:272–80.
- [76] Xue Z, Hutchinson JW. A comparative study of impulse-resistant metal sandwich plates. *Int J Impact Eng* 2004;30:1283–305.
- [77] Fan Z, Ye G, Li S, Bai Z, Yong Q, Zhang Y, et al. Compression performance and failure mechanism of honeycomb structures fabricated with reinforced wood. *Structures* 2023;48:1868–82.
- [78] Deshpande VS, Ashby MF, Fleck NA. Foam topology: Bending versus stretching dominated architectures. *Acta Mater* 2001;49:1035–40.
- [79] Liu S, Lu G, Chen Y, Leong YW. Deformation of the Miura-ori patterned sheet. *Int J Mech Sci* 2015;99:130–42.
- [80] Gattas JM, You Z. The behaviour of curved-crease foldcores under low-velocity impact loads. *Int J Solids Struct* 2015;53:80–91.
- [81] Heimbs S. Foldcore sandwich structures and their impact behaviour: An overview. In: Abrate S, Castanié B, Rajapakse YDS, editors. *Dyn. Fail. Compos. Sandw. Struct. Solid Mech. its Appl.*, vol. 192, Springer, Dordrecht; 2013, p. 491–544.

- [82] Gattas JM, You Z. Quasi-static impact of indented foldcores. *Int J Impact Eng* 2014;73:15–29.
- [83] Fischer S. Aluminium foldcores for sandwich structure application: Mechanical properties and FE-simulation. *Thin-Walled Struct* 2015;90:31–41.
- [84] Li Z, Chen W, Hao H. Numerical study of open-top truncated pyramid folded structures with interconnected side walls against flatwise crushing. *Thin-Walled Struct* 2018;132:537–48.
- [85] Ma J, Chai S, Chen Y. Geometric design, deformation mode, and energy absorption of patterned thin-walled structures. *Mech Mater* 2022;168:104269.
- [86] Ha NS, Lu G. Thin-walled corrugated structures: A review of crashworthiness designs and energy absorption characteristics. *Thin-Walled Struct* 2020;157:106995.
- [87] Xu B, Wang C, Wang S. Crushing behaviours and energy absorption characteristics of square antiprisms structure against flatwise crushing. *Int J Impact Eng* 2022:104398.
- [88] Ma J, Dai H, Chai S, Chen Y. Energy absorption of sandwich structures with a kirigami-inspired pyramid foldcore under quasi-static compression and shear. *Mater Des* 2021;206.
- [89] Li Z, Yang Q, Fang R, Chen W, Hao H. Crushing performances of Kirigami modified honeycomb structure in three axial directions. *Thin-Walled Struct* 2021;160:107365.
- [90] Zheng X, Lee H, Weisgraber TH, Shusteff M, DeOtte J, Duoss EB, et al. Ultralight, ultrastiff mechanical metamaterials. *Science* (80-) 2014;344:1373–7.
- [91] Mukhopadhyay T, Adhikari S. Stochastic mechanics of metamaterials. *Compos Struct* 2017;162:85–97.
- [92] Xu M, Liu D, Wang P, Zhang Z, Jia H, Lei H, et al. In-plane compression behavior of hybrid honeycomb metastructures: Theoretical and experimental

- studies. *Aerosp Sci Technol* 2020;106:106081.
- [93] Vo NH, Pham TM, Hao H, Bi K, Chen W. Impact load mitigation of meta-panels with single local resonator. *Eng Struct* 2022;265:114528.
- [94] Chen Y, Xu R, Lu C, Liu K, Feng J, Sareh P. Multi-stability of the hexagonal origami hyper based on group theory and symmetry breaking. *Int J Mech Sci* 2023;247:108196.
- [95] Sareh P, Chermprayong P, Emmanuelli M, Nadeem H, Kovac M. Rotorigami: A rotary origami protective system for robotic rotorcraft. *Sci Robot* 2018;3:5228.
- [96] Ren X, Das R, Tran P, Ngo TD, Xie YM. Auxetic metamaterials and structures: A review. *Smart Mater Struct* 2018;27:023001.
- [97] Kelkar PU, Kim HS, Cho KH, Kwak JY, Kang CY, Song HC. Cellular auxetic structures for mechanical metamaterials: A review. *Sensors (Switzerland)* 2020;20:3132.
- [98] Hao J, Han D, Zhang XG, Zhang Y, Jiang W, Teng XC, et al. Novel dual-platform lightweight metamaterials with auxeticity. *Eng Struct* 2022;270:114891.
- [99] Yang Q, Li Z, Hao H, Chen W. Compressive mechanical properties and dynamic behaviour of origami-inspired tri-directional auxetic metastructure. *Eng Struct* 2023;281:115751.
- [100] Zhao X, Wei L, Wen D, Zhu G, Yu Q, Ma ZD. Bending response and energy absorption of sandwich beams with novel auxetic honeycomb core. *Eng Struct* 2021;247:113204.
- [101] Chen G, Zhang P, Deng N, Cai S, Cheng Y, Liu J. Paper tube-guided blast response of sandwich panels with auxetic re-entrant and regular hexagonal honeycomb cores – An experimental study. *Eng Struct* 2022;253:113790.
- [102] Chen G, Cheng Y, Zhang P, Cai S, Liu J. Blast resistance of metallic double arrowhead honeycomb sandwich panels with different core configurations

- under the paper tube-guided air blast loading. *Int J Mech Sci* 2021;201:106457.
- [103] Schenk M, Guest SD, McShane GJ. Novel stacked folded cores for blast-resistant sandwich beams. *Int J Solids Struct* 2014;51:4196–214.
- [104] Li Q, Zhi X, Fan F. Dynamic crushing of uniform and functionally graded origami-inspired cellular structure fabricated by SLM. *Eng Struct* 2022;262:114327.
- [105] Li Q, Zhi X, Fan F. Quasi-static compressive behaviour of 3D-printed origami-inspired cellular structure: experimental, numerical and theoretical studies. *Virtual Phys Prototyp* 2022;17:69–91.
- [106] Schenk M, Guest SD. Geometry of Miura-folded metamaterials. *Proc Natl Acad Sci U S A* 2013;110:3276–81.
- [107] Harris JA, McShane GJ. Metallic stacked origami cellular materials: Additive manufacturing, properties, and modelling. *Int J Solids Struct* 2020;185–186:448–66.
- [108] Ha NS, Lu G. A review of recent research on bio-inspired structures and materials for energy absorption applications. *Compos Part B Eng* 2020;181:107496.
- [109] Zhang W, Xu J, Yu TX. Dynamic behaviors of bio-inspired structures: Design, mechanisms, and models. *Eng Struct* 2022;265:114490.
- [110] Siddique SH, Hazell PJ, Wang H, Escobedo JP, Ameri AAH. Lessons from nature: 3D printed bio-inspired porous structures for impact energy absorption – A review. *Addit Manuf* 2022;58:103051.
- [111] Lam L, Chen W, Hao H, Li Z, Ha NS, Pham TM. Numerical study of bio-inspired energy-absorbing device using shear thickening fluid (STF). *Int J Impact Eng* 2022;162:104158.
- [112] Lam L, Chen W, Hao H, Li Z, Ha NS. Dynamic crushing performance of bio-inspired sandwich structures with beetle forewing cores. *Int J Impact Eng* 2023;173:104456.

- [113] Yao R, Pang T, He S, Li Q, Zhang B, Sun G. A bio-inspired foam-filled multi-cell structural configuration for energy absorption. *Compos Part B Eng* 2022;238:109801.
- [114] Deng X, Qin S, Huang J. Crashworthiness analysis of gradient hierarchical multicellular columns evolved from the spatial folding. *Mater Des* 2022;215:110435.
- [115] Qin S, Deng X, Liu X. Crashworthiness analysis of bioinspired hierarchical gradient multicell tubes under axial impact. *Thin-Walled Struct* 2022;179:109591.
- [116] Chen J, Huang J, Pan L, Zhao T, Zhang X, Lin H. The 3D lightweight structural characteristics of the beetle forewing: Verification. *Structures* 2021;33:2943–9.
- [117] Zhang W, Yin S, Yu TX, Xu J. Crushing resistance and energy absorption of pomelo peel inspired hierarchical honeycomb. *Int J Impact Eng* 2019;125:163–72.
- [118] He Q, Feng J, Chen Y, Zhou H. Mechanical properties of spider-web hierarchical honeycombs subjected to out-of-plane impact loading. *J Sandw Struct Mater* 2020;22:771–96.
- [119] Yang X, Sun Y, Yang J, Pan Q. Out-of-plane crashworthiness analysis of bio-inspired aluminum honeycomb patterned with horseshoe mesostructure. *Thin-Walled Struct* 2018;125:1–11.
- [120] Fang J, Sun G, Qiu N, Pang T, Li S, Li Q. On hierarchical honeycombs under out-of-plane crushing. *Int J Solids Struct* 2018;135:1–13.
- [121] Hu D, Wang Y, Song B, Dang L, Zhang Z. Energy-absorption characteristics of a bionic honeycomb tubular nested structure inspired by bamboo under axial crushing. *Compos Part B Eng* 2019;162:21–32.
- [122] Zhang W, Yu TX, Xu J. Uncover the underlying mechanisms of topology and structural hierarchy in energy absorption performances of bamboo-inspired tubular honeycomb. *Extrem Mech Lett* 2022:101640.

- [123] Ingrole A, Aguirre TG, Fuller L, Donahue SW. Bioinspired energy absorbing material designs using additive manufacturing. *J Mech Behav Biomed Mater* 2021;119:104518.
- [124] Zhang X, Chen J, Okabe Y, Zhang P, Xiong X, Yu X. Influence of honeycomb dimensions and forming methods on the compressive properties of beetle elytron plates. *J Sandw Struct Mater* 2020;22:28–39.
- [125] Chen J, Zhang X, Okabe Y, Xie J, Xu M. Beetle elytron plate and the synergistic mechanism of a trabecular-honeycomb core structure. *Sci China Technol Sci* 2019;62:87–93.
- [126] Meng L, Liang H, Yu H, Yang J, Li F, Wang Z, et al. The energy absorption and bearing capacity of light-weight bio-inspired structures produced by selective laser melting. *J Mech Behav Biomed Mater* 2019;93:170–82.
- [127] Chen J, Zhang X, Okabe Y, Saito K, Guo Z, Pan L. The deformation mode and strengthening mechanism of compression in the beetle elytron plate. *Mater Des* 2017;131:481–6.
- [128] Chen J, Yu X, Xu M, Okabe Y, Zhang X, Tuo W. The compressive properties and strengthening mechanism of the middle-trabecular beetle elytron plate. *J Sandw Struct Mater* 2020;22:948–61.
- [129] Yang X, Ma J, Shi Y, Sun Y, Yang J. Crashworthiness investigation of the bio-inspired bi-directionally corrugated core sandwich panel under quasi-static crushing load. *Mater Des* 2017;135:275–90.
- [130] Ha NS, Lu G, Xiang X. Energy absorption of a bio-inspired honeycomb sandwich panel. *J Mater Sci* 2019;54:6286–300.
- [131] Kaminski R, Speck T, Speck O. Adaptive spatiotemporal changes in morphology, anatomy, and mechanics during the ontogeny of subshrubs with square-shaped stems. *Am J Bot* 2017;104:1157–67.
- [132] Challapalli A, Li G. 3D printable biomimetic rod with superior buckling resistance designed by machine learning. *Sci Rep* 2020;10:1–9.

- [133] Sun J, Bhushan B. Structure and mechanical properties of beetle wings: A review. *RSC Adv* 2012;2:12606–23.
- [134] Yang ZX, Dai ZD, Guo C. Morphology and mechanical properties of *Cybister* elytra. *Chinese Sci Bull* 2010;55:771–6.
- [135] Chen J, Ni Q-Q, Xie J. The Lightweight Composite Structure and Mechanical Properties of the Beetle Forewing. In: Hu N, editor. *Compos. Their Prop.*, Rijeka: IntechOpen; 2012, p. 359–90.
- [136] Le VT, Ha NS, Goo NS. Thermal Protective Properties of the *Allomyrina dichotoma* Beetle Forewing for Thermal Protection Systems. *Heat Transf Eng* 2019;40:1539–49.
- [137] Iwamoto M, Chen J, Kurashiki K, Ni Q-Q. Chitin fibre and its laminated structure of the fore-wing of beetle. *WIT Trans Built Environ* 2002;59:653.
- [138] Zhang Z, Jia H, Sun J, Tong J. Nanoindentation investigation of the stress exponent for the creep of dung beetle (*Copris ochus* Motschulsky) cuticle. *Bioengineered* 2016;7:357–64.
- [139] Sun J, Wu W, Liu C, Tong J. Investigating the nanomechanical properties and reversible color change properties of the beetle *Dynastes tityus*. *J Mater Sci* 2017;52:6150–60.
- [140] Ji B, Gao H. A study of fracture mechanisms in biological nano-composites via the virtual internal bond model. *Mater Sci Eng A* 2004;366:96–103.
- [141] Huang W, Zaheri A, Jung JY, Espinosa HD, Mckittrick J. Hierarchical structure and compressive deformation mechanisms of bighorn sheep (*Ovis canadensis*) horn. *Acta Biomater* 2017;64:1–14.
- [142] Jaslow CR, Biewener AA. Strain patterns in the horncores, cranial bones and sutures of goats (*Capra hircus*) during impact loading. *J Zool* 1995;235:193–210.
- [143] Sun J, Ling M, Wang Y, Chen D, Zhang S, Tong J, et al. Quasi-Static and Dynamic Nanoindentation of Some Selected Biomaterials. *J Bionic Eng*

2014;11:144–50.

- [144] Jaslow CR. Mechanical properties of cranial sutures. *J Biomech* 1990;23:313–21.
- [145] Lee N, Horstemeyer MF, Rhee H, Nabors B, Liao J, Williams LN. Hierarchical multiscale structure - Property relationships of the red-bellied woodpecker (*Melanerpes carolinus*) beak. *J R Soc Interface* 2014;11.
- [146] Courtney M, Courtney A. Sheep Collisions: the Good, the Bad, and the TBI. *ArXiv Phys Educ* 2007.
- [147] Lee N, Williams LN, Mun S, Rhee H, Prabhu R, Bhattarai KR, et al. Stress wave mitigation at suture interfaces. *Biomed Phys Eng Express* 2017;3:035025.
- [148] Wang L, Cheung Jason JTM, Pu F, Li D, Zhang M, Fan Y. Why do woodpeckers resist head impact injury: A biomechanical investigation. *PLoS One* 2011;6:11120101001.
- [149] Waitukaitis SR, Jaeger HM. Impact-activated solidification of dense suspensions via dynamic jamming fronts. *Nature* 2012;487:205–9.
- [150] Wu X, Zhong F, Yin Q, Huang C. Dynamic response of shear thickening fluid under laser induced shock. *Appl Phys Lett* 2015;106:071903.
- [151] Lim AS, Lopatnikov SL, Wagner NJ, Gillespie JW. Investigating the transient response of a shear thickening fluid using the split Hopkinson pressure bar technique. *Rheol Acta* 2010;49:879–90.
- [152] Pinto F, Meo M. Design and Manufacturing of a Novel Shear Thickening Fluid Composite (STFC) with Enhanced out-of-Plane Properties and Damage Suppression. *Appl Compos Mater* 2017;24:643–60.
- [153] Gürgen S, Kuşhan MC, Li W. Shear thickening fluids in protective applications: A review. *Prog Polym Sci* 2017;75:48–72.
- [154] Gürgen S, de Sousa RJA. Rheological and deformation behavior of natural smart suspensions exhibiting shear thickening properties. *Arch Civ Mech Eng*

2020;20:1–8.

- [155] Lee YS, Wagner NJ. Dynamic properties of shear thickening colloidal suspensions. *Rheol Acta* 2003;42:199–208.
- [156] Fu K, Wang H, Chang L, Foley M, Friedrich K, Ye L. Low-velocity impact behaviour of a shear thickening fluid (STF) and STF-filled sandwich composite panels. *Compos Sci Technol* 2018;165:74–83.
- [157] Afeshejani SHA, Sabet SAR, Zeynali ME, Atai M. Energy Absorption in a Shear-Thickening Fluid. *J Mater Eng Perform* 2014;23:4289–97.
- [158] Yang J, Liu Z, Liu K, Li X, Ma S, Yan Z. Study on the blasting damage of prestressed rock-like specimens with different coupling mediums. *Int J Impact Eng* 2023;181:104758.
- [159] Tan Z, Li W, Huang W. The effect of graphene on the yarn pull-out force and ballistic performance of Kevlar fabrics impregnated with shear thickening fluids. *Smart Mater Struct* 2018;27:075048.
- [160] Lomakin E V., Mossakovsky PA, Bragov AM, Lomunov AK, Konstantinov AY, Kolotnikov ME, et al. Investigation of impact resistance of multilayered woven composite barrier impregnated with the shear thickening fluid. *Arch Appl Mech* 2011;81:2007–20.
- [161] Lee YS, Wetzel ED, Wagner NJ. The ballistic impact characteristics of Kevlar® woven fabrics impregnated with a colloidal shear thickening fluid. *J Mater Sci* 2003;38:2825–33.
- [162] Zhang Q, Qin Z, Yan R, Wei S, Zhang W, Lu S, et al. Processing technology and ballistic-resistant mechanism of shear thickening fluid/high-performance fiber-reinforced composites: A review. *Compos Struct* 2021;266:113806.
- [163] Kanesalingam S, Nayak R, Wang L, Padhye R, Arnold L. Stab and puncture resistance of silica-coated Kevlar–wool and Kevlar–wool–nylon fabrics in quasistatic conditions. *Text Res J* 2019;89:2219–35.
- [164] Wei M, Lin K, Sun L. Shear thickening fluids and their applications. *Mater Des*

2022;216:110570.

- [165] Decker MJ, Halbach CJ, Nam CH, Wagner NJ, Wetzel ED. Stab resistance of shear thickening fluid (STF)-treated fabrics. *Compos Sci Technol* 2007;67:565–78.
- [166] Caglayan C, Osken I, Ataalp A, Turkmen HS, Cebeci H. Impact response of shear thickening fluid filled polyurethane foam core sandwich composites. *Compos Struct* 2020;243.
- [167] Soutrenon M, Michaud V. Impact properties of shear thickening fluid impregnated foams. *Smart Mater Struct* 2014;23.
- [168] Liu X, Huo J, Li TT, Wang H, Wu L, Lin JH, et al. Mechanical properties of a STF capsule filled flexible polyurethane composite foam. *Mater Lett* 2020;269.
- [169] Zhang X, Wang P, Kurkin A, Chen Q, Gong X, Zhang Z, et al. Mechanical response of shear thickening fluid filled composite subjected to different strain rates. *Int J Mech Sci* 2021;196:106304.
- [170] Zhang X, Zhang H, Wang P, Chen Q, Li X, Zhou Y, et al. Optimization of shear thickening fluid encapsulation technique and dynamic response of encapsulated capsules and polymeric composite. *Compos Sci Technol* 2019;170:165–73.
- [171] Wu L, Wang J, Jiang Q, Lu Z, Wang W, Lin JH. Low-velocity impact behavior of flexible sandwich composite with polyurethane grid sealing shear thickening fluid core. *J Sandw Struct Mater* 2020;22:1274–91.
- [172] Zhao F, Wu L, Lu Z, Lin J-H, Jiang Q. Design of shear thickening fluid/polyurethane foam skeleton sandwich composite based on non-Newtonian fluid solid interaction under low-velocity impact. *Mater Des* 2022;213:110375.
- [173] Gürgen S, Fernandes FAO, de Sousa RJA, Kuşhan MC. Development of Eco-friendly Shock-absorbing Cork Composites Enhanced by a Non-Newtonian Fluid. *Appl Compos Mater* 2021;28:165–79.
- [174] Hu Q, Lu G, Hameed N, Tse KM. Dynamic compressive behaviour of shear thickening fluid-filled honeycomb. *Int J Mech Sci* 2022;229:107493.

- [175] Gu ZP, Wu XQ, Li QM, Yin QY, Huang CG. Dynamic compressive behaviour of sandwich panels with lattice truss core filled by shear thickening fluid. *Int J Impact Eng* 2020;143:103616.
- [176] Kiliçaslan C, Güden M, Odaci IK, Taşdemirci A. The impact responses and the finite element modeling of layered trapezoidal corrugated aluminum core and aluminum sheet interlayer sandwich structures. *Mater Des* 2013;46:121–33.
- [177] Wang Y, Zhai X, Wang W. Numerical studies of aluminum foam filled energy absorption connectors under quasi-static compression loading. *Thin-Walled Struct* 2017;116:225–33.
- [178] Yuan L, Dai H, Song J, Ma J, Chen Y. The behavior of a functionally graded origami structure subjected to quasi-static compression. *Mater Des* 2020;189:108494.
- [179] Yang Q, Li Z, Chen W, Hao H. Parametric Study of Truncated Square Pyramid Folded Structure for Effective Energy Absorption under Static and Dynamic Crushing. *J Aerosp Eng* 2022;35:04022086.
- [180] Nieh TG, Higashi K, Wadsworth J. Effect of cell morphology on the compressive properties of open-cell aluminum foams. *Mater Sci Eng A* 2000;283:105–10.
- [181] Wang Z, Liu J, Hui D. Mechanical behaviors of inclined cell honeycomb structure subjected to compression. *Compos Part B Eng* 2017;110:307–14.
- [182] Smart MetalTM stabilized aluminum foam n.d. <https://www.cymat.com/smart-metal/> (accessed August 2, 2021).
- [183] Li Z, Wen X, Wen Y, Chen W, Hao H, Zhang Y, et al. Crashworthiness analysis and parametric investigation on kirigami corrugated structures. *Thin-Walled Struct* 2022;181:110136.
- [184] Ha NS, Pham TM, Vo NH, Hao H. Dynamic crushing characteristics of bio-inspired minimal surface primitive structures. *Compos Struct* 2023;304:116438.

- [185] Li Z, Chen W, Hao H, Yang Q, Fang R. Energy absorption of kirigami modified corrugated structure. *Thin-Walled Struct* 2020;154:106829.
- [186] Zurnaci E, Gökkaya H. The effect of core configuration on the compressive performance of metallic sandwich panels. *Mater Tehnol* 2019;53:859–64.
- [187] Deng X, Qin S, Huang J. Out-of-plane impact analysis for a bioinspired sinusoidal honeycomb. *Mech Adv Mater Struct* 2021.
- [188] Lam L, Chen W, Hao H, Li Z. Crushing behaviour of corrugated tilted honeycomb core inspired by plant stem. *Thin-Walled Struct* 2023;188:110852.
- [189] ASTM. E8/E8M-13 standard test methods for tension testing of metallic materials. ASTM International; 2013.
- [190] Wang L, Sun J, Ding T, Liang Y, Ho JCM, Lai MH. Manufacture and behaviour of innovative 3D printed auxetic composite panels subjected to low-velocity impact load. *Structures* 2022;38:910–33.
- [191] Zhang X, Bi K, Li H, Pham TM, Han Q, Du X. Impact force profiles of steel pipes under drop weight impact. *Structures* 2023;52:1101–15.
- [192] Fujimoto Y, Liu C, Tanaka Y, Shintaku E, Nakanishi T. Thorn-Shape Waveform and Double-Strike Phenomenon Seen in the Impact Force of Soft Materials. *World J Mech* 2015;05:59–69.
- [193] Li H, Chen W, Huang Z, Hao H, Ngo TT, Pham TM, et al. Dynamic response of monolithic and precast concrete joint with wet connections under impact loads. *Eng Struct* 2022;250:113434.
- [194] Li W, Gu YZ, Han LH, Zhao XL, Wang R, Nassirnia M, et al. Behaviour of ultra-high strength steel hollow tubes subjected to low velocity lateral impact: Experiment and finite element analysis. *Thin-Walled Struct* 2019;134:524–36.
- [195] Tachibana S, Masuya H, Nakamura S. Performance based design of reinforced concrete beams under impact. *Nat Hazards Earth Syst Sci* 2010;10:1069–78.
- [196] Day J. Guidelines for ALE Modeling in LS-DYNA. Livermore Software

Technology Corporation; 2009.

- [197] Hao H, Hao Y, Li J, Chen W. Review of the current practices in blast-resistant analysis and design of concrete structures. *Adv Struct Eng* 2016;19:1193–223.
- [198] Gladman B. LS-DYNA keyword user's manual–Volume II–Material Models. Livermore, CA: Livermore Software Technology Corporation; 2020.
- [199] Mooney M. A theory of large elastic deformation. *J Appl Phys* 1940;11:582–92.
- [200] Rivlin RS. Large elastic deformations of isotropic materials IV. further developments of the general theory. *Philos Trans R Soc London Ser A, Math Phys Sci* 1948;241:379–97.
- [201] Liu H, Zhang ET, Wang G, Ng BF. In-plane crushing behavior and energy absorption of a novel graded honeycomb from hierarchical architecture. *Int J Mech Sci* 2022;221:107202.
- [202] Yao S, Chen Z, Xu P, Li Z, Zhao Z. Experimental and numerical study on the energy absorption of polyurethane foam-filled metal/composite hybrid structures. *Metals (Basel)* 2021;11:118.
- [203] Zhu F, Zhao L, Lu G, Wang Z. Structural Response and Energy Absorption of Sandwich Panels with an Aluminium Foam Core under Blast Loading. *Adv Struct Eng* 2008;11:525–36.
- [204] Shah QH, Topa A. Modeling large deformation and failure of expanded polystyrene crushable foam using LS-DYNA. *Model Simul Eng* 2014;2014:1–7.
- [205] Chen J, Fang H, Liu W, Zhu L, Zhuang Y, Wang J, et al. Energy absorption of foam-filled multi-cell composite panels under quasi-static compression. *Compos Part B Eng* 2018;153:295–305.
- [206] Wang X, Yu RP, Zhang QC, Li L, Li X, Zhao ZY, et al. Dynamic response of clamped sandwich beams with fluid-filled corrugated cores. *Int J Impact Eng* 2020;139:103533.

- [207] Fu K, Wang H, Zhang YX, Ye L, Escobedo JP, Hazell PJ, et al. Rheological and energy absorption characteristics of a concentrated shear thickening fluid at various temperatures. *Int J Impact Eng* 2020;139.
- [208] Tran QH, Champliand H, Feng Z, Dao TM. Analysis of the asymmetrical roll bending process through dynamic FE simulations and experimental study. *Int J Adv Manuf Technol* 2014;75:1233–44.
- [209] Li Z, Yang Q, Fang R, Chen W, Hao H. Origami metamaterial with two-stage programmable compressive strength under quasi-static loading. *Int J Mech Sci* 2021;189:105987.
- [210] Zhang J, Karagiozova D, You Z, Chen Y, Lu G. Quasi-static large deformation compressive behaviour of origami-based metamaterials. *Int J Mech Sci* 2019;153–154:194–207.
- [211] Hallquist JO. *LS-DYNA Theory Manual*. Livermore, CA: Livermore Software Technology Corporation; 2006.
- [212] Jing L, Yang F, Zhao L. Perforation resistance of sandwich panels with layered gradient metallic foam cores. *Compos Struct* 2017;171:217–26.
- [213] Chen W, Hao H. Numerical study of blast-resistant sandwich panels with rotational friction dampers. *Int J Struct Stab Dyn* 2013;13.
- [214] Lee S, Barthelat F, Hutchinson JW, Espinosa HD. Dynamic failure of metallic pyramidal truss core materials - Experiments and modeling. *Int J Plast* 2006;22:2118–45.
- [215] Maloy SA, Gray GT, Cady CM, Rutherford RW, Hixson RS. The influence of explosive-driven “Taylor-Wave” Shock prestraining on the structure/property behavior of 304 stainless steel. *Metall Mater Trans A Phys Metall Mater Sci* 2004;35 A:2617–24.
- [216] Chen T, Pauly M, Reis PM. A reprogrammable mechanical metamaterial with stable memory. *Nature* 2021;589:386–90.

Every reasonable effort has been made to acknowledge the owners of copyright material. I would be pleased to hear from any copyright owner who has been omitted or incorrectly acknowledged.

Appendix A Statement of contribution of co-authors

To whom it may concern,

I, Lalin Lam, conducted numerical investigations, data processing and analysis, and wrote the manuscripts for the papers titled as follows. The co-authors reviewed and edited the manuscripts and contributed intellectual input towards the simulations, data processing and data analysis.

- 1. Crushing behaviour of corrugated tilted honeycomb core inspired by plant stem.**
- 2. Dynamic crushing and energy absorption of bio-inspired shear thickening fluid-filled origami metastructure.**

(.....)

I, as co-author, endorse that this level of contribution by the candidate indicated above is appropriate.

(Assoc. Prof. Wensu Chen) (.....)

(Prof. Hong Hao) (.....)

(Assoc. Prof. Zhejian Li) (.....)

To whom it may concern,

I, Lalin Lam, conducted experimental investigations, data processing and analysis, and wrote the manuscript for the paper titled “**Impact performance of sandwich cladding with corrugated tilted honeycomb core**”. The second, third, and fifth co-authors reviewed and edited the manuscript and contributed intellectual input towards the experiments, data processing and data analysis. The fourth co-authors provided assistances including set-up, data recording throughout the impact tests.

(.....)

I, as co-author, endorse that this level of contribution by the candidate indicated above is appropriate.

(Assoc. Prof. Wensu Chen) (.....)

(Prof. Hong Hao) (.....)

(Dr. Zhijie Huang) (.....)

(Assoc. Prof. Zhejian Li) (.....)

To whom it may concern,

I, Lalin Lam, conducted numerical investigations, data processing and analysis, and wrote the manuscript for the paper titled “**Dynamic crushing performance of bio-inspired sandwich structures with beetle forewing cores**”. The co-authors reviewed and edited the manuscript and contributed intellectual input towards the simulations, data processing and data analysis.

(.....)

I, as co-author, endorse that this level of contribution by the candidate indicated above is appropriate.

(Assoc. Prof. Wensu Chen) (.....)

(Prof. Hong Hao) (.....)

(Assoc. Prof. Zhejian Li) (.....)

(Dr. Ngoc San Ha) (.....)

To whom it may concern,

I, Lalin Lam, conducted numerical investigations, data processing and analysis, and wrote the manuscript for the paper titled “**Numerical study of bio-inspired energy-absorbing device using shear thickening fluid (STF)**”. The co-authors reviewed and edited the manuscript and contributed intellectual input towards the simulations, data processing and data analysis.

(.....)

I, as co-author, endorse that this level of contribution by the candidate indicated above is appropriate.

(Assoc. Prof. Wensu Chen) (.....)

(Prof. Hong Hao) (.....)

(Assoc. Prof. Zhejian Li) (.....)

(Dr. Ngoc San Ha) (.....)

(Assoc. Prof. Thong M. Pham) (.....)

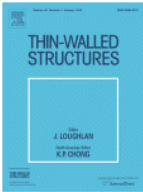
Appendix B Copyright clearance

The proof of the rights granted by publisher for the publication that form the chapters of this thesis are attached below.

Chapter 3

Lam L, Chen W, Hao H, Li Z. Crushing behaviour of corrugated tilted honeycomb core inspired by plant stem. *Thin-Walled Structures* 2023;188:110852.

<https://doi.org/10.1016/j.tws.2023.110852>



Crushing behaviour of corrugated tilted honeycomb core inspired by plant stem
Author: Lalin Lam,Wensu Chen,Hong Hao,Zhejiang Li
Publication: Thin-Walled Structures
Publisher: Elsevier
Date: July 2023
© 2023 The Author(s). Published by Elsevier Ltd.

Journal Author Rights

Please note that, as the author of this Elsevier article, you retain the right to include it in a thesis or dissertation, provided it is not published commercially. Permission is not required, but please ensure that you reference the journal as the original source. For more information on this and on your other retained rights, please visit: <https://www.elsevier.com/about/our-business/policies/copyright#Author-rights>

BACK **CLOSE WINDOW**

Chapter 4

Lam L, Chen W, Hao H, Huang Z, Li Z. Impact performance of sandwich cladding with corrugated tilted honeycomb core. *Structures* 2024;61:106072.

<https://doi.org/10.1016/j.istruc.2024.106072>



Impact performance of sandwich cladding with corrugated tilted honeycomb core
Author: Lalin Lam,Wensu Chen,Hong Hao,Zhijie Huang,Zhejiang Li
Publication: Structures
Publisher: Elsevier
Date: March 2024
© 2024 The Author(s). Published by Elsevier Ltd on behalf of Institution of Structural Engineers.

Journal Author Rights


Please note that, as the author of this Elsevier article, you retain the right to include it in a thesis or dissertation, provided it is not published commercially. Permission is not required, but please ensure that you reference the journal as the original source. For more information on this and on your other retained rights, please visit: <https://www.elsevier.com/about/our-business/policies/copyright#Author-rights>

BACK **CLOSE WINDOW**

Chapter 5

Lam L, Chen W, Hao H, Li Z, Ha NS. Dynamic crushing performance of bio-inspired sandwich structures with beetle forewing cores. International Journal of Impact Engineering 2023;173:104456.

<https://doi.org/10.1016/j.ijimpeng.2022.104456>



Dynamic crushing performance of bio-inspired sandwich structures with beetle forewing cores

Author: Lalin Lam, Wensu Chen, Hong Hao, Zhejian Li, Ngoc San Ha
Publication: International Journal of Impact Engineering
Publisher: Elsevier
Date: March 2023

© 2022 Elsevier Ltd. All rights reserved.

Journal Author Rights

Please note that, as the author of this Elsevier article, you retain the right to include it in a thesis or dissertation, provided it is not published commercially. Permission is not required, but please ensure that you reference the journal as the original source. For more information on this and on your other retained rights, please visit: <https://www.elsevier.com/about/our-business/policies/copyright#Author-rights>

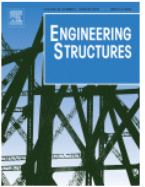
BACK

CLOSE WINDOW

Chapter 6

Lam L, Chen W, Hao H, Li Z. Dynamic crushing and energy absorption of bio-inspired shear thickening fluid-filled origami metastructure. Engineering Structures 2024;299:117122.

<https://doi.org/10.1016/j.engstruct.2023.117122>



Dynamic crushing and energy absorption of bio-inspired shear thickening fluid-filled origami metastructure

Author: Lalin Lam, Wensu Chen, Hong Hao, Zhejian Li
Publication: Engineering Structures
Publisher: Elsevier
Date: 15 January 2024

© 2023 The Author(s). Published by Elsevier Ltd.

Creative Commons

This is an open access article distributed under the terms of the [Creative Commons CC-BY](https://creativecommons.org/licenses/by/4.0/) license, which permits unrestricted use, distribution, and reproduction in any medium, provided the original work is properly cited.

You are not required to obtain permission to reuse this article.


To request permission for a type of use not listed, please contact [Elsevier](https://www.elsevier.com/permissions) Global Rights Department.

Are you the [author](#) of this Elsevier journal article?

Chapter 7

Lam L, Chen W, Hao H, Li Z, Ha NS, Pham TM. Numerical study of bio-inspired energy-absorbing device using shear thickening fluid (STF). International Journal of Impact Engineering 2022;162:104158.

<https://doi.org/10.1016/j.ijimpeng.2022.104158>



Numerical study of bio-inspired energy-absorbing device using shear thickening fluid (STF)

Author: Lalin Lam,Wensu Chen,Hong Hao,Zhejiang Li,Ngoc San Ha,Thong M. Pham

Publication: International Journal of Impact Engineering

Publisher: Elsevier

Date: April 2022

© 2022 Elsevier Ltd. All rights reserved.

Journal Author Rights

Please note that, as the author of this Elsevier article, you retain the right to include it in a thesis or dissertation, provided it is not published commercially. Permission is not required, but please ensure that you reference the journal as the original source. For more information on this and on your other retained rights, please visit: <https://www.elsevier.com/about/our-business/policies/copyright#Author-rights>

[BACK](#) [CLOSE WINDOW](#)